

**Polycyclic Aromatic Hydrocarbons  
in Disks around Young  
Solar-type Stars**

Cover : Spitzer image of the star-forming region L1688 in  $\rho$  Ophiuchus (courtesy NASA/JPL-Caltech/L. Allen, L. Cieza). The large-scale diffuse red emission (mostly on the rear cover) is due to Polycyclic Aromatic Hydrocarbons present in the remnant molecular cloud. Within this cloud, several clusters of young stars with circumstellar disks of dust and gas have formed, which show up in green and red on the front cover. Among these is IRS 48, studied in Chapter 3.

**Polycyclic Aromatic Hydrocarbons  
in Disks around Young  
Solar-type Stars**

PROEFSCHRIFT

ter verkrijging van  
de graad van Doctor aan de Universiteit Leiden,  
op gezag van de Rector Magnificus prof. mr. P. F. van der Heijden,  
volgens besluit van het College voor Promoties  
te verdedigen op dinsdag 23 oktober 2007  
klokke 16.15 uur

door

Vincent Carlo Geers  
geboren te Naarden, Nederland  
in 1980

## PROMOTIECOMMISSIE

Promotor : Prof. dr. E. F. van Dishoeck

Referent : Dr. L. Testi (Istituto Nazionale di Astrofisica, Italy;  
European Southern Observatory)

Overige leden : Dr. B. Brandl  
Prof. dr. C. Dominik (Universiteit van Amsterdam;  
Radboud Universiteit)  
Dr. C. P. Dullemond (Max-Planck Institut für Astronomie,  
Germany)  
Dr. M. R. Hogerheijde  
Prof. dr. K. H. Kuijken

---

# Contents

<b>1</b>	<b>Introduction</b>	<b>1</b>
1.1	Protoplanetary disks and their evolution . . . . .	1
1.2	Polycyclic Aromatic Hydrocarbons . . . . .	3
1.2.1	Structure and excitation of PAHs . . . . .	3
1.2.2	Evolution of PAHs in space . . . . .	5
1.2.3	Why study PAHs? . . . . .	7
1.3	Mid-infrared observations . . . . .	8
1.4	Radiative transfer modeling . . . . .	9
1.5	Outline of this thesis . . . . .	10
1.6	Future prospects . . . . .	11
<b>2</b>	<b>C2D Spitzer-IRS spectra of disks around T Tauri stars. PAH emission features</b>	<b>13</b>
2.1	Introduction . . . . .	14
2.2	Observations and data reduction . . . . .	15
2.3	T Tauri stars with PAH features . . . . .	16
2.3.1	Identification of PAH features . . . . .	16
2.3.2	Spatial extent of PAH emission . . . . .	20
2.3.3	Statistics . . . . .	22
2.4	Analysis of PAH features . . . . .	23
2.4.1	Overview of detected PAH features . . . . .	23
2.4.2	Line flux determination . . . . .	26
2.4.3	Comparison of PAH features . . . . .	28
2.5	PAH emission from disks . . . . .	29
2.5.1	Disk model . . . . .	29
2.5.2	Dependence on spectral type . . . . .	31
2.5.3	Additional UV radiation and relation with H $\alpha$ . . . . .	34
2.5.4	PAH abundance . . . . .	36
2.5.5	Disk geometry . . . . .	36
2.5.6	Model summary . . . . .	39
2.6	Conclusions and future work . . . . .	39
2.7	Appendix: Model tests and comparison with Habart et al. 2004 . . . . .	41
2.8	Appendix: Further constraints of the PAH detection rate toward T Tauri disks . . . . .	45

<b>3</b>	<b>Spatial separation of small and large grains in the transitional disk around the young star IRS 48</b>	<b>49</b>
3.1	Introduction . . . . .	50
3.2	Observations of IRS 48 and data reduction . . . . .	50
3.3	Results . . . . .	52
3.4	Discussion . . . . .	54
3.4.1	Gap in the disk . . . . .	54
3.4.2	Source of central luminosity . . . . .	55
3.4.3	PAH feature strength . . . . .	56
<b>4</b>	<b>Spatially extended PAHs in circumstellar disks around T Tauri and Herbig Ae stars</b>	<b>59</b>
4.1	Introduction . . . . .	60
4.2	Observations and data reduction . . . . .	61
4.2.1	Source selection . . . . .	61
4.2.2	ISAAC L-band spectroscopy . . . . .	62
4.2.3	NACO L-band spectroscopy . . . . .	63
4.2.4	VISIR N-band spectroscopy . . . . .	63
4.2.5	Measuring spatial extent . . . . .	63
4.3	Results and discussion . . . . .	65
4.3.1	PAH detections and statistics . . . . .	65
4.3.2	Spatial extent . . . . .	69
4.4	Conclusions . . . . .	82
4.5	Appendix: Spatial extent models . . . . .	84
<b>5</b>	<b>Lack of PAH emission toward low-mass embedded young stellar objects</b>	<b>89</b>
5.1	Introduction . . . . .	90
5.2	Observations and data reduction . . . . .	91
5.3	Results and discussion . . . . .	93
5.3.1	VLT-ISAAC spectra . . . . .	93
5.3.2	Spitzer spectra . . . . .	95
5.4	Radiative transfer model . . . . .	96
5.4.1	Physical structure . . . . .	96
5.4.2	Treatment of dust and PAHs . . . . .	97
5.4.3	Modeling results . . . . .	99
5.4.4	Summary and caveats . . . . .	105
5.4.5	PAH evolution from clouds to disks . . . . .	107
5.5	Conclusions . . . . .	108
	<b>Bibliography</b>	<b>110</b>
	<b>Nederlandse Samenvatting</b>	<b>113</b>
	<b>Curriculum Vitae</b>	<b>121</b>

**Nawoord**

**123**





---

# CHAPTER 1

---

## Introduction

In the past decade, the topic of formation of low-mass stars comparable to our own Sun has become one of the most rapidly developing fields in modern astrophysics. The arrival of highly sensitive ground and space based telescopes at mid-infrared (IR) wavelengths has enabled us for the first time to study the faint solar-type young stars in nearby molecular clouds during their early formation phases. Many questions still remain unanswered. How many solar-type stars harbour circumstellar disks, what is the typical mass and size of those disks and how many of those remain long enough to allow planet formation to occur? What is the initial composition of the dust in the circumstellar disk and how does it evolve? How can the small grains grow to kilometer-sized planetesimals?

The aim of this thesis is to study the dust around solar-type young stars. In particular, we focus on one specific species of dust, namely the Polycyclic Aromatic Hydrocarbons (PAHs), a family of large molecules, or small grains, that have been widely observed in nearby star forming regions. We address the following questions. Are PAHs present in low-mass young star systems? Are they associated with the remnant cloud environment or located in the disks? What can we learn about their typical size, as a first step toward growth of larger grains? Can we use their presence as tracers of the structure and evolution of disks? How do they influence disk properties? What is their chemical evolution from cloud to disk?

In this introduction first a short overview of the properties and evolution of protoplanetary disks and PAHs is given, followed by a short description of our observing and modeling methods and ending with an outline of this thesis, the main questions and the main results.

### 1.1 PROTOPLANETARY DISKS AND THEIR EVOLUTION

A brief overview of our current understanding of intermediate and low-mass star formation, as it emerged in Shu et al. (1987), is given below. This picture is based and supported by the study of the nearest regions of isolated single-star formation.

Stars are formed within molecular clouds: cold ( $T \sim 10$  K), dark, dense clouds of

gas and dust at relative high density ( $\sim 10^4 - 10^5 \text{ cm}^{-3}$ ), with sizes of up to a parsec and mass between  $10^2$  and  $10^3 M_\odot$ . In terms of mass, the molecular gas dominates, with an assumed gas to dust ratio of 100 to 1. Although initially supported against gravitational collapse by magnetic fields and turbulence, random pockets of local overdensity will inevitably form. These overdense regions can develop into small cores of up to a few solar mass which can collapse, attract more mass and eventually develop into one or more stars. While the cloud matter continues to accrete inwards to the protostar, the non-zero angular momentum of the cloud will cause an accretion disk to form. At this point, the main source of energy is the release of gravitational energy by the contracting proto-star. This source is normally still completely embedded in the molecular cloud and thus unobservable at all wavelengths except at the millimeter and radio wavelengths. This phase is called the Class 0 phase, and is believed to happen relatively quickly (within  $10^4$  years after collapse).

As matter continues to fall onto the disk and accrete through the disk toward the star, a powerful stellar outflow can develop at both stellar poles, along the rotational axis. Evidence for these outflows has been observed in many cases. The accretion process through the disk heats up the dust and gas and, in addition to the millimeter, the source becomes also observable at infrared wavelengths. During this phase, the class 0-I stage, of about  $10^5$  years, the central star and hot dust in the inner disk can still be obscured by the surrounding envelope, depending on the inclination of the system and outflows toward the observer.

Inevitably the cloud material will run out and once the infall of matter onto the disk stops, the accretion rate of mass through the disk will drop off strongly, reducing the disk luminosity. Around the same time, the stellar wind from the central star will start to blow away the remaining low density cloud material above and below the disk and the entire system becomes visible at UV, optical and near-infrared wavelengths. This phase is called the Class II phase and can last from  $10^6$  to  $10^7$  years.

From  $10^6$  to  $10^7$  years, the star further contracts until hydrogen fusion starts in the center and it ends up at the zero-age-main-sequence. Gas and dust start to be removed from the disk through a variety of processes, including photo-evaporation. In the meantime, the dust in the high density regions of the disk is presumed to grow to micron and cm sized pebbles, through collision and sticking. The larger kilometer sized rocky bodies which form will start to capture more dust grains through gravitational attraction. At this point in the dust and disk evolution, these so-called planetesimals will start, through gravitational interaction, to influence the structure of the circumstellar disk and form planets, and the larger of these planets can carve out gaps at particular radii in the disk. Observationally, these gaps of warm dust in the inner parts of the disk become evident through a lack of near- and mid-infrared emission, and these disks are referred to as “cold disks” or elsewhere “transitional” disks. Throughout this phase, an increasing fraction of the small dust grains are no longer of the population that originally accreted from the cloud onto the disk, but rather produced by collisions of planetesimals. The disk is evolving into a so-called “debris” disk.

Eventually, the continued stellar wind and radiation pressure of the central star will erode the dust that has not yet been captured into larger planetesimals and planets

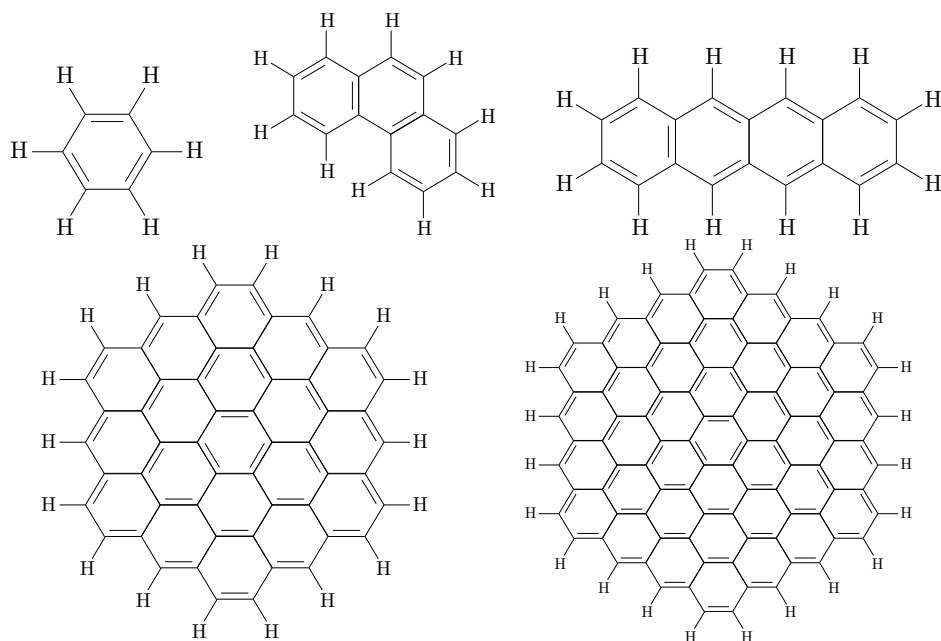


**Figure 1.1:** Molecule structure of benzene ( $C_6H_6$ ), phenanthrene ( $C_{14}H_{10}$ ), tetracene ( $C_{18}H_{12}$ ),  $C_{54}H_{18}$  and  $C_{96}H_{24}$ .

from the circumstellar disk, until only a star and planetary system remains. My thesis is concerned with the class I and II phases, up to the transition to the debris disk stage.

## 1.2 POLYCYCLIC AROMATIC HYDROCARBONS

From the interstellar medium (ISM) to planet-forming disks, the size, structure and composition of dust grains is known to vary significantly. In general, the dust grains are dominated by silicate and carbonaceous grains and are relatively small ( $0.01\text{-}1\ \mu\text{m}$ ) in most environments except for planet-forming disks. In molecular clouds and circumstellar disks, these grains provide the main source of opacity in the mid-infrared, and are important in the coupling of the radiation field with the temperature of the dust and gas. Second, they are believed to be an important catalyst of chemical reactions through grain surface chemistry. PAHs are another repository for one of the most abundant heavy elements, carbon, and play a similar role as small grains in terms of heating and chemistry, while at the same time their molecular structure distinguishes them from big grains, in particular their method of excitation.

### 1.2.1 Structure and excitation of PAHs

PAHs are hexagonal planar rings of carbon atoms, where each carbon atom is bound to 2 other carbon atoms and one hydrogen atom. The 4th electron bond of each carbon atom is shared in a delocalised bond among all neighbouring carbon atoms, which results in a so-called aromatic structure called the benzene ring. A single ring is called

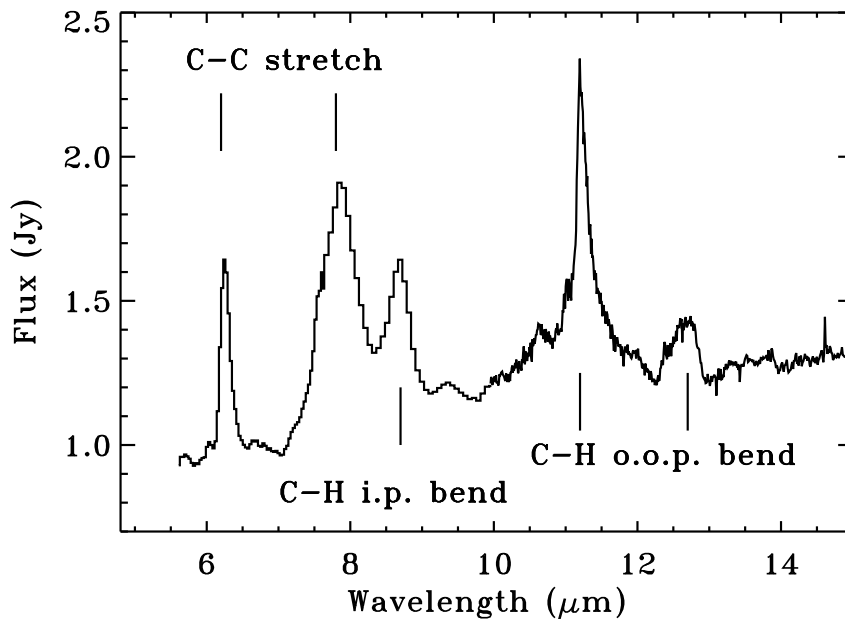


**Figure 1.2:** Spitzer IRS spectrum of the young star RR Tau, with 6.2, 7.7, 8.6, 11.2, 12.7  $\mu\text{m}$  PAH features indicated (i.p.: in plane; o.o.p.: out of plane).

a monocyclic aromatic hydrocarbon (MAH) and forms the building blocks for larger molecules consisting of several MAHs, forming a polycyclic aromatic hydrocarbon (PAH), see Figure 1.1.

The main source of excitation of PAH molecules is through the absorption of (far-) UV photons, which causes a transition to an upper electronic state, although larger optical wavelength photons can also contribute. The molecule quickly makes radiationless transitions to the electronic ground state, converting most of the energy into vibrational energy, through the many available C-C and C-H bonds. Following this, the vibrationally excited molecule cools through vibrational transitions, resulting in radiation of mainly infrared photons. A detailed description of PAH photo-physics is given in Tielens (2005).

PAHs therefore have a very distinct emission spectrum in the mid-IR, dominated by main features at 3.3, 6.2, 7.7, 8.6, 11.2 and 12.7  $\mu\text{m}$  (see Fig. 1.2). These are actually not single features, but rather emission bands, comprised of the large number of vibrational transitions of C-H and C-C bonds, which make up the general structure of the PAHs. In addition, very large PAHs are believed to cause broad emission plateaus underneath these emission bands.

The size of PAHs and the inclusion of elements heavier than hydrogen affect the available vibrational transitions in the molecule and influence the strength and shape of the PAH emission bands. To date, no single PAH emission feature from astronomical observations has been uniquely identified with a single PAH species. A further complication is that within any astrophysical environment, there will likely be a range

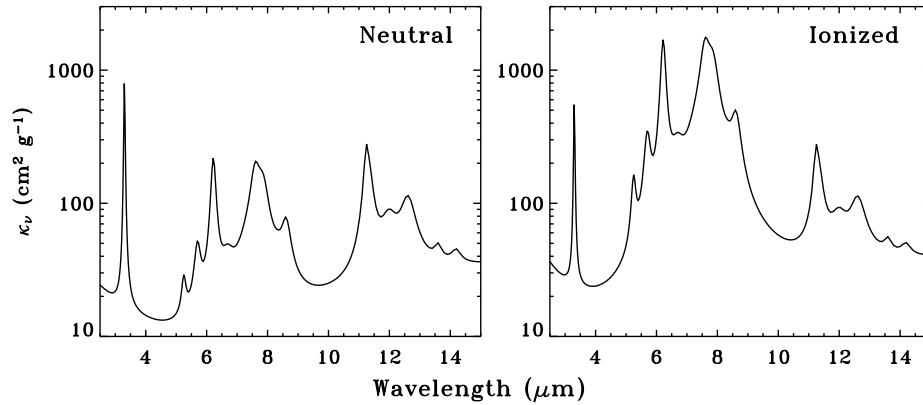


**Figure 1.3:** PAH opacities of neutral (left) and single ionized (right)  $C_{100}H_{24}$ , based on Draine & Li (2007) and Mattiotta et al. (2005). Note the order of magnitude enhancement of the 6.2, 7.7 and 8.6  $\mu\text{m}$  features for the ionized species.

of differently sized and shaped PAHs present, all contributing to the emission bands.

The ionization state of PAHs has a particularly strong effect on the PAH spectrum (e.g. Bauschlicher 2002). Neutral PAH molecules have relatively strong 3.3, 11.3 and 12.7  $\mu\text{m}$  features, all associated with C-H bonds, while ionization will increase the relative strength of the 6.2, 7.7 and 8.6 features which are primarily caused by C-C bonds, see Figure 1.3. Thus, searches for PAHs such as those in this thesis need to cover both classes of features.

## 1.2.2 Evolution of PAHs in space

PAHs have been observed toward a wide range of varying astrophysical environments, ranging from evolved AGB stars, the ISM to young stars with disks, see Figure 1.4 (Hony et al. 2001; Peeters et al. 2002). PAHs are believed to be created in the outflows of carbon-rich AGB stars. The outflow wind combines high density, high temperature and high carbon abundance and thus provides the conditions for PAH formation. The growth of PAHs is believed to occur through the formation of a first monocyclic carbon ring molecule from acetylene, addition of hydrogen atoms to form a MAH, and followed by growth through addition of rings by substitution of H-atoms with hydrocarbons, eventually allowing for chains of rings with typically a few tens to a few hundred carbon atoms.

The outflow of the AGB star deposits the PAH molecules in the ISM, where its evolution is similar to dust. It can still grow by coagulation and clustering, and it can accrete or be accreted onto other dust grains. Hydrogen atoms can be replaced by heavier elements, such as nitrogen. Exposure to high UV fields, cosmic rays or supernova pressure shocks in the medium can cause destruction. Observationally, however, PAHs behave very differently from large dust species. The heat capacity of these 20-100 carbon atom molecules is smaller than that of typical dust grains, which means

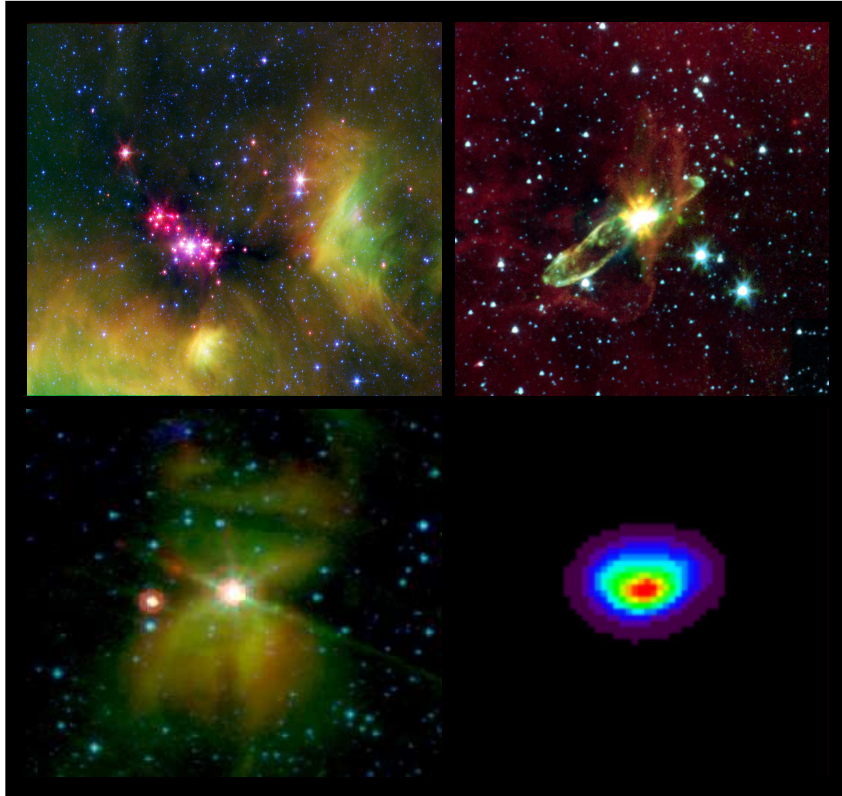


**Figure 1.4:** PAH emission observed toward a variety of astrophysical environments: diffuse interstellar dust in the Serpens star-forming region (PAH  $8 \mu\text{m}$  indicated in green, top-left,  $\sim 2$  pc on the side), molecular cloud with embedded object HH 46 and outflows (PAH  $8 \mu\text{m}$  indicated in red, top-right, 0.7 pc on the side), VV-Ser, young star with disk in remnant cloud (bottom-left,  $5 \times 10^4$  AU on the side), close-up of circumstellar disk around IRS 48 at  $11.25 \mu\text{m}$  (bottom-right, 600 AU on the side). Data in the first three panels all come from the c2d Spitzer Legacy program, the IRS 48 image is taken with VLT-VISIR.

Credits: top-left: Spitzer IRAC+MIPS image of Serpens cluster (courtesy NASA/JPL-Caltech/L. Cieza (UT Austin)); top-right: Spitzer IRAC image of HH46 (NASA/JPL-Caltech/A. Noriega-Crespo (SSC/Caltech), Digital Sky Survey); bottom-left: Spitzer IRAC+MIPS image VV Ser (Pontoppidan et al. 2007, ApJ, 656, 991); bottom-right: VLT-VISIR  $11.2 \mu\text{m}$  image (of IRS 48, Chapter 3.

that they will be transiently heated to high temperatures. This causes PAHs to emit at mid-infrared wavelengths, even in environments where the expected dust temperature in radiative equilibrium with the (inter-)stellar radiation field is expected to be too low for significant mid-IR radiation. This observational presence of PAHs toward many lines of sight, associated not only with AGB outflows, but also with the ISM and nearby star-forming regions, suggests that PAHs are present in these environments, and that they are sufficiently large to prevent destruction. The cosmic abundance of carbon locked up in PAHs in the ISM inferred from mid-IR observations of Galactic cirrus and photo-dissociation regions is  $5 \times 10^{-5}$  with respect to hydrogen, which implies a typical PAH abundance of  $5 \times 10^{-7}$ , considering that the average PAH is estimated to be composed of about 100 carbon atoms.

In the dense environments of molecular clouds, the low temperature leads to the expectation that PAHs are (partly/completely) incorporated into the water and CO ice mantles that form on the surfaces of dust grains. In this phase, grain surface chemistry may play an important role in modifying the composition of the PAHs, most likely through replacement of hydrogen atoms at the periphery with heavier elements or small molecular groups. As will be shown in this thesis, PAH emission is not seen toward YSO's in this embedded phase.

In the class I and II phase, accretion and radiation of the central source heats up the material in the disk, causing evaporation of the ice and enclosed molecules, such as the PAHs, into the gas. The radiation field of the central source is orders of magnitude higher than the interstellar radiation field, both providing more UV to excite the PAHs and make the distinct features reappear. The intense UV is also expected to destroy PAHs located in the inner few AU of the disk.

### 1.2.3 Why study PAHs?

PAHs play an important role in the environments where they are observed. In the ISM, PAHs can dominate the heating and cooling of the gas through photoelectric emission, infrared emission, electronic recombination and collisional cooling between dust and gas. The PAHs are a good tracer of UV, and thus indirectly of star formation in the high opacity environments of molecular clouds and even toward galaxies out to high redshifts.

In circumstellar disks, PAHs provide a tracer of the strength of the stellar radiation field. This is due to the strong dependence of PAH emission on direct excitation by UV and optical emission coupled with a weak dependence on the temperature of the surrounding matter of gas and dust. In particular, PAHs could trace the geometrical structure of localised high opacity regions, such as the geometry of circumstellar disks at larger radii.

PAHs can influence the disk structure. For example, the high opacity of PAHs could significantly reduce the stellar FUV radiation field in the inner disk. Through photoionization PAHs can produce energetic electrons, which form a major heating mechanism for the gas in the upper layers of the disk where gas and dust temperatures are not well coupled. At the same time, this process influences the charge balance in the disk, while the distinct dependence of its IR emission features on the ionization state make PAHs a good tracer of ionization level in the disk.

PAHs can play an important role in the chemistry in circumstellar disks. They are among the largest molecules detected in space, and sometimes rather considered as small grains. The large surface area of PAH molecules has been proposed to be a possible site for surface chemistry, such as for the formation of H<sub>2</sub> and water. In particular in circumstellar disks, where classical grains have grown to large sizes, the formation of H<sub>2</sub> on PAHs may be the most efficient process, thus increasing the influence of PAHs on the entire disk chemistry.

At the start of this thesis, PAHs had been observed with ISO toward about 15 young intermediate-mass Herbig Ae stars (Acke & van den Ancker 2004), but not yet toward

**Table 1.1:** Characteristics of the IR instruments used in this thesis.

	VLT-ISAAC	VLT-VISIR	VLT-NACO	Spitzer IRS (space)
array	1024x1024	256x256	1024 x 1024	128x128 (echelle)
coverage	2.8–4.2 $\mu\text{m}$ spec	7.8–14 $\mu\text{m}$ spec N-band imaging Q-band imaging	3.2–3.8 $\mu\text{m}$ spec	10–35 $\mu\text{m}$ 5–15 $\mu\text{m}$
spectral res. ( $\lambda/\Delta\lambda$ )	600	350	700	low-res: 64–128 high-res: 600
spatial res.	$\sim 0.2''$ or seeing	$\sim 0.15''$ or seeing	$\sim 0.1''$	Short-Low: $\sim 1.8''$ Short-High: $\sim 2.3''$
PAH feature coverage	3.3	8.6, 11.2, 12.7	3.3	6.2, 7.7, 8.6, 11.2, 12.7

solar-mass stars.

### 1.3 MID-INFRARED OBSERVATIONS

Spectroscopic observations provide crucial information about the physical state and composition of the gas and dust. Many of the important dust solid-state features as well as emission lines from gas-phase atoms and molecules occur in the infrared regime.

The past decade has seen the arrival of powerful 8m class telescopes coupled with high resolution, high sensitivity infrared detectors. The results in this thesis are largely driven by the new mid-infrared capabilities available at the Paranal Observatory in Chile operated by the European Southern Observatory and through the launch of the NASA Spitzer Space Telescope. These instruments are briefly described below, their relevant characteristics are summarized in Table 1.1.

The Infrared Spectrometer and Array Camera (ISAAC) mounted on the Very Large Telescope (VLT) Antu allows full L and M-band spectra at moderate spectral resolution and high spatial resolution in a single setting, which makes ISAAC a very efficient instrument for surveys of the 3.3  $\mu\text{m}$  PAH feature. A useful feature of this instrument is the ability to rotate the camera and observing slit. For example, when observing circumstellar disks for which the orientation on the sky is known from previous observations, this allows alignment of the slit parallel or perpendicular to the semi-major axis of the disk, important for studying the spatial extent of features in both directions. The spatial resolution of these observations are often dominated by seeing.

The Naos Conica (NACO) array on VLT-Yepun is a near-infrared detector instrument coupled to an adaptive optics module, which allows observations with unprecedented high spatial resolution, on or close to the diffraction limit of the 8 meter telescopes. This high resolution allows us in Chapter 4 to constrain the origin of dust and 3.3  $\mu\text{m}$  PAH emission on small scales of only 10–30 AU, i.e., comparable to the size of our solar system.

The VISIR spectrometer and imager on VLT-Melipal allows for high sensitivity mid-



infrared spectroscopy and imaging in two atmospheric windows, the 8–13  $\mu\text{m}$  N-band and the 16.5–24.5  $\mu\text{m}$  Q-band. This allowed us to study the spatial extent of small and large grains in Chapter 3, and to survey the 8.6, 11.2 and 12.7  $\mu\text{m}$  PAH features in Chapter 4.

The strong shared advantages of the ground-based instruments are the combination of high spatial resolution with high spectral resolution, but the largest downside is the requirement of observing through the Earth’s atmosphere. Large parts of the infrared spectrum are completely opaque due to atmospheric absorption by water, carbon-dioxide and other molecules. Even between those opaque parts, in the atmospheric windows where the transmission of the atmosphere allows infrared observations, the presence of specific atmospheric absorption lines, such as the 3.31–3.32  $\mu\text{m}$  methane lines, will cause noise in the spectrum of the science object. This will lower the potential sensitivity of instruments, making it hard to observe faint sources. Several PAH features, in particular the strong 6.2  $\mu\text{m}$  band, are completely obscured from Earth.

The NASA Spitzer Space Telescope, launched in August 2003, provides a very sensitive infrared observatory in space and a successor to the ESA Infrared Space Observatory (ISO). It offers imaging at 3.6, 4.5, 5.8, 8.0, 24, 70 and 160  $\mu\text{m}$  and low and moderate resolution spectroscopy from 5–35  $\mu\text{m}$ , which covers all major PAH features with the exception of the 3.3  $\mu\text{m}$  feature. Free from observing through the atmosphere, it has a very high sensitivity. Spitzer spectroscopy obtained in context of the “Cores to Disks” Spitzer Legacy program (‘c2d’) (Evans et al. 2003) is used in Chapter 2 and 5 to survey the presence of PAH features around intrinsically weaker low-mass young stars with disks, sources which were too faint for ISO.

## 1.4 RADIATIVE TRANSFER MODELING

Radiation, recorded in spectra and images, is the only information one can acquire about the distant astronomical objects. The environments of young stellar objects embedded in envelopes or surrounded by circumstellar disks are optically thick at UV, visual and near-infrared wavelengths. Therefore the source of the radiation, the central star, is often completely obscured, its radiation being scattered by the surrounding dust particles and/or absorbed and re-emitted at longer wavelengths. This process influences the dust temperature and thus indirectly also the gas temperature in the disk, which in turn influences the structure of the disk. To properly interpret this information, models of the process of radiative transfer are needed.

In all chapters of this thesis, comparison of spectra and images with model calculations have utilized the radiative transfer model RADMC presented in Dullemond et al. (2001). This is a 3D axisymmetric radiative transfer code, which computes the absorption, scattering and emission of photons, and the dust temperature. Using a ray tracer, the results can be visualized in simulated spectra and images.

As part of this thesis, a separate module computing the PAH emission was included in the RADMC code, allowing the inclusion of excitation of non-thermal quantum-heated grains by UV and optical radiation. This module stores energy received by

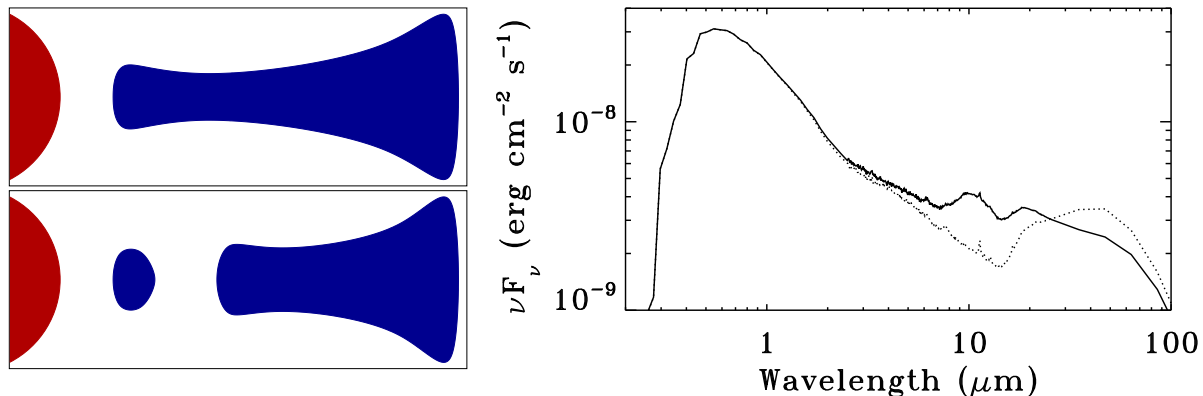


**Figure 1.5:** Model SED of a 6000 K star with a circumstellar disk, sketched in top-left (solid line). The SED of the same model after introducing a gap (density lowered by factor  $10^{-6}$ ) in the disk from 1–40 AU, sketched in bottom-left, is included (dotted line). In this model, the grains have grown to  $\sim 1 \mu\text{m}$  size, so that the silicate emission is suppressed. Note that the sketches are not to scale.

PAHs during an initial radiative transfer calculation, calculates the emission spectrum based on the discrete transitions of the PAH molecules included, following the emission model described in Visser et al. (2007), which is included in the second radiative transfer calculation. This process can be iterated if necessary. Model parameters that can be varied to fit the observations include the disk flaring, the incident radiation field and the PAH abundance. Example SEDs of disks with and without a gap are shown in Figure 1.5.

## 1.5 OUTLINE OF THIS THESIS

In this thesis we address the following main questions. What happens to PAHs in the embedded phase of a forming star? Are PAHs present in low-mass young star systems? Does the PAH emission originate from the envelope or from the disk? What do they tell us about disk structure and evolution and grain growth? What can we say about the evolution of PAHs during star formation and their typical size?

In Chapter 2, we present a survey with Spitzer of PAH features in a sample of intermediate and low-mass stars with disks, and compare the results with model predictions of PAH emission from flaring disks. In Chapter 3, we present VISIR images and a spectrum of IRS 48, a young M-type star with very strong PAH features, which appears to have a 60 AU radius gap in the disk as seen in large grains at  $18.9 \mu\text{m}$  but with PAHs originating from inside the gap. In Chapter 4, we present an ISAAC, VISIR and NACO survey of the spatial extent of PAH features in protoplanetary disks, and compare with model predictions. In Chapter 5, we present an ISAAC and VISIR survey of PAH features toward embedded young stars, and compare the results with model predictions.

The main conclusions of this thesis can be summarized as follows:

- PAHs are shown to be present in several T Tauri disks, but at an abundance 10-100 times lower than standard interstellar values. The detection rate of only 11-14% is small compared to that toward intermediate-mass stars ( $\sim 54\%$ ). At our average derived PAH abundance, PAH emission features around stars with  $T_{\text{eff}} \leq 4200$  K fall below the Spitzer IRS detection limit. The  $11.2 \mu\text{m}$  PAH feature is most easily detected, with the  $7.7$  and  $8.6 \mu\text{m}$  bands readily masked by silicate emission.
- High spatial resolution spectroscopy confirms that the PAH features detected toward young stars are directly associated with the circumstellar disk and not due to the presence of a tenuous envelope.
- A new class of disks with weak mid-IR continuum emission and very strong PAH features is found. This class represents a small percentage ( $\sim 5\%$ ) of the total population of disks surveyed. Among disks around low-mass stars with PAH detections, it represents a large fraction. This is partially due to a detection effect, where the lower disk continuum between  $5\text{--}15 \mu\text{m}$  due to absence of dust results in higher feature-to-continuum ratios for the PAH features. These disks are believed to harbour gaps and/or holes with strong PAH emission originating at, or inwards from, the outer edge of the gap. This evidence for separation of small and large grains implies that their populations evolve differently.
- PAHs are not detected toward the majority ( $\geq 97\%$ ) of a sample of 80 embedded sources. Comparison with model calculations show that this detection rate is consistent with a PAH abundance at least  $20\text{--}50\times$  lower than in the ISM. Variability in luminosity, UV excess and/or envelope mass can change this conclusion to a typical factor of  $10\text{--}20$ . In these cold dense environments, two possibilities for lowering the abundance of a species are recognized: coagulation or dust growth and freeze-out of the PAHs onto larger grains. Thus, PAHs likely enter the protoplanetary disks frozen out on grains.

## 1.6 FUTURE PROSPECTS

The sample of PAHs detected toward T Tauri disks ( $\sim 5$ ) is relatively small (Chapter 2 and 3). A larger sample is needed to draw statistically relevant conclusions on the similarities and/or differences of the kind of PAHs (size, shape, charge) in these sources. Spitzer spectra of several hundred additional sources have been obtained in other programs and can be studied using the Spitzer archive. Detailed studies of feature strength and shape can place PAHs around T Tauri disks in the context of earlier studies toward disks around intermediate mass stars and the ISM. For the small sample of T Tauri detections, high spatial resolution imaging in mid-IR and sub-mm can provide a test for the presence of gaps in small and large dust populations in the disks. Spatially resolved spectroscopy using adaptive optics and/or interferometry with, e.g., VLT-NACO, VLT-MIDI and in the future JWST-MIRI, will allow us to put much stronger constraints on the spatial extent of PAHs in disks, as shown with VLT-NACO for a few sources in Chapter 4.

## REFERENCES

- Acke, B. & van den Ancker, M. E. 2004, *A&A*, 426, 151
- Bauschlicher, Jr., C. W. 2002, *ApJ*, 564, 782
- Draine, B. T. & Li, A. 2007, *ApJ*, 657, 810
- Dullemond, C. P., Dominik, C., & Natta, A. 2001, *ApJ*, 560, 957
- Evans, N. J., Allen, L. E., Blake, G. A., et al. 2003, *PASP*, 115, 965
- Hony, S., Van Kerckhoven, C., Peeters, E., et al. 2001, *A&A*, 370, 1030
- Mattioda, A. L., Hudgins, D. M., & Allamandola, L. J. 2005, *ApJ*, 629, 1188
- Peeters, E., Hony, S., Van Kerckhoven, C., et al. 2002, *A&A*, 390, 1089
- Shu, F. H., Adams, F. C., & Lizano, S. 1987, *ARA&A*, 25, 23
- Tielens, A. G. G. M. 2005, *The Physics and Chemistry of the Interstellar Medium* (Cambridge University Press)
- Visser, R., Geers, V. C., Dullemond, C. P., et al. 2007, *A&A*, 466, 229

---

## CHAPTER 2

---

# C2D Spitzer-IRS spectra of disks around T Tauri stars. PAH emission features

V.C. Geers, J.-C. Augereau, K.M. Pontoppidan, C.P. Dullemond, R. Visser, J.E. Kessler-Silacci, N.J. Evans, II, E.F. van Dishoeck, G.A. Blake, A.C.A. Boogert, J.M. Brown, F. Lahuis and B. Merín

*Astronomy & Astrophysics* 2006, 459, 545<sup>1</sup>

### Abstract

WE search for Polycyclic Aromatic Hydrocarbon (PAH) features towards young low-mass (T Tauri) stars and compare them with surveys of intermediate mass (Herbig Ae/Be) stars. The presence and strength of the PAH features are interpreted with disk radiative transfer models exploring the PAH feature dependence on the incident UV radiation, PAH abundance and disk parameters. Spitzer Space Telescope 5–35  $\mu\text{m}$  spectra of 53 pre-main sequence stars with disks were obtained, consisting of 37 T Tauri, 7 Herbig Ae/Be and 9 stars with unknown spectral type. Compact PAH emission is detected towards at least 9 sources of which 5 are Herbig Ae/Be stars. The 11.2  $\mu\text{m}$  PAH feature is detected in all of these sources, as is the 6.2  $\mu\text{m}$  PAH feature for the 5 sources for which short wavelength data are available. However, the 7.7 and 8.6  $\mu\text{m}$  features appear strongly in only 1 of these 4 sources. Based on the 11.2  $\mu\text{m}$  feature, PAH emission is observed towards at least 4 T Tauri stars, with 1 tentative detection, resulting in a PAH detection rate of 11–14%. The lowest mass source with PAH emission in our sample is T Cha with a spectral type G8. All 4 sources in our sample with evidence for dust holes in their inner disk show PAH emission, increasing the feature/continuum ratio. Typical 11.2  $\mu\text{m}$  line intensities are an order of magnitude lower than those observed for the more massive Herbig Ae/Be stars. Measured line fluxes indicate PAH abundances that are factors of 10–100 lower than standard interstellar values. Conversely, PAH features from disks exposed to stars with  $T_{\text{eff}} \leq 4200$  K

---

<sup>1</sup>Including appendix 2.8, which appeared after publication and provides further constraints on the PAH detection rate, as noted in the modified abstract.

without enhanced UV are predicted to be below the current detection limit, even for high PAH abundances. Disk modeling shows that the 6.2 and 11.2  $\mu\text{m}$  features are the best PAH tracers for T Tauri stars, whereas the 7.7 and 8.6  $\mu\text{m}$  bands have low feature over continuum ratios due to the strongly rising silicate emission.

## 2.1 INTRODUCTION

Polycyclic Aromatic Hydrocarbons (PAHs) have been observed in a wide variety of sources in our own and external galaxies. Within the Milky Way PAHs are observed in the diffuse medium, dense molecular clouds, circumstellar envelopes, and (proto-)planetary nebulae (see Peeters et al. 2004 for a summary). A common characteristic of all of these sources is that they are exposed to copious ultraviolet (UV) photons. The UV radiation drives the molecules into excited electronic states, which subsequently decay to lower electronic states through a non-radiative process called internal conversion, followed by vibrational emission in the available C-H and C-C stretching and bending vibrational modes at 3.3, 6.2, 7.7, 8.6, 11.2, 12.8 and 16.4  $\mu\text{m}$ . Thus, PAH molecules form an important diagnostic of UV radiation.

In recent years, PAH emission has also been detected from disks around young stars in ground-based and *Infrared Space Observatory* (ISO) spectra (Van Kerckhoven et al. 2000; Hony et al. 2001; Peeters et al. 2002; van Boekel et al. 2004; Przygodda et al. 2003; Acke & van den Ancker 2004). The PAH emission is thought to originate from the surface layer of a (flaring) disk exposed to radiation from the central star (cf. models by Manske & Henning 1999; Habart et al. 2004, hereafter H04). Indeed, ground-based spatially resolved observations show that the features come from regions with sizes typical of that of a circumstellar disk (radius  $<12$  AU at 3.3  $\mu\text{m}$ ,  $<100$  AU at 11.2  $\mu\text{m}$ ) (Geers et al. 2005; van Boekel et al. 2004; Habart et al. 2005). Searches for PAHs in disks are important because in addition to being a tracer of the strength of the stellar radiation field and disk geometry, the PAHs also affect the disk structure and chemistry. For example, the high opacity of PAHs at FUV wavelengths (Mattioda et al. 2005) could significantly reduce the stellar UV radiation in the inner disk while photoionization of PAHs produces energetic electrons which are a major heating mechanism for the gas in the upper layers of the disk where the gas and dust temperatures are not well coupled (Jonkheid et al. 2004; Kamp & Dullemond 2004).

Detections of PAH features also provide diagnostics of the presence of small grains in the surface layers of disks and the dust evolution through grain growth and dust settling. Evidence for grain growth has been found from modeling of the silicate features from Herbig Ae/Be (hereafter HAeBe) (van Boekel et al. 2004) and T Tauri disks (Przygodda et al. 2003; Kessler-Silacci et al. 2005, 2006) and more indirectly from the modeling of the observed  $\text{H}_2$  emission features from T Tauri disks (Bergin et al. 2004). PAHs are considered to be on the small end of the size distribution of grains. An important question is whether PAHs have a different timescale for settling and/or growth compared to that of larger silicate/carbon dust grains.

So far, most data obtained on PAHs refer to relatively bright features in the spectra of intermediate mass HAeBe stars. A recent ISO spectroscopic survey has detected

PAH features, in particular the most frequently observed  $6.2\ \mu\text{m}$  feature, towards 57% of a sample of 46 HAeBe stars (Acke & van den Ancker 2004). Meeus et al. (2001) classified the ISO observed spectral energy distributions (SEDs) of these intermediate mass young stars into two groups (group I and II). Dominik et al. (2003) interpreted these SEDs in the context of a passive disk model with a puffed-up inner rim (Dullemond et al. 2001) and proposed that group I sources with larger mid-infrared excess have flaring disks while group II sources are consistent with small and/or self-shadowed disks. Acke & van den Ancker (2004) showed that the group I sources with strong mid-infrared relative to near-infrared excess display significantly more PAH emission than the group II sources with weaker mid-infrared excesses, consistent with the idea that the PAH emission originates mostly from the disk surface.

The arrival of the Spitzer Space Telescope (Werner et al. 2004) with the InfraRed Spectrograph (IRS) (Houck et al. 2004) provides the opportunity to extend these studies to disks around fainter low mass T Tauri stars. For sources of spectral type G and later, the stellar UV field is orders of magnitude weaker than for HAeBe stars, which will directly affect the PAH excitation and emission. On the other hand, enhanced UV radiation has been detected for some T Tauri stars (e.g., Costa et al. 2000, Bergin et al. 2003). Such an enhanced UV field should be directly reflected in the intensity of the PAH features if these molecules are present in normal abundances. Furthermore, ionized PAHs can be excited by less energetic, optical photons from these cooler stars (Mattioda et al. 2005).

In this paper we present detections of PAH features toward T Tauri stars from our initial set of Spitzer IRS 5–38  $\mu\text{m}$  spectroscopic observations that were taken as part of the Spitzer Legacy program “From Molecular Cores to Planet-Forming Disks” (Evans et al. 2003) (hereafter c2d). The c2d targets consist of a large number of sources with infrared excess in five of the nearest large star-forming regions: Chamaeleon, Lupus, Ophiuchus, Perseus and Serpens. In Paper I, the silicate 10 and 20  $\mu\text{m}$  features from pre-main sequence stars with disks are presented and analyzed (Kessler-Silacci et al. 2006). The data are used here to search for PAH features and address a number of outstanding questions. For how many low mass stars can PAH features be found and how does this compare to HAeBe stars? Can limits be put on the abundance of PAHs and thus indirectly on that of the smallest grains? Which factors influence the appearance of PAH features in disks? Can we quantify any additional UV or optical radiation from the strength of the PAH features?

Section 2.2 describes the sample selection, observations and reduction method. The results for the observed PAH features are presented in Sect. 2.3 and discussed in Sects. 2.4 and 2.5. Conclusions are presented in Sect. 2.6.

## 2.2 OBSERVATIONS AND DATA REDUCTION

Mid-infrared spectra were obtained for intermediate and low mass stars with circumstellar disks with the IRS aboard Spitzer as part of the c2d Legacy program. All targets were observed with the Short-High (SH) module (spectral resolving power of  $R \sim 600$ ) covering the wavelength range 10–20  $\mu\text{m}$  and thereby potential PAH features at 11.2

and  $12.8\ \mu\text{m}$ . For a fraction of our sources, Short-Low (SL) observations ( $R \sim 100$ ,  $5\text{--}14.5\ \mu\text{m}$ ) were obtained as well, which cover the  $6.2$ ,  $7.7$ ,  $8.6$ ,  $11.2$  and  $12.8\ \mu\text{m}$  PAH features. For the remainder of our sources, the SL observations are in the Guaranteed Time Observation (GTO) IRS program (J.R. Houck) and were at the time of paper submission not yet available.

The original sample selection of the c2d program is described in Evans et al. (2003). In our sample of sources observed to date there are 7 HAeBe stars, 38 T Tauri stars and 9 sources without known spectral types. These include the 40 T Tauri stars and 7 HAeBe stars in Kessler-Silacci et al. (2006), although we label 4 of their T Tauri sources here as “unclassified” for lack of spectral type (RNO 15, IRAS 03446+3254, VSSG1, CK 4) and we label 1 of their HAeBe stars here as a T Tauri star since it has spectral type M6 (DL Cha). In addition, we have added the c2d IRS spectra taken for 1 HAeBe star (HD101412), 1 T Tauri star, Sz 84, and 5 sources without known spectral types (EC 69, EC 88, EC 90, EC 92, RNO 91). Our current sample of 54 sources is therefore comparable in size to that of the HAeBe stars observed with ISO. We grouped the sample sources in intermediate and low mass young stars following Thé et al. (1994), as HAeBe stars with spectral types of F7 and earlier, and T Tauri stars with spectral type F8 and later. A summary of the properties of all disk sources can be found in Kessler-Silacci et al. (2006, Paper I) and Merín et al. (in prep.). The sample includes the spectrum of an off-position, taken toward the Ophiuchus cloud at a position devoid of infrared sources, to compare with a typical interstellar medium PAH spectrum.

All spectra were extracted from the SSC pipeline version S12.0.2 BCD images, using the c2d reduction pipeline (Kessler-Silacci et al. 2006 and Lahuis, in preparation). The processing includes bad-pixel correction through interpolation using a source profile fit in the cross-dispersion direction. The source profile fitting also gives an estimate of the local sky contribution in the high-resolution spectra. The extracted spectra are defringed using the IRSFRINGE package developed by the c2d team and individual orders are in some cases corrected by small scaling corrections ( $\lesssim 5\%$ ) to match the order with the shortest wavelength. Sky subtraction is applied and in a few cases the SH module is scaled down ( $\lesssim 5\%$ ) in flux to match the SL spectrum.

## 2.3 T TAURI STARS WITH PAH FEATURES

### 2.3.1 Identification of PAH features

Among the 54 disk sources observed to date, a relatively small sample of 8 sources shows one or more clear emission feature that we attribute to PAHs (Fig. 2.1). Table 2.1 summarizes the characteristics of these sources. They consist of 3 T Tauri stars and 5 HAeBe stars. Besides the PAH features, some sources show the  $\text{H}_2$  S(2) line, whereas the  $[\text{N}_e\text{II}]$   $12.8\ \mu\text{m}$  line is detected toward T Cha. Unlabelled narrow features are likely spurious.

Disk sources with PAH emission features were identified as follows. When both SL and SH spectra are available, we required detection of both a clear  $11.2\ \mu\text{m}$  feature and a clear  $6.2$ ,  $7.7$  and/or  $8.6\ \mu\text{m}$  feature. For sources where only a SH spectrum is



**Table 2.1:** Sources with potential PAH emission and their characteristics

Name	RA (J2000)	Dec (J2000)	AOR key	Modules <sup>a</sup>	Dist. [pc]	Sp. Type	H $\alpha$ (Å)	Ref
LkH $\alpha$ 330	03 45 48.3	+32 24 12	0005634816	SL LL1 SH LH	250	G3e <sup>e</sup>	11.4 <sup>b</sup> -20.3	3; 4,5; 4,5
RR Tau	05 39 30.5	+26 22 27	0005638400	SL LL1 SH LH	160	A0e-A0IVe <sup>e</sup>	21.2	11; 12,13; 5
HD 98922	11 22 31.7	-53 22 12	0005640704	SH LH	>540 <sup>f</sup>	B9Ve <sup>e</sup>	27.9	1; 17; 10
HD 101412	11 39 44.5	-60 10 28	0005640960	SL SH LH	160	B9.5Ve <sup>e</sup>	20.4	10; 16; 10
T Cha	11 57 13.5	-79 21 32	0005641216	SH LH	66 <sup>+19</sup> <sub>12</sub>	G8e <sup>e</sup>	2-10	1; 2; 2,18
HD 135344	15 15 48.4	-37 09 16	0005657088	SH LH	140	F4Ve	17.4	8; 9; 10
EM* SR 21 N	16 27 10.3	-24 19 13	0005647616	SH LH	125	G2.5	0.54	6; 7; 19
VV Ser	18 28 47.9	+00 08 40	0005651200	SL SH LH	259	A0Ve	22-51 <sup>c</sup> -81.3	14; 13; 15,4,10
Off-position	16 24 00	-24 00 00	0005654272	SH LH	-	-	-	-
VSSG 1 <sup>d</sup>	16 26 18.9	-24 28 20	0005647616	SH LH	125	...	...	6; -; -
Haro 1-17 <sup>d</sup>	16 32 21.9	-24 42 15	0011827712	SL LL1 SH LH	125	M2.5e <sup>e</sup>	15	6; 2; 2

<sup>a</sup> SL = SL1 + SL2<sup>b</sup> average from 3 measurements<sup>c</sup> average from 19 measurements<sup>d</sup> PAH feature detected in background spectrum, not associated with the source<sup>e</sup> label 'e' added to spectral type here, based on H $\alpha$  > 0, not taken from reference.<sup>f</sup> distance uncertain

References for distance; spectral type; H $\alpha$ : 1: van den Ancker et al. (1998), 2: Alcalá et al. (1993), 3: Enoch et al. 2005, 4: Fernandez et al. (1995), 5: Cohen & Kuhl (1979), 6: Assumed distance to Oph cloud (de Geus et al. 1989), 7: Prato et al. (2003), 8: Acke & van den Ancker (2004), 9: Dunkin et al. (1997), 10: Acke et al. (2005), 11: Assumed distance to Taurus-Auriga cloud Kenyon et al. (1994), 12: Hernández et al. (2004), 13: Mora et al. (2001), 14: Straizys et al. (1996), 15: Finkenzeller & Mundt (1984), 16: Thé et al. (1994), 17: Houk (1978), 18: Alcalá et al. (1995), 19: Martin et al. (1998).

Note: sources in the bottom portion of the Table have spectra with PAH features that are fully attributed to background emission.

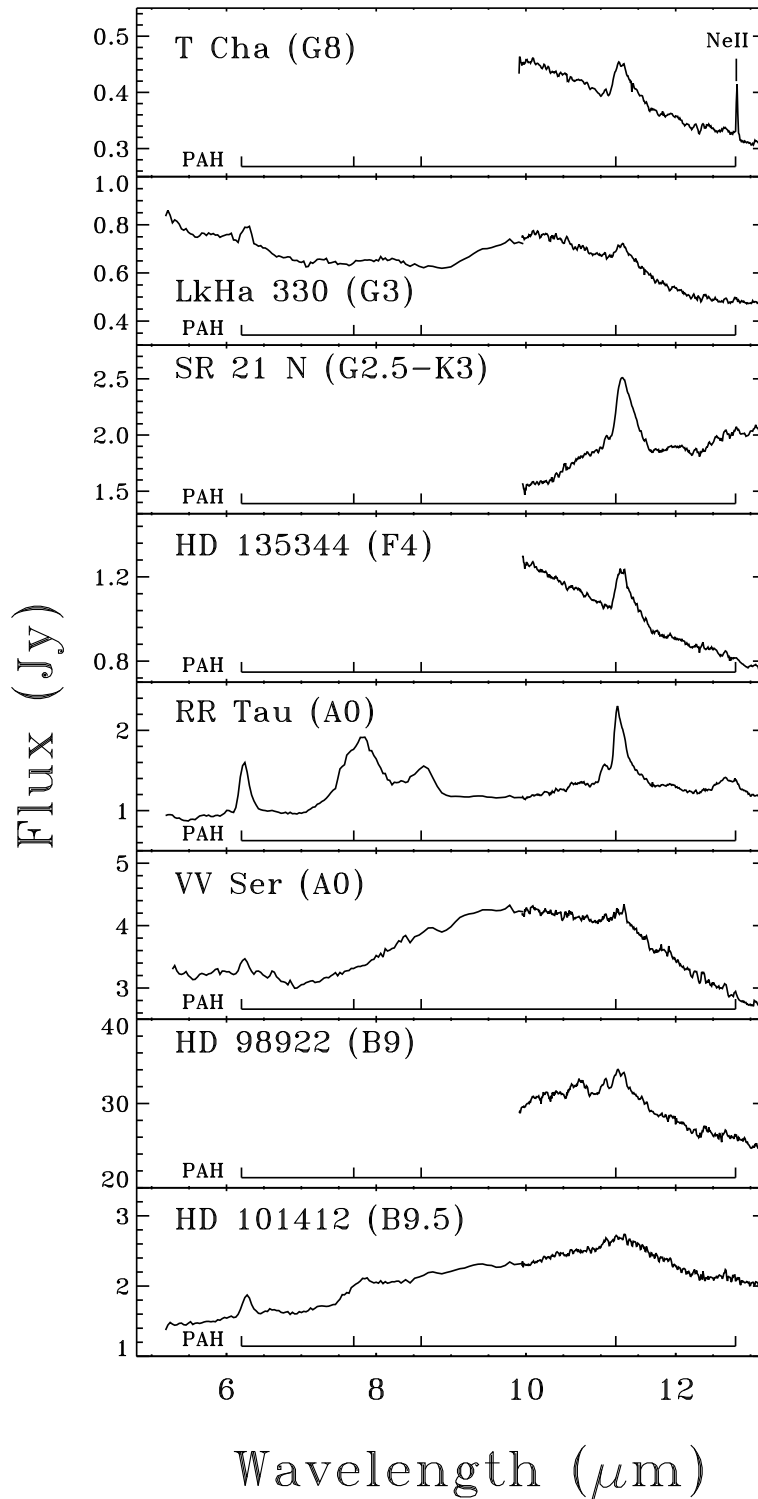


**Figure 2.1:** Spitzer IRS spectra of sources with PAH features, comprised of the SL (5–10  $\mu\text{m}$ ) and SH (10–20  $\mu\text{m}$ ) modules. The location of PAH features is indicated with markers at 6.2, 7.7, 8.6, 11.2 and 12.8  $\mu\text{m}$ .

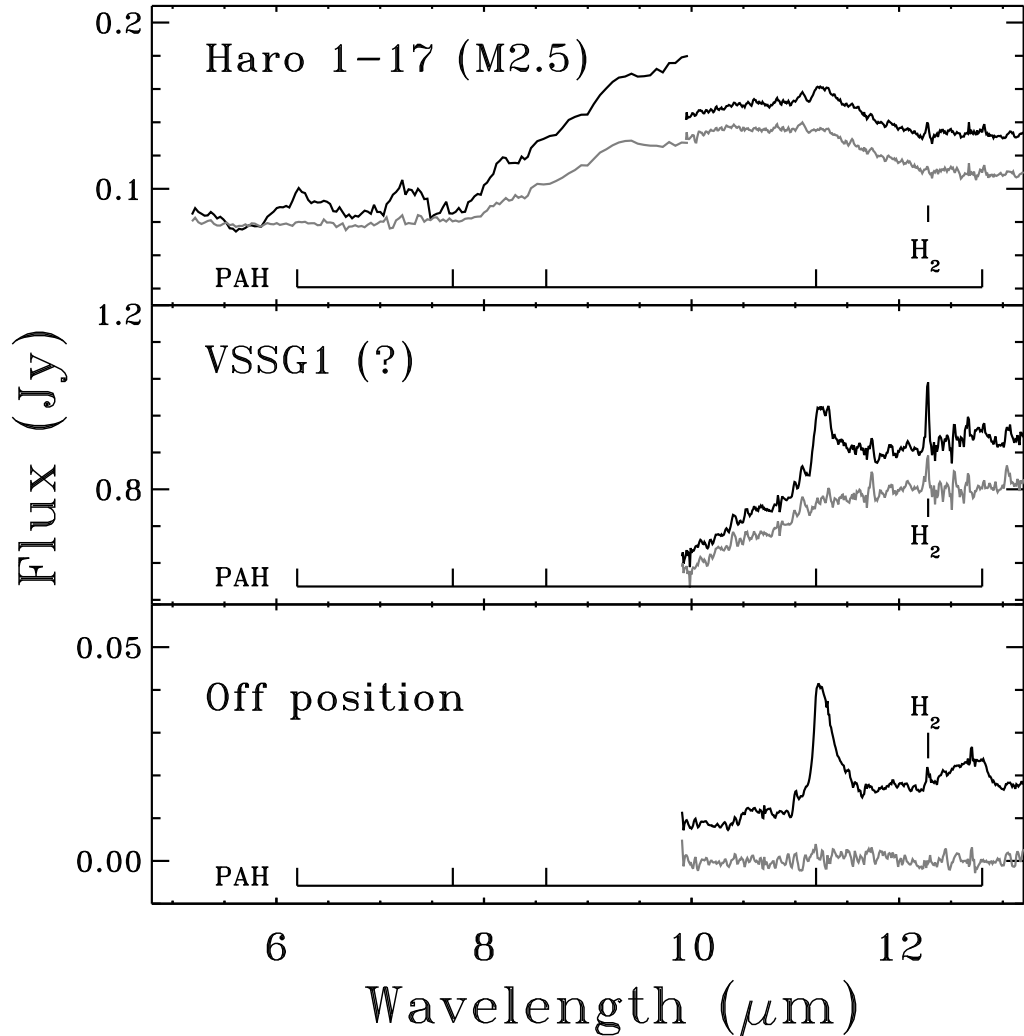


**Figure 2.2:** Spitzer IRS spectra (black line) of sources with PAH features that are associated with extended cloud emission, comprised of the SL (5–10  $\mu\text{m}$ ) and SH (10–20  $\mu\text{m}$ ) modules. The extended emission corrected spectrum is shown in grey. The location of PAH features is indicated with markers at 6.2, 7.7, 8.6, 11.2 and 12.8  $\mu\text{m}$ .

available ( $\lambda > 10 \mu\text{m}$ ), the identification is more critical and largely relies on both the presence of a clear feature at 11.2  $\mu\text{m}$  and its shape. We compared potential 11.2  $\mu\text{m}$  features with that observed in the off-position spectrum and selected the sources with the lowest residuals, see Sect. 2.4.3.

This method can introduce a bias against sources with mixed crystalline silicate and PAH features, because crystalline forsterite has a characteristic feature at almost the same central wavelength as the 11.2  $\mu\text{m}$  PAH feature. To distinguish between these two possible assignments, we searched for other crystalline silicate features at wavelengths longer than 11.2  $\mu\text{m}$  (e.g. 16.2, 18.9, 23.7 and 33.6  $\mu\text{m}$ ). The large wavelength coverage out to 35  $\mu\text{m}$  is a significant advantage compared with ground-based data. Three of

the five HAeBe and 2 of the 3 T Tauri sources show (tentative) evidence for crystalline silicates at longer wavelengths, indicated in Table 2.2 (Kessler-Silacci et al. 2006). In these sources, a contribution from crystalline silicates to the observed 11.2–11.3  $\mu\text{m}$  feature cannot be excluded. The sources illustrate well the difficulties inherent in the identification of PAH emission features at 11.2  $\mu\text{m}$  when lacking any information on the presence/absence of other characteristic PAH features at shorter wavelengths. We note also that the 11.2  $\mu\text{m}$  PAH feature can be blended with the broad amorphous silicate feature whose strength and spectral width vary with grain size. This may have led us to miss sources with weak 11.2  $\mu\text{m}$  emission from PAHs (see discussion in Sect. 2.3.3), although the characteristic shape of the 11.2  $\mu\text{m}$  PAH feature can help in distinguishing between PAHs and silicates, as discussed in Sect. 2.4.3.

Finally, sources with PAH features but showing silicate and/or ice features in absorption have been excluded from the sample presented here. For comparison, Fig. 2.2 includes observations of the off-source spectrum and of two more late type sources, Haro 1-17 and VSSG1 which were selected on the above mentioned criteria but for which background extraction shows that the PAH emission features are fully associated with the extended cloud emission (see below).

### 2.3.2 Spatial extent of PAH emission

An important question is whether the PAH emission originates primarily from the star+disk system or from an extended nebulosity around the star. To properly answer this question, either spatially resolved spectra or images in specific PAH band filters (both at feature wavelength and slightly off-peak for determination of strength and extent of continuum emission) with sufficient (subarcsec) spatial resolution are required. Since such data are lacking for our sample we use the extracted background and long-slit spectra to provide constraints on the extent of the emission.

The SL spectra are taken using long-slit spectroscopy and the 2D spectral images can be used to determine if the features are seen extended along the entire width of the slit. An example 2D spectral image of module SL1 is shown for RR Tau in Fig. 2.3, where no extended emission is seen along the slit. The pixel size of the SL module is 1.8'', which means that any feature originating from a region smaller than 2 pixels (e.g. 540 AU at 150 pc) will be spatially unresolved. A similar lack of extended emission in SL1 is seen for all of our PAH sources with the exception of Haro 1-17. Thus, the PAH emission for these sources is constrained to originate from a region of at most 3.6''.

The SL spectra presented have been corrected for the estimated background contribution (see Sect. 2.2). In 4 of the 5 SL spectra (LkH $\alpha$  330, RR Tau, HD 101412 and VV Ser), the features remain after background subtraction and are concluded to be associated with the source. However, for 1 source, Haro 1-17, the sky-corrected SL spectrum shows no PAH features (see Fig. 2.2). The PAH emission seen towards this source is concluded to be entirely due to background emission.

A number of the sources were only observed in SH for which the width of the slit is too small to directly extract the continuum flux outside the source profile. Here, the background contribution is estimated from fitting a standard star source profile plus

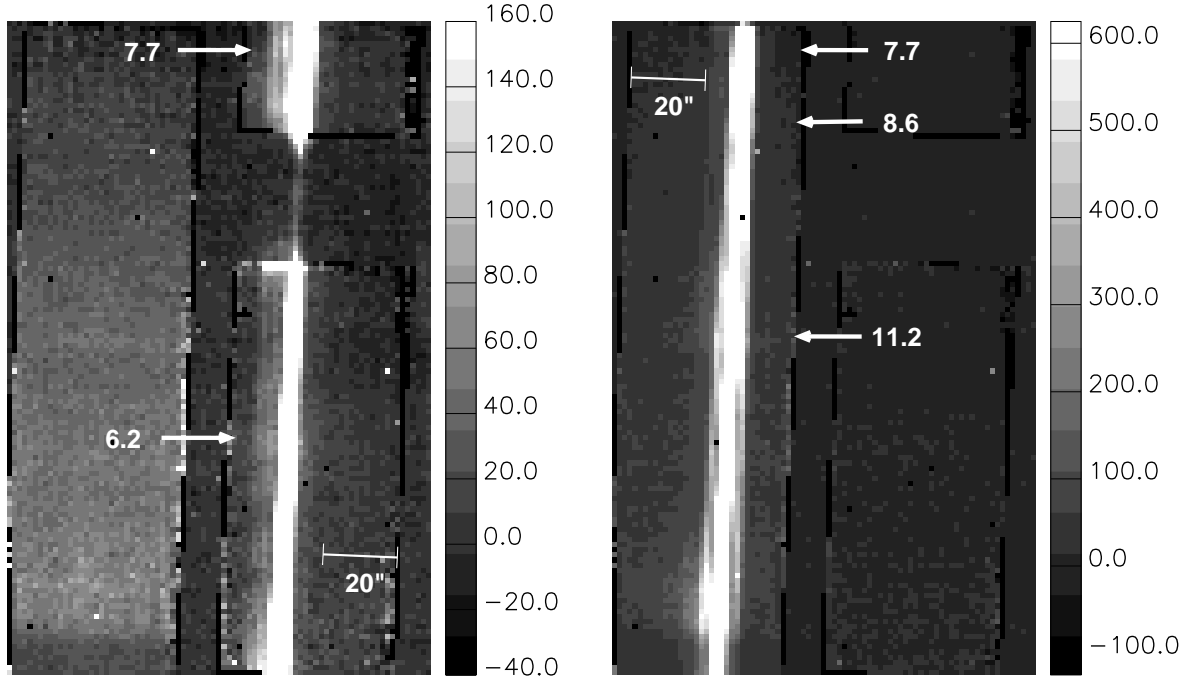


**Figure 2.3:** 2D spectral image of modules SL2 (left panel) and SL1 (right panel) for RR Tau. The quantity shown is the ADU in units of  $e^-s^{-1}$ . The positions of the 6.2, 7.7, 8.6 and 11.2  $\mu\text{m}$  PAH features are indicated with labels. The horizontal bar at bottom right of the left panel and top left of the right panel indicates a spatial extent of 20''.

a flat continuum flux to the measured source profile. This background subtraction is more difficult, since the small slit length of only 11.2'' (5 pixels) makes the source profile fits less accurate.

For all presented sources, the SH source and sky spectra were inspected for PAH features. Two SH background spectra, one with extended PAH features (VSSG1) and one without (RR Tau) are shown in Fig. 2.4. The extracted background spectra for SH show no PAH features for 8 of the 10 sources in our sample with PAH emission. The two sources with features in the background spectra are Haro 1-17 and VSSG1. In both cases, removing the background emission entirely removes the 11.2  $\mu\text{m}$  PAH feature from the source spectrum (Fig. 2.2). It is concluded that for these two sources the PAH features are fully due to background emission.

The environment around one source, the Herbig Ae star VV Ser, is discussed extensively by Pontoppidan et al. (2006). Based on IRAC and MIPS images, it is shown that VV Ser is surrounded by a bright and extremely large ( $\sim 6'$ ) nebulosity emitting at 8, 24 and 70  $\mu\text{m}$ , which is not seen in near infrared images. They conclude that the emission is due to a mix of quantum-heated PAHs and Very Small Grains (VSGs) present

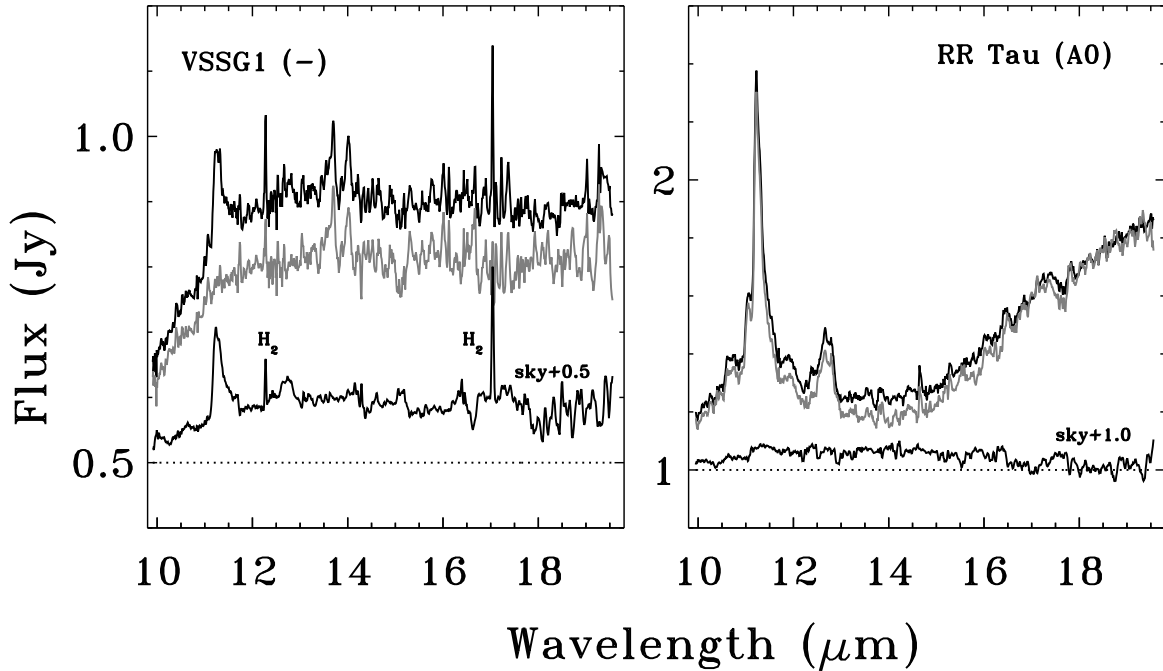


**Figure 2.4:** IRS SH spectra for VSSG 1 and RR Tau. Bottom (black): extracted sky spectrum. Middle (grey): source spectra corrected for background. Top (black): source spectra. The sky spectra are shifted by +0.5 and +1.0 Jy respectively for purpose of clarity.

in the low-density nebula. The PAH emission lines in the spectrum must originate from within  $1.8'' - 2.35''$  or 450 – 600 AU (half-slit width SL–SH). In their best-fit model they require a central cavity of 15000 AU, so the extended nebulosity is not expected to account for the observed PAH features although they note that it cannot be ruled out that a small clump of PAH material is present nearer to the star. Here we assume the emission is from PAHs in the circumstellar disk.

In summary, we conclude that the PAH emission from most of our sources does not originate from extended diffuse fore- or background emission and must instead originate from the observed young stars with disks.

### 2.3.3 Statistics

Within our current c2d sample, clear PAH features are detected in most (5 out of 7) HAeBe stars while only 3 out of 38 T Tauri stars show features consistent with the presence of PAH molecules. Interestingly, the PAH detection rate is 100% for the 4 sources (HD135344, SR 21N, LkH $\alpha$  330 and T Cha) with SEDs characteristic of cold disks, i.e., sources with SEDs that lack excess emission in the 3–13  $\mu\text{m}$  region, indicative of an inner hole in the dust disk (Brown et al., in prep). These 4 sources are also the 4 lowest mass sources (spectral type F4 – G8) with PAH detections.

The c2d sample of PAH detections is biased towards sources with either a strong

11.2  $\mu\text{m}$  feature or multiple PAH features from SH and SL observations. This excludes potential sources with weak PAH features for which only SH observations are available now: since we cannot assign the origin of this 11.2  $\mu\text{m}$  feature to either PAH or crystalline forsterite, these sources are, for now, excluded. This includes 17 sources with tentative 11.2  $\mu\text{m}$  detections: 14 T Tauri stars, 1 Herbig Ae star and 2 unclassified sources. The 14 T Tauri stars are DoAr 24E, EC 82, GW Lup, GY 23, HT Lup, Krautter's Star, RU Lup, SX Cha, SY Cha, SZ 73, VW Cha, VZ Cha, V710 Tau (binary) and WX Cha. Future SL data will be able to confirm or dismiss the presence of PAHs in these sources.

Finally, in the current sample there are 28 sources with no clear 11.2  $\mu\text{m}$  PAH feature, consisting of 1 Herbig Ae star, 21 T Tauri stars and 6 sources with no known spectral type. From our present sample, the lower limit to the detection rate of PAH emission features toward T Tauri stars is about 8%. This detection rate goes up to 45% if tentative detections are included. PAH emission is only detected toward the 3 more massive T Tauri stars of spectral type G of our sample, which consists mostly of K–M type stars.

The rather small fraction (8%) of low mass stars in our c2d sample with PAH emission features, based on the 11.2  $\mu\text{m}$  PAH feature, contrasts with the large fraction (57% according to Acke & van den Ancker 2004) for intermediate mass stars detected with ISO based on the 6.2  $\mu\text{m}$  PAH feature. If only the 11.2  $\mu\text{m}$  features are considered, their detection rate drops to 48% based on their Table 3. However, this potentially includes sources with only crystalline silicate emission.

## 2.4 ANALYSIS OF PAH FEATURES

### 2.4.1 Overview of detected PAH features

Table 2.2 summarizes the detected PAH features and measured line fluxes. The spectrum of RR Tau nicely shows all the main PAH bands detectable in the IRS spectral window at 6.2, 7.7, 8.6, 11.2, 12.8  $\mu\text{m}$  (Fig. 2.1) and even 16.4  $\mu\text{m}$  (not shown). In contrast with the other sources, it has clear 7.7 and 8.6  $\mu\text{m}$  features, attributed to C–C stretching transitions and C–H in plane bending transitions. These features are either less obviously detected above the silicate continuum or simply absent in the 4 other sources with SL spectra. LkH $\alpha$  330 is a clear example of a spectrum with a 6.2  $\mu\text{m}$  C–C stretching feature and a 11.2  $\mu\text{m}$  C–H out-of-plane bending feature but no 7.7, 8.6 nor 12.8  $\mu\text{m}$  features. The 7.7 and 8.6  $\mu\text{m}$  features are generally found to be well correlated with the 6.2  $\mu\text{m}$  feature (Peeters et al. 2002) and their absence is thus puzzling in our high sensitivity spectra. Spoon et al. (2002) show that silicate absorption can strongly mask the 8.6  $\mu\text{m}$  PAH feature; in our case the silicate is in emission, however. According to Acke & van den Ancker (2004) (see their Table 3), four HAeBe stars observed with ISO similarly show 6.2 and 11.2  $\mu\text{m}$  emission but no features at 7.7 or 8.6  $\mu\text{m}$ . Two of these sources, HD 163296 and VV Ser, are also in the c2d sample (the other two are HD 142666 and HD 144432). This absence is further discussed in Sect. 2.5.5, in the

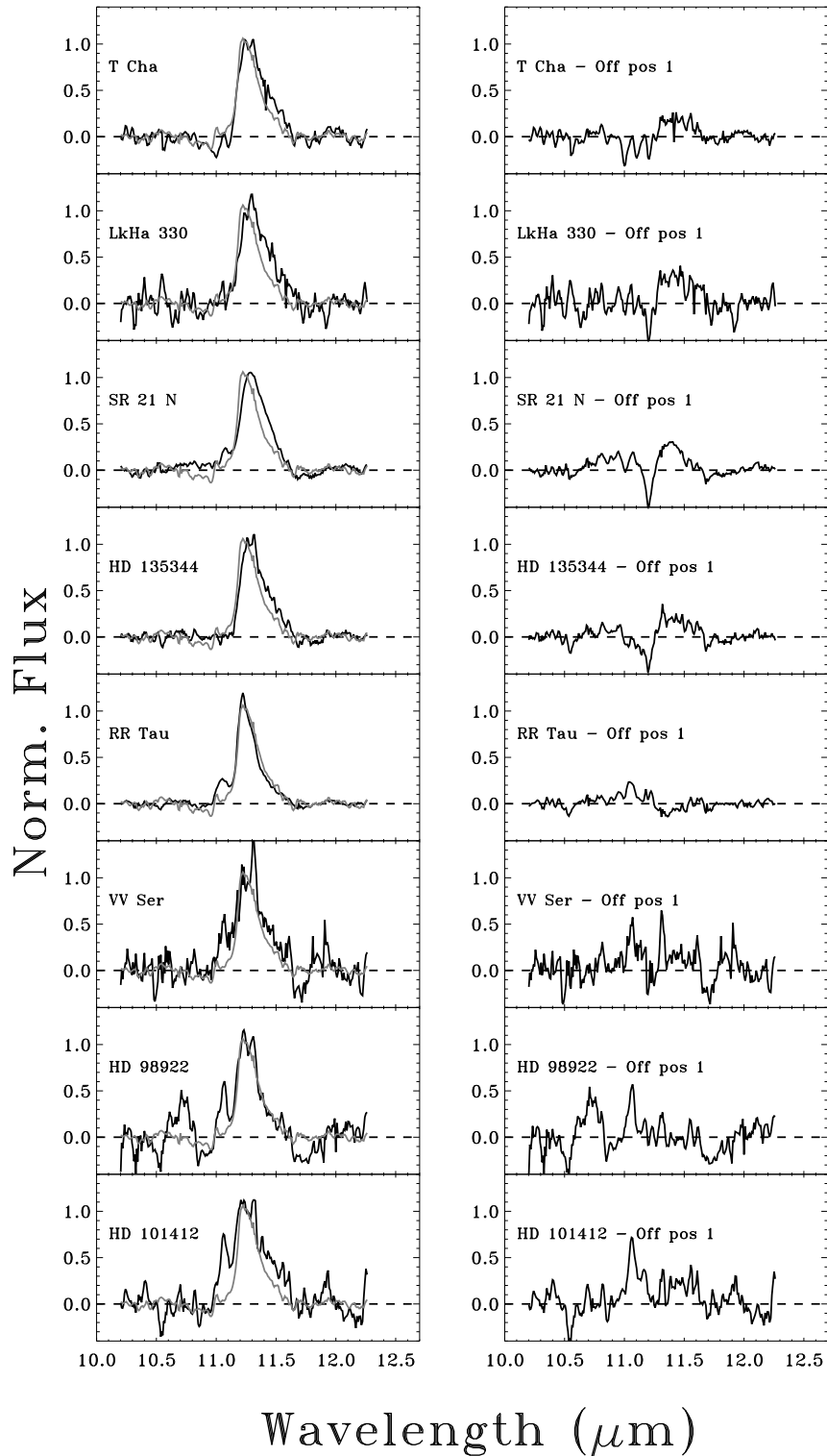


**Figure 2.5:** Left panel: Blow-up of the SH spectra around the continuum-subtracted  $11.2 \mu\text{m}$  PAH feature, normalized to the fitted peak flux (black line). Overplotted in light grey for comparison is the SH spectrum of the off-position. Right panel: Plot of the difference between the source and the off-position spectra.



Table 2.2: Line fluxes and feature/continuum ratio of PAH features in  $W m^{-2}$ .

Name	Line flux			feature/continuum			cryst. sil. <sup>c</sup>
	6.2 $\mu m$ (SL)	11.2 $\mu m$ (SL)	11.2 $\mu m$ (SH)	12.8 $\mu m$ (SH)	6.2 $\mu m$ (SL)	11.2 $\mu m$ (SH)	
LkH $\alpha$ 330	$1.7 \times 10^{-15}$	$7.7 \times 10^{-16}$	$5.1 \times 10^{-16}$	$\leq 2.5 \times 10^{-16}$	1.21	1.12	T
RR-Tau	$9.6 \times 10^{-15}$	$5.0 \times 10^{-15}$	$4.5 \times 10^{-15}$	$1.3 \times 10^{-15}$	1.71	1.57	Y
HD 98922	- <sup>a</sup>	- <sup>a</sup>	$1.4 \times 10^{-14}$	$4.0 \times 10^{-15}$	-	1.06	Y
HD 101412	$4.0 \times 10^{-15}$	$2.2 \times 10^{-15}$	$1.5 \times 10^{-15}$	$3.0 \times 10^{-16}$	1.19	1.08	Y <sup>d</sup>
T Cha	- <sup>a</sup>	- <sup>a</sup>	$3.3 \times 10^{-16}$	$1.1 \times 10^{-16}$	-	1.15	N
HD 135344	- <sup>a</sup>	- <sup>a</sup>	$1.2 \times 10^{-15}$	$1.1 \times 10^{-16}$	-	1.19	N
EM* SR 21 N	- <sup>a</sup>	- <sup>a</sup>	$4.0 \times 10^{-15}$	$4.1 \times 10^{-16}$	-	1.32	T
VV Ser	$2.6 \times 10^{-15}$	$3.1 \times 10^{-15}$	$2.3 \times 10^{-15}$	$1.2 \times 10^{-15}$	1.07	1.07	Y
Off-position 1	- <sup>a</sup>	- <sup>a</sup>	$1.4 \times 10^{-16}$	$5.5 \times 10^{-17}$	-	-	-
VSSG 1 <sup>b</sup>	- <sup>a</sup>	- <sup>a</sup>	$8.6 \times 10^{-16}$	$2.4 \times 10^{-16}$	-	-	Y
Haro 1-17 <sup>b</sup>	$4.5 \times 10^{-16}$	$\leq 2.5 \times 10^{-16}$	$\leq 2.5 \times 10^{-16}$	$\leq 2.5 \times 10^{-16}$	-	-	Y

<sup>a</sup> no SL spectra available

<sup>b</sup> PAH feature detected in background spectrum, not associated with the source

<sup>c</sup> crystalline silicates detected in either 28–29, or 33–35  $\mu m$ , from Kessler-Silacci et al. 2006, Table 2; “Y” if detected, “N” if not detected, or “T” if the identification is tentative.

<sup>d</sup> derived in this study

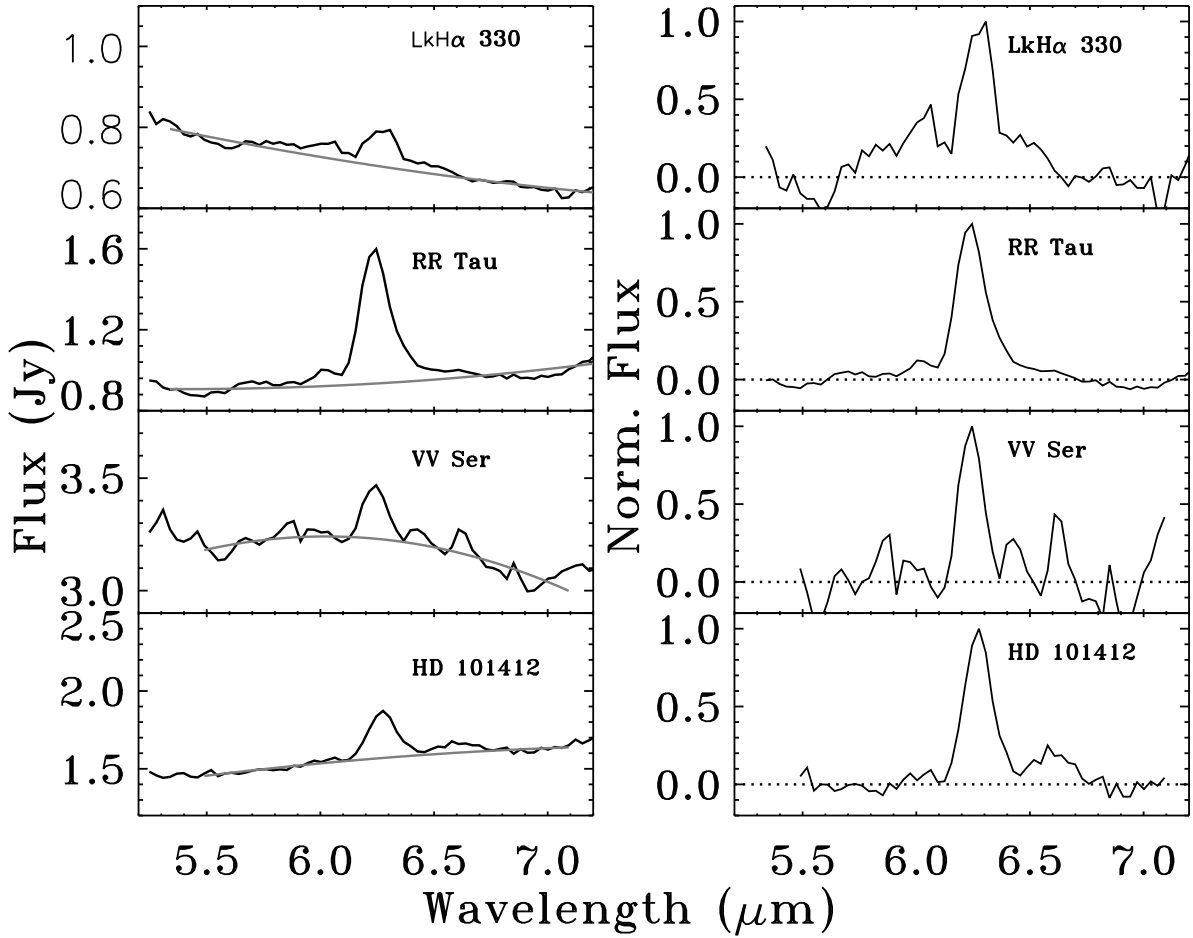


**Figure 2.6:** **Left:** Blow-up of the Spitzer-IRS low resolution spectra around the  $6.2 \mu\text{m}$  PAH feature. A simple fit of the continuum flux is plotted with a dotted line. **Right:** Continuum subtracted spectra, normalised to the peak flux of the PAH feature.

context of a disk model which demonstrates the lower contrast of the  $7.7$  and  $8.6 \mu\text{m}$  features with respect to the continuum emission from the disk.

#### 2.4.2 Line flux determination

To determine the strength of the PAH features, the continuum emission needs to be subtracted. As a simple approximation we derive a local pseudo-continuum by fitting a 2D polynomial to the spectrum around the individual PAH features, where the continuum is selected by hand. For the  $11.2 \mu\text{m}$  feature, a polynomial is fitted to the emission at  $10.5\text{--}11.0$  and  $11.8\text{--}12.2 \mu\text{m}$ . The continuum emission below the  $6.2 \mu\text{m}$  emission is estimated between  $5.5$  and  $7.1 \mu\text{m}$ . We do not include the  $7.7$  and  $8.6 \mu\text{m}$  features in Table 2.2 because these do not appear significantly in our sources with SL data, with the exception of RR Tau. The  $12.8 \mu\text{m}$  line fluxes extracted from SL are within the uncertainty consistent with those extracted from SH.

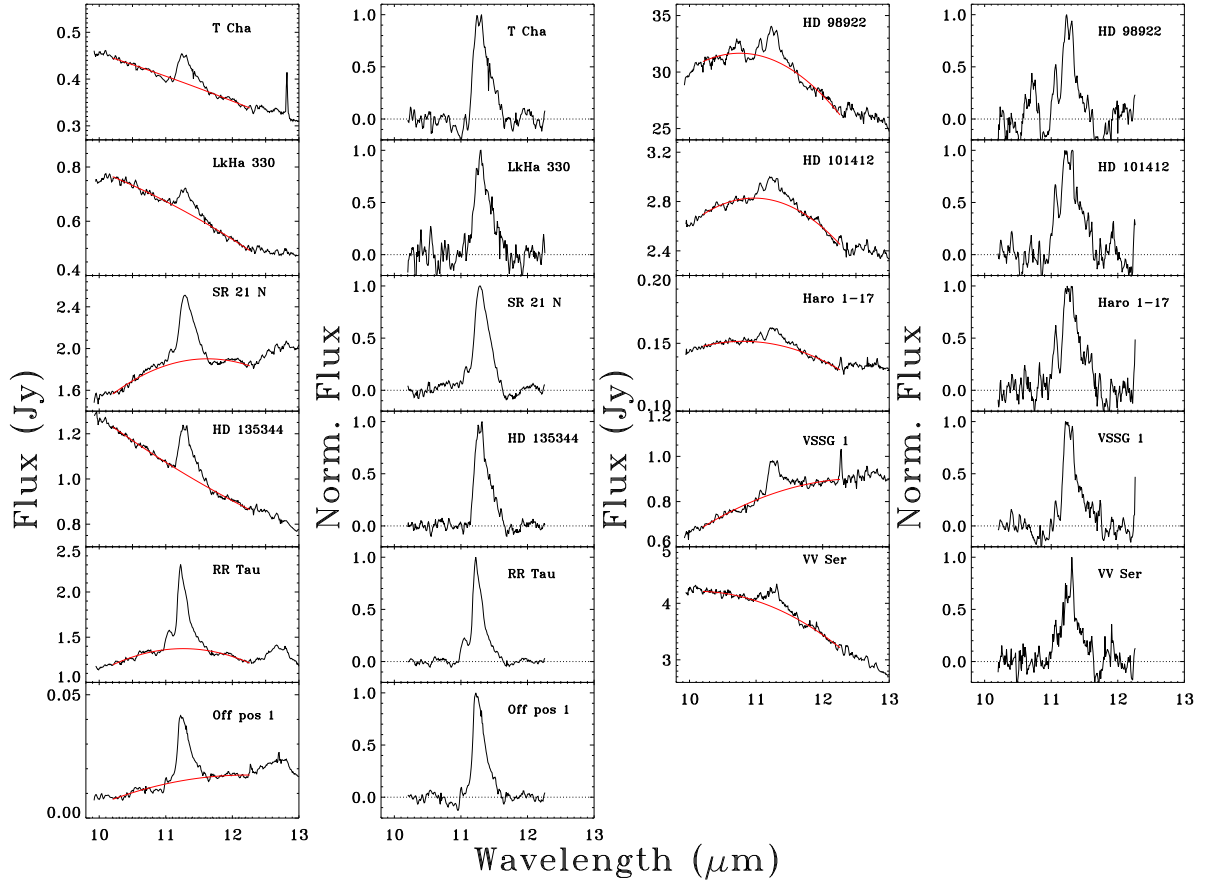


**Figure 2.7:** **Left:** Blow-up of the Spitzer IRS high resolution spectra around the  $11.2 \mu\text{m}$  PAH feature. A simple fit of the continuum flux below the PAH feature is plotted with a dotted line. **Right:** Continuum subtracted spectra, normalised to the peak flux of the PAH feature.

The continuum-subtracted features are integrated between fixed wavelengths, in particular between  $6.0$  and  $6.6 \mu\text{m}$  for the  $6.2 \mu\text{m}$  PAH feature, between  $10.9$  and  $11.6 \mu\text{m}$  for the  $11.2 \mu\text{m}$  feature and between  $11.8$  and  $13.2 \mu\text{m}$  for the  $12.8 \mu\text{m}$  feature. The resulting continuum subtracted features are shown in Figs. 2.5, 2.6, 2.7) and 2.8.

The measured line fluxes are summarized in Table 2.2. Thanks to the increased sensitivity of Spitzer, our derived line fluxes for clearly detected PAH features are an order of magnitude lower than what was previously possible with ISO. Our weakest detected feature is the  $11.2 \mu\text{m}$  PAH feature in T Cha with a line flux of  $3.3 \times 10^{-16} \text{ W m}^{-2}$ . A mean  $3\sigma$  sensitivity limit of  $2.5 \times 10^{-16} \text{ W m}^{-2}$  is derived from the noise determination in the continuum adjacent to the PAH features, though this limit varies somewhat from source to source, depending on differences in the  $S/N$  of the reduced spectra and on the presence of residual reduction artifacts for a few cases. For a small number of sources the sensitivity limit reaches a few  $\times 10^{-17} \text{ W m}^{-2}$ .

Three H AeBe stars in our sample —HD 135344, RR Tau and VV Ser— have previously been observed with ISO, albeit with much lower  $S/N$  ratio (Acke & van den Ancker 2004). For RR Tau, our derived line flux for the  $6.2 \mu\text{m}$  feature agrees within

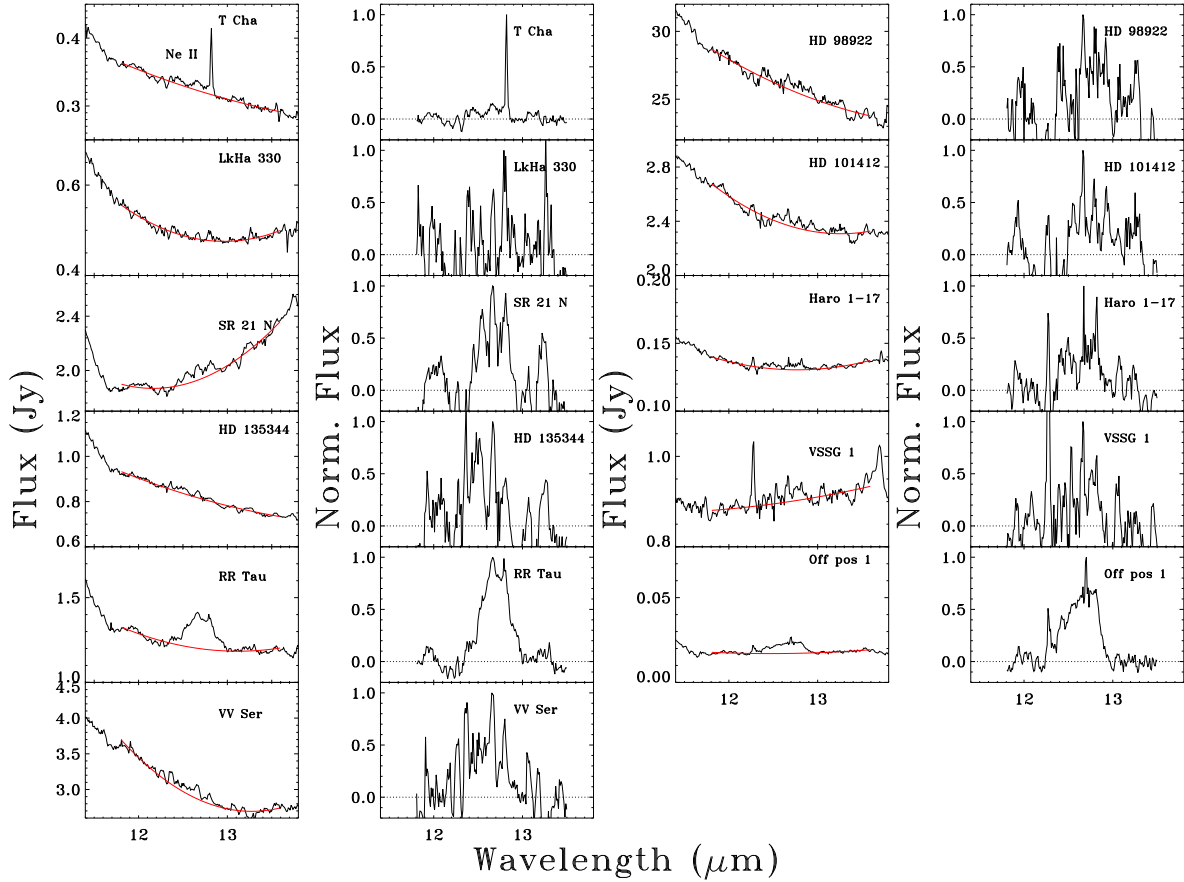


**Figure 2.8:** **Left:** Blow-up of the Spitzer IRS high resolution spectra around the  $12.8 \mu\text{m}$  PAH feature. A simple fit of the continuum flux below the PAH feature is plotted with a dotted line. **Right:** Continuum subtracted spectra, normalised to the peak flux of the PAH feature.

$\sim 5\%$  with the ISOPHOT-S spectra, while the  $11.2 \mu\text{m}$  feature is larger by about a factor 2 in the IRS spectrum. For HD 135344, we derive a slightly higher  $11.2 \mu\text{m}$  line flux than the ISO upper limit. For VV Ser, our derived  $6.2 \mu\text{m}$  line flux is about 4 times weaker, whereas our  $11.2 \mu\text{m}$  detection is consistent with the ISO data.

Sloan et al. (2005) have presented Spitzer SL observations for 4 H AeBe stars with spectra showing PAH features but no silicate dust features, among which HD 135344 is included in our sample. They report clear  $6.2$ , “ $7.9$ ”,  $11.3$  and  $12.7 \mu\text{m}$  features for all of their sources (HD 34282, HD 135344, HD 141569, HD 169142). For HD135344 the  $7.9 \mu\text{m}$  feature is weaker and broader and the  $8.6 \mu\text{m}$  feature is absent. Their derived line flux for the  $11.2 \mu\text{m}$  PAH feature is consistent with ours within 10%.

### 2.4.3 Comparison of PAH features

In a previous study of a diverse sample of interstellar and circumstellar sources, planetary nebulae, reflection nebulae HII regions and galaxies (van Dienenhoven et al. 2004), the  $11.2 \mu\text{m}$  PAH feature of almost all YSO’s, non-isolated H AeBe stars and HII regions

was found to have a similar asymmetric profile with a FWHM of  $\sim 0.17 \mu\text{m}$ , and a peak wavelength in the range of  $11.2 - 11.24 \mu\text{m}$ . The single isolated HAeBe source in their sample, HD 179218, shows a broader  $11.2 \mu\text{m}$  PAH feature with a peak wavelength of  $\sim 11.25 \mu\text{m}$ . Our peak position lies in the range  $11.25 - 11.32 \mu\text{m} \pm 0.03 \mu\text{m}$ , but this determination is influenced by the uncertainty in the continuum fit, and the shift to longer wavelengths may be partially explained by the presence of a  $11.3 \mu\text{m}$  feature from crystalline silicates.

Figure 2.5 shows a comparison of the continuum-subtracted  $11.2 \mu\text{m}$  features from all SH spectra. The off-source PAH feature, which is clearly not contaminated by silicate emission, is included. Both the source and the off-source features are normalized to the peak flux. In the right panel of Fig. 2.5 the difference between the two features is shown.

For T Cha, LkHa 330, SR 21 N and HD 135344, the  $11.2 \mu\text{m}$  feature is broader than, as well as redshifted with respect to, the off-position feature. Of these, T Cha and HD 135344 show no evidence for crystalline silicates at  $28\text{-}29$  and  $33.6 \mu\text{m}$  (Kessler-Silacci et al. 2006), while LkH $\alpha$  330 and SR 21 N show tentative crystalline features. Thus, the presence of a  $11.3 \mu\text{m}$  crystalline silicate feature cannot readily explain the broadening of the measured feature for these sources. Such a broad shape has been seen before in the planetary nebulae IRAS 17047-5650 and IRAS 21282+5050 (Hony et al. 2001). Pech et al. (2002) proposed anharmonicity as an explanation of the broadening and used a PAH emission model to fit the  $11.2 \mu\text{m}$  feature of IRAS 21282+5050 with a combination of the fundamental ( $v = 1 \rightarrow 0$ ) and hot bands ( $v = 2 \rightarrow 1$  and  $v = 3 \rightarrow 2$ ) of the transition. These hot bands would point to very hot PAHs being present, presumably in the innermost part of the disk where the radiation field is strongest.

For the HAeBe sources RR Tau, VV Ser, HD 98922 and HD 101412, the peak wavelength of the  $11.2 \mu\text{m}$  PAH feature is very similar to that of the off-position feature. For RR Tau, the PAH feature compares very well with the off-source feature, both in shape and peak position, showing little to no residual after subtraction. For the other 3 sources, subtracting the off-position feature leaves several residual features, hinting at the presence of crystalline features, which are also seen at longer wavelengths.

## 2.5 PAH EMISSION FROM DISKS

### 2.5.1 Disk model

The strength of the PAH emission features is known to depend on the strength of the UV and optical radiation field, but in disks several additional parameters can affect the appearance of the PAH features. Here we address the question as to how the PAH features are affected by the spectrum of the central source, the PAH abundance and the flaring geometry of the disk. A related question is why no PAH features are seen in at least half of our sample of T Tauri disks, in contrast to the findings for HAeBe stars.

We use the 3-dimensional Monte Carlo radiative transfer code RADMC (Dullemond & Dominik 2004), for which a module to treat the emission from quantum-

heated PAH molecules and Very Small Grains has been included. This module will be described in detail in Dullemond et al. (in prep.), but a rough description has been given by Pontoppidan et al. (2006). A template model is set up using the following model parameters. A Kurucz model spectrum is taken for the central star with  $T_{\text{eff}} = 10000$  K, but the stellar parameters (luminosity, stellar radius) were chosen from evolutionary tracks by Siess et al. (2000) for an age of 3 Myr. The disk is modeled with  $M_{\text{disk}} = 1 \times 10^{-2} M_{\odot}$ , an inner radius set by a dust evaporation temperature of 1300 K, and an outer radius of 300 AU. The disk is flaring, with the vertical pressure scale height (in units of radius) at the inner rim  $H_p/R_{\text{in}} = 0.02$  and at the outer edge  $H_p/R_{\text{out}} = 0.14$ . The disk is modeled to be close to face-on ( $i = 5.7^\circ$ ), to maximize the strength of the PAH features. The spectra are scaled to a distance to the observer of 150 pc.

The PAH emission is calculated for an equal mix of neutral and singly ionized  $\text{C}_{100}\text{H}_{24}$  molecules, adopting the Draine & Li (2001) PAH emission model, using the “thermal continuous” approximation. Multi-photon events are included for the PAH excitation, following the method outlined by Siebenmorgen et al. (1992). Enhancement factors for the integrated cross sections of the 6.2, 7.7 and 8.6  $\mu\text{m}$  bands ( $E_{6.2} = 3$ ,  $E_{7.7} = 2$ ,  $E_{8.6} = 2$ ) as suggested by Li & Draine (2001) are taken into account, as also implemented in H04. The actual ionization state of PAH, which varies as a function of location in the disk, can affect the 7.7 and 8.6  $\mu\text{m}$  features relative to 11.2 and 3.3  $\mu\text{m}$  but this will be explored further in future models which include a full ionization balance of multiple PAH species in disks (Visser et al. in prep). We include the opacities from Mattioda et al. (2005) for near-infrared wavelengths. Several model tests were performed, which are presented in Appendix 2.7, including a comparison with H04.

PAH destruction is expected to occur in a strong UV radiation field, when the PAH molecules, through multi-photon events, absorb more than 21 eV in an interval shorter than their cooling timescale (Guhathakurta & Draine 1989). If the PAH destruction happens on a shorter timescale than the lifetime of the disk, this can have an effect on the PAH abundance in, and expected PAH emission from, the inner region of the disk. This effect will be stronger for smaller ( $N_c < 50$ ) PAHs, and depends on the assumed temperature at which the PAHs dissociate. Model calculations by Visser et al. (in prep.) show that for PAHs with  $N_c = 100$  the lifetime is larger than the lifetime of the disk, and therefore the PAHs are kept at constant abundance throughout the entire the disk. Tests with removing PAHs inwards from a destruction radius  $R_{\text{PAH,in}}$  (by setting their abundance to zero) show that the results do not depend sensitively on the choice of  $R_{\text{PAH,in}}$  when it is of order 1 AU.

In our template model, we use the PAH abundance of H04, who adopt a fraction of 23 % of available carbon being locked up in  $\text{C}_{100}\text{H}_{24}$  PAHs, corresponding to a carbon abundance with respect to hydrogen of  $5 \times 10^{-5}$ . For a single PAH species with  $N_c = 100$  ( $\text{C}_{100}\text{H}_{24}$ ) this leads to an abundance of  $5 \times 10^{-7}$ . In our model the abundance is set as a fraction of dust mass. Assuming  $\text{C}_{100}\text{H}_{24}$  (molecular mass:  $2.04 \times 10^{-21}$  g) and a dust-to-gas ratio of 1 to 100, the PAH abundance of  $5 \times 10^{-7}$  with respect to hydrogen corresponds to a mass fraction of 0.061 gram of PAH per gram of dust, of which 50% ionized and 50% neutral. Such an abundance is at the high end of that inferred for general interstellar clouds (Cesarsky et al. 2000; Habart et al. 2001). Indeed,

the parameters chosen in our model and that of H04 maximize the PAH emission.

## 2.5.2 Dependence on spectral type

Since UV and optical radiation incident on the disk surface provides the main PAH excitation mechanism, the PAH features must depend on the spectral type of the illuminating star. To address this influence our template disk model is calculated for a range of Kurucz stellar spectra, with  $T_{\text{eff}} = 10000, 8000, 6000, 5000$  and  $4000$  K, corresponding to spectral types A0, A6, G0, K2 and K7, respectively (Gray & Corbally 1994). Stellar parameters are again taken from evolutionary tracks (Siess et al. 2000) for an age of 3 Myr. The disk parameters were modified slightly in 1 iteration to ensure hydrostatic equilibrium throughout the disk, except for the inner rim. The model SEDs for the different central stars and absolute continuum subtracted fluxes for the PAH features are presented in Fig. 2.9. A blowup of the standard model spectrum is shown in Fig. 2.10.

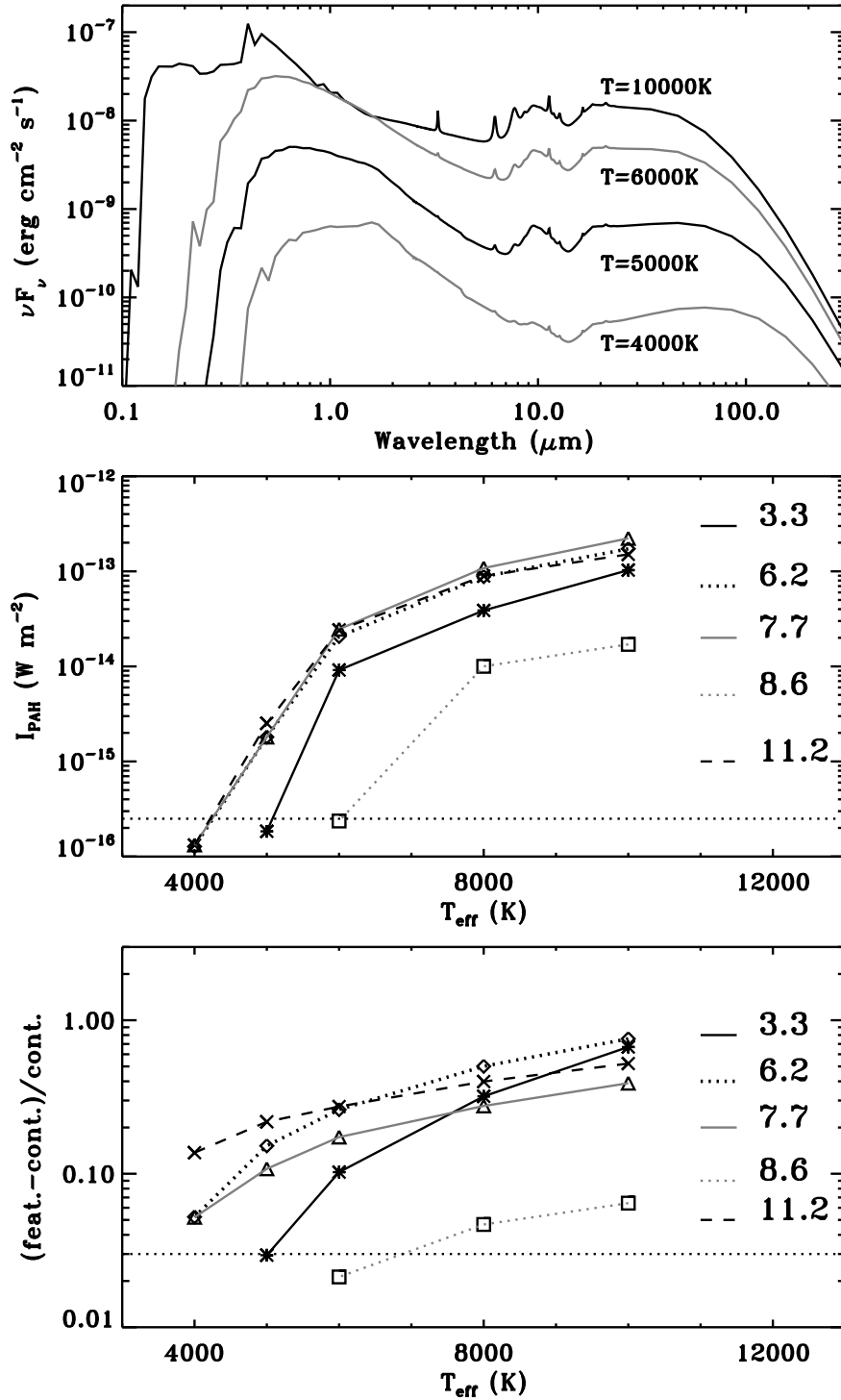
Since the absolute strength of the PAH features scales foremost with the total radiation that is absorbed by the PAHs, it also depends on disk parameters that are unrelated to the PAHs themselves. To evaluate the role of the disk continuum, we present feature/continuum ratios in Fig. 2.9 as well.

It is seen that with decreasing  $T_{\text{eff}}$  both the line flux as well as the feature / continuum ratio decrease for the 3.3, 6.2, 7.7, 8.6 and 11.2  $\mu\text{m}$  features (Fig. 2.9). The rate of decrease in line flux is similar for all features, as is that of the feature/continuum ratio except for the 3.3  $\mu\text{m}$  feature. The latter feature disappears more rapidly with decreasing  $T_{\text{eff}}$  because the continuum emission at 3.3  $\mu\text{m}$  decreases at a slower rate compared to the longer wavelengths. For all  $T_{\text{eff}}$  considered, the 8.6  $\mu\text{m}$  feature has the lowest feature to continuum ratio, from  $\lesssim 7$  to  $\lesssim 3\%$ , which can be clearly seen in Fig. 2.10. When the PAH molecules are assumed to be 100% neutral  $\text{C}_{100}\text{H}_{24}$ , the feature/continuum ratio of the 6.2, 7.7 and 8.6  $\mu\text{m}$  bands decreases by a factor  $\sim 2-3$ , while that of the 3.3 and 11.2  $\mu\text{m}$  features increases by a factor  $\sim 1.5-3$  (Fig. 2.10).

These models show that the 6.2 and 11.2  $\mu\text{m}$  features are the most suitable tracers for the presence of PAHs in disks around late type T Tauri stars owing to their relatively high feature/continuum ratio, and this qualitatively agrees with the fact that these two features are always present in our T Tauri stars with PAH detection. Quantitatively, Fig. 2.9 shows that, for the current model assumptions, the PAH features become difficult to observe for  $T_{\text{eff}} < 4200$  K (later than K6) even with a relatively high PAH abundance of  $\sim 6\%$  of the dust mass in the entire disk and large flaring angles.

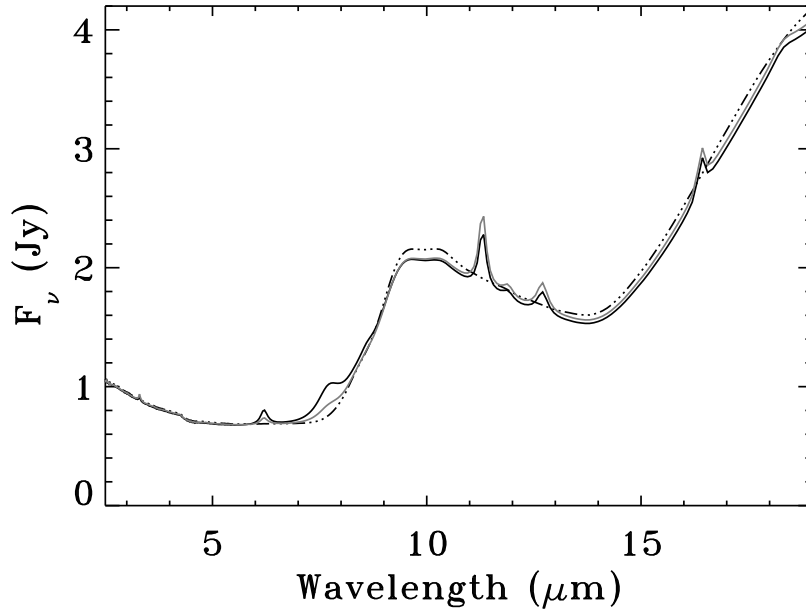
The observed 11.2  $\mu\text{m}$  line fluxes have all been rescaled to a distance of  $d = 150$  pc, and are plotted in Fig. 2.11 together with the models. Also included is our typical  $3\sigma$  limit for a source at 150 pc. For comparison we added a small subsample of 12 Herbig Ae stars, selected from Acke & van den Ancker (2004), and rescaled to 150 pc. Stars with unknown distance and/or poorly known spectral type were excluded. The observed feature/continuum ratios for the two strongest features, 6.2 and 11.2  $\mu\text{m}$ , are compared with models in Fig. 2.12.

Figure 2.11 shows that our template model (solid line) predicts a larger  $I_{\text{PAH}}$  than



**Figure 2.9:** Top panel: Model SEDs of a star+disk with PAHs, for different spectral types of the star, with  $T_{\text{eff}} = 10000, 6000, 5000$  and  $4000$  K at a distance of  $150$  pc. Middle panel: PAH line flux of the various features for the corresponding models, including also  $T_{\text{eff}} = 8000$  K. Bottom panel: Feature to continuum ratio of the PAH features. The dotted line indicates our  $3\sigma$  observational limits.





**Figure 2.10:** Blowup of the standard model spectrum of a star+disk with PAHs, for  $T_{\text{eff}} = 6000$  K with template parameters (dark solid line), without PAHs (dash-dotted line), with only neutral  $\text{C}_{100}\text{H}_{24}$  PAH (light solid line). Note that the 11.2 and 6.2  $\mu\text{m}$  features are clearly visible on top of the continuum, whereas the 7.7 and 8.6  $\mu\text{m}$  features are masked by the rising 10  $\mu\text{m}$  silicate feature.

observed, with the exception of one source (HD 98922) for which the distance is uncertain. A lower observed 11.2  $\mu\text{m}$  flux can be caused by a number of conditions such as a lower PAH abundance, a smaller flaring angle or a disk orientation close to edge-on (see below). Included in Fig. 2.11 are two additional model runs, where the PAH abundance has been lowered by a factor of 10 (dashed line) and 100 (dash-dotted line). Most of the observations fall within the predictions of these two models. Only the model with a 100 $\times$  lower PAH abundance predicts a 11.2  $\mu\text{m}$  feature strength for G-type stars below our Spitzer detection limit at  $d = 150$  pc. One source, T Cha, is detected despite the fact it falls below this formal detection limit because it has a distance of  $d = 66$  pc.

Figure 2.12 indicates that the template model fits the observed 11.2  $\mu\text{m}$  feature / continuum ratios for the 4 low mass sources, even though it overpredicts  $I_{\text{PAH}}$ . The model with 10 $\times$  lower PAH abundance fits the feature/continuum ratio of three of our HAeBe stars. However both models with 10 $\times$  and 100 $\times$  lower (below plot limit) PAH abundance predict a feature/continuum ratio below our Spitzer detection limit for spectral types below G0. This suggests that the small number of T Tauri detections (3 out of 38) are presumably outliers, with abnormally high feature/continuum PAH features. This discrepancy will be further discussed in Sect. 2.5.5 and is most likely due to an abnormally low continuum in these sources.

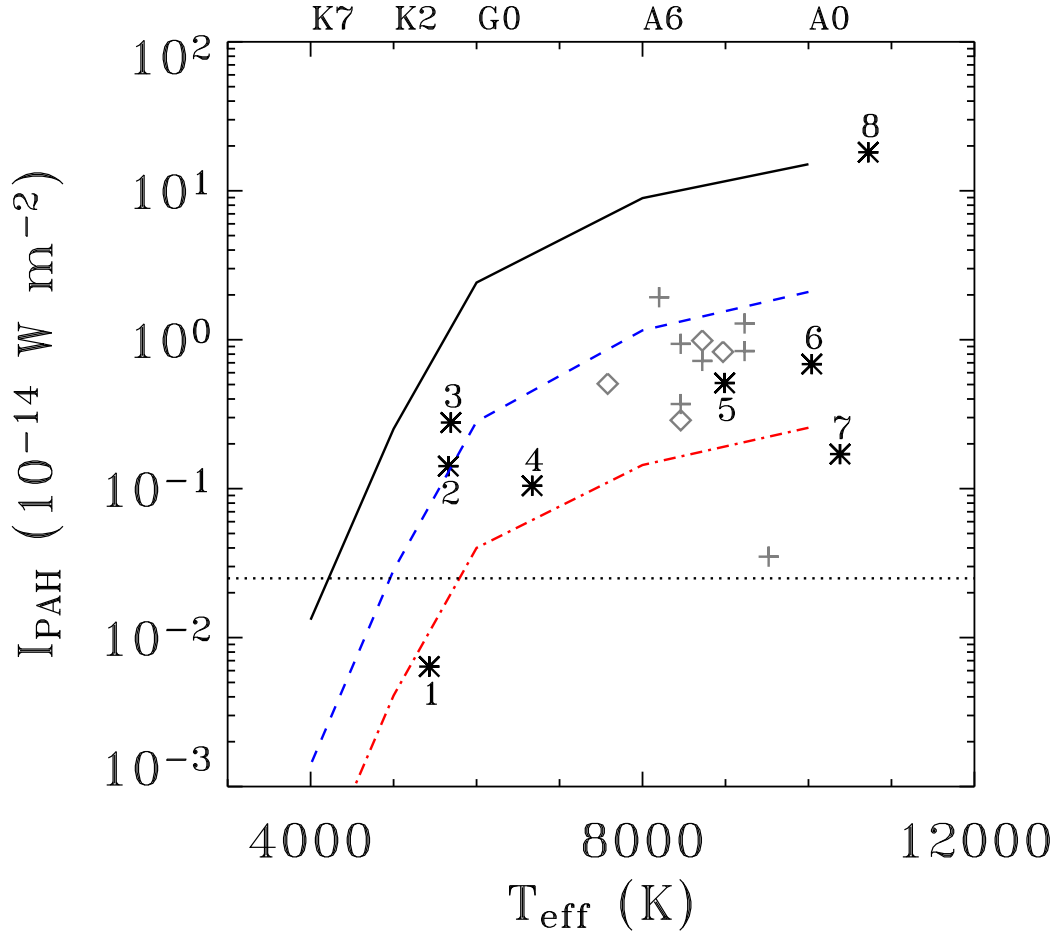


**Figure 2.11:** Strength of 11.2  $\mu\text{m}$  PAH feature  $I_{\text{PAH}}$  (scaled to a distance of 150 pc) versus  $T_{\text{eff}}$ . Black solid line represents our template model, based on Fig. 2.9; dashed and dash-dotted lines represent our models with a 10x and 100x lower PAH abundance respectively. Black ‘\*’ symbols are for c2d sources. Grey diamonds are ISO upper limits of the 11.2  $\mu\text{m}$  feature strength for Herbig Ae sources, grey ‘+’ symbols are ISO detections. c2d sources are labelled as follows. 1: T Cha; 2: LkH $\alpha$  330; 3: SR 21 N; 4: HD 135344; 5: RR Tau; 6: VV Ser; 7: HD 101412; 8: HD 98922. The dotted grey line indicates our typical  $3\sigma$  sensitivity limit of  $2.5 \times 10^{-16} \text{ W m}^{-2}$  for sources at  $d = 150$  pc.

### 2.5.3 Additional UV radiation and relation with H $\alpha$

The models presented in Sect. 2.5.2 include only the stellar radiation, but not any additional sources of UV. Excess UV radiation compared with the stellar photosphere has been observed from at least some T Tauri stars (e.g., Herbig & Goodrich 1986, Costa et al. 2000, Bergin et al. 2003). From a constructed composite FUV spectrum, derived from two K7 sources representative of low-mass T Tauri stars, Bergin et al. (2003, and references therein) find an overall FUV continuum flux at  $r = 100$  AU on the order of a few hundred times the Habing field. The effect of this additional UV is to shift absolute feature strengths to those appropriate for higher  $T_{\text{eff}}$ , close to  $T_{\text{eff}} \sim 10000$  K.

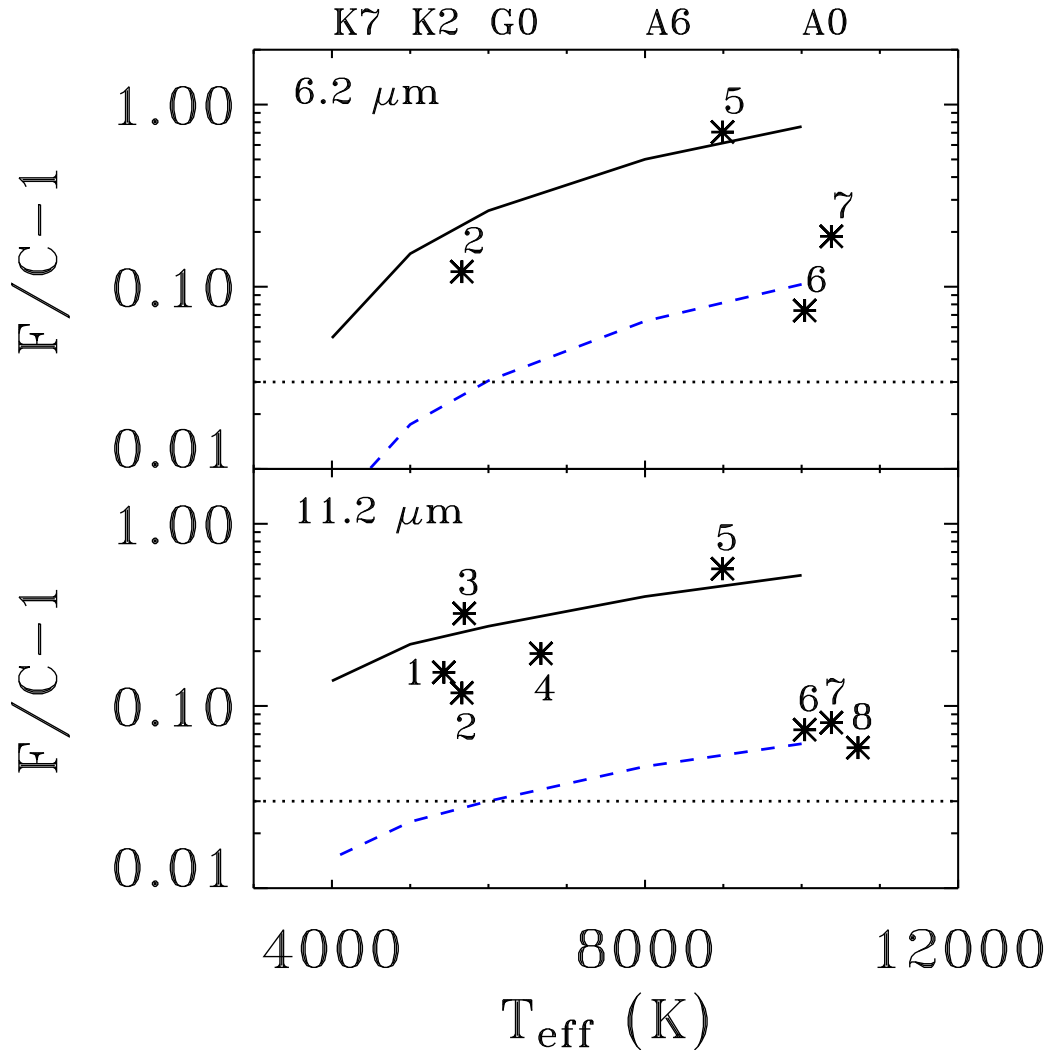


**Figure 2.12:** Feature / continuum ratio for the 6.2 and 11.2  $\mu\text{m}$  PAH features; solid line represents our template model, based on Fig. 2.9; dashed line represents our model with a 10x lower PAH abundance.

If a large fraction of T Tauri stars would have such additional UV radiation this leads to the question why not more sources were detected, since the feature strength should be more than sufficient if PAHs are present at our template abundance. This would further strengthen the evidence for low PAH abundances in a large fraction of T Tauri disks.

The origin of excess UV radiation from T Tauri stars is not fully clear, but is usually thought to originate from the shock in the magnetospheric accretion column associated with material falling from the inner disk onto the stellar surface. One indication of accretion activity is the strength of the  $H\alpha$  emission line, measured in  $H\alpha$  equivalent width (EW) (Cabrit et al. 1990). Literature values of  $H\alpha$  EW measurements are listed in Table 2.1. In our sample, LkH $\alpha$  330 is a classical T Tauri star ( $H\alpha$  EW  $\geq 10 \text{ \AA}$ ),

while T Cha should be classified as a weak line T Tauri star ( $H\alpha$  EW  $< 10 \text{ \AA}$ ). We find no correlation between the  $11.2 \mu\text{m}$  PAH feature strength and  $H\alpha$  EW. However, single measurements of  $H\alpha$  EW may not necessarily be a reliable tracer of the average accretion luminosity. As an example, for T Cha the quoted  $H\alpha$  EW of  $2 \text{ \AA}$  by Alcalá et al. (1993) is indicative of a low accretion rate, while Sylvester et al. (1996) have later classified it as a YY Orionis star with strong UV continuum emission and substantial variability on short timescales. Another problem is that not all of this UV radiation from the accretion shock may reach the disk, but can be absorbed by the overlying accretion column and/or any bi-polar outflow material (Alexander et al. 2005).

An alternative interpretation of the enhanced UV radiation is stellar activity, especially at later evolutionary stages when the accretion becomes less important. This mechanism has been used by Kamp & Sammar (2004) to model the UV field around young G-type stars.

#### 2.5.4 PAH abundance

The discussion in Sect. 2.5.1 has illustrated some of the effects of the PAH abundance on the PAH features. As seen in Figs. 2.11 and 2.12, the PAH features decrease in line flux and feature to continuum ratio with decreasing PAH abundance, with a similar trend for all the PAH features. Decreasing the PAH abundance also affects the overall SED, increasing the continuum radiation at wavelengths longer than  $2 \mu\text{m}$  and at UV wavelengths around  $0.2 \mu\text{m}$ .

For sources with detected  $11.2 \mu\text{m}$  PAH feature, the line strengths indicate PAH abundances between 10 and  $100\times$  lower than the template model abundance, i.e., between 0.06 and 0.6 % of dust mass. With respect to hydrogen, this translates to PAH abundances between  $5 \times 10^{-9}$  and  $5 \times 10^{-8}$ . Geometry affects these numbers by at most a factor of a few (see Sect. 2.5.5). Thus, the absence of PAH features in the majority of our T Tauri sources may be partly caused by a lower PAH abundance than found in molecular clouds. However, this does not mean that PAHs are absent; even at these lower abundances, PAHs can still have an important influence in terms of UV opacities and heating rates in the surface layer of the disk (Jonkheid et al., submitted). For comparison, the PAH abundance inferred for the HD 141569 transitional disk is 0.00035% compared to dust (Li & Lunine 2003) or  $1.5 \times 10^{-10}$  with respect to hydrogen (Jonkheid et al. 2006).

#### 2.5.5 Disk geometry

Finally, the effect of the disk geometry on the PAH features is addressed. The template disk and PAH model is used, again with  $T_{\text{eff}} = 10000 \text{ K}$ . The pressure scale height of the disk at the outer radius is varied between  $H_p/R_{\text{out}} = 0.06$  and  $0.22$ , while the pressure scale height of the inner rim is kept constant at  $H_p/R_{\text{in}} = 0.02$ . This illustrates the effect on the PAH features of a flaring disk versus a flatter disk. SEDs for varying values of the scale height of the outer disk are shown in Fig. 2.13. The line flux of the PAH features is found to slowly decrease as the disk becomes less flared by lowering the outer

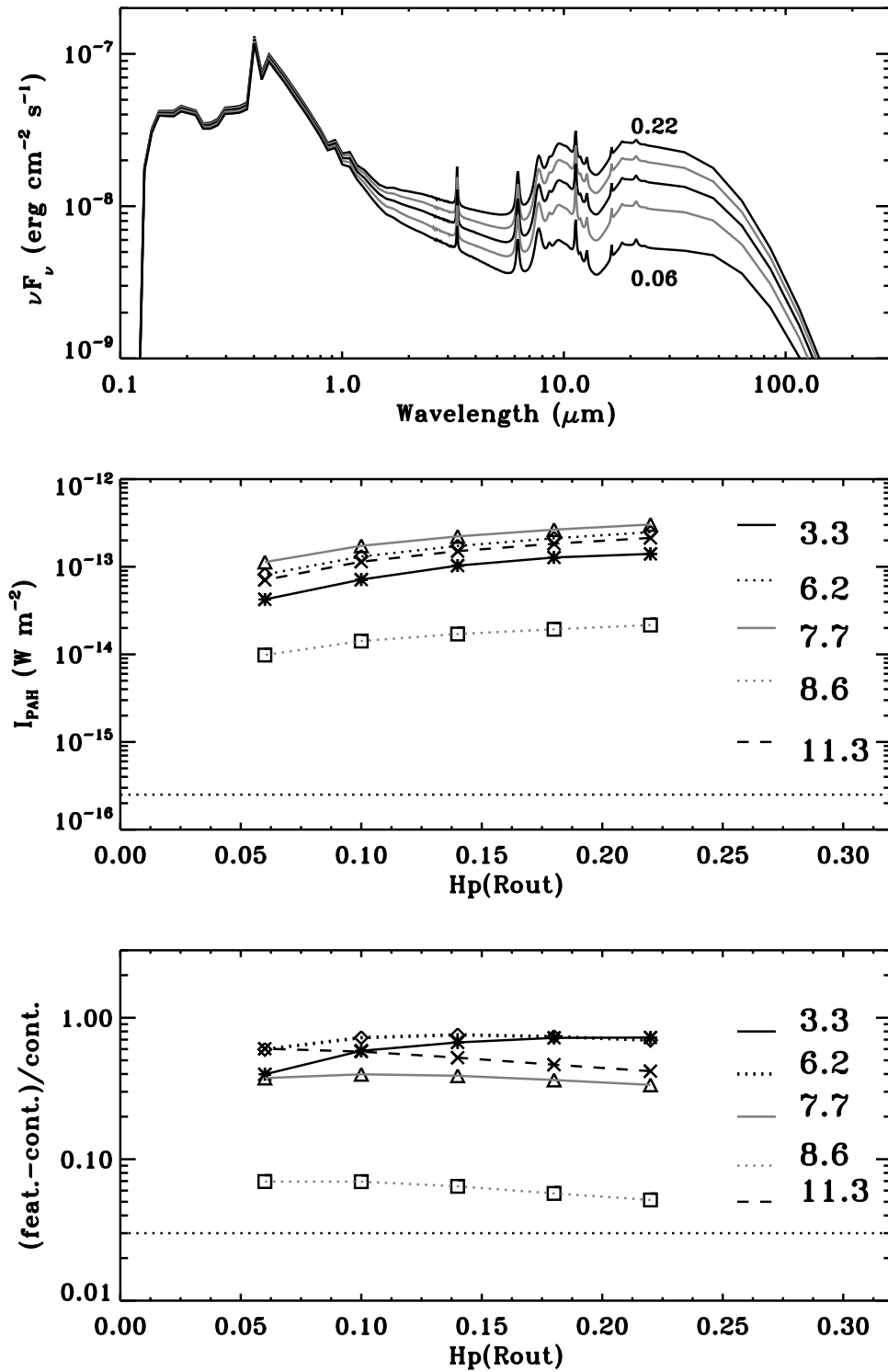


**Figure 2.13:** **Top panel:** Model SEDs of a star+disk with PAH, with scale height of outer disk  $H/R_{\text{out}} = 0.06, 0.1, 0.14, 0.18$  and  $0.22$  at a distance of 150 pc. **Middle panel:** PAH line fluxes for the corresponding models. **Bottom panel:** Feature to continuum ratio of the various features. The dotted line indicates our observational limits.

disk scale height from  $H/R_{\text{out}} = 0.22$  to  $0.06$ . The feature over continuum ratio is found to increase slightly with decreasing  $H/R_{\text{out}}$  for most features, with the exception of the  $3.3$  and  $6.2 \mu\text{m}$  features, where the feature/continuum ratio decreases for  $H/R_{\text{out}} < 0.1$ . This trend is caused by a more rapid decrease of the silicate continuum flux compared to the PAH peak flux. All the main PAH features can be distinguished for the flaring disk, although the  $8.6 \mu\text{m}$  feature has a low feature to continuum ratio of  $\sim 3\text{--}10\%$ .

To compare this scenario to our PAH detections, a measure for the flaring index of the disk is taken to be the shape of the SED, obtained by dividing the observed  $\nu F_\nu$  at  $35 \mu\text{m}$  over  $13 \mu\text{m}$  (Kessler-Silacci et al. 2006). This ratio is compared to the measured  $11.2 \mu\text{m}$  line flux. No clear evidence for a correlation between the  $11.2 \mu\text{m}$  line strength and a rising/non-rising SED is found. Together with the lack of strong changes Fig. 2.13, this suggests that disk flaring alone is not sufficient to explain the PAH non-detections in our sample.

A second geometry effect, disk thickness, can have a direct effect on the PAH feature strength  $I_{\text{PAH}}$ . A geometrically thicker disk captures a larger portion of the stellar radiation field than a flatter disk, and hence the response in *both* the dust continuum *and* the PAH features is stronger. Observations of spectral energy distributions of disks around pre-main-sequence stars have indicated that disk geometries vary strongly from source to source (Meeus et al. 2001), and that this factor can therefore potentially affect the spectrum. Test model runs show that increasing the disk geometrical thickness by a factor 2, by increasing the pressure scale height  $H_p$  throughout the entire disk, introduces an increase in  $I_{\text{PAH}}$  of  $\sim 1.5\text{--}2$ , while the ratio of PAH feature over continuum ratio decreases by a factor  $\sim 1.4\text{--}1.8$ . The disk would have to be a factor  $\sim 60\text{--}80$  thinner for the PAH features to have been undetectable for  $T_{\text{eff}} < 6000 \text{ K}$  (G0), for the template abundance.

A third geometry effect, inclination, affects both  $I_{\text{PAH}}$  and the feature over continuum ratio. Our template models are run for face-on disks ( $i = 5^\circ$ ). When the template model is observed at angles up to  $i \sim 60^\circ$ ,  $I_{\text{PAH}}$  remains relatively unchanged ( $< 3\%$ ) and the feature over continuum increases by about  $10\%$ . For an almost edge-on disk ( $i = 80^\circ$ ),  $I_{\text{PAH}}$  has decreased by  $\sim 40\%$ , while the feature over continuum is a factor  $\sim 4$  larger. Inclination may be an explanation for some of the sources with abnormally large F/C ratio, compared with their feature strength, e.g. RR Tau.

A fourth geometry effect which could explain an unusually high feature/continuum ratio is the introduction of a large scale gap in the inner dust disk, for example as the result of dust coagulation or possibly through clearing by one or more planet(s), although the latter would require extreme circumstances. This lowers the  $3\text{--}13 \mu\text{m}$  continuum flux while keeping the PAH feature strength the same. The motivation for this explanation comes from the SED of the small fraction of T Tauri stars in our sample that are detected, all of which have a higher  $11.2 \mu\text{m}$  feature/continuum ratio than would be consistent with their  $11.2 \mu\text{m}$  fluxes within the standard model. The SEDs of these 4 detected sources show remarkably low emission at  $10 \mu\text{m}$  followed by a steep rise towards  $20 \mu\text{m}$ , suggestive of a gap opening up in the dust disk (Brown et al., in prep.). Examples of similar SEDs include those of DM Tau, GM Aur and CoKu Tau/4 (e.g. D'Alessio et al. 2005), for which the continuum flux around  $11 \mu\text{m}$  is also depressed

by more than an order of magnitude compared with that of a standard T Tauri star in Taurus.

### 2.5.6 Model summary

In summary, all three effects of reducing the stellar temperature (and thus the amount of optical and UV radiation), reducing the PAH abundance, and decreasing the flaring angle or thickness of the disk are shown to decrease the absolute strength of the PAH features, as expected. The feature over continuum ratio trends are similar for the 6.2, 7.7, 8.6 and 11.2  $\mu\text{m}$  PAH features. That of the 8.6  $\mu\text{m}$  is the lowest in all models, with typical values of  $< 6\text{--}10\%$  even for models which maximize the features, which can qualitatively explain the observed lack of this feature.

The 11.2  $\mu\text{m}$  feature remains one of the strongest features in all models explored and this is qualitatively consistent with our observations. For the template model parameters which maximize the PAH features, PAHs are observable within the mean sensitivity limit of our observations for  $T_{\text{eff}} \geq 4200$  K (K6). For a  $10\times$  lower PAH abundance, the features are still above our sensitivity limit for  $T_{\text{eff}} \geq 4900$  K (K2), but now the feature/continuum ratio becomes the limiting factor, with values  $\lesssim 5\%$  for  $T_{\text{eff}} \leq 6000$  K (G0). This partly explains the absence of any PAH features in the spectra of more than half of the sources in the sample considered, which consists mostly of late K and M type stars.

## 2.6 CONCLUSIONS AND FUTURE WORK

Spitzer-IRS spectra were obtained for a set of 54 pre-main sequence stars with disks, including 38 T Tauri stars and 7 Herbig Ae stars. The observations are an order of magnitude more sensitive than those used in previous surveys of PAHs in disks. We detect PAH features in at least 3 T Tauri stars, with an additional 14 tentative detections to be confirmed, resulting in a lower limit to the PAH detection rate in T Tauri stars of 8%. Spitzer SL observations are needed to confirm the presence of the PAH features for sources where we currently only see the 11.2  $\mu\text{m}$  feature in the SH spectrum. All 4 sources that show hints for inner holes in their dust disk also show clear 11.2  $\mu\text{m}$  PAH feature.

The lowest mass source with PAH emission in our sample is T Cha with spectral type G8. The derived 11.2  $\mu\text{m}$  line intensities are between a few  $\times 10^{-15}$  and  $3.3 \times 10^{-16}$   $\text{W m}^{-2}$ , which is typically an order of magnitude lower than what was observed for HAeBe stars with ISO.

Radiative transfer modeling of disks coupled with PAH emission models shows that for stars of late spectral type, the 11.2  $\mu\text{m}$  feature is expected to be the best tracer of the presence of PAHs. The models also show that the 7.7 and 8.6  $\mu\text{m}$  PAH features are most affected by veiling by the continuum due to strongly rising silicate emission, resulting in low feature over continuum ratios.

For the small number of T Tauri sources detected as well as for the Herbig stars, the

measured PAH line fluxes and feature/continuum ratios are lower than those found from our template disk model which maximizes the PAH emission. Variations of the model parameters indicate that the most likely explanation is lower PAH abundances by factors of 10–100, with geometry affecting these conclusions at the level of a factor of a few. The high feature/continuum ratios for the detected T Tauri stars are due to their abnormally low continuum at 11  $\mu\text{m}$  caused by the dust holes in their inner disks.

The template model predictions indicate that the 11.2  $\mu\text{m}$  feature strength becomes undetectable at our sensitivity limit when  $T_{\text{eff}} < 4200$  K (K6). This likely explains the absence of PAH features for the majority of sources in our sample which have spectral types later than K0 ( $\sim 70\%$ ). If a large fraction of these sources would have excess UV radiation at the level detected for some K7 stars, then the absence of PAH features implies a lower PAH abundance by at least an order of magnitude. The same conclusion holds for the 11 out of 38 sources with spectral types earlier than K6 which are not detected. Geometry affects these conclusions by a factor of a few. Thus, the lack of PAH detections does not mean that PAHs are absent in these disks; even at lower abundances they do need to be considered since they can affect disk structure, chemistry and gas heating.

In a follow-up paper, the combination of 5–35  $\mu\text{m}$  spectra for the entire sample with IRAC and MIPS photometry will be used to improve the uncertainty in the PAH detection rate and to compare the PAH sources in terms of their disk SEDs and interpret this with the disk modeling.

Ground-based spectra using instruments like VLT-ISAAC and VLT-VISIR on 8-m class telescopes will be able to both search for presence of the 3.3  $\mu\text{m}$  PAH feature as well as better characterize the shape of the 8.6 and 11.2  $\mu\text{m}$  PAH feature through higher spectral resolution. Through higher spatial resolution, they will also permit us to put a stronger constraint on the spatial extent of the PAH features from T Tauri disks.

## ACKNOWLEDGEMENTS

Support for this work, part of the Spitzer Legacy Science Program, was provided by NASA through contracts 1224608, 1230779 and 1256316 issued by the Jet Propulsion Laboratory, California Institute of Technology, under NASA contract 1407. Astrochemistry in Leiden is supported by a NWO Spinoza grant and a NOVA grant, and by the European Research Training Network “The Origin of Planetary Systems” (PLANETS, contract number HPRN-CT-2002-00308). B. Merín acknowledges funding from the “Fundación Ramón Areces (Spain). The authors wish to thank Louis Allamandola and Andrew Mattioda for discussions and new opacities and Emilie Habart for comparisons with her models.



## 2.7 APPENDIX: MODEL TESTS AND COMPARISON WITH HABART ET AL. 2004

There are various differences in the modeling approach between the Habart et al. (2004) paper and our models, which are summarized in Table 2.3. First, the H04 model is a 1+1-D model, meaning that the model consists of a series of vertical 1-D models at different radii, combined to make a full disk structure. This method follows the irradiation-angle philosophy used in many other models as well, e.g. D’Alessio et al. (1998), Bell et al. (1997), Dullemond et al. (2002). In our model we use full 3-D radiative transfer based on an axisymmetric disk density structure. Our model therefore also includes emission from the dust inner rim, contrary to the approach of H04. Our 3-D approach allows radiative energy to be exchanged between adjacent radii, which is not possible in the 1+1D approach. Consequently the model SEDs differ somewhat between these two types of models. Specifically, for a flaring disk, the radiation will more readily escape in the polar direction than in the radial direction, because of the larger optical depth in the latter direction. When the disk is viewed face-on, the SED will be boosted in the 3-D approach compared to the 1+1-D approach by up to  $\sim 40\%$ . Moreover, the axisymmetric 3-D models described here allow the treatment of radiative transfer in disk geometries that are not flaring, e.g. self-shadowed disks (see Section 2.5 for examples). On the other hand, in our models the vertical geometric thickness of the disk is only *estimated* to be roughly consistent with hydrostatic equilibrium, whereas the H04 model includes detailed hydrostatic equilibrium. The results of these two approaches, however, are nearly identical.

There are also fundamental differences in the opacities and the treatment of dust grains in the radiative transfer. Most importantly, H04 thermally decouple the carbon grains from the silicate grains, while we have both grain types at the same temperature and mix the opacities into a single opacity. Our assumption may be more realistic because silicate and carbon grains can only have different temperatures at the same location in the disk if such grains are physically disconnected. Only a small amount of coagulation is required to get these grains in physical contact, forcing them to have the same temperature. The result is that the silicate feature strength over the continuum is much stronger in our case than in the case of H04, as can be seen in their Figure 3 as compared to our Fig. 2.10. If the graphite is decoupled from the silicate, the graphite heats up and the silicate cools down due to the much lower optical/NIR opacity of silicate compared with graphite. The superheated graphite emission therefore fills in the spectrum on both sides of the silicate feature in the case of thermally decoupled grains.

For stars with lower effective temperature, radiation at longer wavelengths becomes more important. Our models include the new PAH opacities of Mattioda et al. (2005) at optical and near-infrared wavelengths, which are higher than those adopted by H04. In our model we do not include PAH-destruction in the inner disk, in contrast with H04. Test models with and without PAH destruction show only small differences, however.

The biggest differences between H04 and our models are likely due to the treat-

ment of the stellar radiation. Our models assume that the full stellar flux can irradiate the disk, whereas H04 assume that the disk goes all the way to the stellar surface and occults the lower half of the star. Hence the H04 models have only half the illuminating flux as ours. Moreover, they include the star as a blackbody emitter with main sequence stellar parameters, while in our model we use a Kurucz model with pre-main sequence values.

To quantitatively compare the two models, we have plotted our PAH intensities in the same way as H04, as functions of the integrated stellar radiation field in the FUV (6–13.6 eV, 912–2050 Å) wavelength range. The UV flux is usually specified relative to the average interstellar radiation field from Habing (1968) integrated over this wavelength range, which is  $1.6 \times 10^{-3} \text{ erg cm}^{-2} \text{ s}^{-1}$  (Tielens & Hollenbach 1985). This quantity is most often referred to as  $G_0$  but we refer to it here as  $\chi$  to be consistent with H04. H04 assume a single blackbody for the stellar radiation field for stars of spectral type B5–G0 and rescale the flux from the stellar surface  $R_*$  to the flux at a distance from the star of 150 AU, as a reference point in the middle of their disk.

We have calculated  $\chi$  for our models as presented in Fig. 2.11 using Kurucz spectra and pre-main sequence parameters. The results are presented in Fig. 2.14. Moreover, we have run our template model assuming a blackbody stellar spectrum and main-sequence stellar parameters, with  $T_{\text{eff}} = 15000, 12300, 10500, 8500, 7000, 6000$  and  $5000$  K, corresponding to spectral types B4, B7, A0, A3, F2, F9 and K2, respectively (Gray & Corbally 1994). Fig. 2.15 shows the results for the template PAH abundance (same as H04, dark solid line) and  $10\times$  lower (dashed line) and includes the model prediction by H04 (light solid line). The observational data are included in both figures, with  $\chi$  computed from the spectral types in the same way as described above for the pre-main sequence stars.

It is seen from Fig. 2.14 and Fig. 2.15 that for the same PAH abundance, our models predict factors of 4–5 stronger PAH features than the H04 models. In fact, our entire SED (continuum *and* features) is stronger than in their models. This means that our model disk absorbs more stellar radiation and hence re-emits more radiation in the infrared, both in PAHs and in thermal continuum. A factor of two can be traced back to the different assumption for the irradiative flux, whereas another  $\sim 40\%$  is due to the “boosting” effect in the 3-D versus 1+1-D approach in this near-face-on geometry. The remaining factor of  $\sim 2$  is ascribed to the other differences described above in terms of disk structure, geometry, treatment of dust grains, PAH destruction and PAH opacities. Another difference is that our template model assumes a mix of neutral and ionized PAHs whereas that of H04 assumes only neutral PAHs. A comparison of feature-over-continuum ratios, in which many of these effects drop out, would be instructive but H04 do not quote such values.

Comparison of Fig. 2.14 and Fig. 2.15 shows that the  $11.2 \mu\text{m}$  fluxes are lower if blackbody radiation is assumed with main sequence stellar parameters, especially for T Tauri stars (later than F8). Both our blackbody models with  $10\times$  lower abundance as well as the H04 models with ISM abundance fit the ISO and Spitzer detections for most of the HAeBe and T Tauri stars. These two models predict that for T Tauri stars of spectral type later than F5 and G5 respectively,  $I_{\text{PAH}}$  falls below our Spitzer detection

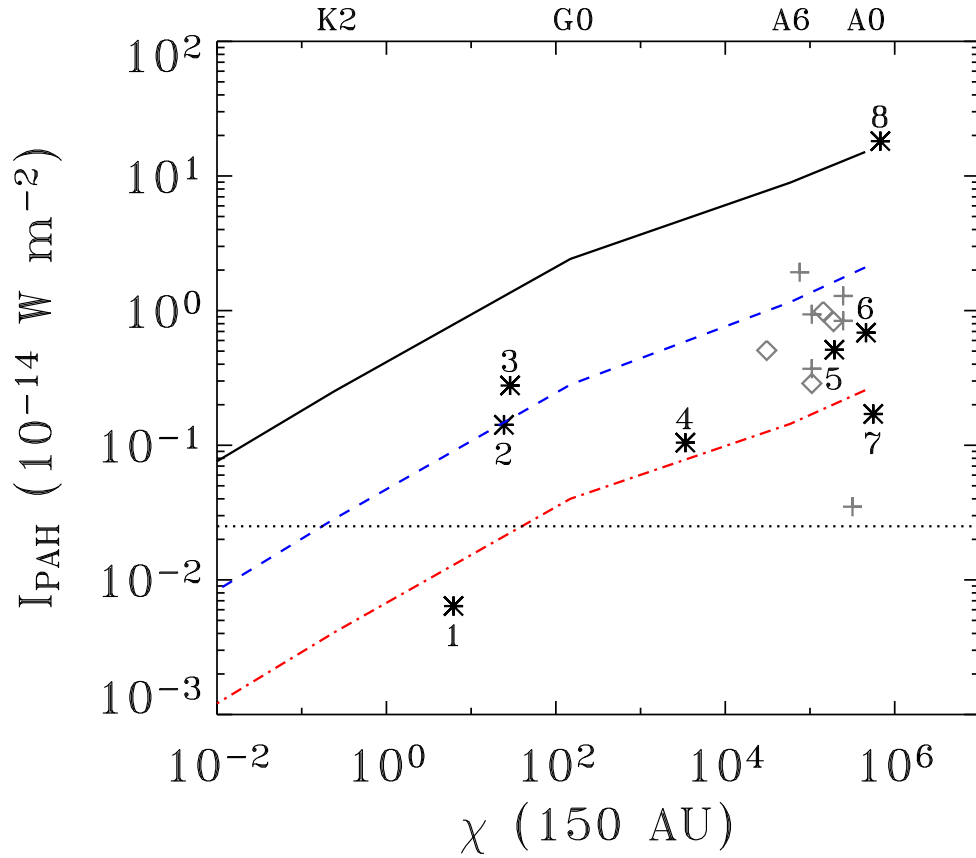


**Figure 2.14:** Strength of  $11.2 \mu\text{m}$  PAH feature  $I_{\text{PAH}}$  (scaled to a distance of 150 pc) versus  $\chi$ , the integrated FUV field (6–13.6eV) for a ZAMS star, after Habart et al. (2004, their Figure 8). Solid line represents our template model, based on Fig. 2.9; dashed and dash-dotted lines represent our models with a 10x and 100x lower PAH abundance respectively. Black ‘\*’ symbols are for c2d sources. Grey diamonds are ISO upper limits of the  $11.2 \mu\text{m}$  feature strength for Herbig Ae sources, grey ‘+’ symbols are ISO detections. c2d sources are labelled as follows. 1: T Cha; 2: LkH $\alpha$  330; 3: SR 21 N; 4: HD 135344; 5: RR Tau; 6: VV Ser; 7: HD 101412; 8: HD 98922. The dotted grey line indicates our typical  $3\sigma$  sensitivity limit of  $2.5 \times 10^{-16} \text{ W m}^{-2}$  for sources at  $d = 150 \text{ pc}$ .

limit for  $d = 150 \text{ pc}$ , for these abundances. However, the H04 models underpredict the detected  $11.2 \mu\text{m}$  strengths of some of the lowest luminosity sources in our sample, whereas our models with standard PAH abundance come much closer. In general, the PAH emission from T Tauri stars, when detected, appear better modeled with Kurucz spectra for pre-main sequence stars than with blackbody spectra for main sequence parameters. Overall, the main conclusions from our paper are not affected qualitatively if the H04 models with blackbodies were used to interpret the data. Quantitatively, the threshold for detection shifts to later spectral types (G5 versus F5), while the inferred PAH abundances are factors of 4–5 higher in the H04 models.

Finally, we note that a multitude of tests of our code were performed in addition

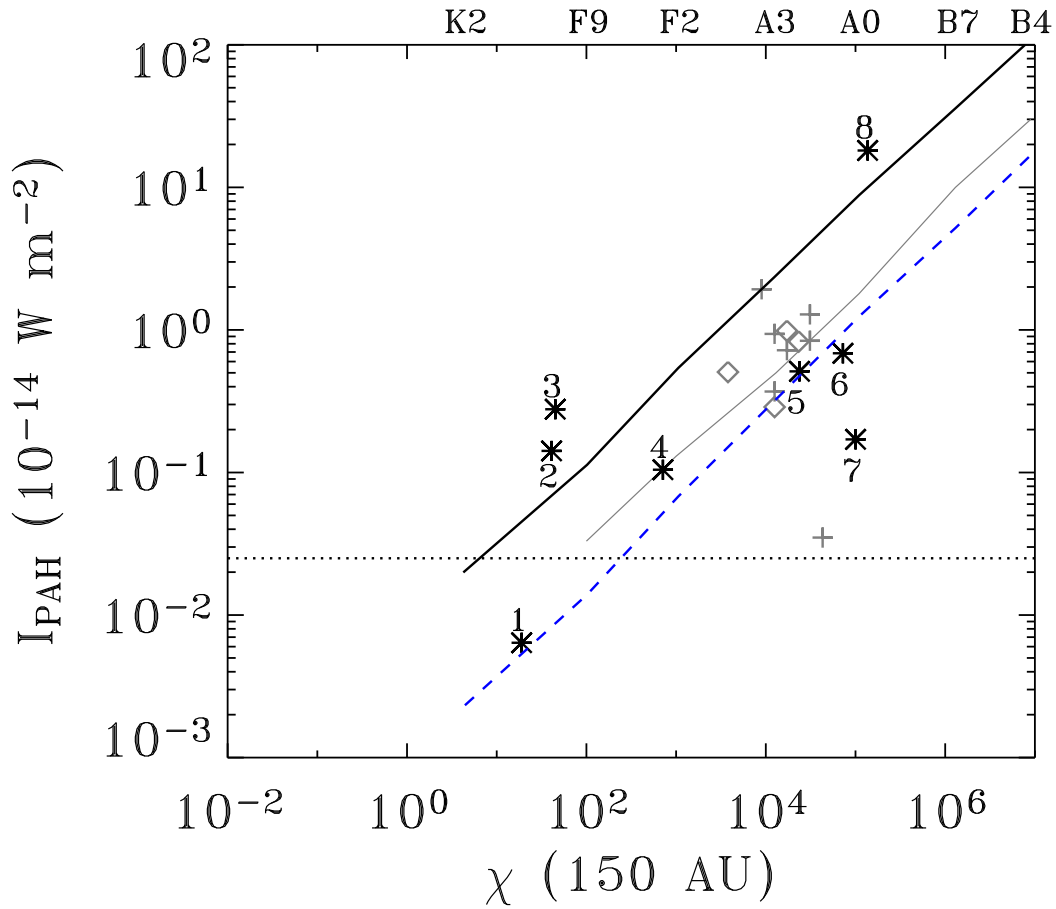


**Figure 2.15:** As Fig. 2.14, but assuming a blackbody stellar spectrum and main-sequence stellar parameters. Dark solid line represents our template model, dashed line our model with a  $10\times$  lower PAH abundance. Light solid line represents the H04 disk model results for the  $11.2\ \mu\text{m}$  feature.

to the tests that the RADMC code already has gone through (e.g. Pascucci et al. 2004). We tested that our model conserves luminosity; we compared the SED without PAHs to the SED produced by the Chiang & Goldreich-type model described in Dullemond et al. (2001); we estimated what the SED strength should be on the basis of the disk geometric thickness; and we performed optically thin models consisting purely of PAH grains and compared to the models of Li & Draine (2001). All these tests confirmed the validity of the models.

**Table 2.3:** List of differences between the model presented here and that of Habart et al. (2004).

Model aspect	This paper	H04
Radiative transfer	Axisymmetric 3-D	1+1-D
Disk structure	Inner rim	-
$\rho(Z)$	Parametrized	Self-consistent
Stellar spectrum	Kurucz	BB
Stellar parameters	PMS	MS
Stellar flux	100%	50%
PAH evaporation	1/2	yes
$T$ -decoupling	no	yes
Optical-IR PAH opacities	Li & Draine (2001), Mattioda et al. (2005)	Li & Draine (2001), Desert et al. (1990)

## 2.8 APPENDIX: FURTHER CONSTRAINTS OF THE PAH DETECTION RATE TOWARD T TAURI DISKS

Since publication of this Chapter in *Astronomy & Astrophysics*, additional Spitzer Short-Low observations as well as an improved “optimal extraction” technique have become available. In this appendix, these improved and extra observations are used to confirm or dismiss the previous tentative detections and put more stringent constraints on the PAH detection rate toward T Tauri disks.

The previously reported detection rate toward T Tauri disks was at least 3 out of 38. In addition, tentative 11.2  $\mu\text{m}$  detections were found toward 14 T Tauri stars. Wavelength coverage at 5–10  $\mu\text{m}$  was necessary to confirm the presence of 6.2, 7.7 and/or 8.6  $\mu\text{m}$  features.

The following 14 T Tauri stars had only 10–37  $\mu\text{m}$  wavelength coverage, and showed tentative 11.2  $\mu\text{m}$  PAH detections: DoAr 24E, EC 82, GW Lup, GY 23, HT Lup, Krautter’s Star, RU Lup, SX Cha, SY Cha, SZ 73, VW Cha, VZ Cha, V710 Tau (binary) and WX Cha.

Spitzer Short-Low observations, obtained in the context of the IRS Guaranteed Time Observation program (PID: 2, PI: J. Houck) were obtained from the Spitzer archive for all 14 T Tauri stars. The reduction was performed using the optimal PSF extraction technique developed within the c2d program, to allow separation of the compact source and extended emission components (Lahuis et al. 2007). The source size is determined from the width of the PSF function fitted to the source, compared to the width of the PSF function fit for standard calibrator stars. Comparison of the optimal PSF extraction and the full aperture extraction provides a direct estimate of any potential extended emission. The details of the observations and reduction procedures are described in Lahuis et al. (2006) and Lahuis (2007, thesis Chap. 3).

The resulting constraints for the 14 tentative detections are listed in Table 2.4. One of the 14 T Tauri stars, GY 23, was misclassified and resembles more an embedded class I source, and is therefore removed from the sample. The Short-Low observations for

**Table 2.4:** List of new constraints on previous tentative PAH detections.

Name	Comments
EC 82	confirmed 6.2 $\mu\text{m}$ PAH
DoAr 24E	no PAHs detected
GW Lup	no PAHs detected
HT Lup	no PAHs detected
RU Lup	no PAHs detected
SX Cha	no PAHs detected
Sz 73	no PAHs detected
Sz 102	no PAHs detected
V710 Tau (binary)	no PAHs detected
VW Cha	no PAHs detected
VZ Cha	no PAHs detected
WX Cha	no PAHs detected
SY Cha	source not detected in SL (pointing?)
GY 23	embedded object

one target, SY Cha, do not show a source detection, presumably due to mispointing by  $\sim 8''$ ; this target remains a tentative PAH detection.

The presence of PAHs is confirmed for one of the 14 tentative detections, EC 82, due to the detection of the 6.2  $\mu\text{m}$  PAH features. For the remaining 11 sources, no PAH features are observed at 6.2, 7.7 and/or 8.6  $\mu\text{m}$ .

In summary, our sample of T Tauri stars is reduced in size to 37, instead of 38. PAHs are detected toward 4 out of 37 sources (T Cha, SR 21A, LkH $\alpha$  330 and EC 82), and tentatively detected toward 1 source (SY Cha). This corresponds to an PAH detection rate of 11–14%. No PAHs are detected toward 32 out of 37 sources (86%).

## REFERENCES

- Acke, B. & van den Ancker, M. E. 2004, *A&A*, 426, 151  
Acke, B., van den Ancker, M. E., & Dullemond, C. P. 2005, *A&A*, 436, 209  
Alcalá, J. M., Covino, E., Franchini, M., et al. 1993, *A&A*, 272, 225  
Alcala, J. M., Krautter, J., Schmitt, J. H. M. M., et al. 1995, *A&AS*, 114, 109  
Alexander, R. D., Clarke, C. J., & Pringle, J. E. 2005, *MNRAS*, 358, 283  
Bell, K. R., Cassen, P. M., Klahr, H. H., & Henning, T. 1997, *ApJ*, 486, 372  
Bergin, E., Calvet, N., D'Alessio, P., & Herczeg, G. J. 2003, *ApJ*, 591, L159  
Bergin, E., Calvet, N., Sitko, M. L., et al. 2004, *ApJ*, 614, L133  
Cabrit, S., Edwards, S., Strom, S. E., & Strom, K. M. 1990, *ApJ*, 354, 687  
Cesarsky, D., Lequeux, J., Ryter, C., & Gérin, M. 2000, *A&A*, 354, L87  
Cohen, M. & Kuhl, L. V. 1979, *ApJS*, 41, 743

- D'Alessio, P., Canto, J., Calvet, N., & Lizano, S. 1998, *ApJ*, 500, 411
- D'Alessio, P., Hartmann, L., Calvet, N., et al. 2005, *ApJ*, 621, 461
- de Geus, E. J., de Zeeuw, P. T., & Lub, J. 1989, *A&A*, 216, 44
- Desert, F.-X., Boulanger, F., & Puget, J. L. 1990, *A&A*, 237, 215
- Dominik, C., Dullemond, C. P., Waters, L. B. F. M., & Walch, S. 2003, *A&A*, 398, 607
- Draine, B. T. & Li, A. 2001, *ApJ*, 551, 807
- Dullemond, C. P. & Dominik, C. 2004, *A&A*, 417, 159
- Dullemond, C. P., Dominik, C., & Natta, A. 2001, *ApJ*, 560, 957
- Dullemond, C. P., van Zadelhoff, G. J., & Natta, A. 2002, *A&A*, 389, 464
- Dunkin, S. K., Barlow, M. J., & Ryan, S. G. 1997, *MNRAS*, 286, 604
- Evans, N. J., Allen, L. E., Blake, G. A., et al. 2003, *PASP*, 115, 965
- Fernandez, M., Ortiz, E., Eiroa, C., & Miranda, L. F. 1995, *A&AS*, 114, 439
- Finkenzeller, U. & Mundt, R. 1984, *A&AS*, 55, 109
- Geers, V. C., Augereau, J.-C., Pontoppidan, K. M., et al. 2005, High resolution infrared spectroscopy in astronomy, by H.U. Kaeufl, R. Siebenmorgen, and A.F.M. Moorwood. ESO astrophysics symposia, Berlin: Springer., 239
- Gray, R. O. & Corbally, C. J. 1994, *AJ*, 107, 742
- Guhathakurta, P. & Draine, B. T. 1989, *ApJ*, 345, 230
- Habart, E., Natta, A., & Krügel, E. 2004, *A&A*, 427, 179
- Habart, E., Natta, A., Testi, L., & Carillet, M. 2005, ArXiv Astrophysics e-prints
- Habart, E., Verstraete, L., Boulanger, F., et al. 2001, *A&A*, 373, 702
- Habing, H. J. 1968, *Bull. Astron. Inst. Netherlands*, 19, 421
- Hernández, J., Calvet, N., Briceño, C., Hartmann, L., & Berlind, P. 2004, *AJ*, 127, 1682
- Hony, S., Van Kerckhoven, C., Peeters, E., et al. 2001, *A&A*, 370, 1030
- Houck, J. R., Roellig, T. L., van Cleve, J., et al. 2004, *ApJS*, 154, 18
- Houk, N. 1978, Michigan catalogue of two-dimensional spectral types for the HD stars (Ann Arbor : Dept. of Astronomy, University of Michigan)
- Jonkheid, B., Faas, F. G. A., van Zadelhoff, G.-J., & van Dishoeck, E. F. 2004, *A&A*, 428, 511
- Jonkheid, B., Kamp, I., Augereau, J.-C., & van Dishoeck, E. F. 2006, *A&A*, 453, 163
- Kamp, I. & Dullemond, C. P. 2004, *ApJ*, 615, 991
- Kamp, I. & Sammar, F. 2004, *A&A*, 427, 561
- Kenyon, S. J., Dobrzycka, D., & Hartmann, L. 1994, *AJ*, 108, 1872
- Kessler-Silacci, J., Augereau, J.-C., Dullemond, C. P., et al. 2006, *ApJ*, 639, 275
- Kessler-Silacci, J. E., Hillenbrand, L. A., Blake, G. A., & Meyer, M. R. 2005, *ApJ*, 622, 404
- Lahuis, F., Kessler-Silacci, J. E., Evans, II, N. J., et al. 2006, "c2d Spectroscopy Explanatory Supplement" (Pasadena: *Spitzer* Science Center)
- Lahuis, F., van Dishoeck, E. F., Blake, G. A., et al. 2007, *ApJ*, 665, 492

- Li, A. & Draine, B. T. 2001, *ApJ*, 554, 778
- Li, A. & Lunine, J. I. 2003, *ApJ*, 594, 987
- Manske, V. & Henning, T. 1999, *A&A*, 349, 907
- Martin, E. L., Montmerle, T., Gregorio-Hetem, J., & Casanova, S. 1998, *MNRAS*, 300, 733
- Mattioda, A. L., Hudgins, D. M., & Allamandola, L. J. 2005, *ApJ*, 629, 1188
- Meeus, G., Waters, L. B. F. M., Bouwman, J., et al. 2001, *A&A*, 365, 476
- Mora, A., Merín, B., Solano, E., et al. 2001, *A&A*, 378, 116
- Pascucci, I., Wolf, S., Steinacker, J., et al. 2004, *A&A*, 417, 793
- Pech, C., Joblin, C., & Boissel, P. 2002, *A&A*, 388, 639
- Peeters, E., Hony, S., Van Kerckhoven, C., et al. 2002, *A&A*, 390, 1089
- Peeters, E., Spoon, H. W. W., & Tielens, A. G. G. M. 2004, *ApJ*, 613, 986
- Prato, L., Greene, T. P., & Simon, M. 2003, *ApJ*, 584, 853
- Przygodda, F., van Boekel, R., Àbrahàm, P., et al. 2003, *A&A*, 412, L43
- Siebenmorgen, R., Kruegel, E., & Mathis, J. S. 1992, *A&A*, 266, 501
- Siess, L., Dufour, E., & Forestini, M. 2000, *A&A*, 358, 593
- Sloan, G. C., Keller, L. D., Forrest, W. J., et al. 2005, *ApJ*, 632, 956
- Spoon, H. W. W., Keane, J. V., Tielens, A. G. G. M., et al. 2002, *A&A*, 385, 1022
- Straizys, V., Cernis, K., & Bartasiute, S. 1996, *Baltic Astronomy*, 5, 125
- Sylvester, R. J., Skinner, C. J., Barlow, M. J., & Mannings, V. 1996, *MNRAS*, 279, 915
- Thé, P. S., de Winter, D., & Perez, M. R. 1994, *A&AS*, 104, 315
- Tielens, A. G. G. M. & Hollenbach, D. 1985, *ApJ*, 291, 722
- van Boekel, R., Waters, L. B. F. M., Dominik, C., et al. 2004, *A&A*, 418, 177
- van den Ancker, M. E., de Winter, D., & Tjin A Djie, H. R. E. 1998, *A&A*, 330, 145
- van Diedenhoven, B., Peeters, E., Van Kerckhoven, C., et al. 2004, *ApJ*, 611, 928
- Van Kerckhoven, C., Hony, S., Peeters, E., et al. 2000, *A&A*, 357, 1013
- Werner, M. W., Roellig, T. L., Low, F. J., et al. 2004, *ApJS*, 154, 1



---

---

## CHAPTER 3

---

# Spatial separation of small and large grains in the transitional disk around the young star IRS 48

V.C. Geers, K.M. Pontoppidan, E.F. van Dishoeck, C.P. Dullemond, J.-C. Augereau, B. Merín, I. Oliveira, J. W. Pel

*Astronomy & Astrophysics* 2007, 469, L35

### Abstract

WE present spatially resolved mid-infrared images of the disk surrounding the young star IRS 48 in the Ophiuchus cloud complex. The disk exhibits a ring-like structure at  $18.7\ \mu\text{m}$ , and is dominated by very strong emission from polycyclic aromatic hydrocarbons at shorter wavelengths. This allows a detailed study of the relative distributions of small and large dust grains. Images of IRS 48 in 5 mid-infrared bands from  $8.6$  to  $18.7\ \mu\text{m}$  as well as a low resolution N-band spectrum are obtained with VLT-VISIR. Optical spectroscopy is used to determine the spectral type of the central star and to measure the strength of the  $\text{H}\alpha$  line. The  $18.7\ \mu\text{m}$  ring peaks at a diameter of 110 AU, with a gap of  $\sim 60$  AU. The shape of the ring is consistent with an inclination of  $i = 48^\circ \pm 8^\circ$ . In contrast, the  $7.5\text{--}13\ \mu\text{m}$  PAH emission bands are centered on the source and appear to fill the gap within the ring. The measured PAH line strengths are 10–100x stronger than those typically measured for young M0 stars and can only be explained with a high PAH abundance and/or strong excess optical/UV emission. The morphology of the images, combined with the absence of a silicate emission feature, imply that the inner disk has been cleared of micron-sized dust but with a significant population of PAHs remaining. We argue that the gap can be due to grain growth and settling or to clearing by an unseen planetary or low-mass companion. IRS 48 may represent a short-lived transitional phase from a classical to a weak-line T Tauri star.

### 3.1 INTRODUCTION

The number of circumstellar dust disks detected around young stars has increased dramatically over the last decades thanks to a variety of ground- and space-based observations. Studies of the Spectral Energy Distributions (SEDs) of young stellar objects at various ages indicate how these disks evolve from optically thick, massive gas-rich disks to the more optically thin, tenuous gas-poor disks by a combination of gas accretion, grain growth, planet formation and photo-evaporation of the gas.

Only very few spatially resolved mid-infrared images have been presented. Some tenuous disks around 5-15 Myr stars show evidence for gap formation and spiral arm structures (e.g. Jayawardhana et al. 1998; Augereau et al. 1999; Liu 2004), and this has been interpreted as evidence for the presence of forming planets clearing out a ring of dust and gas. For younger disks around  $\sim 1$  Myr old stars, there is still very little direct evidence for the formation of gaps (Fujiwara et al. 2006).

An obvious step toward the formation of planetesimals in disks is the coagulation and growth of the sub-micron sized grains accreted from the proto-stellar envelope (Dominik et al. 2007). Although the end results are plainly visible in our own planetary system, as well as in the emerging wealth of exo-solar planets, the details and mechanisms of dust evolution in proto-planetary disks are not well understood. Very strong grain growth may lower the dust opacity enough to form an apparent gap in the disk at mid-infrared wavelengths, similar to those attributed to dust clearing by planets (D'Alessio et al. 2005; Tanaka et al. 2005). A wide range of recent observational results indeed suggest that significant grain growth is a common occurrence in disks (e.g. van Boekel et al. 2005; Kessler-Silacci et al. 2006; Natta et al. 2007).

However, some observations complicate this picture. A subset of protoplanetary disks shows strong emission features from extremely small grains – Polycyclic Aromatic Hydrocarbons (PAHs) (Acke & van den Ancker 2004; Geers et al. 2006), even in disks with apparent gaps. How do these disks fit into the general picture of grain evolution? Are they evidence of grain size segregation, leaving only the small grains in the upper layers of the disk? Is gas still present in these regions?

In this letter, we present one of the first spatially resolved mid-infrared images and spectroscopy of a disk around a young (few Myr) star with a rising mid-IR SED, IRS 48 in Ophiuchus (Wilking et al. 1989) (catalogued as WLY 2-48, 16 27 37.19, -24 30 35.0 J2000), which is no longer surrounded by an envelope. This source shows exceptionally strong PAH emission at 3.3 and 7.7–12.3  $\mu\text{m}$  in the inner part of the disk *as well as an apparent inner gap seen at 18.7  $\mu\text{m}$* . We will discuss the origin of the 18.7  $\mu\text{m}$  gap in the context of the PAH images which show that the gap is not *cleared* of material.

### 3.2 OBSERVATIONS OF IRS 48 AND DATA REDUCTION

Images were obtained with VISIR on the Very Large Telescope in 5 mid-infrared bands at 8.6, 9.0, 11.3, 11.9 and 18.7  $\mu\text{m}$  on June 9, 2005 (Fig. 3.1). VISIR N-band spectroscopy was taken on June 12, 2005, in the low resolution settings at 8.8, 9.8, 11.4 and 12.2  $\mu\text{m}$ , with a typical resolving power of  $\lambda/\Delta\lambda \sim 300$  (Fig. 3.2). The telescope was operated

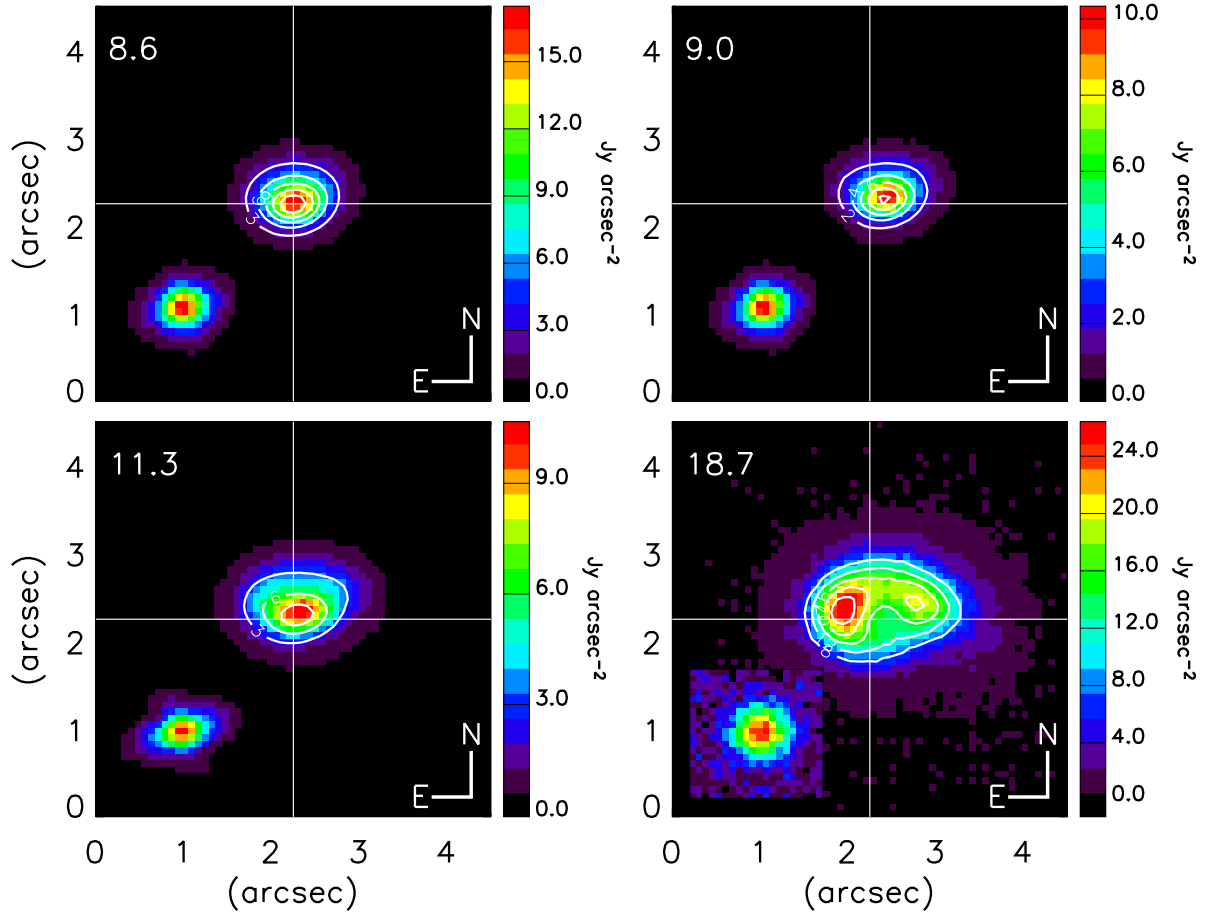


**Figure 3.1:** VISIR images of IRS 48, with PSF standard shown in inserts; the crosshair indicates the center of the emission at  $8.6 \mu\text{m}$ . All images up to  $12 \mu\text{m}$  are dominated by PAH emission. The  $11.9 \mu\text{m}$  image (not shown) is similar to that at  $11.3 \mu\text{m}$ . The contours are indicated for 3, 6, 9, 12, 15 ( $8.6 \mu\text{m}$ ), 2, 4, 6, 8, 10 ( $9.0 \mu\text{m}$ ), 3, 6, 9, 12 ( $11.3 \mu\text{m}$ ) and 8, 12, 16, 20, 24 ( $18.7 \mu\text{m}$ )  $\text{Jy arcsec}^{-2}$ .

using a standard chop-nod scheme with chop-throws of  $10''$ . The data were reduced using a combination of the ESO pipeline (v. 1.3.7) and our own IDL routines.

A WYFFOS optical spectrum was obtained at the William Herschel Telescope (WHT) on La Palma on May 4, 2006, with a resolving power of  $R \sim 1600$  (Fig. 3.3). It indicates a M0 spectral type ( $T_{\text{eff}} = 3800 \text{ K}$ ) with an error of less than 2 spectral subtypes.  $A_v = 7 \pm 1 \text{ mag}$  is derived from the optical spectrum as in Oliveira et al. (in prep.).  $\text{H}\alpha$  is detected with an Equivalent Width (EW) of  $5.9 \text{ \AA}$ , which classifies IRS 48 as a weak-line T Tauri star. Our derived spectral type is much later than that of Luhman & Rieke (1999), who found it to be earlier than F3 based on a K-band spectrum (taken sometime between July 1994 and June 1996). This discrepancy remains to be understood and will be discussed in §3.4.2.

Photometry used to construct the SED (Fig. 3.4) includes NOMAD (Zacharias et al. 2004), USNO-B (Monet et al. 2003), 2MASS (Skrutskie et al. 2006), ISOCAM (Bontemps et al. 2001), Spitzer Space Telescope IRAC and MIPS ( $3.6, 4.5, 5.8, 8.0, 24, 70 \mu\text{m}$ ) from

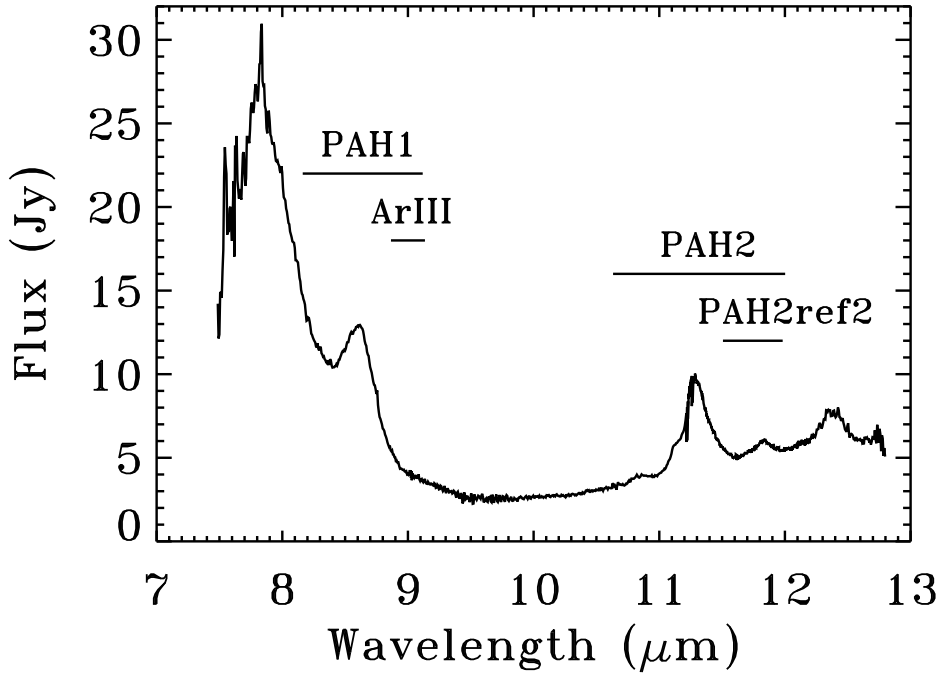


**Figure 3.2:** VLT-VISIR N-band spectrum of IRS 48. Spectral width of transmission curves of VISIR image filters are indicated.

the c2d legacy program database (Evans et al. 2003) and IRAM 1.3 mm (André & Montmerle 1994).

### 3.3 RESULTS

The circumstellar disk is spatially resolved in all 5 VISIR images, shown in Fig. 3.1. An extent of 1.2–1.9'' is derived along the semi-major axis, corresponding to 150–230 AU diameter; the actual extent increases with wavelength. Ducourant et al. (2005) measured a proper motion consistent with the surrounding Oph sources placing IRS 48 firmly at a distance of 125 pc (de Geus et al. 1989). All 5 bands are resolved with respect to the standard star PSF along the east-west direction, showing elongated surface brightness profiles consistent with a circumstellar disk. We derive an inclination of  $i = 48^\circ \pm 8^\circ$  from the semi-major and minor axes of ellipsoidal contours fitted to the 18.7  $\mu\text{m}$  image, and a position angle of  $98 \pm 3^\circ$  East of North.

The most striking result is that the 18.7  $\mu\text{m}$  Q-band image shows an asymmetry in the surface brightness and a gap in the center. We interpret the apparent shape as being due to an inclined ring-shaped disk. No point source is seen within this gap. Its diameter as measured from the inner edges of the ring along the semi-major axis equals 0.5'' or  $\sim 60$  AU, corresponding to a gap with a radius of  $\sim 30$  AU. In contrast, the PAH emission at 8.6 and 11.3  $\mu\text{m}$  is centrally peaked with resolved wings beyond a point-source, and it appears to originate from the apparent gap in the Q2 image.

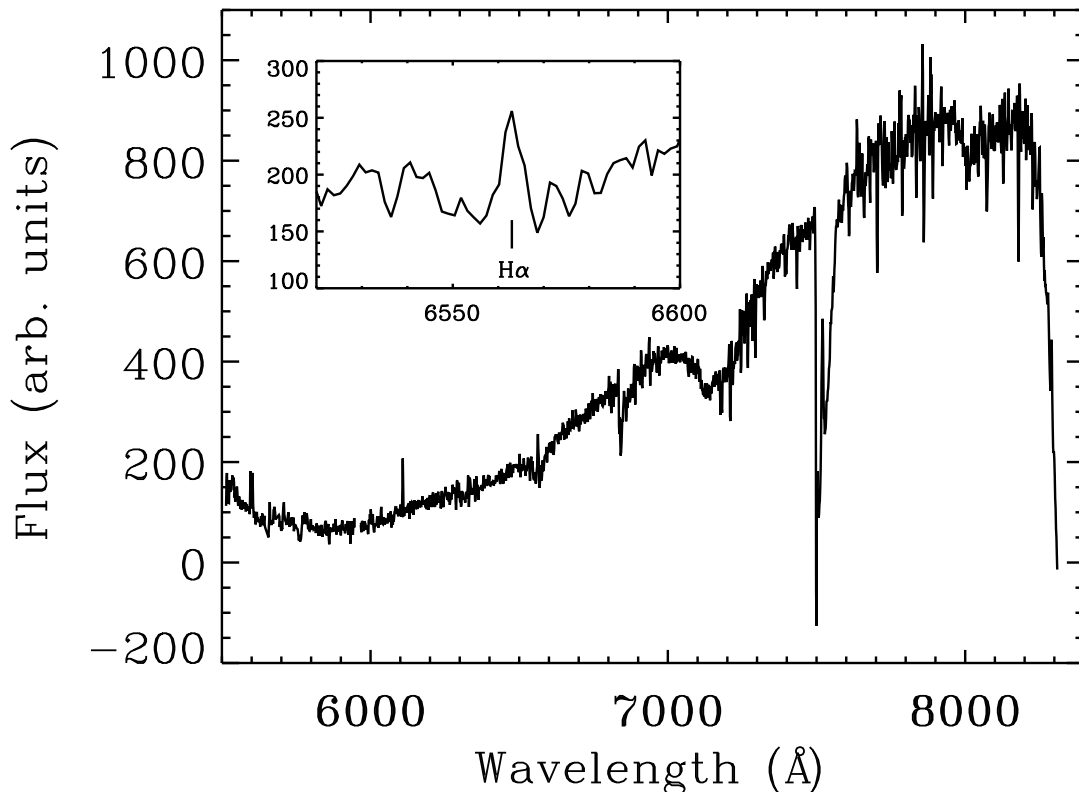


**Figure 3.3:** WHT-WYFFOS optical spectrum of IRS 48. The inset shows a blow-up of the H $\alpha$  line.

The center of the images shifts by  $\sim 0.2''$ , likely due to pointing error, as indicated by similar shifts in the standard star positions. The PAH off-band filters at  $9.0$  and  $11.9 \mu\text{m}$  both resemble the  $8.6$  and  $11.3 \mu\text{m}$  images respectively. Given the strength of the PAHs (see Fig. 3.2), it is assumed that both off-band filters also probe PAH emission or very small grains.

The VISIR N-band spectrum (Fig. 3.2) shows clear PAH features at  $8.6$ ,  $10.8$ ,  $11.3$ ,  $11.9$  and  $12.5 \mu\text{m}$ . Our  $11.3 \mu\text{m}$  line flux is  $2.5 \times 10^{-14} \text{ W m}^{-2}$ . The PAH features around this M0 star are as strong as the strongest features observed around Herbig Ae/Be stars (Acke et al. 2004), and make it the latest type young star with detected PAHs. No silicate emission feature at  $9.7 \mu\text{m}$  is detected. A VLT-ISAAC L-band ( $2.8\text{--}4.2 \mu\text{m}$ ) spectrum, obtained as part of the ice survey by van Dishoeck et al. (2003), taken on 2002, May 5 (sample and reduction described in Pontoppidan et al. 2003), shows the presence of a strong  $3.3 \mu\text{m}$  PAH feature and the  $4.05 \mu\text{m}$  Br $\alpha$  line (included in Fig. 3.4).

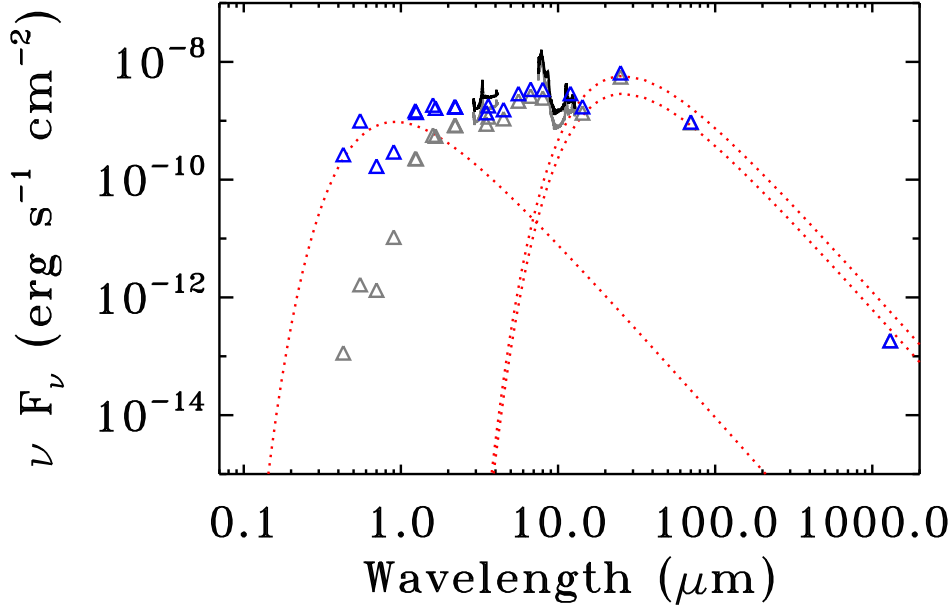


**Figure 3.4:** The SED of IRS 48 based on the photometry listed in §3.2. Grey triangles are literature photometry, blue triangles are dereddened, with  $A_v = 7$ ; black solid lines are ISAAC L-band and VISIR N-band spectra; orange dotted lines show 3 blackbodies, at  $T_{\text{eff}} = 4000$  K ( $0.63 L_{\odot}$ ) and 140 K, the latter scaled to 1.9 and  $3.8 L_{\odot}$ .

## 3.4 DISCUSSION

### 3.4.1 Gap in the disk

Gaps in disks around T Tauri stars have been inferred for a few sources (Calvet et al. 2005; Sicilia-Aguilar et al. 2006; Brown et al. submitted) but entirely on the basis of the SED, not spatially resolved images such as presented here. The  $18.7 \mu\text{m}$  image suggests a gap with a radius of 30 AU in the dust disk. However, the PAH-band images show that this gap cannot be entirely devoid of small particles. The near-infrared excess at  $1\text{--}3 \mu\text{m}$  also suggests that some hot dust still exists in a small ring of material or a puffed-up inner rim in the inner few AU, i.e., the disk shows a gap and not a hole. Interestingly, the SED of IRS 48 (Fig. 3.4) does not reveal the presence of a gap, possibly due to masking of the dip at  $\sim 5\text{--}15 \mu\text{m}$  by the strong PAH features and other types of very small grains (VSGs) present in the gap. Quantum-heated PAHs and very small grains reach a much higher average temperature than thermal grains, radiating strongly in distinct PAH features and continuum at  $5\text{--}15 \mu\text{m}$ , while being weaker at  $20 \mu\text{m}$ .

Gaps in disks have been interpreted in the context of photo-evaporation of gas and small dust grains by the central star. This mechanism is excluded here since it should create a similar gap in the PAH filter images. Another way to make an apparent gap is

to lower the dust opacity by grain growth, effectively removing the silicate dust particles responsible for the continuum emission between a few and  $\sim 15 \mu\text{m}$ . Theoretical models show that grain growth occurs on short time scales, with the shortest growth times in the inner parts of the disk (Weidenschilling 1997; Dullemond & Dominik 2005). Furthermore, larger grains settle to the mid-plane faster than smaller grains, creating a strong size segregation in the vertical direction, which would explain the strong feature/continuum ratio of the PAH features (Dullemond et al. *subm.*). The lack of a significant silicate feature at  $9.7 \mu\text{m}$  supports the idea that in the inner disk most of the dust is in larger micron-sized grains. However, this scenario has difficulties explaining the presence of a sharply defined ring structure.

A third way of gap formation is by the clearing out of gas and dust by a planet forming inside the disk (e.g. Klahr & Lin 2001) or a low-mass companion. Planets are expected to clear out larger ( $>100 \mu\text{m}$ ) grains much more rapidly than gas and small particles by tidal interaction and can cause sharp edges in images (Paardekooper & Mellema 2004; Quillen et al. 2004). Particularly, Rice et al. (2006) predict that larger dust grains are filtered out at the outer edge, presumably leading to a build-up of large dust grains and a clearly defined ring of material at the outer edge, while smaller grains (e.g. PAHs) continue to accrete inwards along with the gas, which would explain the continued presence of PAH emission in the gap. Interferometric observations at millimeter wavelengths to constrain the distribution of even larger (mm-sized) particles can further test these scenarios.

### 3.4.2 Source of central luminosity

The SED of IRS 48 is peculiar for several reasons. It shows a very strong bump at  $25 \mu\text{m}$  which appears to be consistent with a single temperature blackbody of  $\sim 140 \text{ K}$ . This emission bump includes  $18 \mu\text{m}$  and should be associated with the “ring” seen in the Q2-band image. The apparent luminosity from the  $25 \mu\text{m}$  bump is  $\sim 1.9\text{--}3.8 L_{\odot}$ . If this ring is assumed to be the sole source of the bump and if we assume the ring to be an optically thick annulus with a covering fraction of at most 0.2 with respect to the star, it follows that the central source should have a luminosity of at least  $10\text{--}20 L_{\odot}$ , which is more than 20 times stronger than expected for a 1 Myr M0 star.

External heating by nearby bright sources can be excluded from our own VISIR, Spitzer IRAC and ESO archive NACO images, as well as recent multiplicity surveys (Haisch et al. 2004). The possibility of a close ( $< 175 \text{ AU}$ ) binary with a higher mass early type star can be excluded for lack of spectral features associated with early type stars in our optical spectrum.

The most likely scenario is the presence of excess UV emission, which is absorbed by a local foreground layer of material, such as a strongly inclined disk with an inner rim that is puffed up due to temporary accretion events, or absorption by the flared outer disk. A fully edge-on disk is considered unlikely; it could produce the observed SED, but it would be inconsistent with the Q2-band image.

One example of excess luminosity is through accretion. This would require an accretion luminosity much larger than the star itself. No X-ray emission has been de-

tected toward this object by Chandra nor XMM-Newton (Grosso, priv. comm.) and both  $H\alpha$  and  $Pf\beta$  are relatively weak, which argues against strong accretion.

An alternative explanation might be that this disk has recently undergone a FU Orionis outburst. During a major FU Ori-type accretion event, the temperature of the disk increases over a span of 1–10 years from a few hundred to a few thousand K, and will dominate the spectrum even for optical wavelengths (Hartmann 2001). The apparent spectral type can change by several types, from late K-M to F-G type. This may explain the discrepancy between the <F3 spectral type determination observed between 1994 and 1996 and the M0 type determination in 2006. Heating of the disk would help the PAHs in two ways: any PAHs trapped in ices would be evaporated boosting the PAH abundance and the PAHs could be thermally excited.

### 3.4.3 PAH feature strength

IRS 48 is exceptional in its very prominent PAH features, both in strength and feature-over-continuum ratios, 100–1000 times stronger than recent model predictions for M0 stars (Geers et al. 2006). Comparing our measured  $11.3\ \mu\text{m}$  line strength with their Fig. 9, we find that it would be consistent with the radiation field of a  $\sim 6000$  K central star, in a disk model with a PAH abundance of  $5 \times 10^{-5}$  with respect to hydrogen, typical of the general interstellar medium but higher than inferred for disks. Assuming this abundance, the strong PAH features would be consistent with excess optical/UV luminosity at a level corresponding to several hundred times the average interstellar radiation field at a radius of 100 AU, which is consistent with recent optical/UV strengths of T Tauri stars inferred by Bergin et al. (2003).

The case of IRS 48 suggests that the combination of high feature-over-continuum PAH bands and the absence of silicate features together with a rising SED at  $\lambda > 12\ \mu\text{m}$  is also an indicator for the presence of gap formation through grain growth, which is not revealed in broadband SEDs. Mid-infrared spectroscopy and high-spatial resolution narrow-band imaging with 8-m class telescopes, combined with millimeter interferometric imaging, of a much larger sample of objects is crucial to determine whether IRS 48 is just a peculiar object or whether it forms part of a new class of transitional disks.

## ACKNOWLEDGEMENTS

We thank A. Smette for crucial help in obtaining the VISIR data and N. Grosso for providing X-ray information. KMP is supported by NASA through Hubble Fellowship grant 01201.01 awarded by the STScI, which is operated by the AURA, for NASA, under contract NAS 5-26555. Astrochemistry in Leiden is supported by a Spinoza grant from the Netherlands Organization for Scientific Research (NWO).



## REFERENCES

- Acke, B. & van den Ancker, M. E. 2004, *A&A*, 426, 151
- André, P. & Montmerle, T. 1994, *ApJ*, 420, 837
- Augereau, J. C., Lagrange, A. M., Mouillet, D., & Ménard, F. 1999, *A&A*, 350, L51
- Bergin, E., Calvet, N., D'Alessio, P., & Herczeg, G. J. 2003, *ApJ*, 591, L159
- Bontemps, S., André, P., Kaas, A. A., et al. 2001, *A&A*, 372, 173
- Calvet, N., D'Alessio, P., Watson, D. M., et al. 2005, *ApJ*, 630, L185
- D'Alessio, P., Hartmann, L., Calvet, N., et al. 2005, *ApJ*, 621, 461
- de Geus, E. J., de Zeeuw, P. T., & Lub, J. 1989, *A&A*, 216, 44
- Dominik, C., Blum, J., Cuzzi, J. N., & Wurm, G. 2007, in *Protostars and Planets V*, University of Arizona Press, ed. B. Reipurth, D. Jewitt, & K. Keil, 783–800
- Ducourant, C., Teixeira, R., Périé, J. P., et al. 2005, *A&A*, 438, 769
- Dullemond, C. P. & Dominik, C. 2005, *A&A*, 434, 971
- Evans, N. J., Allen, L. E., Blake, G. A., et al. 2003, *PASP*, 115, 965
- Fujiwara, H., Honda, M., Kataza, H., et al. 2006, *ApJ*, 644, L133
- Geers, V. C., Augereau, J.-C., Pontoppidan, K. M., et al. 2006, *A&A*, 459, 545
- Haisch, Jr., K. E., Greene, T. P., Barsony, M., & Stahler, S. W. 2004, *AJ*, 127, 1747
- Hartmann, L. 2001, *Accretion Processes in Star Formation* (Cambridge University Press)
- Jayawardhana, R., Fisher, S., Hartmann, L., et al. 1998, *ApJ*, 503, L79+
- Kessler-Silacci, J., Augereau, J.-C., Dullemond, C. P., et al. 2006, *ApJ*, 639, 275
- Klahr, H. H. & Lin, D. N. C. 2001, *ApJ*, 554, 1095
- Liu, M. C. 2004, *Science*, 305, 1442
- Luhman, K. L. & Rieke, G. H. 1999, *ApJ*, 525, 440
- Monet, D. G., Levine, S. E., Canzian, B., et al. 2003, *AJ*, 125, 984
- Natta, A., Testi, L., Calvet, N., et al. 2007, in *Protostars and Planets V*, University of Arizona Press, ed. B. Reipurth, D. Jewitt, & K. Keil, 767–781
- Paardekooper, S.-J. & Mellema, G. 2004, *A&A*, 425, L9
- Pontoppidan, K. M., Fraser, H. J., Dartois, E., et al. 2003, *A&A*, 408, 981
- Quillen, A. C., Blackman, E. G., Frank, A., & Varnière, P. 2004, *ApJ*, 612, L137
- Rice, W. K. M., Armitage, P. J., Wood, K., & Lodato, G. 2006, *MNRAS*, 373, 1619
- Sicilia-Aguilar, A., Hartmann, L., Calvet, N., et al. 2006, *ApJ*, 638, 897
- Skrutskie, M. F., Cutri, R. M., Stiening, R., et al. 2006, *AJ*, 131, 1163
- Tanaka, H., Himeno, Y., & Ida, S. 2005, *ApJ*, 625, 414
- van Boekel, R., Min, M., Waters, L. B. F. M., et al. 2005, *A&A*, 437, 189
- van Dishoeck, E. F., Dartois, E., Pontoppidan, K. M., et al. 2003, *The Messenger*, 113, 49
- Weidenschilling, S. J. 1997, *Icarus*, 127, 290

Willing, B. A., Lada, C. J., & Young, E. T. 1989, *ApJ*, 340, 823

Zacharias, N., Monet, D. G., Levine, S. E., et al. 2004, in *Bulletin of the American Astronomical Society*, 1418–+

---

## CHAPTER 4

---

# Spatially extended PAHs in circumstellar disks around T Tauri and Herbig Ae stars

V.C. Geers, E.F. van Dishoeck, R. Visser, K.M. Pontoppidan, J.-C. Augereau, E. Habart  
and A.M. Lagrange

Accepted for publication in *Astronomy & Astrophysics*

### Abstract

**T**O determine the presence and location of the emission from Polycyclic Aromatic Hydrocarbons (PAHs) towards low and intermediate mass young stars with disks using large aperture telescopes. VLT-VISIR N-band spectra and VLT-ISAAC and VLT-NACO L-band spectra of 29 sources are presented, spectrally resolving the 3.3, 8.6, 11.2 and 12.6  $\mu\text{m}$  PAH features. Spatial extent profiles of the features and the continuum emission are derived and used to associate the PAH emission with the disks. The results are discussed in the context of recent PAH emission disk models. The 3.3, 8.6 and 11.2  $\mu\text{m}$  PAH features are detected toward a small fraction of the T Tauri stars, with typical upper limits between  $1 \times 10^{-15}$  and  $5 \times 10^{-17} \text{ W m}^{-2}$ . All 11.2  $\mu\text{m}$  detections from a previous Spitzer survey are confirmed with (tentative) 3.3  $\mu\text{m}$  detections, and in all PAH sources both the 8.6 and the 11.2  $\mu\text{m}$  features are detected. For 6 detections, the spatial extent of the PAH features is confined to scales typically smaller than 0.12–0.34'', consistent with the radii of 12–60 AU disks at their distances (typically 150 pc). For 3 additional sources, WL 16, HD 100546 and TY CrA, one or more of the PAH features are more extended than the hot dust continuum of the disk, whereas for Oph IRS 48, the size of the resolved PAH emission is confirmed to be smaller than that of the large grains. For HD 100546, the 3.3  $\mu\text{m}$  emission is confined to a small radial extent of  $12 \pm 3$  AU, most likely associated with the outer rim of the gap in this disk. Gaps with radii out to 10–30 AU may also affect the observed PAH extent for other sources. For both Herbig Ae and T Tauri stars, the small measured extents of the 8.6 and 11.2  $\mu\text{m}$  features are consistent with larger ( $\geq 100$  carbon atoms) PAHs.

## 4.1 INTRODUCTION

Mid-infrared (IR) spectroscopy from the ground, with the Infrared Space Observatory (ISO), and recently with the Spitzer Space Telescope has revealed that low (T Tauri) and intermediate mass (Herbig Ae/Be) pre-main-sequence stars often show silicate bands in emission (e.g., Meeus et al. 2001; Honda et al. 2003; van Boekel et al. 2004; Kessler-Silacci et al. 2006). Yet only a small fraction of the T Tauri stars, 8% (Geers et al. 2006), shows clear Polycyclic Aromatic Hydrocarbon (PAH) features, which is low compared to 54% detected in Herbig Ae/Be stars (Acke & van den Ancker 2004; Habart et al. 2004). Geers et al. (2006) argued that their low PAH detection rate is consistent with a 10–100x lower PAH abundance in the disks, compared to the ISM. One difficulty has been to properly identify PAH features in mid-IR spectra, in the presence of strong silicate features. The 11.2  $\mu\text{m}$  band can be confused with the 11.2  $\mu\text{m}$  crystalline forsterite feature and it can also be blended with the broad amorphous silicate feature whose strength and spectral width varies with grain size.

The 3.3  $\mu\text{m}$  feature, obtainable through ground-based studies, is another diagnostic of the presence of PAHs in disks. This broad feature is comparatively isolated and is expected to be tightly correlated with the 11.2  $\mu\text{m}$  feature since both involve C–H vibrations, as confirmed by ISO data (e.g. Peeters et al. 2004). Confirming the presence of PAHs in the few T Tauri sources where they have tentatively been seen is the first aim of this paper.

The second aim is to determine whether the PAH emission comes from the disk or rather from an extended remnant envelope of dust around the star. With Spitzer spectroscopy the spatial resolution of  $\sim 3''$  at 10  $\mu\text{m}$  in the high resolution mode corresponds to spatial scales of 300–900 AU for typical nearby star forming regions ( $d = 100\text{--}300$  pc).

Ground-based observations of the 3.3 as well as the 8.6 and 11.2  $\mu\text{m}$  bands with 8m class telescopes provide a spatial resolution of  $< 0.3''$  (at 10  $\mu\text{m}$ ), which is an order of magnitude higher than that of Spitzer. Recent ground-based spatially resolved observations of a number of Herbig Ae stars at typical distances of 100–150 pc have shown that the measured PAH features come from regions with sizes typical of a circumstellar disk (radius  $< 12$  AU at 3.3  $\mu\text{m}$ ,  $< 100$  AU at 11.2  $\mu\text{m}$ ) (Habart et al. 2004; Geers et al. 2005; Lagage et al. 2006; Doucet et al. 2007). Spatially resolved mid-infrared spectroscopy was presented by van Boekel et al. (2004) for 3 bright Herbig Ae stars, who found that the 8.6, 11.2 and 12.7  $\mu\text{m}$  features are extended with respect to the continuum emission, on scales of (several) 100 AU. Habart et al. (2006) presented VLT-NACO observations resolving the 3.3  $\mu\text{m}$  PAH feature above the continuum emission for 4 Herbig Ae/Be sources, with typically 50% of the intensity coming from within radii smaller than 30 AU. In contrast, observations of WL 16 by Ressler & Barsony (2003) show spatially resolved PAH emission with an extent of  $880 \times 400$  AU at 1% of the peak level.

The above mentioned observations support the recent modeling results by Habart et al. (2004), Geers et al. (2006) and Visser et al. (2007), which indicate that most ( $\sim 80\%$ ) of the spatially extended PAH emission comes from within a radius  $\sim 120\text{--}170$  AU, with the exception of the 3.3  $\mu\text{m}$  feature for which they predict that half of the emission

should originate from  $<50\text{--}160$  AU from a typical Herbig Ae/Be star, which depends strongly on the size of the PAH molecules. No such data yet exist for T Tauri stars, except for the unusual target IRS 48, a M0 star for which Geers et al. (2007) measured PAH features with a radial spatial extent of  $\sim 75\text{--}90$  AU.

Determining the presence and location of PAHs in the T Tauri disks is significant for several reasons. Due to their high opacity at UV wavelengths, PAHs can be used as a tracer of the strength of the UV radiation field, while at the same time their presence in the inner disk can have a strong influence on the amount of UV that is received by the outer disk. Also, the strength of PAH features from the outer disk provides a tool to determine if the disk is flat or flaring (Dullemond & Dominik 2004; Acke & van den Ancker 2004; Habart et al. 2004). PAHs in the surface layer of the (outer) disk are an important heating mechanism of the gas through photo-ionization producing energetic electrons (Jonkheid et al. 2004). This in turn influences the outer disk chemistry and line emission. PAHs and Very Small Grains (VSGs) also become an important site for  $\text{H}_2$  formation when the classical grains have grown to  $\mu\text{m}$  or mm sizes (Jonkheid et al. 2006).

High spatial resolution images taken in narrow band filters centered at particular emission features are one method to constrain the spatial extent of the emitting species but a good discrimination between the contribution of silicates and PAHs to the mid-infrared excess emission is essential here. Long-slit infrared spectrometers such as ISAAC, VISIR and NACO, installed on the 8m class VLT telescopes, allow for both spectrally as well as spatially resolved observations of disks around young (pre-) main sequence stars.

In this article we present the results of two of such surveys, carried out with the VLT-ISAAC and VLT-VISIR instruments. In addition, VLT-NACO L-band spectroscopy is obtained on two sources, making use of adaptive optics to obtain even higher spatial resolution. The aim of this work is to obtain a limited survey of the 3.3 and 11.2  $\mu\text{m}$  features, with a focus on low mass T Tauri stars with disks, to study the usefulness of the 3.3  $\mu\text{m}$  feature as a PAH tracer compared with the 11.2  $\mu\text{m}$  feature and to study the spatial extent of the PAH emission in the context of the disk.

## 4.2 OBSERVATIONS AND DATA REDUCTION

### 4.2.1 Source selection

The sample contains 19 T Tauri stars and 10 Herbig Ae/Be stars and was selected as follows: 17 T Tauri stars in the nearby star forming regions Chamaeleon, Lupus, Ophiuchus and Serpens were chosen from the sample observed with Spitzer Infrared Spectrograph (IRS) in the context of the “Cores to Disks” (c2d) Legacy program (Evans et al. 2003). All their sources with definite and tentative PAH detections (Geers et al. 2006) were chosen, including 4 Herbig Ae stars. In addition, as part of a backup program during pointing limited nights with strong winds, 4 additional young stars in the Serpens and Corona Australis star forming regions, found in IRAC + MIPS imaging surveys, were observed with ISAAC. One source, HD 100546 was observed in an

earlier ISAAC program. Three sources, IRS 48, WL 16 and EC 82 were added to the VISIR N-band program after serendipitous discovery of the  $3.3 \mu\text{m}$  PAH band in the L-band spectra in an ISAAC survey of embedded sources (Pontoppidan et al. 2003). The final source list is given in Table 4.1.

#### 4.2.2 ISAAC L-band spectroscopy

L-band spectroscopy was obtained with ISAAC, the Infrared Spectrometer And Array Camera, installed at the VLT Antu at ESO's Paranal Observatory in Chile, in the nights of June 16, 2000 (HD 100546), August 9–14, 2005 and April 17–18, 2006 in the low resolution ( $\lambda/\Delta\lambda = 600$ ) spectroscopic mode in the spectral domain  $2.8\text{--}4.2 \mu\text{m}$  using a  $0.6'' \times 120''$  slit. The telescope was operated using a chop throw of  $20''$  and a nod throw of  $20''$ . Due to chopping these observations are only sensitive to spatially extended emission of at most  $10''$ . For flux calibration and telluric line correction several standard stars were observed. The data were reduced using our own IDL routines, first described in Pontoppidan et al. (2003). The individual frames were corrected for the non-linearity of the detector array and distortion corrected using a startrace map; bad pixels and cosmic ray hits were removed before co-adding, using a shift and add procedure to correct for telescope jitter. From the combined frames, both the positive and the two negative spectral traces were extracted and co-added. For correction of the telluric features the extracted source spectrum is divided by the similarly extracted standard star spectrum using an optimal small wavelength shift and an exponential airmass correction between the source and the standard, requiring that the pixel-to-pixel noise on the continuum of the final science spectrum is minimized. Before this exponential airmass correction is applied, the detector and filter response curves are removed in order to obtain a spectrum of the true atmospheric absorption. These curves are obtained by fitting an envelope to both the standard star spectrum and a spectrum of the approximate atmospheric transmission and by taking the ratio of the two envelopes. Flux calibration is performed by dividing the science spectrum by an observed standard star and multiplying by a blackbody with the effective temperature of the standard star. Airmass correction was applied by multiplying the flux of the science target by the factor  $10^{-0.4\text{Ext}_L(\text{AM}_{\text{st}} - \text{AM}_{\text{sc}})}$  where we use for the L-band atmospheric extinction,  $\text{Ext}_L = 0.08 \text{ magn.} \times \text{airmass}^{-1}$ , the value provided by ESO on the ISAAC webpage<sup>1</sup>. The flux calibration is estimated to be accurate to 30%. The spectrum is wavelength calibrated relative to the atmospheric transmission spectrum and is accurate to  $\sim 0.003 \mu\text{m}$ . Note that the observation campaign in August 2005 suffered from poor weather conditions, with strong winds and variable seeing. Part of the nights were pointing limited to the North due to strong winds, which led to a relatively large fraction of the backup program sample of Serpens sources being observed. A summary of the presented observations is given in Table 4.1.

<sup>1</sup>[http://www.eso.org/instruments/isaac/imaging\\_standards.html](http://www.eso.org/instruments/isaac/imaging_standards.html)

### 4.2.3 NACO L-band spectroscopy

L-band spectroscopy was obtained with NAOS-CONICA installed at the VLT-Yepun at ESO's Paranal Observatory in Chile, in service mode, in the nights of 25–26 March and 10 April of 2005 in the medium ( $R = 700$ ) resolution spectroscopic mode in the spectral domain 3.20–3.76  $\mu\text{m}$  using a  $0.172'' \times 28''$  slit. The data were reduced using our own IDL routines, following a similar procedure as for the ISAAC data. The spectrum is wavelength calibrated relative to the atmospheric transmission spectrum and is accurate to  $\sim 0.008 \mu\text{m}$ . Flux calibration is performed using ISAAC spectro-photometry, estimated to be accurate to 30%. One source, WL 16, was observed with the long-slit of the spectrograph aligned in 2 settings, both perpendicular as well as parallel to the semi-major axis of the disk, which is at a position angle of  $60 \pm 2^\circ$  (Ressler & Barsony 2003). A summary of the observations is given in Table 4.1.

### 4.2.4 VISIR N-band spectroscopy

N-band spectroscopy was obtained with VISIR installed at the VLT-Melipal at ESO's Paranal Observatory in Chile, in the nights of 3–7 May of 2006 in the low resolution ( $R \sim 350$ ) spectroscopic mode in the spectral domain 7.7–12.5  $\mu\text{m}$  using a  $0.75'' \times 32.3''$  slit. All sources were observed with the 8.5 and 11.4  $\mu\text{m}$  settings to cover the main 8.6 and 11.2  $\mu\text{m}$  PAH features. In addition a few sources were observed with the 8.1 and/or 12.2  $\mu\text{m}$  settings to cover the red wing of the 7.7  $\mu\text{m}$  as well as the 12.7  $\mu\text{m}$  PAH feature. Most of the nights were characterized by strong winds, pointing limited to the south and highly variable seeing. The telescope was operated using chop and nod throws of  $8''$ . Due to chopping these observations are only sensitive to spatially extended emission of at most  $4''$ . For flux calibration and telluric line correction several standard stars were observed. The data were reduced using our own IDL routines, following a similar procedure as for the ISAAC data. Flux calibration is performed using Spitzer IRAC 8  $\mu\text{m}$  photometry where possible. The uncertainty in the flux calibration is estimated to be 30%. The spectrum is wavelength calibrated using the ESO VISIR pipeline (v. 1.3.7) by comparison with atmospheric lines and is accurate to  $\sim 10^{-4} \mu\text{m}$ . A summary of the observations is given in Table 4.1.

### 4.2.5 Measuring spatial extent

The FWHM of the spatial profile of the ISAAC spectra is derived from the co-added 2D spectral images, by fitting a Gaussian profile for each wavelength bin. For the ISAAC data, distortion correction was not performed because this correction was found to introduce a semi-sinusoidal pattern. The spatial extent of the PAH feature at 3.3  $\mu\text{m}$  is measured with respect to the extent of the disk continuum emission at 3.3  $\mu\text{m}$ , interpolated between the continua points at 3.1 and 3.5  $\mu\text{m}$ . The extent in arcseconds is converted to a radial extent from the center in AU for sources with known distances.

Because of the variable seeing during a large part of our program, the atmospheric seeing is assumed to dominate the FWHM of the ISAAC and VISIR observations and

**Table 4.1:** Summary of observations.

Target	RA (2000)	Dec (2000)	Date	Sp. Type	Dist. (pc)	Ref.
<b>ISAAC L-band</b>						
SX Cha	10 55 59.73	-77 24 39.9	17-04-2006	M0	178	K06; W97
SY Cha	10 56 30.45	-77 11 39.3	18-04-2006	M0.5	178	K06; W97
WX Cha	11 09 58.74	-77 37 08.9	19-04-2006	K7-M0	178	K06; W97
HD 98922	11 22 31.7	-53 22 12	19-04-2006	B9	>540	A98; H78
HD 101412	11 39 44.5	-60 10 28	19-04-2006	B9.5	160	T94; A05
HD 100546	11 33 25.44	-70 11 41.2	16-06-2000	B9	103	A98; A98
T Cha	11 57 13.49	-79 21 31.4	18-04-2006	G8	66	A93; A98
IRAS 12535-7623	12 57 11.73	-76 40 11.1	19-04-2006	M0	...	K06; -
HT Lup	15 45 12.86	-34 17 30.6	09-08-2005	K2	140	H94; H93
GW Lup	15 46 44.73	-34 30 35.5	14-08-2005	M2-M4	140	H94; H93
SZ 73	15 47 56.94	-35 14 34.7	13-08-2005	M0	140	H94; H93
GQ Lup	15 49 12.10	-35 39 05.1	10-08-2005	K7-M0	140	H94; H93
HD 141569	15 49 57.75	-03 55 16.4	13-08-2005	B9.5-A0	100	AU04; AU04
IM Lup	15 56 09.22	-37 56 05.8	14-08-2005	M0	150–360	H94; H93, K01
RU Lup	15 56 42.30	-37 49 15.4	10-08-2005	K7-M0	150–360	H94; H93, K01
DoAr 24E	16 26 23.26	-24 20 59.8	15-08-2005	K0	125	K06; G89
Em* SR 21A	16 27 10.28	-24 19 12.7	15-08-2005	G2.5	125	P03; G89
Em* SR 9	16 27 40.29	-24 22 04.0	10-08-2005	K5-M2	125	L99; G89
Haro 1-17	16 32 21.93	-24 42 14.8	14-08-2005	M2.5	125	A93; G89
V1121 Oph	16 49 15.30	-14 22 08.7	10-08-2005	K5	-	V00; -
Wa Oph 6	16 48 45.62	-14 16 36.0	11-08-2005	K	-	G07; -
VV Ser	18 28 47.86	+00 08 39.8	11-08-2005	A0V	259	M01; S96
CoKu Ser G6	18 29 01.23	+00 29 33.0	11-08-2005	K3	259	C79; S96
HD 176386	19 01 38.89	-36 53 27.0	14-08-2005	B9.5	140	G93; S00
TY CrA	19 01 40.79	-36 52 34.2	14-08-2005	B9	140 <sup>a</sup>	V00; S00
T CrA	19 01 58.78	-36 57 49.9	10-08-2005	F0e	140 <sup>a</sup>	F84; S00
<b>VISIR N-band</b>						
SY Cha	10 56 30.45	-77 11 39.3	06-05-2006	M0	178	K06; W97
WX Cha	11 09 58.74	-77 37 08.9	06-05-2006	K7-M0	178	K06; W97
HD 98922	11 22 31.7	-53 22 12	07-05-2006	B9	>540	A98; H78
HD 101412	11 39 44.5	-60 10 28	07-05-2006	B9.5	160	T94; A05
T Cha	11 57 13.49	-79 21 31.4	04-05-2006	G8	66	A93; A98
WL 16	16 27 02.5	-24 37 30	06-05-2006	B8-A7	125	L99; G89
SR 21A	16 27 10.3	-24 19 13	06-05-2006	G2.5	125	P03; G89
Oph IRS 48	16 27 37.19	-24 30 35.0	12-06-2005	M0	125	O07; G89
VV Ser	18 28 47.86	+00 08 39.8	07-05-2006	A0V	259	M01; S96
EC 82	18 29 56.80	+01 14 46.0	07-05-2006	M0	259	K06; S96
<b>NACO L-band</b>						
WL 16 set 1	16 27 02.5	-24 37 30	25-03-2005	B8-A7	125	L99; G89
WL 16 set 2	16 27 02.5	-24 37 30	26-03-2005	B8-A7	125	L99; G89
WL 16 set 3	16 27 02.5	-24 37 30	10-04-2005	B8-A7	125	L99; G89
Oph IRS 48	16 27 37.19	-24 30 35.0	10-04-2005	M0	125	O07; G89

<sup>a</sup>: all CrA sources assumed to be at same distance as that derived by S00 for HD 176386.

References for spectral type, distance: A93: Alcalá et al. (1993), A98: van den Ancker et al. (1998), A04: Acke & van den Ancker (2004), AU04: Augereau & Papaloizou (2004), A05: Acke et al. (2005), C79: Cohen & Kuhl (1979), C06: Comerón (2007), D97: Dunkin et al. (1997), F84: Finkenzeller & Mundt (1984), G89: de Geus et al. (1989), G93: Grady et al. (1993), G07: Grankin et al. (2007), H78: Houk (1978), H93: Hughes et al. (1993), H94: Hughes et al. (1994), K01: Knude & Nielsen (2001), K06: Kessler-Silacci et al. (2006), L99: Luhman & Rieke (1999), M01: Mora et al. (2001), O07: Oliveira et al. (2007, in prep.), P03: Prato et al. (2003), R03: Ressler & Barsony (2003), S00: Siebenmorgen et al. (2000), S96: Strazys et al. (1996), T94: Thé et al. (1994), V00: Valenti et al. (2000), W97: Whittet et al. (1997),



the spatial blurring introduced by instrumental optics is ignored. The standard star is assumed to be an unresolved point source and where possible, its measured FWHM is used as a measure of the point-spread-function. Only for the case of HD 100546, the conditions were good enough to match the source and standard spectra by applying differential airmass and seeing corrections.

For the VISIR and NACO data, the extent of the spatial profile is derived as the standard deviation of the flux distribution  $F_i$  over the spatial pixels  $x_i$ . For each wavelength bin, the standard deviation  $\sigma^2$  is calculated as  $\Sigma(x_i - C)^2 \times F_i / \Sigma F_i$ , with centroid  $C = \Sigma(x_i \times F_i) / \Sigma F_i$ . Assuming a normal distribution,  $3\sigma$  corresponds to 99% of the spatial extent of the flux. The NAOS-CONICA observations of WL 16 and IRS 48 are taken using the adaptive optics (AO) system. This results in high angular resolution observations which were typically close to the diffraction limit ( $\sim 0.1''$  at  $3.3\ \mu\text{m}$ ).

## 4.3 RESULTS AND DISCUSSION

### 4.3.1 PAH detections and statistics

The L-band spectra are presented in Figs. 4.1 and 4.2. Table 4.2 lists the line intensities of the detected PAH features. The N-band spectra are shown in Figs. 4.3 and 4.4.

We detect the  $3.3\ \mu\text{m}$  PAH feature in 6 out of 24 sources, of which 4 Herbig Ae/Be stars (TY CrA, HD 100546, HD 98922, HD 101412) and 2 T Tauri stars (SR 21A, IRS 48). For VV Ser and T Cha, a marginal feature is found. The HI Br  $\alpha$ , Pf  $\gamma$ , Pf  $\delta$  and 10-5 transition lines are seen in the majority of the sample, of which the HI Pf  $\delta$  line lies superposed on the  $3.3\ \mu\text{m}$  feature. Note that we do not detect the  $3.3\ \mu\text{m}$  feature toward the Herbig Ae star HD 141569. A tentative  $11.2\ \mu\text{m}$  feature was presented by Sylvester et al. (1996) and later clearly detected by Sloan et al. (2005). This absence of the  $3.3$  and presence of the  $11.2\ \mu\text{m}$  feature is consistent with the model prediction of Li & Lunine (2003), where the  $3.3\ \mu\text{m}$  feature is weak due to the high degree of ionization in this disk (Allamandola et al. 1999).

In the N-band spectra, PAH features are detected in 3 Herbig Ae / Be (WL 16, HD 98922, HD 101412) and 4 T Tauri stars (T Cha, SR 21A, IRS 48, EC 82), shown in Figs. 4.3 and 4.4. In all cases, except EC 82, both the  $8.6$  and the  $11.2\ \mu\text{m}$  features are detected. For WL 16 and IRS 48, additional features at  $11.9$  and  $12.8\ \mu\text{m}$  are clearly seen.

The  $3.3\ \mu\text{m}$  PAH band is observed in only a very small number of T Tauri stars, 2 out of 18. Compared to Geers et al. (2006), all Herbig Ae and T Tauri stars with  $11.2\ \mu\text{m}$  Spitzer detections also show  $3.3\ \mu\text{m}$  features in this L-band survey, confirming the detections. In addition, we find  $3.3\ \mu\text{m}$  PAH features in a few sources that were not included in the Spitzer sample: IRS 48, WL 16 and HD 100546, all of which were known to have PAHs based on previous data (Malfait et al. 1998; Ressler & Barsony 2003; Geers et al. 2005). Conversely, we have not found any new T Tauri disks with PAHs at  $3.3\ \mu\text{m}$ . The sensitivity varied significantly throughout the nights but typical upper limits between  $1 \times 10^{-15}$  and  $5 \times 10^{-17}\ \text{W m}^{-2}$  are obtained for the  $3.3\ \mu\text{m}$  PAH feature, comparable to the Spitzer study of Geers et al. (2006) for the  $11.2\ \mu\text{m}$  feature.

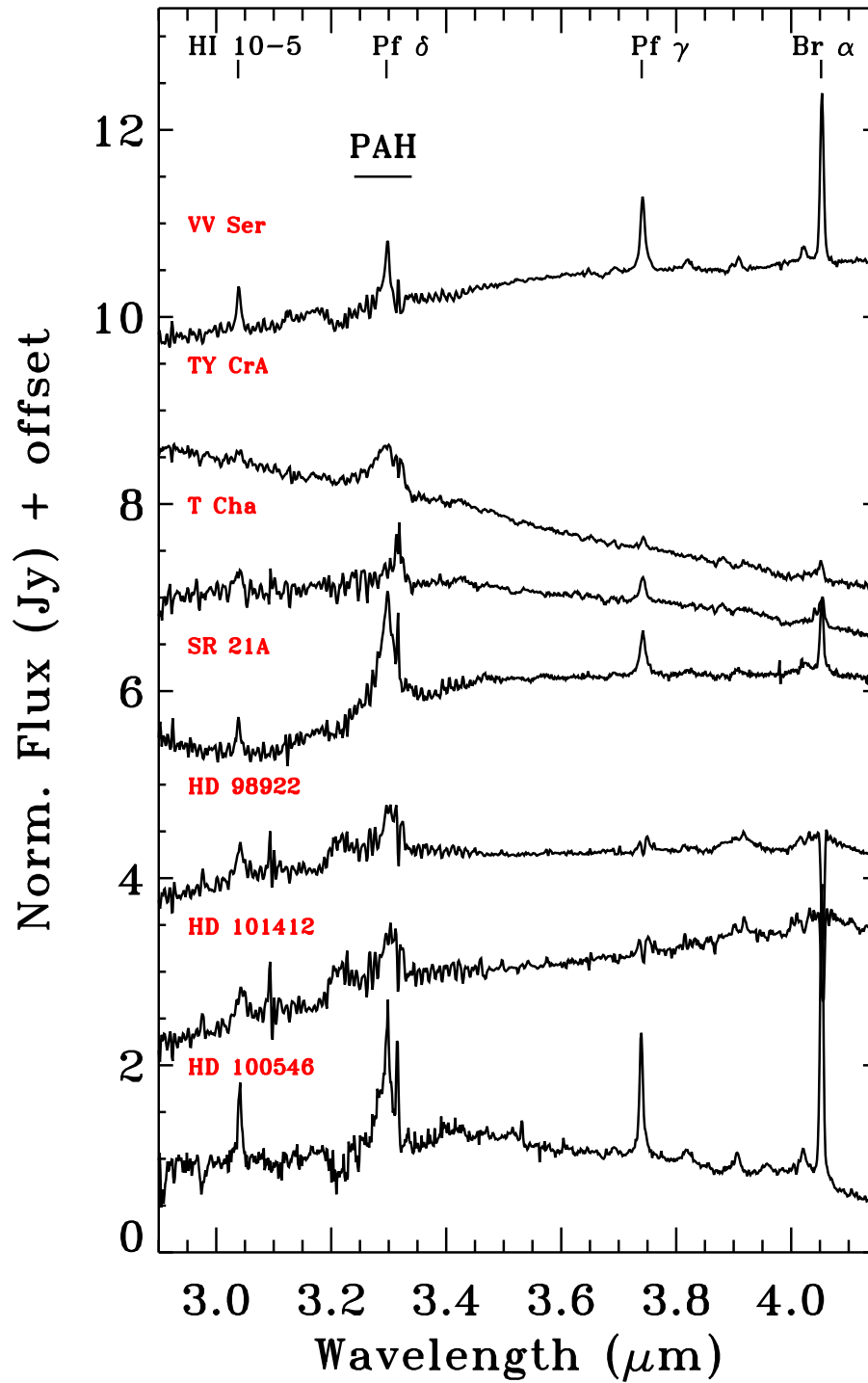


Figure 4.1: ISAAC L-band spectra of sample with 3.3  $\mu\text{m}$  PAH detection.

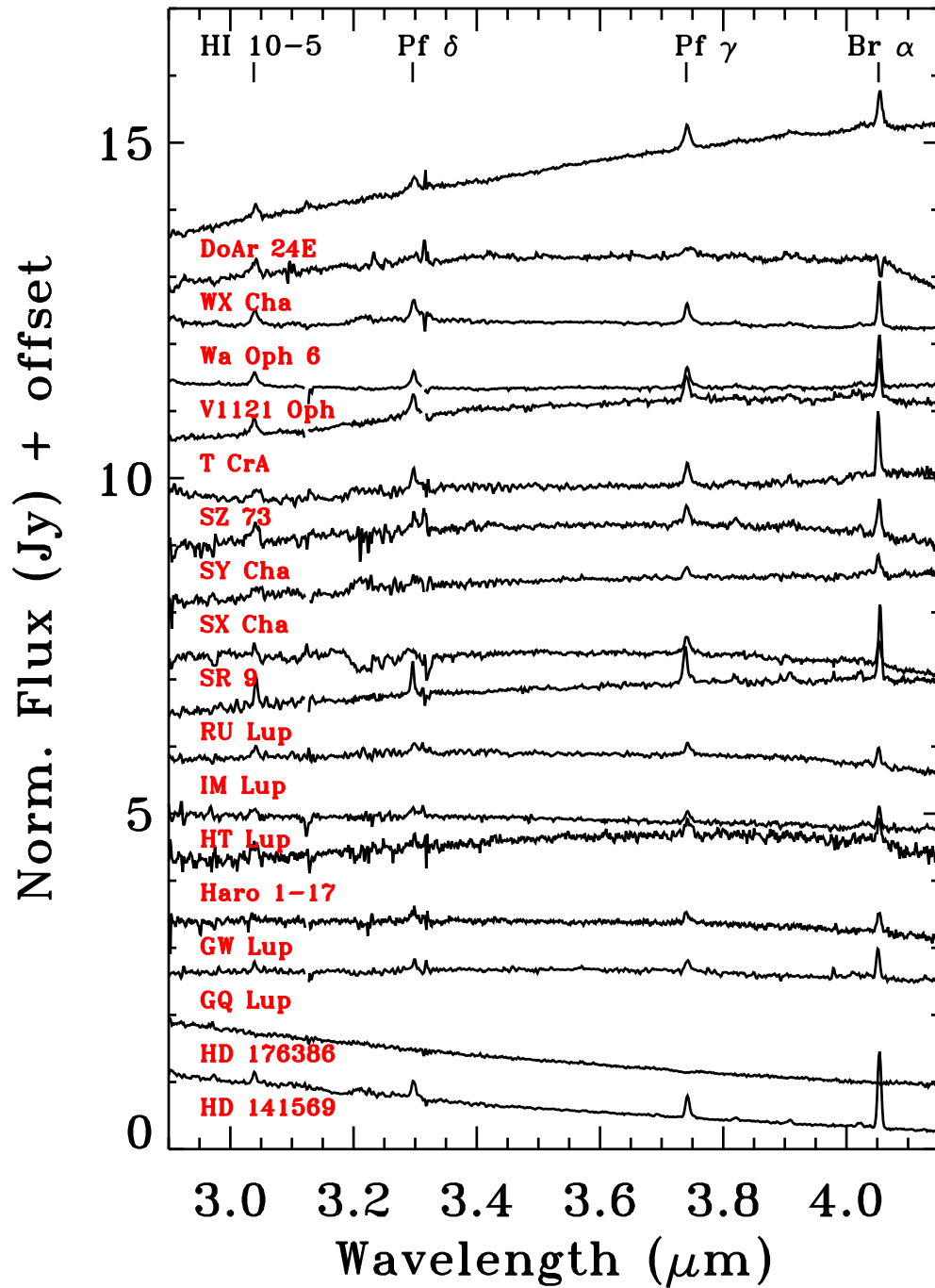


Figure 4.2: ISAAC L-band spectra of sample without  $3.3 \mu\text{m}$  PAH detection.

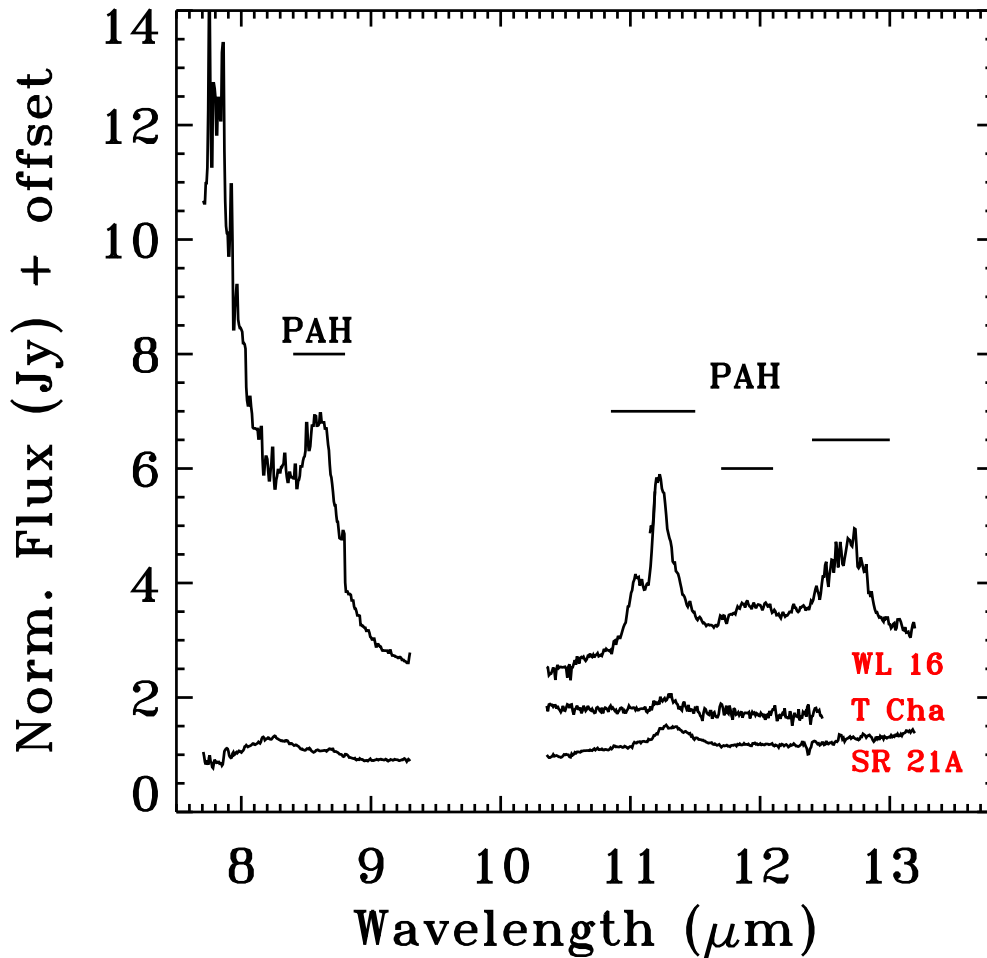
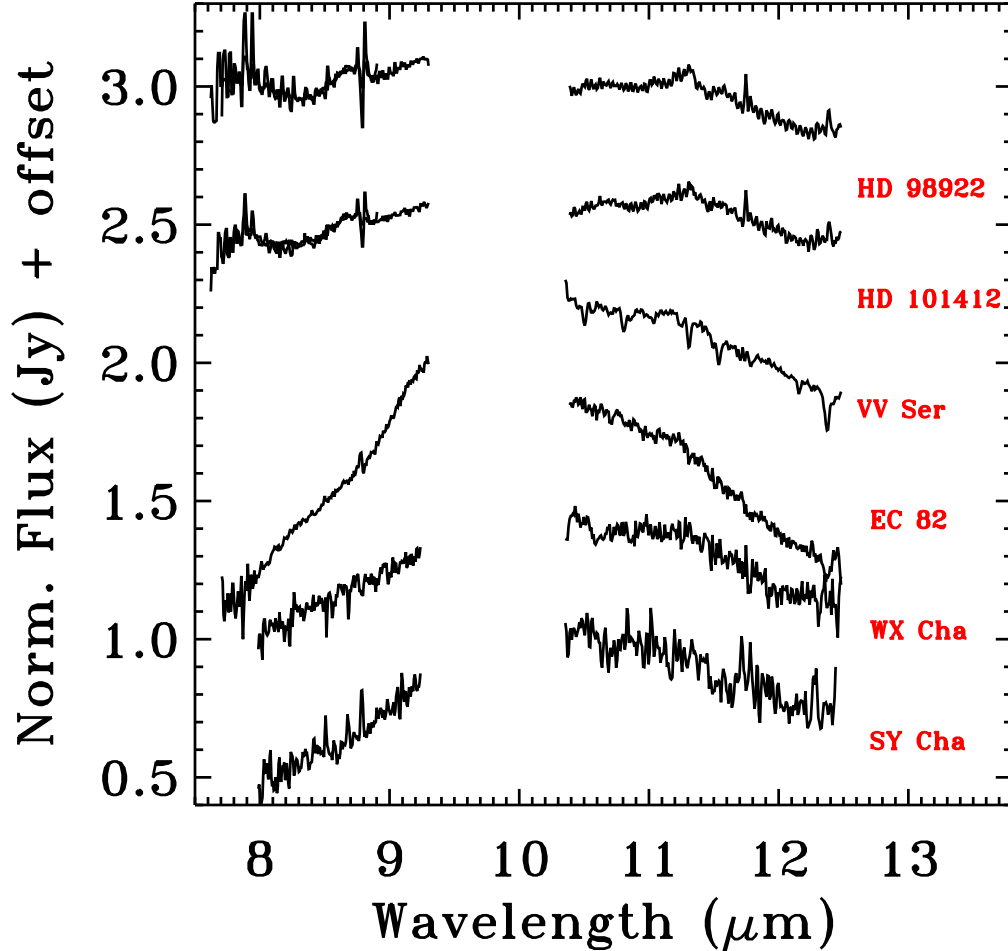


Figure 4.3: VISIR N-band spectra of the sources with PAH detections.

The  $11.2 \mu\text{m}$  feature is equally observed in only a small fraction of our T Tauri sample observed with VISIR. The Spitzer detections of Geers et al. (2006) are confirmed, and derived line intensities are consistent for most sources. The VISIR spectrum of VV Ser suffers from poor telluric correction and does not show a clear  $11.2 \mu\text{m}$  feature, in contrast with the Spitzer data. The spectra of HD 98922 and HD 101412 confirm the same weak, broad and confused  $11.2 \mu\text{m}$  line noted to be possibly due to crystalline silicates (Geers et al. 2006). For both sources, Kessler-Silacci et al. (2006) confirmed the presence of crystalline silicates from detection of the 23 and  $33 \mu\text{m}$  crystalline silicate features. However, the presence of  $8.6 \mu\text{m}$  detections in both VISIR spectra strengthens the conclusion that PAHs also contribute to the  $11.2 \mu\text{m}$  feature. In five sources both the  $3.3$  and  $11.2 \mu\text{m}$  PAH features are detected (HD 98922, HD 101412, IRS 48, WL 16 and SR 21A). One source, T Cha, has  $11.2 \mu\text{m}$  clearly detected but  $3.3 \mu\text{m}$  only marginally.



**Figure 4.4:** VISIR N-band spectra of the sources with marginal (top 4) and no PAH detections (bottom 2).

### 4.3.2 Spatial extent

Table 4.3 lists the radial spatial extent of the PAH features in half-width at half-maximum (HWHM). Spatial extent profiles are shown for a few sources, HD 100546, TY CrA, SR 21A, WL 16 and IRS 48 in the lower panels of Figs. 4.5–4.14. These figures show in the top panel the spectrum and in the bottom panel the diameter (full-width at half-maximum, or FWHM) of the spatial profile fit as a function of wavelength, for both the science source (in black) as well as the telluric and PSF standard star (in grey).

The majority of sources with PAH detections show no spatial extent of the features beyond the surrounding continuum emission from the disk at  $3.3 \mu\text{m}$ , confining the source to the same spatial extent as the disk continuum emission. In many cases the upper limit on the spatial extent is close to that of SR 21A, with a radius of  $0.33''$  (41

AU at  $d = 125$  pc), an example of a source with very strong unresolved PAH features (Fig. 4.11). These observations constrain the origin of the PAH emission from T Tauri sources to the circumstellar disk.

The hydrogen emission lines, 10-5, Pf  $\delta$ , Pf  $\gamma$  and Br  $\alpha$  are detected in the majority of the spectra, and are in all cases spatially unresolved. These lines are expected to originate from hot ionized gas in the very inner parts of the star+disk system, close to the surface of the central star.

The maximum spatial extent can be observed either when the disk is fully face-on or when it is inclined at a moderate degree with the slit of the spectrograph aligned with the semi-major axis of the disk. For most sources, the inclination and position angle of the disk are unknown and thus the derived spatial extents are in most cases treated as a lower limit for the disk component. For a typical  $45^\circ$  inclination, assuming a circular disk and aligning perpendicular to the apparent semi-major axis, this would lead to an underestimate of the extent by a factor of 1.4. In the following, individual cases are discussed.

### HD 100546

In HD 100546 (Fig. 4.5) the long-slit of ISAAC was aligned to the semi-major axis of the disk, to measure the maximum spatial extent of the emission. The  $3.3 \mu\text{m}$  PAH feature is spatially resolved, with a radial extent of  $0.40''$ , found to be slightly larger than the neighboring  $3 \mu\text{m}$  continuum extent. After correcting for the difference in airmass and seeing with respect to the standard star spectrum, we find that the feature has a spatial extent of  $0.12'' \pm 0.032''$ , and that the continuum emission is essentially unresolved. Assuming a distance of 103 pc, this corresponds to a radial extent of  $12 \pm 3$  AU.

HD 100546 is one of the most nearby isolated Herbig Be stars for which a circumstellar disk has been firmly established through space and ground based spectroscopy and imaging. Physical parameters for HD 100546 and its distance have been derived from Hipparcos observations (van den Ancker et al. 1998): it is a B9Ve star with a mass of  $2.4 M_\odot$ . The circumstellar disk has been resolved through imaging at visible (Grady et al. 2001), near-infrared (Pantin et al. 2000; Augereau et al. 2001), mid-infrared (Liu et al. 2003) and millimetre (Wilner et al. 2003) wavelengths. Augereau et al. (2001) observed an elliptical structure, consistent with an extended inclined disk, based on HST/NICMOS2 coronagraphic imaging at  $1.6 \mu\text{m}$  and derived values for the disk inclination and position angle adopted here.

Bouwman et al. (2003) modeled the spatial distribution and chemical composition of the dust around HD 100546, and found that the data required the presence of a small grain component at  $\sim 200$  K, inconsistent with a uniform flaring disk (Dullemond et al. 2001). Instead, they proposed that the disk of HD 100546 has a gap between  $\sim 1$  and 10 AU and is 'puffed up' at a radius of about 10 AU. Based on these results they conclude that the observations of the spectral energy distribution (SED) of HD 100546 are consistent with a largely cleared-out inner region between the inner rim and 10 AU and that most of the disk material is located in the outer parts of the disk. This conclusion was subsequently confirmed by Acke & van den Ancker (2006b). Our derived spatial extent of the  $3.3 \mu\text{m}$  feature of  $12 \pm 3$  AU would place the PAHs responsible for the  $3.3$

**Table 4.2:** Summary of PAH feature intensity in  $W \text{ m}^{-2}$  and presence of HI lines.

Source	H lines	3.3 $\mu\text{m}$	8.6 $\mu\text{m}$	11.2 $\mu\text{m}$	12.7 $\mu\text{m}$
SX Cha	Y	$\leq 1.9 \times 10^{-15}$	-	-	-
SY Cha	Y	$\leq 8.0 \times 10^{-17}$	-	-	-
WX Cha	Y	$\leq 2.7 \times 10^{-16}$	N	N	-
HD 98922	Y	$4.4 \times 10^{-14}$	Y	Y	-
HD 101412	Y	$2.8 \times 10^{-15} \text{ }^a$	Y	Y	-
HD 100546	Y	Y	-	-	-
T Cha	Y	$\leq 2.5 \times 10^{-15}$	-	-	-
IRAS 12535-7623	Y	N	-	-	-
HT Lup	Y	$\leq 1.3 \times 10^{-15}$	-	-	-
GW Lup	Y	$\leq 2.4 \times 10^{-16}$	-	-	-
SZ 73	Y	$9.4 \times 10^{-16} \text{ }^a$	-	-	-
GQ Lup	Y	$\leq 5.4 \times 10^{-16}$	-	-	-
HD 141569	Y	$\leq 6.9 \times 10^{-16}$	-	-	-
IM Lup	Y	$\leq 1.9 \times 10^{-15}$	-	-	-
RU Lup	Y	$\leq 5.7 \times 10^{-15} \text{ }^a$	-	-	-
DoAr 24E	Y	$\leq 4.1 \times 10^{-16}$	-	-	-
WL 16	Y	$\leq 9.6 \times 10^{-17}$	Y	Y	Y
Em* SR 21A	Y	$3.5 \times 10^{-15}$	Y	Y	T
Oph IRS 48	Y	$2.4 \times 10^{-15}$	Y	Y	Y
Em* SR 9	Y	$\leq 9.7 \times 10^{-16} \text{ }^a$	-	-	-
Haro 1-17	Y	$\leq 4.5 \times 10^{-17}$	-	-	-
V1121 Oph	Y	$1.2 \times 10^{-15} \text{ }^a$	-	-	-
Wa Oph 6	Y	$2.3 \times 10^{-15} \text{ }^a$	-	-	-
VV Ser	Y	$\leq 9.8 \times 10^{-16}$	-	T	-
CoKu Ser G6	T	N	-	-	-
EC 82	-	-	N	T	-
HD 176386	N	$\leq 4.2 \times 10^{-16}$	-	-	-
TY CrA	Y	$4.5 \times 10^{-15}$	-	-	-
T CrA	Y	$\leq 3.9 \times 10^{-15}$	-	-	-

- : not observed

<sup>a</sup> Line intensity affected by HI Pf  $\delta$  line

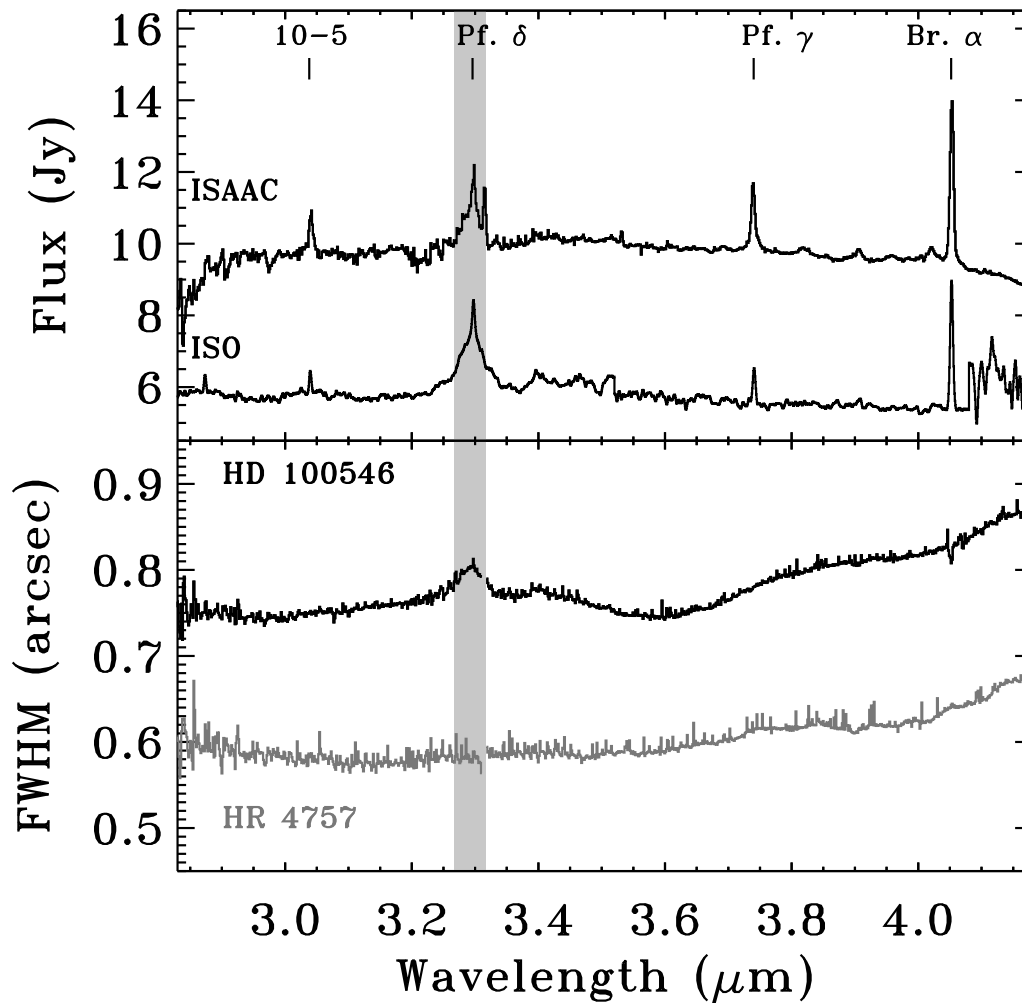


**Figure 4.5:** (Upper panel) ISAAC L-band spectrum of HD 100546, scaled by a factor 1.25 to match the ISO spectrum and then shifted by +4Jy for clarity. The grey band highlights the position and FWHM of the 3.3  $\mu\text{m}$  PAH feature as determined in this paper. (Lower panel) FWHM of the spatial profile, as extracted from 2D spectral image, of HD 100546 (*black line*) and its corresponding standard HR 4757 (*grey line*). The FWHM of the latter agrees with that of the HD 100546 continuum after correction for airmass and seeing differences.



**Table 4.3:** Summary of the radial spatial extent of the PAH feature (half-width at half-maximum).

Source	3.3 $\mu\text{m}$		8.6 $\mu\text{m}$		11.2 $\mu\text{m}$		12.7 $\mu\text{m}$	
PAH detected and spatially resolved								
HD 100546	0.12''	12 AU	-	-	-	-	-	-
TY CrA	0.39''	55 AU	-	-	-	-	-	-
WL 16	-	-	0.43''	54 AU	0.49''	61 AU	0.46''	58 AU
IRS 48	0.11''	14 AU	0.25''	31 AU	0.32''	40 AU	0.33''	41 AU
PAH detected but spatially unresolved								
HD 98922	$\leq 0.24''$	$\leq 130 \text{ AU}^a$	$\leq 0.17''$	$\leq 92 \text{ AU}$	$\leq 0.15''$	$\leq 81 \text{ AU}$	-	-
HD 101412	$\leq 0.24''$	$\leq 38 \text{ AU}$	$\leq 0.16''$	$\leq 26 \text{ AU}$	$\leq 0.15''$	$\leq 24 \text{ AU}$	-	-
Em* SR 21A	$\leq 0.33''$	$\leq 41 \text{ AU}$	$\leq 0.16''$	$\leq 20 \text{ AU}$	$\leq 0.17''$	$\leq 21 \text{ AU}$	$\leq 0.15''$	$\leq 19 \text{ AU}$
T Cha	$\leq 0.34''$	$\leq 22 \text{ AU}$	-	-	$\leq 0.19''$	$\leq 13 \text{ AU}$	-	-
EC 82	-	-	$\leq 0.18''$	$\leq 47 \text{ AU}$	$\leq 0.23''$	$\leq 60 \text{ AU}$	-	-

<sup>a</sup> : uncertain distance to source

$\mu\text{m}$  emission at the puffed-up rim at the outer edge of the cleared out region where a relatively large fraction of UV radiation is intercepted.

Habart et al. (2006) report the presence of a 5-10 AU radial gap in the 3.3  $\mu\text{m}$  PAH spatial distribution, and a clear extension to at least 50 AU radially, which is larger than the typical extent (30 AU) found in their sample. This gap is not seen in our ISAAC data because of our lower spatial resolution. Our ISAAC HWHM of the spatial extent of  $\sim 12$  AU is smaller than their full 50 AU extent, presumably from our lower sensitivity to weaker extended emission with ISAAC. Their PAH distribution is consistent with our finding that the PAH emission is dominated by the dust rim at the outer edge of the gap.

## TY CrA

For TY CrA (Fig. 4.6), the 3.3  $\mu\text{m}$  feature is found to be spatially resolved (0.78'', corresponding to a radial extent of 54 AU) compared with the underlying 3.3  $\mu\text{m}$  disk continuum (0.73'', or 51 AU radially). The coordinates of this compact component match within 1'' with the optical multiple star system and with the nearest bright 2MASS Ks-band source. TY CrA is a very strong X-ray source, surrounded by a strong reflection nebula. Unpublished Spitzer/IRAC observations show a large extended nebulosity at 8  $\mu\text{m}$  around this source (Allen, priv. comm.), confirming that PAHs are present on even larger scales as shown by Siebenmorgen et al. (2000) at 11.28  $\mu\text{m}$ . The spatial emission profile of the 3.3  $\mu\text{m}$  feature is shown in Fig. 4.7, which confirms the presence of the weak extended PAH emission. PAH features have been previously observed toward this star with ISO (Klaas et al. 2006; Acke & van den Ancker 2006a). NACO imaging revealed this system to be a possible quadruple system of low-mass M type stars (Chauvin et al. 2003), possibly affecting the circumstellar disk(s) structure and resulting PAH emission.

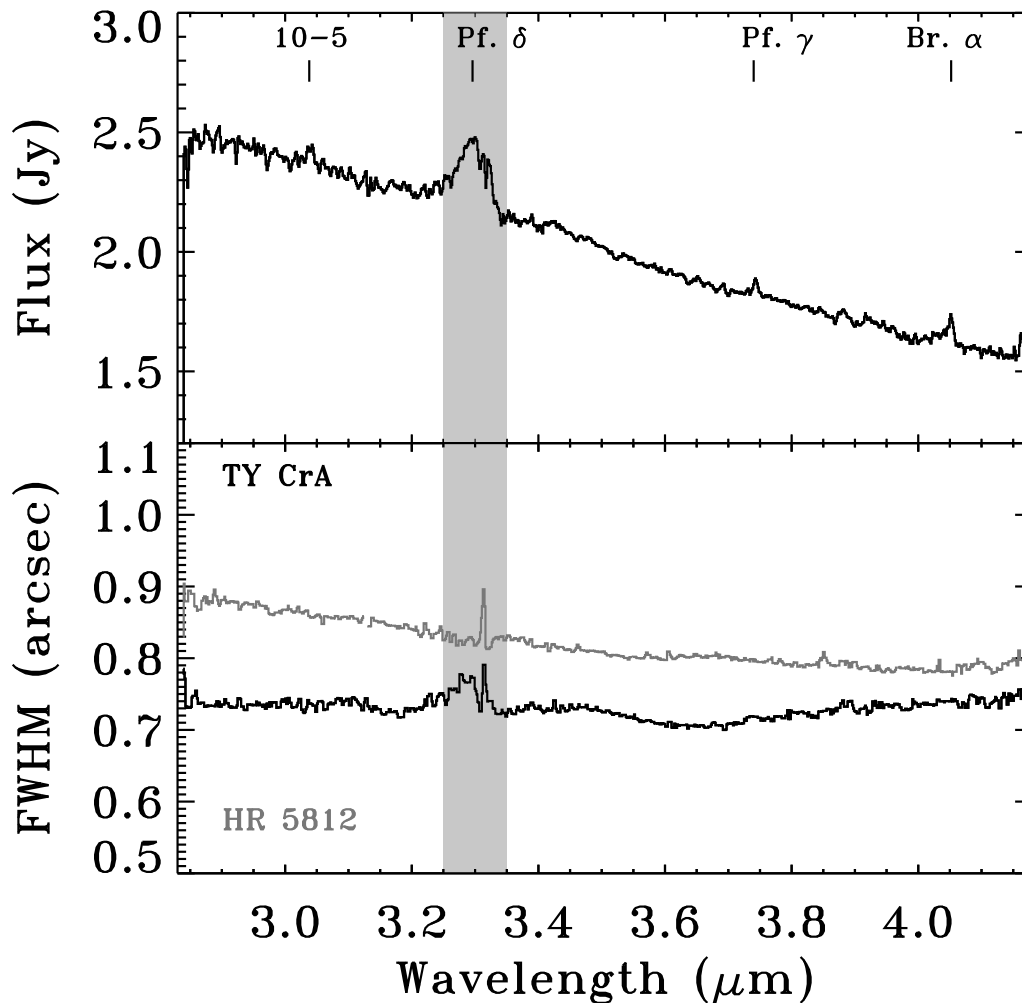


**Figure 4.6:** (Upper panel) ISAAC L-band spectrum of TY CrA. (Lower panel) FWHM of spatial profile of TY CrA and standard star HR 5812.

## WL 16

For WL16, the disk continuum emission at 8–13  $\mu\text{m}$  is resolved with a radial extent of about 0.4'' (50 AU) (Figs. 4.8 and 4.9). The 8.6, 11.2 and 12.7  $\mu\text{m}$  PAH features are resolved with respect to the continuum, with radial spatial extents of 0.43'' (54 AU), 0.49'' (61 AU) and 0.46'' (58 AU). The spatial emission profile is shown in the left panel of Fig. 4.7. The PAH emission at 10–13  $\mu\text{m}$  has broad wings in the spatial direction, extending beyond the spatial extent derived using the statistical derivation described in Sec. 4.2.5, illustrating how in certain cases it is hard to quantify the spatial extent in a single number. The extent varies with wavelength, which is not expected from uniform diffuse background PAH emission. Deriving the extent alternatively as 1% of the peak level, we find a value of 80–140 AU, which is about a factor 2.5 lower than that

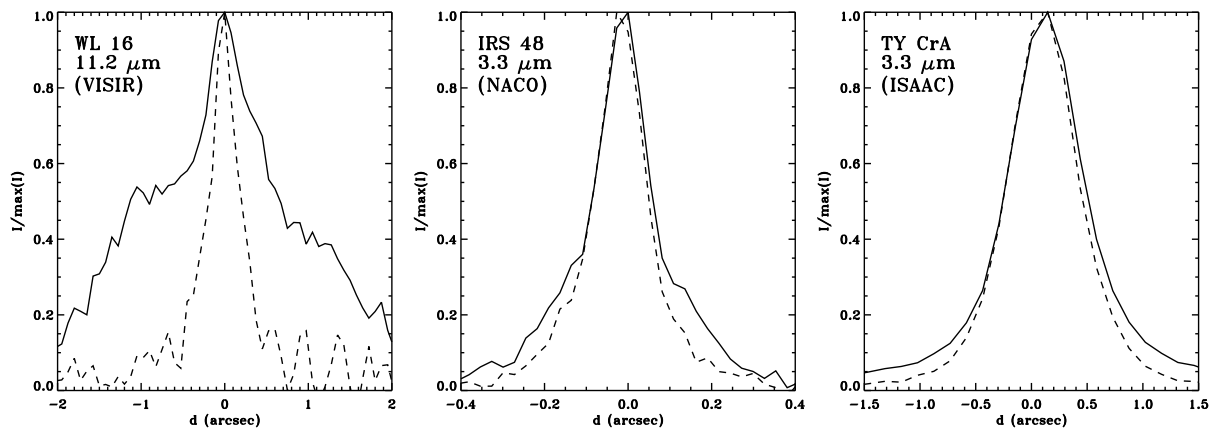


**Figure 4.7:** Observed spatial emission profiles for WL 16 (left), IRS 48 (middle) and TY CrA (right), for the PAH feature at indicated wavelength (solid line) and continuum emission at 10.51, 3.56 and 3.35  $\mu\text{m}$  respectively (dashed line).

found by Ressler & Barsony (2003) of 440 by 220 AU radially, based on Keck imaging covering 7.9 to 24.5  $\mu\text{m}$ . Given the reported semi-major over semi-minor axis ratio of 0.466, the effect of non-alignment of the VISIR slit with the semi-major axis can be at most a factor of 2.

NACO L-band spectroscopy was taken in two settings, aligning the long-slit parallel to the semi-major axis and perpendicular. The 3.3  $\mu\text{m}$  feature is undetected in both orientations (Fig. 4.10). The radial spatial extent of the continuum at 3.3  $\mu\text{m}$  is small and very similar between both orientations. The non-detection at 3.3  $\mu\text{m}$  would be consistent with predominantly ionized PAHs (Allamandola et al. 1999; Li & Draine 2001).

### SR 21A

In contrast with WL 16, SR 21A is a source with very strong 3.3, 8.6 and 11.2  $\mu\text{m}$  features but spatially unresolved. The 3.3, 8.6–11.2  $\mu\text{m}$  disk continuum emission has a radial extent of  $\leq 0.15$ – $0.33''$ , corresponding to  $\sim 19$ – $41$  AU, shown in Figs. 4.11 and 4.12, and in the left panel of Fig. 4.9. This source has been interpreted as a ‘cold disk’ source by Brown et al. (2007) with a gap between 0.45 and 18 AU, but with a large outer disk. The origin of the PAH emission is suspected to arise at the outer edge of the inner disk or within the gas filling the gap, inside 30 AU radius. The unknown position angle may have led to a chance alignment of the slit close to the semi-minor axis of the disk, which may have reduced the apparent spatial extent.

### IRS 48

IRS 48 is the only source in this sample for which all PAH features are spatially resolved. IRS 48 is a low mass M0 star in the  $\rho$  Oph cloud for which strong 3.3, 8.6, 11.2, 11.9 and 12.7  $\mu\text{m}$  PAH features are detected. For this source VISIR images have shown the presence of a 30 AU radius gap in the inner disk (Geers et al. 2007) with

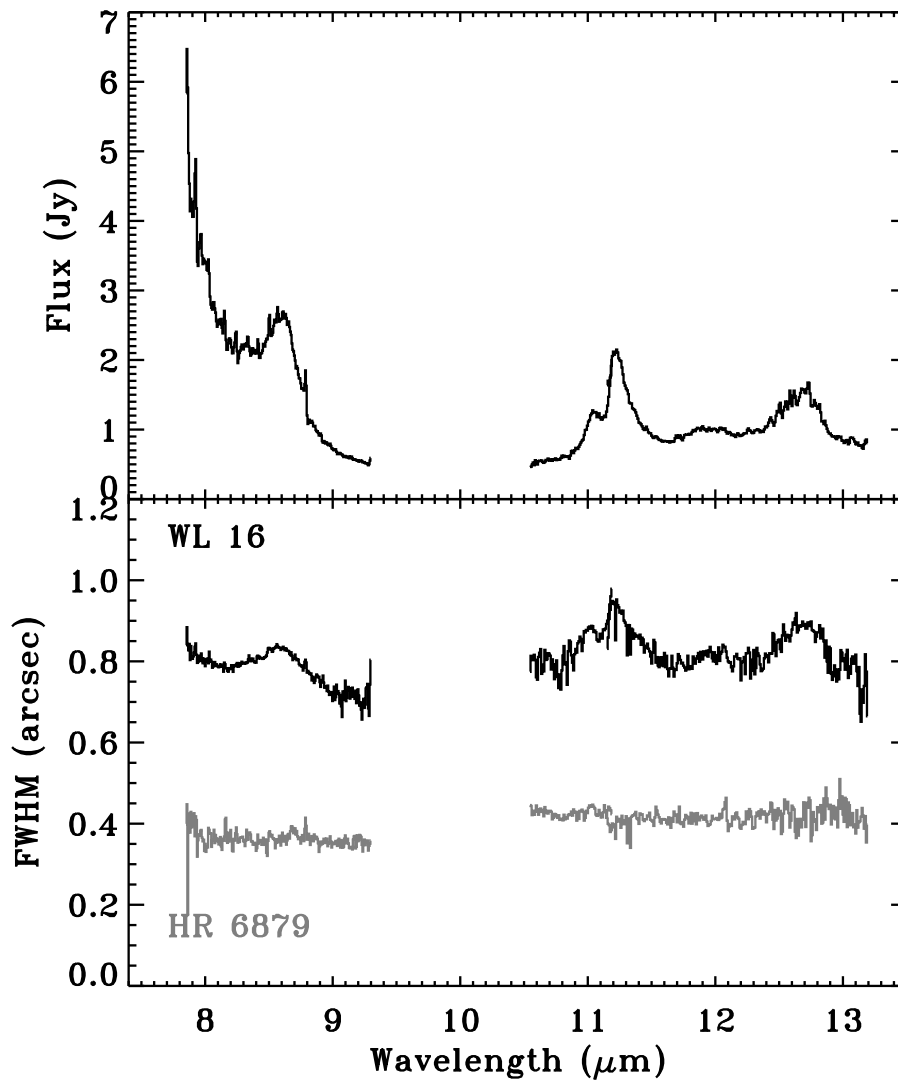


**Figure 4.8:** (Upper panel) VISIR N-band spectrum of WL 16. (Lower panel) FWHM of spatial profile of WL 16 and standard star HR 6879.

the PAH feature emission originating from a region inside the gap. The disk continuum emission at 3–4  $\mu\text{m}$  in the NACO spectrum is spatially resolved with a radial extent rising from 0.06–0.09'' (7.5–11 AU) with wavelength. The 3.3  $\mu\text{m}$  PAH feature is detected and spatially resolved on a radial scale of 0.11'' (or 15 AU) above the extent of the continuum of  $\sim 0.07''$  or 9 AU (Figs. 4.7 and 4.14). Assuming diffraction limit and no influence of seeing and correcting for the contribution of the PSF based on the spatial extent of the underlying continuum, the radial extent of the 3.3  $\mu\text{m}$  features is found to be  $\sim 11$  AU. The disk continuum emission at 8–13  $\mu\text{m}$  in the VISIR spectrum is resolved with a radial extent increasing from 0.25''–0.33'' (31–41 AU). The 8.6, 11.2 and 12.7  $\mu\text{m}$  features are spatially resolved on a radial scale *smaller* than the

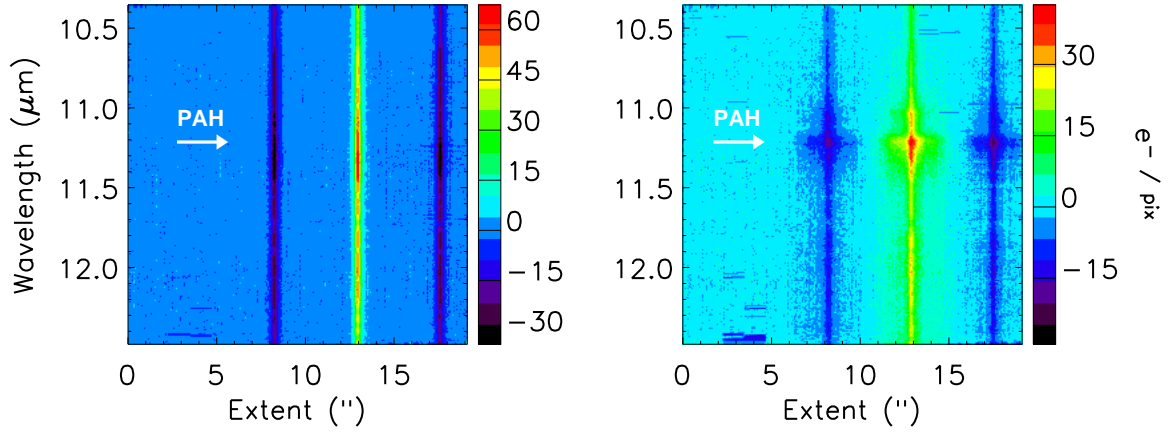


**Figure 4.9:** VISIR 2D spectral image of SR 21A (left) and WL 16 (right); 1 pixel = 0.02719".

surrounding disk continuum, with radial extents of 0.25, 0.32 and 0.33" (31, 40, 41 AU) respectively, half-width at half-maximum (HWHM). These extents are consistent with the full (99%) radial 8.6 and 11.2  $\mu\text{m}$  PAH extent of 75 and 90 AU respectively, found in spatially resolved in VISIR images in Geers et al. (2007). Also, our finding of the smaller feature extent compared with the continuum is consistent with the VISIR images showing PAH emission to be smaller than the mid-IR 18.7  $\mu\text{m}$  emission.

### T Cha

For T Cha, van den Ancker et al. (1998) measured a distance of only 66 pc, making it one of the closest, isolated T Tauri stars, and not part of the Chamaeleon cloud ( $d = 178$  pc). A weak 11.2  $\mu\text{m}$  feature and a marginal 3.3  $\mu\text{m}$  feature are detected. The 3.3  $\mu\text{m}$  feature is unresolved, with a radial spatial extent of the continuum emission of  $\leq 0.34''$ , corresponding to  $\leq 22$  AU. The 11.2  $\mu\text{m}$  feature is also unresolved, with a continuum spatial extent of  $\leq 0.19''$ , corresponding to a radial extent of  $\leq 13$  AU.

### Summary and discussion

Table 4.3 summarizes our detections of spatially resolved PAH features. It tabulates the half-width at half-maximum extent of the emission, assuming it can be fitted with a Gaussian profile. Under this assumption, this HWHM extent corresponds to the radius of the disk, inwards of which 76% of the normalized cumulative emission originates.

This HWHM extent is compared with model predictions by Visser et al. (2007), reproduced in Fig. 4.16 in Appendix 4.5, with an improved extraction technique. Figure 4.15 plots the radial extent of the 3.3  $\mu\text{m}$  versus the 11.2  $\mu\text{m}$  feature, for both model predictions of Herbig Ae stars and T Tauri stars, for both small ( $N_c=50$ ) and large ( $N_c=96$ ) PAHs. The model extent of the 3.3  $\mu\text{m}$  feature varies strongly with PAH size, decreasing by a factor 2-3 when the PAH size is increased by a factor of  $\sim 2$ , while the extent of the 11.2  $\mu\text{m}$  feature is less sensitive. For Herbig Ae stars, the model predicts for

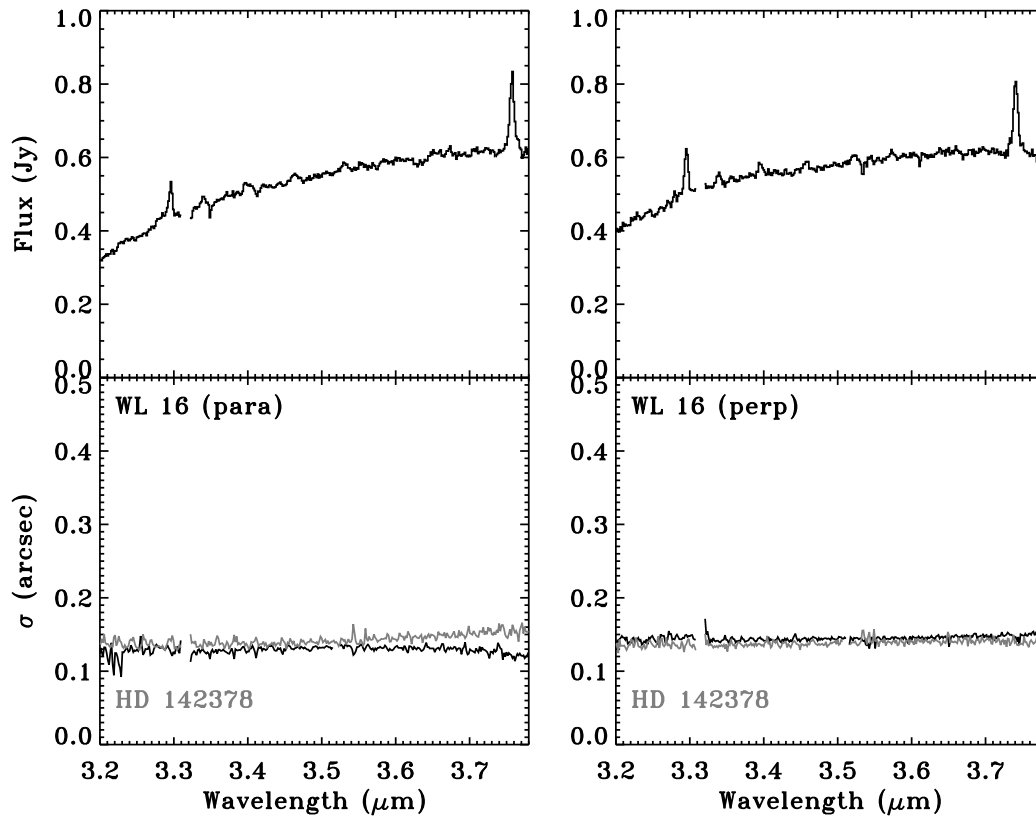


**Figure 4.10:** (Upper-left panel) NACO L-band spectrum of WL 16, slit parallel to semi-major axis of the disk. (Lower-left panel) FWHM of spatial profile of the “parallel” observation of WL 16 (black) and standard star HD 142378 (grey). (Upper-right panel) NACO L-band spectrum of WL 16, slit perpendicular to semi-major axis of the disk. (Lower panel) FWHM of spatial profile of the “perpendicular” observation of WL 16 (black) and standard star HD 142378 (grey).

small PAHs ( $N_c=50$ ) that  $\sim 76\%$  of the PAH emission should originate from a ring with a typical radius of  $\sim 160$  AU for 3.3 and 11.2  $\mu\text{m}$  and 175–190 AU for 6.2, 7.7 and 8.6  $\mu\text{m}$ . For larger PAHs ( $N_c=96$ ) the predicted distribution is more centrally peaked, with 76% of the emission arising inwards of radii of 47, 96, 105, 103, and 117 AU for the 3.3, 6.2, 7.7, 8.6 and 11.2  $\mu\text{m}$  features respectively. In T Tauri disks the small PAH emission is also more centrally peaked, within radii of 15 AU for the 3.3  $\mu\text{m}$  feature, and 50–60 AU for the 6.2, 7.7, 8.6 and 11.2  $\mu\text{m}$  features.

The observed extents for IRS 48, SR 21A, T Cha, HD 101412 and HD 98922 are included in Fig. 4.15. Most PAH detections have upper limits on the radial spatial extent of typically 20–40 AU (with the exception of HD 98922, whose distance is uncertain) while for a few sources the PAH emission is spatially resolved with typical extent of 12–55 AU. One source, IRS 48, has spatially resolved detections of all features.

For all observations with detected PAH features, the (upper limit for the) radial extent of the 11.2  $\mu\text{m}$  feature is a factor of 1.5–6 lower than derived from the prediction

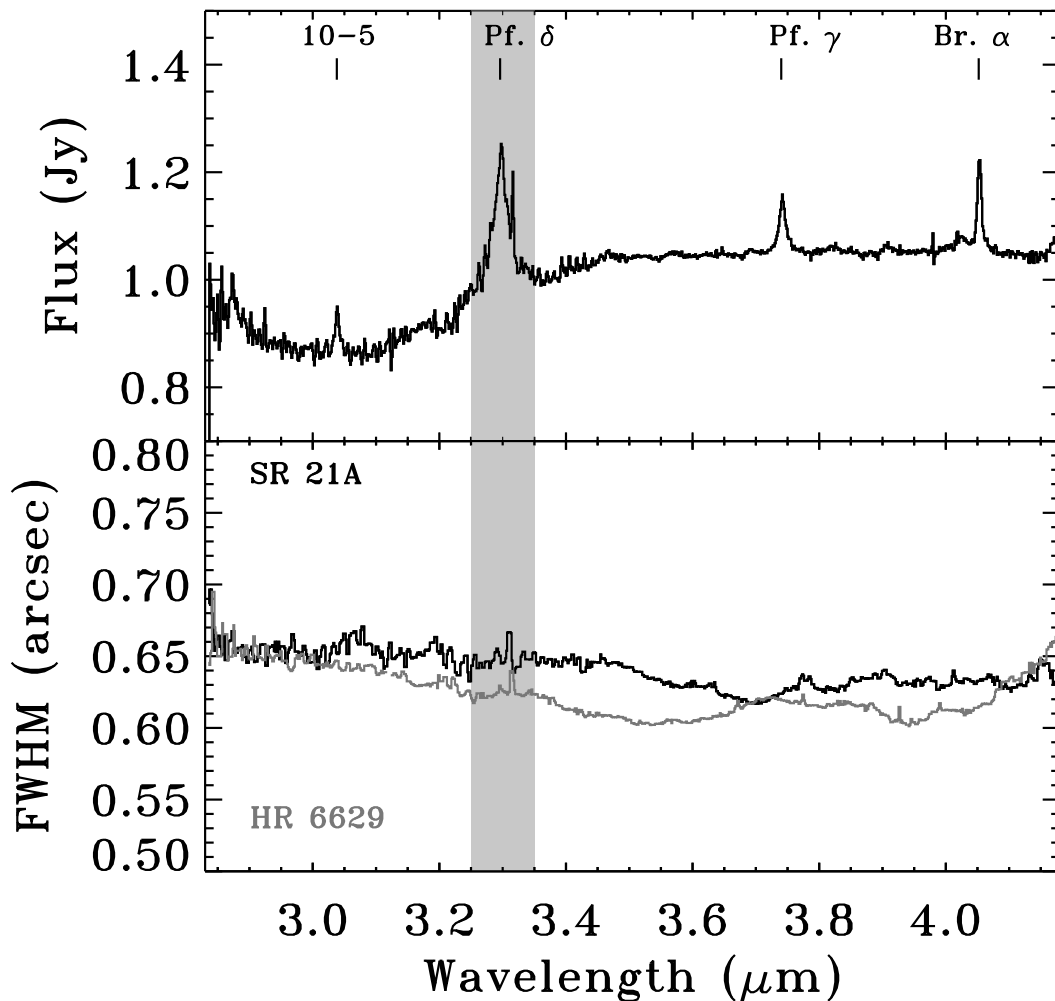


**Figure 4.11:** (Upper panel) ISAAC L-band spectrum of SR 21A. (Lower panel) FWHM of spatial profile of SR 21A and standard star HR 6629.

of the template model and we do not see any evidence for ring-shaped PAH emission as the model predicts. Within the Visser et al. (2007) models, this implies larger PAHs of typically 100 or more carbon atoms. The model prediction by Habart et al. (2004) for Herbig Ae stars with large PAHs ( $N_c=100$ ) is also indicated in Fig. 4.15. Our measurement for the Herbig Ae star, HD 101412, is a factor 6–7 smaller than their and our prediction.

The typical extent of the 3.3  $\mu\text{m}$  feature at 76% of 12–55 AU agrees with the predictions of both Visser et al. (2007) and Habart et al. (2004). Our derived upper limits on the extent of the 8.6 and 11.2  $\mu\text{m}$  features of typically  $\leq 30$  AU, are about a factor 2 smaller than the model predictions, which also hints at the presence of larger PAHs than considered in those models. As noted by Geers et al. (2006), a significant number of these PAH sources are known to have substantial gaps out to 40 AU in their disks

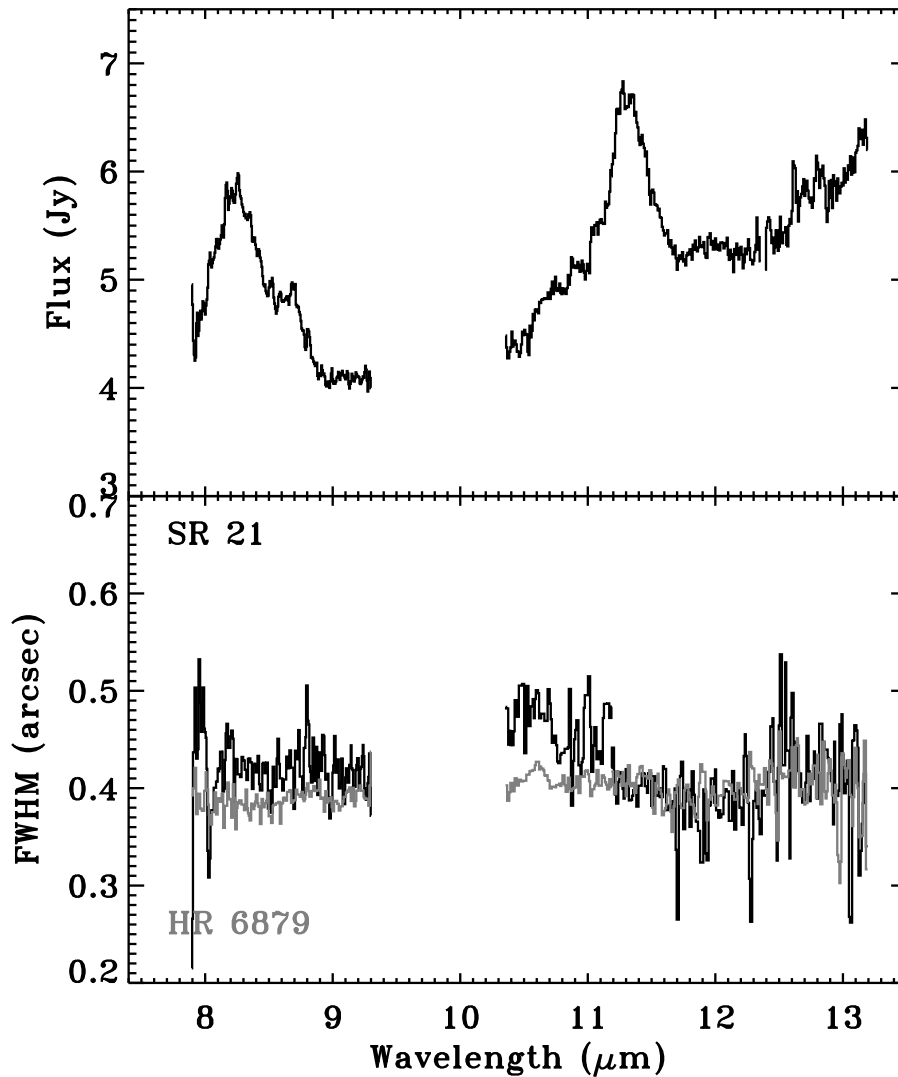


**Figure 4.12:** (Upper panel) VISIR N-band spectrum of SR 21A. (Lower panel) FWHM of spatial profile of SR 21A and standard star HR 6879.

(Brown et al. 2007). The presence of warm  $3 \mu\text{m}$  disk emission suggests these sources have gaps, not holes. These observations put the PAH emission in the inner part of the disk, and in some cases (i.p. HD 100546) it very likely comes from the dust at the outer edge of the gap.

Four out of the five sources with spatially unresolved PAH features (leaving out HD 98922) have average upper limits on the extent of 30–40 AU, with no apparent difference between the Herbig Ae star HD 101412 and the 3 T Tauri stars. Potential misalignment of the slit with the semi-major axis of an inclined disk will reduce the measurable spatial extent (see also Appendix 4.5). In addition, unresolved features could have at least two geometrical causes. A larger inclination of the disk (from face-



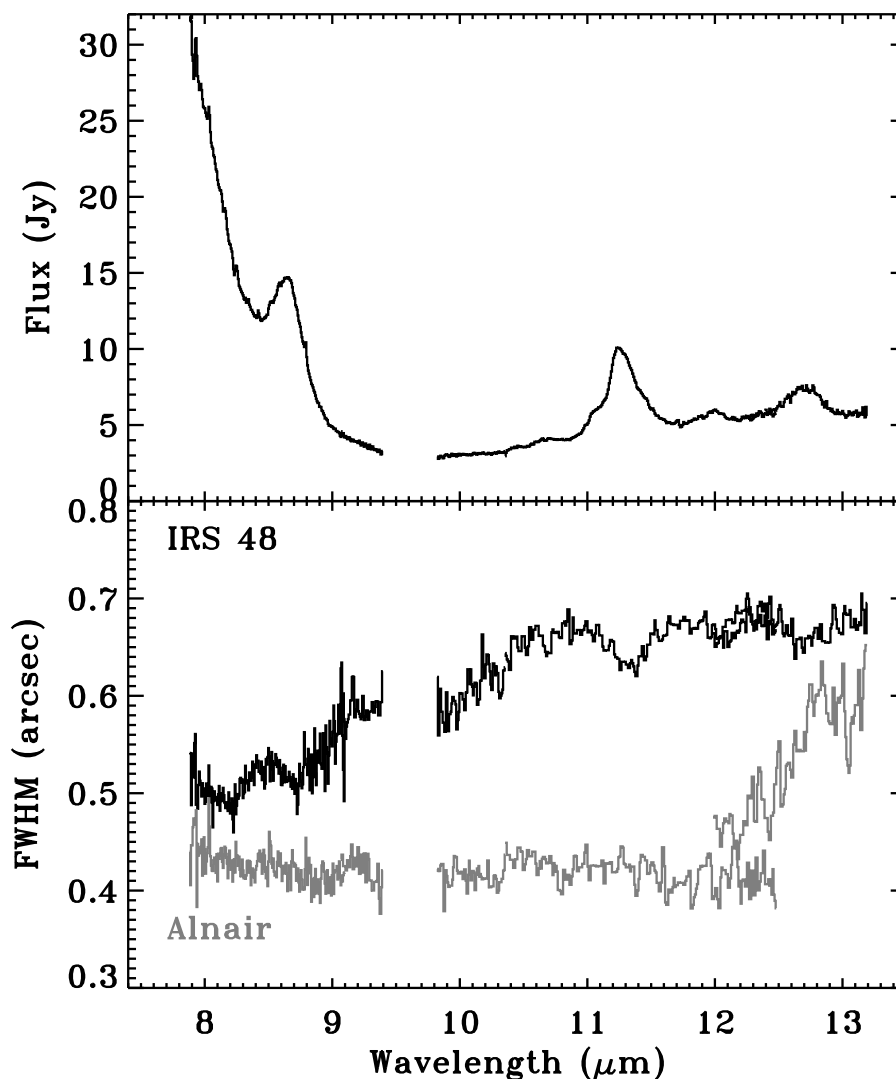


**Figure 4.13:** (Upper panel) VISIR N-band spectrum of IRS 48. (Lower panel) FWHM of spatial profile of IRS 48 and standard star Alnair.

on) would decrease the measurable extent, although at near-IR wavelengths, for close to edge-on disks, scattering could dominate the spatial extent of the source of emission. Four out of the five unresolved sources (excluding EC 82) have no indications of a strong inclination in their SED (Kessler-Silacci et al. 2006). The second geometrical effect is the flaring or the covering fraction of the disk. For a disk with a decreasing covering fraction (through decreasing scale height), the feature to continuum ratio of the PAH features will decrease for very flat disks (Geers et al. 2006). Both HD 101412 and HD 98922 have SEDs consistent with a flat type II source (Meeus et al. 2001), while the SR 21A and T Cha both have SEDs consistent with still moderately large scale height, although the SED interpretation is more complicated due to the suspected presence of

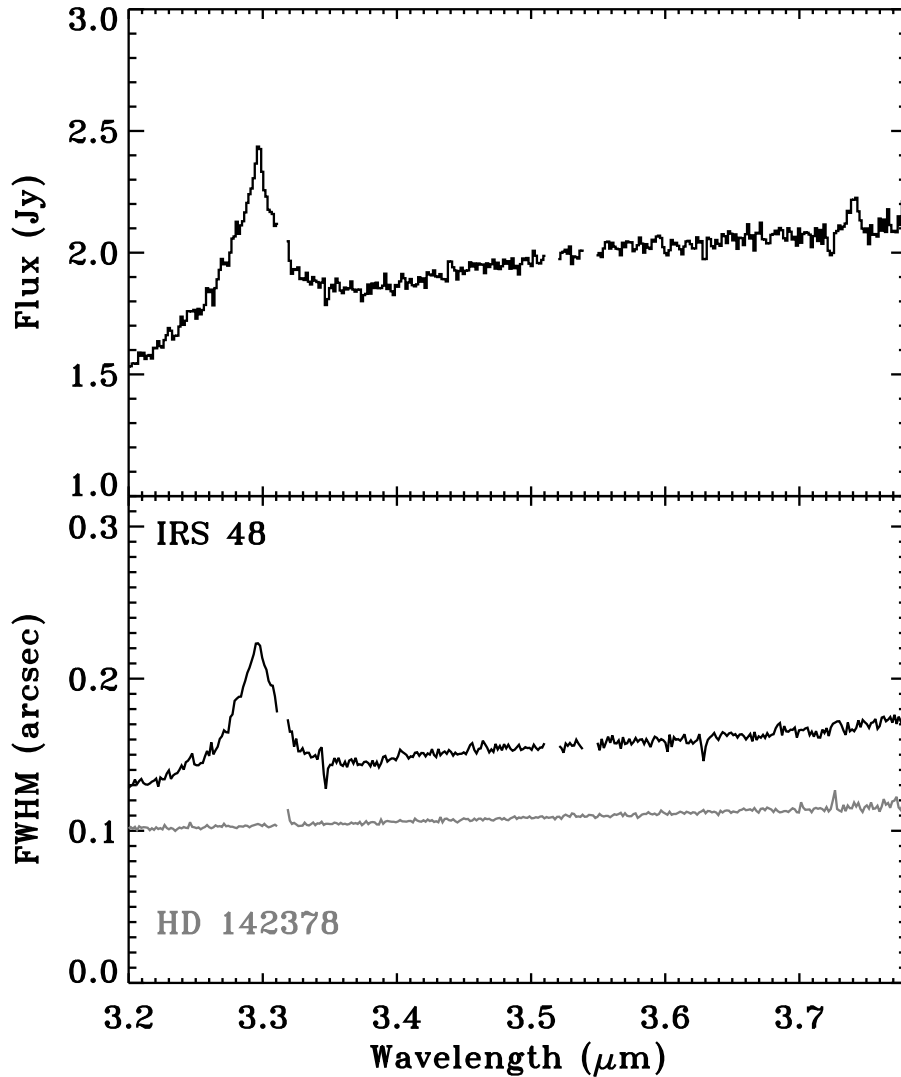


**Figure 4.14:** (Upper panel) NACO L-band spectrum of IRS 48. (Lower panel) FWHM of spatial profile of IRS 48 and standard star HD 142378.

a gap (Brown et al. 2007). Besides geometrical and instrumental effects, the alternative physical interpretation for the small extent could be the presence of predominantly large PAHs, which model predictions show to radiate mostly from smaller scales, as discussed above (Visser et al. 2007).

## 4.4 CONCLUSIONS

We detect the 3.3, 8.6 and 11.2  $\mu\text{m}$  PAH features in a small fraction of our sample of T Tauri stars, with typical upper limits between  $1 \times 10^{-15}$  and  $5 \times 10^{-17} \text{ W m}^{-2}$ . Compared with the Spitzer survey in Geers et al. (2006), we confirm all their 11.2  $\mu\text{m}$  detections

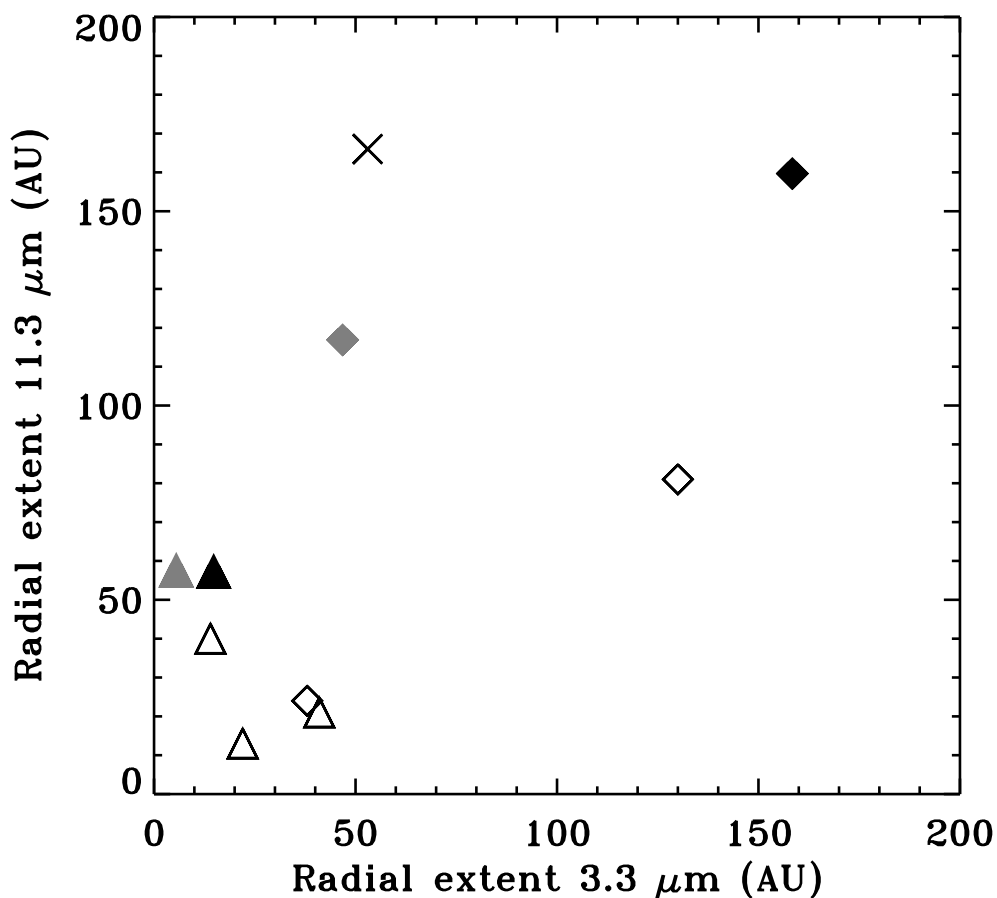


**Figure 4.15:** Radial extent of  $3.3 \mu\text{m}$  feature versus  $11.2 \mu\text{m}$  feature; Herbig Ae stars indicated by filled diamonds, T Tauri stars by filled triangles; models with  $N_c = 96$  indicated by grey,  $N_c=50$  by black. Observations of IRS 48, SR 21A, T Cha, HD 101412 and HD 98922 are indicated by open symbols. Model prediction point extracted from Fig. 4 of Habart et al. (2004) for a disk around a Herbig star for  $N_c = 100$  is indicated by a cross.

and find marginal to clear  $3.3 \mu\text{m}$  detections. The bias in our sample prevents us from deriving an independent detection fraction, but the low number of PAH observations toward T Tauri stars is consistent with the low detection rate of 8% by Geers et al. (2006). In two specific sources, WL 16 and HD 141569, the PAHs are expected to be largely ionized because of the strong  $7.7$  and  $8.6 \mu\text{m}$  features and lack of  $3.3 \mu\text{m}$ .

The spatial extent of the PAH features is shown to be confined to scales smaller than  $0.1 - 0.4''$  (HWHM), corresponding to radial scales of 12–60 AU in the disk, at typical distances of 150 pc, barring exceptional cases with unknown or much larger distances. In a few examples, the PAH features are resolved to be more extended than the hot underlying dust continuum of the disk, whereas in one case, IRS 48, the extent of the PAH emission is confirmed to be less than that of the large grains. The typical extent of the PAH features of 15–60 AU is found to be very similar for both Herbig

Ae and T Tauri stars, and similar for all features. For Herbig Ae stars the small 12–55 AU extent and absence of any ring emission is consistent with the model predictions of larger ( $\geq 100$  carbon atoms) grains. The same conclusion of the need for large PAHs holds for the T Tauri stars where the 8.6 and 11.2  $\mu\text{m}$  features appear to be smaller than predicted, although here the 3.3  $\mu\text{m}$  extent is consistent with smaller ( $\sim 50$  carbon atoms) PAHs. Given the large fraction of disks with gaps and PAHs, future modeling studies of the PAH extent should include the presence of gaps in disks.

## ACKNOWLEDGEMENTS

KMP is supported by NASA through Hubble Fellowship grant 01201.01 awarded by the STScI, which is operated by the AURA, for NASA, under contract NAS 5-26555. Astrochemistry in Leiden is supported by a Spinoza grant from the Netherlands Organization for Scientific Research (NWO).

## 4.5 APPENDIX: SPATIAL EXTENT MODELS

Visser et al. (2007, hereafter V07) modelled the chemistry of and infrared emission from PAHs in circumstellar disks, including an analysis of the spatial extent of the emission. The algorithm to determine the spatial extent of the emission was further improved to allow for a more direct comparison with observed spatial profiles, by summing the emission in a (narrow) slit rather than in concentric rings as done in V07. A simplification was introduced by measuring continuum-subtracted peak intensities instead of spectrally integrated feature fluxes. Since the model features all have the same shape (Draine & Li 2007), this produces the same spatial profiles. The new procedure is essentially the same as that outlined in Sect. 4.2.5 for the observations. The improved profiles for the standard Herbig Ae/Be and T Tauri models ( $R_{\text{disk,in}} = 0.077$  AU,  $R_{\text{disk,out}} = 300$  AU,  $M_{\text{disk}} = 0.01 M_{\odot}$ ) from V07, synthetically observed face-on through a slit wide enough to cover the entire disk, are presented in Fig. 4.16.

If the source does not fit inside the width of the slit, part of the emission originating at large radii is blocked, thus generally reducing the apparent spatial extent compared to observations through a wider slit. This is shown in Fig. 4.17. With a 40 AU slit (0.27'' at 150 pc), the location inside of which 76% of the feature emission originates shifts to smaller radii by the order of 10 – 15% compared to an infinitely wide slit.

The effects of inclination are less straightforward. For objects at an inclination of about  $45^\circ$ , the observed spatial profiles differ only slightly from the face-on profiles if an infinitely wide slit is used. With a narrow slit, part of the emission is obscured asymmetrically across the width of the slit and the emission can appear to become both more or less extended, depending on the details of the source. This also occurs when the source is viewed more edge on, regardless of the width of the slit.

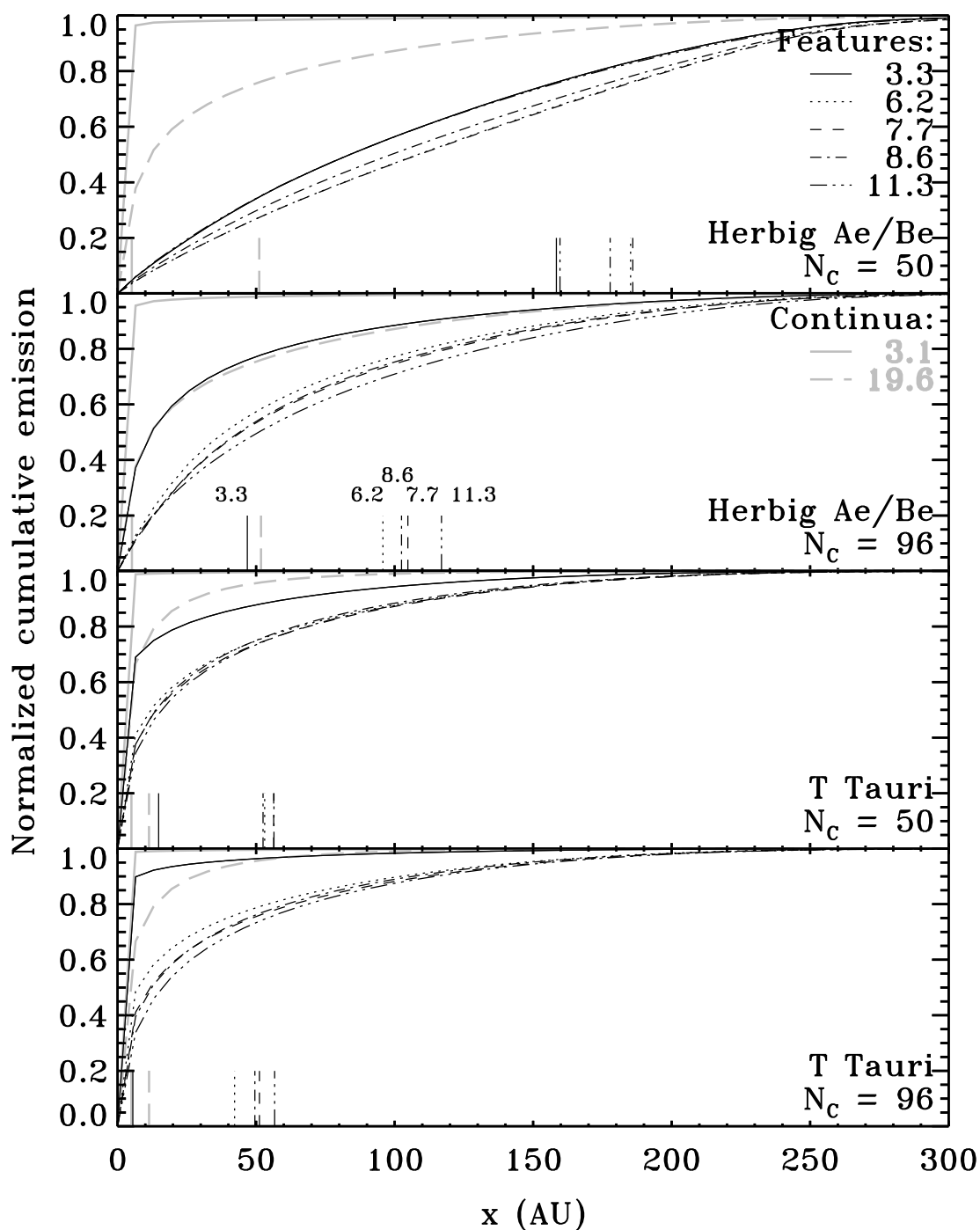


**Figure 4.16:** Normalized cumulative intensity of the five main PAH features (black) and the continua at 3.1 and 19.6  $\mu\text{m}$  (gray) for  $C_{50}H_{18}$  and  $C_{96}H_{24}$  in the standard Herbig Ae/Be and T Tauri model disks (including PAH chemistry) from Visser et al. (2007). The disks were synthetically observed face-on through an infinitely wide slit. The vertical bars indicate where each curve reaches 76%, corresponding to the HWHM of the Gaussians in Sect. 4.2.5.

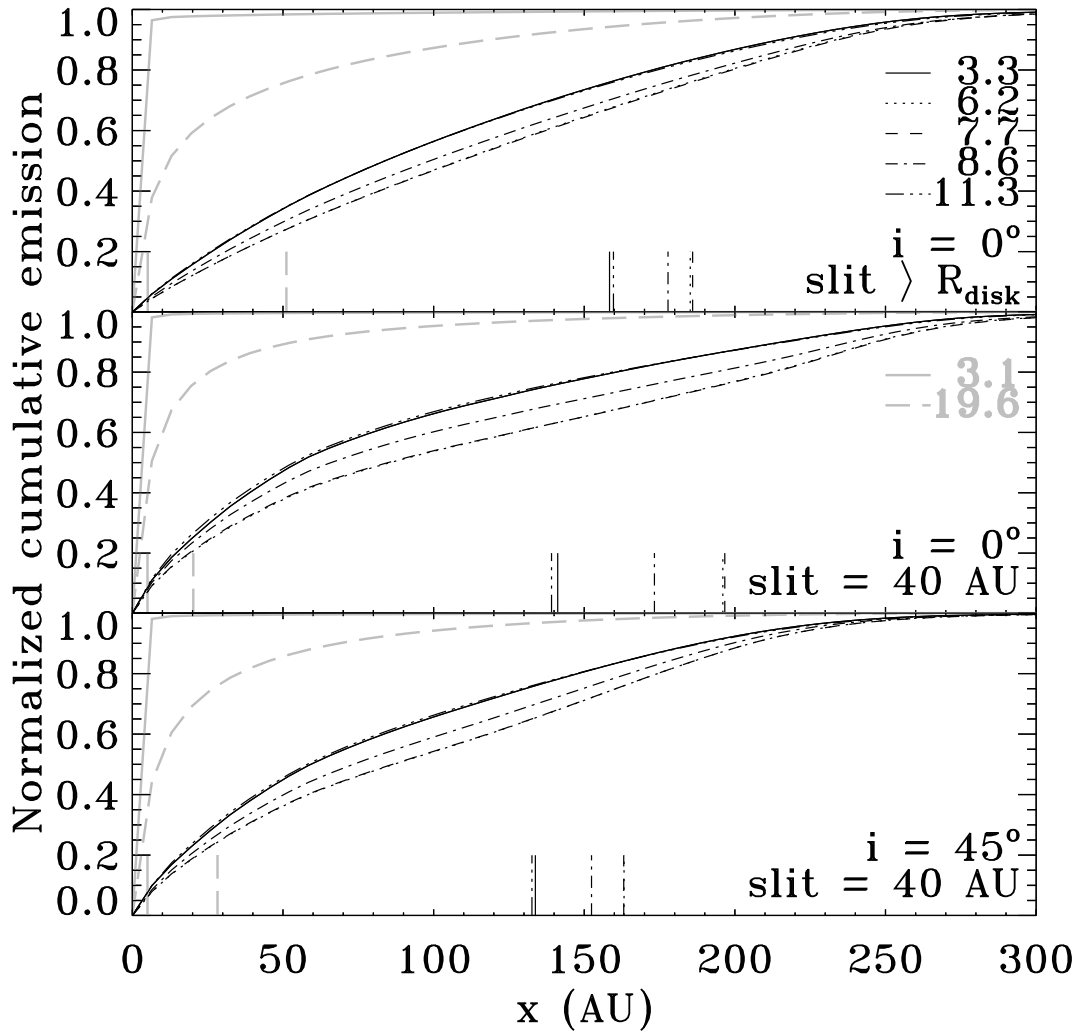


**Figure 4.17:** Normalized cumulative intensity for  $C_{50}H_{18}$  in the standard Herbig Ae/Be model disk (including PAH chemistry) from Visser et al. (2007). The disk was synthetically observed at  $45^\circ$  or through a narrow slit as indicated. Lines and colours are as in Fig. 4.16.

#### REFERENCES

- Acke, B. & van den Ancker, M. E. 2004, *A&A*, 426, 151  
 Acke, B. & van den Ancker, M. E. 2006a, *A&A*, 457, 171  
 Acke, B. & van den Ancker, M. E. 2006b, *A&A*, 449, 267  
 Acke, B., van den Ancker, M. E., & Dullemond, C. P. 2005, *A&A*, 436, 209  
 Alcalá, J. M., Covino, E., Franchini, M., et al. 1993, *A&A*, 272, 225  
 Allamandola, L. J., Hudgins, D. M., & Sandford, S. A. 1999, *ApJ*, 511, L115  
 Augereau, J. C., Lagrange, A. M., Mouillet, D., & Ménard, F. 2001, *A&A*, 365, 78  
 Augereau, J. C. & Papaloizou, J. C. B. 2004, *A&A*, 414, 1153  
 Bouwman, J., de Koter, A., Dominik, C., & Waters, L. B. F. M. 2003, *A&A*, 401, 577

- Brown, J. M., Blake, G. A., Dullemond, C. P., et al. 2007, *ApJ*, 664, L107
- Chauvin, G., Lagrange, A.-M., Beust, H., et al. 2003, *A&A*, 406, L51
- Cohen, M. & Kuhl, L. V. 1979, *ApJS*, 41, 743
- Comerón, F. 2007, in *Handbook of star forming regions*, ed. B. Reipurth (Cambridge Univ. Press)
- de Geus, E. J., de Zeeuw, P. T., & Lub, J. 1989, *A&A*, 216, 44
- Doucet, C., Habart, E., Pantin, E., et al. 2007, *A&A*, 470, 625
- Draine, B. T. & Li, A. 2007, *ApJ*, 657, 810
- Dullemond, C. P. & Dominik, C. 2004, *A&A*, 417, 159
- Dullemond, C. P., Dominik, C., & Natta, A. 2001, *ApJ*, 560, 957
- Dunkin, S. K., Barlow, M. J., & Ryan, S. G. 1997, *MNRAS*, 286, 604
- Evans, N. J., Allen, L. E., Blake, G. A., et al. 2003, *PASP*, 115, 965
- Finkenzeller, U. & Mundt, R. 1984, *A&AS*, 55, 109
- Geers, V. C., Augereau, J.-C., Pontoppidan, K. M., et al. 2006, *A&A*, 459, 545
- Geers, V. C., Augereau, J.-C., Pontoppidan, K. M., et al. 2005, in *High Resolution Infrared Spectroscopy in Astronomy*, ed. H. U. Käufel, R. Siebenmorgen, & A. F. M. Moorwood, 239
- Geers, V. C., Pontoppidan, K. M., van Dishoeck, E. F., et al. 2007, *A&A*, 469, L35
- Grady, C. A., Perez, M. R., & The, P. S. 1993, *A&A*, 274, 847
- Grady, C. A., Polomski, E. F., Henning, T., et al. 2001, *AJ*, 122, 3396
- Grankin, K. N., Melnikov, S. Y., Bouvier, J., Herbst, W., & Shevchenko, V. S. 2007, *A&A*, 461, 183
- Habart, E., Natta, A., & Krügel, E. 2004, *A&A*, 427, 179
- Habart, E., Natta, A., Testi, L., & Carillet, M. 2006, *A&A*, 449, 1067
- Honda, M., Kataza, H., Okamoto, Y. K., et al. 2003, *ApJ*, 585, L59
- Houk, N. 1978, *Michigan catalogue of two-dimensional spectral types for the HD stars* (Ann Arbor : Dept. of Astronomy, University of Michigan)
- Hughes, J., Hartigan, P., & Clampitt, L. 1993, *AJ*, 105, 571
- Hughes, J., Hartigan, P., Krautter, J., & Kelemen, J. 1994, *AJ*, 108, 1071
- Jonkheid, B., Faas, F. G. A., van Zadelhoff, G.-J., & van Dishoeck, E. F. 2004, *A&A*, 428, 511
- Jonkheid, B., Kamp, I., Augereau, J.-C., & van Dishoeck, E. F. 2006, *A&A*, 453, 163
- Kessler-Silacci, J., Augereau, J.-C., Dullemond, C. P., et al. 2006, *ApJ*, 639, 275
- Klaas, U., Walker, H. J., Müller, T. G., Richards, P. J., & Schreiber, J. 2006, *A&A*, 452, 523
- Knude, J. & Nielsen, A. S. 2001, *A&A*, 373, 714
- Lagage, P.-O., Doucet, C., Pantin, E., et al. 2006, *Science*, 314, 621
- Li, A. & Draine, B. T. 2001, *ApJ*, 554, 778
- Li, A. & Lunine, J. I. 2003, *ApJ*, 594, 987
- Liu, W. M., Hinz, P. M., Meyer, M. R., et al. 2003, *ApJ*, 598, L111

- Luhman, K. L. & Rieke, G. H. 1999, *ApJ*, 525, 440
- Malfait, K., Waelkens, C., Waters, L. B. F. M., et al. 1998, *A&A*, 332, L25
- Meeus, G., Waters, L. B. F. M., Bouwman, J., et al. 2001, *A&A*, 365, 476
- Mora, A., Merín, B., Solano, E., et al. 2001, *A&A*, 378, 116
- Pantin, E., Waelkens, C., & Lagage, P. O. 2000, *A&A*, 361, L9
- Peeters, E., Spoon, H. W. W., & Tielens, A. G. G. M. 2004, *ApJ*, 613, 986
- Pontoppidan, K. M., Fraser, H. J., Dartois, E., et al. 2003, *A&A*, 408, 981
- Prato, L., Greene, T. P., & Simon, M. 2003, *ApJ*, 584, 853
- Ressler, M. E. & Barsony, M. 2003, *ApJ*, 584, 832
- Siebenmorgen, R., Prusti, T., Natta, A., & Müller, T. G. 2000, *A&A*, 361, 258
- Sloan, G. C., Keller, L. D., Forrest, W. J., et al. 2005, *ApJ*, 632, 956
- Straizys, V., Cernis, K., & Bartasiute, S. 1996, *Baltic Astronomy*, 5, 125
- Sylvester, R. J., Skinner, C. J., Barlow, M. J., & Mannings, V. 1996, *MNRAS*, 279, 915
- Thé, P. S., de Winter, D., & Perez, M. R. 1994, *A&AS*, 104, 315
- Valenti, J. A., Johns-Krull, C. M., & Linsky, J. L. 2000, *ApJS*, 129, 399
- van Boekel, R., Waters, L. B. F. M., Dominik, C., et al. 2004, *A&A*, 418, 177
- van den Ancker, M. E., de Winter, D., & Tjin A Djie, H. R. E. 1998, *A&A*, 330, 145
- Visser, R., Geers, V. C., Dullemond, C. P., et al. 2007, *A&A*, 466, 229
- Whittet, D. C. B., Prusti, T., Franco, G. A. P., et al. 1997, *A&A*, 327, 1194
- Wilner, D. J., Bourke, T. L., Wright, C. M., et al. 2003, *ApJ*, 596, 597



---

## CHAPTER 5

---

# Lack of PAH emission toward low-mass embedded young stellar objects

V. C. Geers, E. F. van Dishoeck, K. M. Pontoppidan, F. Lahuis, A. Crapsi, C. P. Dullemond

To be submitted to *Astronomy & Astrophysics*

### Abstract

POLYCYCLIC Aromatic Hydrocarbons (PAHs) have been detected toward molecular clouds and some young stars with disks, but have not yet been associated with embedded young stars. We present a sensitive mid-infrared spectroscopic survey of PAH features toward a sample of low-mass embedded class I objects. The aim is to put constraints on the PAH abundance in the embedded phase of star formation using radiative transfer modeling. VLT-ISAAC L-band spectra for 39 sources and Spitzer IRS spectra for 53 sources are presented. Line intensities are compared to recent surveys of Herbig Ae/Be and T Tauri stars. The radiative transfer codes RADMC and RADICAL are used to model the PAH emission from embedded YSO systems consisting of a pre-main-sequence star with a circumstellar disk embedded in an envelope. The dependence of the PAH feature on PAH abundance, stellar radiation field, inclination and the extinction by the surrounding envelope is studied. The  $3.3 \mu\text{m}$  PAH feature is undetected for the majority of the sample (97%), with typical upper limits of  $5 \times 10^{-16} \text{ W m}^{-2}$ . One source originally classified as class I, IRS 48, shows a strong  $3.3 \mu\text{m}$  feature but this source is inferred to have lost most of its envelope. Compact  $11.2 \mu\text{m}$  PAH emission is seen directly toward 2 out of 53 Spitzer spectra of embedded objects. For all 11 sources with both VLT and Spitzer spectra, no PAH features are detected in either. In total, PAH features are detected toward at most 2 out of 80 embedded protostars ( $\lesssim 3\%$ ), much lower than observed for class II T Tauri stars with disks (11–14%). Models predict the  $7.7 \mu\text{m}$  feature as the best tracer of PAH emission, while the  $3.3 \mu\text{m}$  feature is relatively weak, but neither are seen in the observations. Assuming typical class I stellar and envelope parameters, the absence of PAHs emission is most likely explained

by the absence of emitting carriers through a much lower PAH abundance in the gas, e.g., due to freeze-out of PAHs on icy layers on dust grains. Thus, most PAHs likely enter the protoplanetary disks frozen out on grains.

## 5.1 INTRODUCTION

Polycyclic Aromatic Hydrocarbons (PAHs) have been observed toward a wide range of astrophysical environments (Allamandola et al. 1989; Peeters et al. 2002), including the interstellar medium (ISM) and star-forming regions, first hinted at by the discovery of widespread  $12\ \mu\text{m}$  emission using the Infrared Astronomical Satellite (IRAS) (e.g. Cohen et al. 1985). Since PAHs are a good tracer of UV radiation, they are an indirect probe of star formation in the high opacity environments of molecular clouds as well as circumstellar disks. Recent spectroscopic studies have detected PAHs toward a significant fraction, 11–14% and 54% of low-mass and intermediate mass pre-main-sequence (PMS) stars respectively (Acke & van den Ancker 2004; Geers et al. 2006, see also appendix Chapter 2), and recent ground-based high spatial resolution observations show evidence for the PAH emission to originate from the circumstellar disks (Ressler & Barsony 2003; Habart et al. 2006; Geers et al. 2007, Geers et al. 2007b, in press). PAHs are also prominently seen toward photon dominated regions (PDRs) in dense clouds exposed to massive young stars (e.g. Verstraete et al. 1996). However, to this date, no significant PAH emission has been reported to be directly associated with the intermediate class 0–I phase, when a PMS star with circumstellar disk is still embedded in an envelope of gas and dust. Deeply embedded high-mass YSO's also lack prominent PAH emission (van Dishoeck & van der Tak 2000).

PAHs are believed to form in the outflows of carbon-rich AGB stars, which deposit them in the interstellar medium. Their ubiquitous presence in the ISM shows that at least larger PAH molecules (of 50–100 carbon atoms or more) will survive this phase, until being incorporated in molecular clouds. The amount of carbon locked up in PAHs is  $[\text{C}/\text{H}]_{\text{PAH}} \simeq 5 \times 10^{-5}$  (Habart et al. 2004), corresponding PAH abundances of  $\sim 5 \times 10^{-7}$  relative to H, for 100 carbon atoms PAH molecules, making them among the most abundant molecules after  $\text{H}_2$  and CO.

PAHs can play an important role in the star-forming environments. As large molecules, they provide efficient heating of the gas in both the ISM and circumstellar disks. Small dust particles like PAHs have also been suggested as the main formation site of molecules such as  $\text{H}_2$  and water in the later evolutionary phases of circumstellar disks when classical grains have grown to large sizes (Jonkheid et al. 2006).

The shape and relative strength of the PAH features in the  $6\text{--}9\ \mu\text{m}$  region has been shown to vary between various astrophysical environments from AGBs, the ISM to the class II disk sources. This has provided evidence that the emission characteristics of PAHs are sensitive to local physical conditions and that interstellar PAHs undergo processing in space environments (Peeters et al. 2002). Further support for this comes from recent values for the PAH abundance in disk surface layers, which is a factor 10–100 lower than in the ISM for sources with sufficient UV radiation to excite them (Geers et al. 2006). PAHs frozen out on icy grains can chemically react with other molecules to

form a large variety of complex species, including pre-biotic molecules (Bernstein et al. 1999; Ehrenfreund et al. 2006). A study of PAHs toward embedded low-mass young stars is important to find out what happens to PAHs and how large a role they may still play in these embedded objects.

In this paper we present the first mid-infrared spectroscopic survey for PAH emission from embedded low-mass young stellar objects using VLT-ISAAC and Spitzer IRS, in wide range of nearby star-forming regions. We subsequently use a radiative transfer code to model PAH emission from young stars with disks embedded in an envelope, and discuss the observed detection rate in the context of PAH abundance, the strength of UV emission from the protostar and the extinction from the envelope.

## 5.2 OBSERVATIONS AND DATA REDUCTION

A large sample of low-mass embedded objects was selected from two previous mid-infrared studies. A set of 39 sources was selected from a VLT-ISAAC 3–5  $\mu\text{m}$  band survey (van Dishoeck et al. 2003), of which 32 were previously presented in Pontoppidan et al. (2003) and 3 sources in Thi et al. (2006). For this survey L-band spectroscopy was obtained with ISAAC, the Infrared Spectrometer And Array Camera, installed at the VLT Antu at ESO's Paranal Observatory in Chile, in the low resolution ( $R = \lambda/\Delta\lambda = 600\text{--}1200$ ) spectroscopic mode in the spectral domain 2.8–4.2  $\mu\text{m}$  using a  $0.6'' \times 120''$  slit. The telescope was operated using a standard chop-throw scheme with typical chop-throws of 10–20''. A full description of observation and reduction techniques is given in Pontoppidan et al. (2003). These sources were required to have a rising Spectral Energy Distribution (SED) in the mid-infrared as well as the presence of an  $\text{H}_2\text{O}$  ice feature at 3  $\mu\text{m}$ . The selected sources are listed in Table 5.1.

Table 5.1: Summary of observations.

Target	RA [J2000]	Dec [J2000]	Lada class	lineflux 3.3 $\mu\text{m}$	comments
Perseus					
LDN1448 IRS1	3 <sup>h</sup> 25 <sup>m</sup> 09 <sup>s</sup> .4	+30° 46' 21".7	-	-	Spitzer
LDN1448 NA	3 <sup>h</sup> 25 <sup>m</sup> 36 <sup>s</sup> .5	+30° 45' 21".2	-	-	Spitzer
IRAS 03245+3002	3 <sup>h</sup> 27 <sup>m</sup> 39 <sup>s</sup> .0	+30° 12' 59".4	-	-	Spitzer
L1455 SMM1	3 <sup>h</sup> 27 <sup>m</sup> 43 <sup>s</sup> .2	+30° 12' 28".8	-	-	Spitzer
L1455 IRS3	3 <sup>h</sup> 28 <sup>m</sup> 00 <sup>s</sup> .4	+30° 08' 01".3	-	-	Spitzer
IRAS 03254+3050	3 <sup>h</sup> 28 <sup>m</sup> 34 <sup>s</sup> .5	+31° 00' 51".1	-	-	Spitzer
IRAS 03271+3013	3 <sup>h</sup> 30 <sup>m</sup> 15 <sup>s</sup> .2	+30° 23' 48".8	-	-	Spitzer
IRAS 03301+3111	3 <sup>h</sup> 33 <sup>m</sup> 12 <sup>s</sup> .8	+31° 21' 24".1	-	-	Spitzer
B1-a	3 <sup>h</sup> 33 <sup>m</sup> 16 <sup>s</sup> .7	+31° 07' 55".2	-	-	Spitzer
B1-c	3 <sup>h</sup> 33 <sup>m</sup> 17 <sup>s</sup> .9	+31° 09' 31".0	-	-	Spitzer
SSTc2d J033327.3+310710	3 <sup>h</sup> 33 <sup>m</sup> 27 <sup>s</sup> .3	+31° 07' 10".2	-	-	Spitzer
HH 211-mm	3 <sup>h</sup> 43 <sup>m</sup> 56 <sup>s</sup> .8	+32° 00' 50".4	-	-	Spitzer
IRAS 03439+3233	3 <sup>h</sup> 47 <sup>m</sup> 05 <sup>s</sup> .4	+32° 43' 08".4	-	-	Spitzer
IRAS 03445+3242	3 <sup>h</sup> 47 <sup>m</sup> 41 <sup>s</sup> .6	+32° 51' 43".9	-	-	Spitzer
Taurus					
LDN 1489 IRS	04 <sup>h</sup> 04 <sup>m</sup> 42 <sup>s</sup> .9	+26° 18' 56".3	I	≤8.8E-16	ISAAC
Orion					
Reipurth 50	05 <sup>h</sup> 40 <sup>m</sup> 27 <sup>s</sup> .7	-07° 27' 32".1	I	≤1.0E-15	ISAAC
TPSC 78	05 <sup>h</sup> 35 <sup>m</sup> 14 <sup>s</sup> .1	-05° 23' 38".4	I	≤2.3E-16	ISAAC
TPSC 1	05 <sup>h</sup> 35 <sup>m</sup> 14 <sup>s</sup> .5	-05° 23' 54".7	I	≤1.0E-16	ISAAC
Vela					

Target	RA [J2000]	Dec [J2000]	Lada class	lineflux 3.3 $\mu$ m	comments
HH 46 / IRAS 08242-5050	08 <sup>h</sup> 25 <sup>m</sup> 43 <sup>s</sup> .8	-51° 00' 35".6	-	≤1.2E-16	ISAAC, Spitzer
IRAS 08261-5100	08 <sup>h</sup> 27 <sup>m</sup> 38 <sup>s</sup> .9	-51° 10' 37".2	-	-	Spitzer
LLN 20	08 <sup>h</sup> 47 <sup>m</sup> 39 <sup>s</sup> .4	-43° 06' 08".-	I	≤1.1E-16	ISAAC
LLN 33	08 <sup>h</sup> 57 <sup>m</sup> 36 <sup>s</sup> .8	-43° 14' 35".-	I	≤1.3E-16	ISAAC
LLN 47	09 <sup>h</sup> 09 <sup>m</sup> 25 <sup>s</sup> .6	-45° 22' 51".-	I	≤5.3E-16	ISAAC
Chamaeleon					
Ced 110 IRS4 <sup>a</sup>	11 <sup>h</sup> 06 <sup>m</sup> 46 <sup>s</sup> .6	-77° 22' 32".5	-	-	Spitzer
IRAS 11068-7717	11 <sup>h</sup> 08 <sup>m</sup> 15 <sup>s</sup> .1	-77° 33' 53".2	-	≤5.5E-15	ISAAC
Cha IRN	11 <sup>h</sup> 08 <sup>m</sup> 38 <sup>s</sup> .2	-77° 43' 51".7	I	≤4.2E-16	ISAAC
Cha INa 2	11 <sup>h</sup> 09 <sup>m</sup> 36 <sup>s</sup> .6	-76° 33' 39".-	I	≤5.1E-16	ISAAC
IRAS 12553-7651	12 <sup>h</sup> 59 <sup>m</sup> 06 <sup>s</sup> .6	-77° 07' 40".1	-	-	Spitzer
Ophiuchus					
VSSG1 <sup>a</sup>	16 <sup>h</sup> 26 <sup>m</sup> 18 <sup>s</sup> .8	-24° 28' 49".5	I-II	≤9.5E-16	ISAAC, Spitzer
GSS30 IRS 1 <sup>a</sup>	16 <sup>h</sup> 26 <sup>m</sup> 21 <sup>s</sup> .4	-24° 23' 04".2	I	≤8.6E-16	ISAAC, Spitzer
GY 23 <sup>a</sup>	16 <sup>h</sup> 26 <sup>m</sup> 24 <sup>s</sup> .1	-24° 24' 48".2	II	-	Spitzer
VLA 1623-243	16 <sup>h</sup> 26 <sup>m</sup> 26 <sup>s</sup> .4	-24° 24' 30".2	-	-	Spitzer
IRS 14	16 <sup>h</sup> 26 <sup>m</sup> 31 <sup>s</sup> .0	-24° 31' 05".2	-	-	Spitzer
WL 12	16 <sup>h</sup> 26 <sup>m</sup> 44 <sup>s</sup> .2	-24° 34' 48".4	I	≤2.6E-16	ISAAC, Spitzer
OphE-MM3	16 <sup>h</sup> 27 <sup>m</sup> 05 <sup>s</sup> .9	-24° 37' 08".0	-	-	Spitzer
GY 224	16 <sup>h</sup> 27 <sup>m</sup> 11 <sup>s</sup> .2	-24° 40' 46".6	I-II	-	Spitzer
WL 19	16 <sup>h</sup> 27 <sup>m</sup> 11 <sup>s</sup> .7	-24° 38' 32".3	I-II	-	Spitzer
WL 20S	16 <sup>h</sup> 27 <sup>m</sup> 15 <sup>s</sup> .6	-24° 38' 45".6	I	≤2.0E-16	ISAAC, Spitzer
WL 20E	16 <sup>h</sup> 27 <sup>m</sup> 15 <sup>s</sup> .7	-24° 38' 59".8	I	≤2.1E-16	ISAAC
IRS 37	16 <sup>h</sup> 27 <sup>m</sup> 17 <sup>s</sup> .6	-24° 28' 56".6	-	-	Spitzer
IRS 42	16 <sup>h</sup> 27 <sup>m</sup> 21 <sup>s</sup> .5	-24° 41' 43".1	I-II	≤2.0E-15	ISAAC
WL 6	16 <sup>h</sup> 27 <sup>m</sup> 21 <sup>s</sup> .8	-24° 29' 53".2	I	-	Spitzer
CRBR 2422.8-3423 <sup>a</sup>	16 <sup>h</sup> 27 <sup>m</sup> 24 <sup>s</sup> .6	-24° 41' 03".1	I-II	≤8.7E-16	ISAAC, Spitzer
IRS 43	16 <sup>h</sup> 27 <sup>m</sup> 26 <sup>s</sup> .9	-24° 40' 50".8	I	≤4.4E-15	ISAAC
IRS 44	16 <sup>h</sup> 27 <sup>m</sup> 28 <sup>s</sup> .0	-24° 39' 33".5	I	≤1.3E-15	ISAAC
Elias 32	16 <sup>h</sup> 27 <sup>m</sup> 28 <sup>s</sup> .4	-24° 27' 21".2	I-II	≤8.4E-16	ISAAC, Spitzer
IRS 46 <sup>a</sup>	16 <sup>h</sup> 27 <sup>m</sup> 29 <sup>s</sup> .4	-24° 39' 16".2	I	≤1.4E-15	ISAAC, Spitzer
VSSG 17	16 <sup>h</sup> 27 <sup>m</sup> 30 <sup>s</sup> .2	-24° 27' 44".3	I	≤3.9E-16	ISAAC, Spitzer
IRS 48 <sup>a</sup>	16 <sup>h</sup> 27 <sup>m</sup> 37 <sup>s</sup> .2	-24° 30' 35".0	I	3.0E-15	ISAAC
IRS 51	16 <sup>h</sup> 27 <sup>m</sup> 39 <sup>s</sup> .8	-24° 43' 15".1	I-II	≤9.2E-16	ISAAC
IRS 54	16 <sup>h</sup> 27 <sup>m</sup> 51 <sup>s</sup> .8	-24° 31' 45".5	I	≤3.8E-16	ISAAC
IRS 63	16 <sup>h</sup> 31 <sup>m</sup> 35 <sup>s</sup> .7	-24° 01' 29".6	I-II	≤3.2E-15	ISAAC, Spitzer
L1689-IRS5	16 <sup>h</sup> 31 <sup>m</sup> 52 <sup>s</sup> .1	-24° 56' 15".4	-	-	Spitzer
IRAS 16293-2422B	16 <sup>h</sup> 32 <sup>m</sup> 22 <sup>s</sup> .6	-24° 28' 32".2	-	-	Spitzer
IRAS 16293-2422	16 <sup>h</sup> 32 <sup>m</sup> 22 <sup>s</sup> .9	-24° 28' 36".1	-	-	Spitzer
RNO 91 <sup>a</sup>	16 <sup>h</sup> 34 <sup>m</sup> 29 <sup>s</sup> .3	-15° 47' 01".3	I	-	Spitzer
Serpens					
SSTc2d J182901.8+02954	18 <sup>h</sup> 29 <sup>m</sup> 01 <sup>s</sup> .8	+00° 29' 54".2	-	-	Spitzer
SSTc2d J182916.2+01822	18 <sup>h</sup> 29 <sup>m</sup> 16 <sup>s</sup> .2	+00° 18' 22".7	-	-	Spitzer
Serp-S68N	18 <sup>h</sup> 29 <sup>m</sup> 48 <sup>s</sup> .1	+01° 16' 42".6	-	-	Spitzer
EC69	18 <sup>h</sup> 29 <sup>m</sup> 54 <sup>s</sup> .4	+01° 15' 01".8	-	-	Spitzer
SVS 4-2	18 <sup>h</sup> 29 <sup>m</sup> 56 <sup>s</sup> .6	+01° 12' 59".4	-	≤6.4E-17	ISAAC
Serp-SMM4	18 <sup>h</sup> 29 <sup>m</sup> 56 <sup>s</sup> .6	+01° 13' 15".2	-	-	Spitzer
EC 82	18 <sup>h</sup> 29 <sup>m</sup> 56 <sup>s</sup> .9	+01° 14' 46".4	I	≤4.9E-16	ISAAC
EC 90A	18 <sup>h</sup> 29 <sup>m</sup> 57 <sup>s</sup> .3	+01° 14' 03".7	I	≤2.1E-15	ISAAC
EC 90B	18 <sup>h</sup> 29 <sup>m</sup> 57 <sup>s</sup> .3	+01° 14' 03".7	I	≤7.4E-16	ISAAC
EC88	18 <sup>h</sup> 29 <sup>m</sup> 57 <sup>s</sup> .6	+01° 13' 00".5	-	-	Spitzer
SVS 4-3	18 <sup>h</sup> 29 <sup>m</sup> 56 <sup>s</sup> .7	+01° 12' 39".0	-	≤1.4E-16	ISAAC
SVS 4-5	18 <sup>h</sup> 29 <sup>m</sup> 57 <sup>s</sup> .6	+01° 13' 00".2	I	≤1.6E-16	ISAAC
SVS 4-9	18 <sup>h</sup> 29 <sup>m</sup> 58 <sup>s</sup> .1	+01° 12' 39".4	I	≤3.2E-16	ISAAC
Serp-SMM3	18 <sup>h</sup> 29 <sup>m</sup> 59 <sup>s</sup> .2	+01° 14' 00".2	-	-	Spitzer
Coronis Australis					
R CrA IRS 5A	19 <sup>h</sup> 01 <sup>m</sup> 48 <sup>s</sup> .1	-36° 57' 21".9	I	≤4.2E-16	ISAAC
R CrA IRS 5B	19 <sup>h</sup> 01 <sup>m</sup> 48 <sup>s</sup> .1	-36° 57' 21".9	I	≤1.7E-16	ISAAC
R CrA IRS 5A+B	19 <sup>h</sup> 01 <sup>m</sup> 48 <sup>s</sup> .0	-36° 57' 21".6	-	-	Spitzer
HH 100 IRS	19 <sup>h</sup> 01 <sup>m</sup> 50 <sup>s</sup> .7	-36° 58' 09".6	I	≤8.8E-15	ISAAC
R CrA IRS 7A	19 <sup>h</sup> 01 <sup>m</sup> 55 <sup>s</sup> .3	-36° 57' 22".0	I	≤0.000E+0	ISAAC, Spitzer
R CrA IRS 7B	19 <sup>h</sup> 01 <sup>m</sup> 56 <sup>s</sup> .4	-36° 57' 28".1	I	≤7.1E-17	ISAAC, Spitzer
R CrA IRAS32	19 <sup>h</sup> 02 <sup>m</sup> 58 <sup>s</sup> .7	-37° 07' 34".7	-	-	Spitzer

Target	RA [J2000]	Dec [J2000]	Lada class	lineflux 3.3 $\mu\text{m}$	comments
Additional sources					
IRAS 13546-3941	13 <sup>h</sup> 57 <sup>m</sup> 38 <sup>s</sup> .9	-39° 56' 00".2	-	-	Spitzer
IRAS 15398-3359	15 <sup>h</sup> 43 <sup>m</sup> 02 <sup>s</sup> .3	-34° 09' 06".8	-	-	Spitzer
IRAS 23238+7401	23 <sup>h</sup> 25 <sup>m</sup> 46 <sup>s</sup> .7	+74° 17' 37".3	-	-	Spitzer

<sup>a</sup>Known or candidate (edge-on) disk source.

In addition, a sample of 53 Spitzer Space Telescope Infrared Spectrograph (Spitzer IRS) Short-Low (5–14.5  $\mu\text{m}$ ,  $R \sim 100$ ) and Short-High (10–20  $\mu\text{m}$ ,  $R \sim 600$ ) spectra of class I sources, were obtained in the context of the “Cores to Disks” (c2d) Legacy program (Evans et al. 2003) and first presented in Lahuis et al. (in prep.). These sources were selected for showing the silicate 10  $\mu\text{m}$  feature in absorption, and the list includes a small number of known or candidate edge-on disks, which are labelled in Table 5.1. The reduction of the Spitzer spectroscopy was performed using the optimal PSF extraction technique developed within the c2d program, to allow separation of the compact source and extended emission components (Lahuis et al. 2007). The source size is determined from the width of the PSF function fitted to the source, compared to the width of the PSF function fit for standard calibrator stars. Comparison of the optimal PSF extraction and the full aperture extraction provides a direct estimate of any potential extended emission. An application of the same technique to remove background PAH features has been given for the source VSSG 1 in Geers et al. (2006, see their Fig. 4). The details of the observations and reduction procedures are described in Lahuis et al. (2006) and Lahuis (2007, thesis Chap. 3).

In total, the sample contains 80 sources, for which 12 sources were observed with both ISAAC and Spitzer.

## 5.3 RESULTS AND DISCUSSION

### 5.3.1 VLT-ISAAC spectra

The VLT-ISAAC L-band spectra are presented in Fig. 5.1. Only 1 source in this sample shows a clear 3.3  $\mu\text{m}$  PAH emission feature, IRS 48. This source is known to be a M0 star with a spatially resolved disk (Geers et al. 2007), surrounded by a very tenuous envelope at most. No clear PAH feature is seen toward any of the other sources. To derive upper limits for their PAH feature line fluxes, a gaussian with a peak flux equal to the  $3\sigma$  noise and FWHM = 0.07  $\mu\text{m}$  is generated and integrated to retrieve the line flux of the largest feature that would still fall within the noise. The results are listed in Table 5.1.

The hydrogen Pf  $\delta$  (3.296  $\mu\text{m}$ ), Pf  $\gamma$  (3.739  $\mu\text{m}$ ) and Br  $\alpha$  (4.051  $\mu\text{m}$ ) are detected toward most sources, with the exception of IRAS 11068-7717 and Cha IRN. The broad water ice absorption feature can be clearly seen toward the majority of the sources.

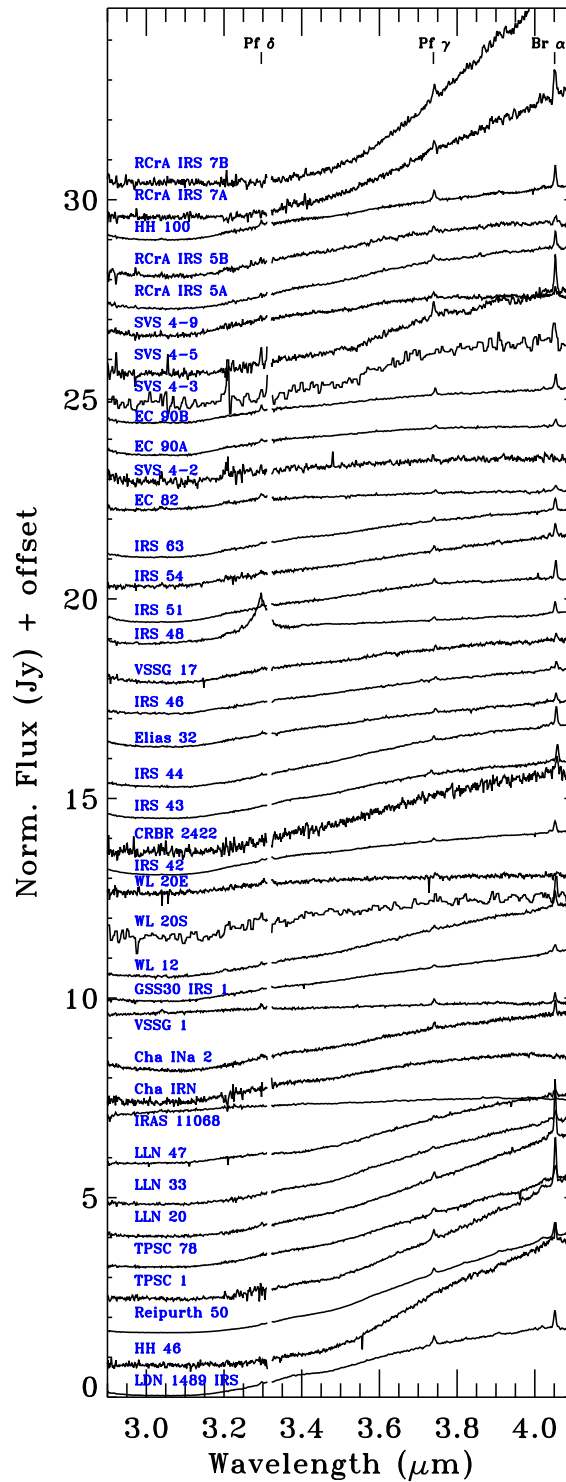


**Figure 5.1:** ISAAC L-band spectra of low-mass embedded sources. The narrow HI lines at 3.3, 3.74 and 4.05  $\mu\text{m}$  are seen in most spectra.

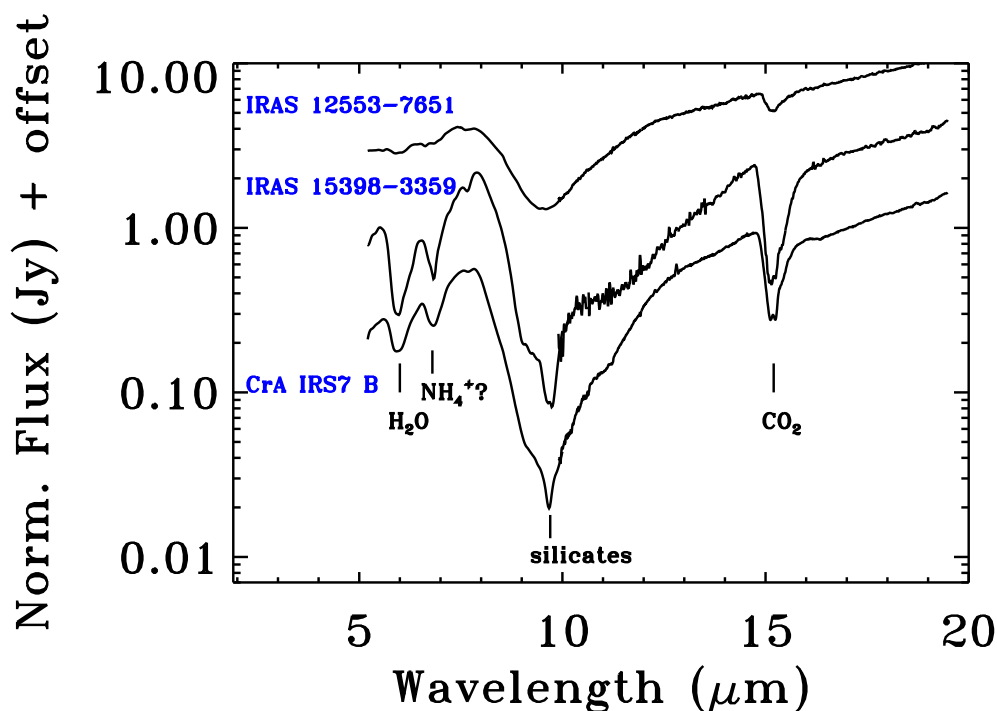


**Figure 5.2:** Spitzer IRS spectra of a sample of low-mass embedded sources without PAH detections.

### 5.3.2 Spitzer spectra

Out of the sample of 53 sources, 50 do not show any PAH features. A selection of Spitzer spectra with PAH non-detections is presented in Fig. 5.2. Silicate, water and  $\text{CO}_2$  absorption are the predominant features in these spectra.

For two Spitzer sources, GY 23 and IRAS 03380+3135, the optimal extraction method produces a spectrum with PAH features, shown in Fig. 5.3. A small source size is derived for both sources, suggesting that the PAH emission is directly associated with the star. It is noted that based on Spitzer IRS, IRAC and MIPS fluxes, both IRAS 03380+3135 and GY 23, previously classified as class I, show a declining SED suggestive of a class II source. For GY 23, no clear absorption features due to ices or silicates are detected. For two sources, VSSG 1 and IRS 14 in Ophiuchus, PAH features are detected from extended background emission, which is assumed not to be directly associated with a central object.

Overall, our detection rate of PAH emission associated with embedded protostars is 2 out of 80 sources corresponding to  $\sim 3\%$ .

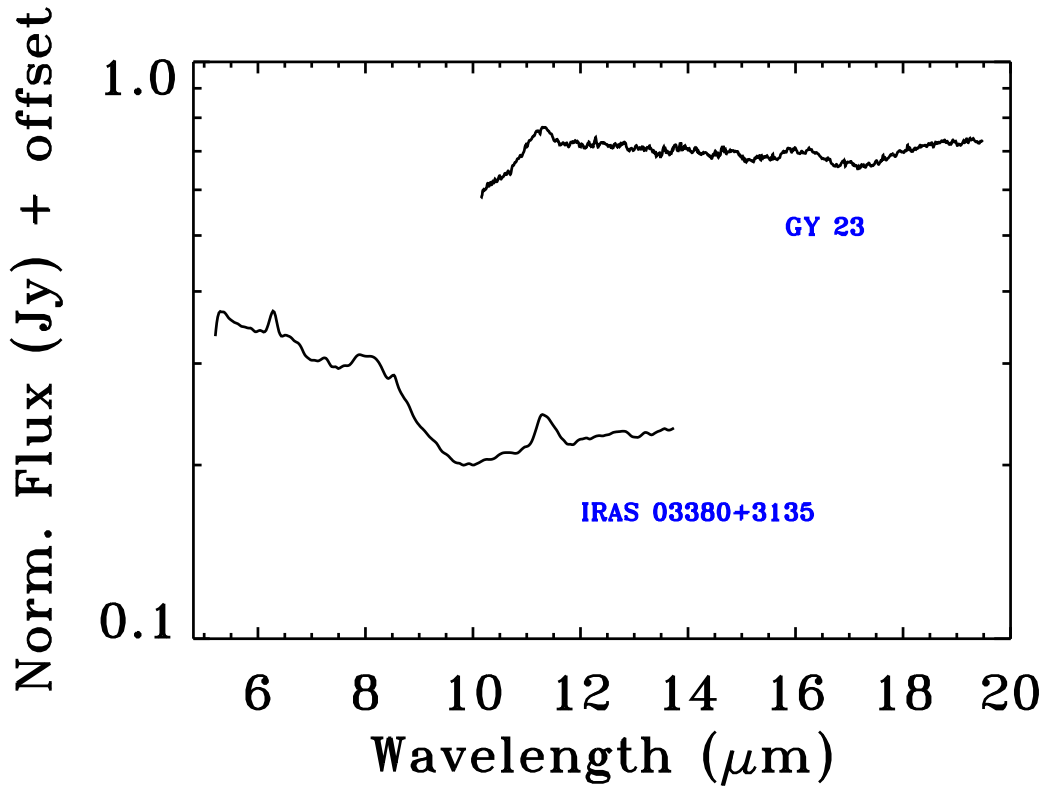


Figure 5.3: Spitzer IRS spectra of 2 low-mass embedded sources with PAH detections.

## 5.4 RADIATIVE TRANSFER MODEL

Here we address the question of where the PAH emission can arise in a disk + envelope system through radiative transfer modeling and what the non-detections imply quantitatively about the PAH abundance.

### 5.4.1 Physical structure

We use the three-dimensional axisymmetric radiative transfer code RADMC (Dullemond & Dominik 2004) to calculate the temperature structure and scattering source function for an embedded YSO using a Monte Carlo technique. This code requires stellar parameters, a stellar radiation field, a density structure and a set of dust opacities. Scattering is assumed to be isotropic. A module to treat the emission from quantum-heated PAH molecules and Very Small Grains, previously described in Geers et al. (2006), has been included. To generate images and spectra, ray-tracing is performed using RADICAL (Dullemond & Turolla 2000). All spectra and SEDs presented here are scaled to a distance to the observer of 150 pc.

The density structure adopted here follows Crapsi et al. (2007, submitted) and is



comprised of three components: the disk, the envelope and the outflow cone. The adopted density structure for the disk has a power-law dependence along the radial coordinate and a gaussian dependence in height, and can be expressed as

$$\rho_{\text{disk}}(r, \theta) = \frac{\Sigma_0 (r/R_0)^{-1}}{\sqrt{2\pi} H(r)} \exp \left\{ -\frac{1}{2} \left[ \frac{r \cos \theta}{H(r)} \right]^2 \right\},$$

where  $\theta$  is the angle from the axis of symmetry. The variation of scale-height, i.e., the flaring of the disk, is described in the function  $H(r) = r \cdot H_0/R_0 \cdot (r/R_0)^{2/7}$ , corresponding to the self-irradiated passive disk of Chiang & Goldreich (1997). In our template model we fix the outer radius  $R_0$  to 300 AU, inner radius  $R_{\text{in}} = 0.1$  AU,  $H_0$  equal to 90 AU, and the disk mass to  $M_{\text{disk}} = 5 \times 10^{-3} M_{\odot}$ .

The envelope density follows the theoretical structure for a rotating and collapsing spheroid as derived by Ulrich (1976), defined by

$$\rho_{\text{env}}(r, \theta) = \rho_0 \left( \frac{R_{\text{rot}}}{r} \right)^{1.5} \left( 1 + \frac{\cos \theta}{\cos \theta_0} \right)^{-0.5} \left( \frac{\cos \theta}{2 \cos \theta_0} + \frac{R_{\text{rot}}}{r} \cos^2 \theta_0 \right)^{-1},$$

where  $\theta_0$  is the solution of the parabolic motion of an infalling particle given by  $r/R_{\text{rot}} \cdot (\cos \theta_0 - \cos \theta) / (\cos \theta_0 \sin^2 \theta_0) = 1$ ,  $R_{\text{rot}}$  is the centrifugal radius of the envelope, and  $\rho_0$  is the density of the equatorial plane at the centrifugal radius. The outer radius of the envelope is fixed to 10 000 AU and the centrifugal radius is set to 300 AU. The value of  $\rho_0$  is varied to cover a range of envelope mass  $M_{\text{env}}$  between 0.1 and 1.5  $M_{\odot}$ , the template model has  $M_{\text{env}} = 1.0 M_{\odot}$ . The inner radius of the envelope is determined by the outflow cavity, which crosses the equatorial plane at  $\sim 20$  AU. The streamline outflow is included by setting the density of the regions where  $\cos \theta_0$  is larger than  $\cos 15^\circ$  to the same value of the density of the envelope at the outer radius. This results in a funnel-shaped cavity which is conical only at large scales, where it presents a semi-aperture of  $15^\circ$ .

For the radiation field, a blackbody spectrum is taken with  $T_{\text{eff}} = 4000$  K and a luminosity of  $6 L_{\odot}$  for the template model. Given the strong dependence of PAHs on UV excitation and observations indicating the presence of UV excess around actively accreting young low-mass PMS stars (Basri & Bertout 1989; Hartmann & Kenyon 1990), models have also been run with the radiation field for  $\lambda < 0.8 \mu\text{m}$  substituted by a modified Draine field (van Dishoeck & Black 1982), scaled up to ensure continuous overlap at  $\lambda < 0.8 \mu\text{m}$ . The resulting spectrum is normalized to a luminosity of  $6 L_{\odot}$ . The excess Draine UV field corresponds to a  $G_0$  of  $8 \times 10^4$  at a radius of 100 AU in the disk.

## 5.4.2 Treatment of dust and PAHs

The optical properties for the dust grain population are obtained from averaging a distribution of silicate and graphite grains covered by ice mantles, based on a new grid of opacity tables generated by Pontoppidan et al. (in prep.). We adopt the set of dust mixtures used in Crapsi et al. (2007, submitted): a mixture of 71% silicates

**Table 5.2:** Parameters of the template model.

Parameter	value
$T_*$	4000 K
$M_*$	1.0 $M_\odot$
$L_*$	6 $L_\odot$
$M_{\text{disk}}$	$5 \times 10^{-2} M_\odot$
$R_{\text{disk,in}}$	0.1 AU
$R_{\text{disk,out}}$	300 AU
$M_{\text{env}}$	1.0 $M_\odot$
$R_{\text{env,out}}$	10000 AU
$R_{\text{rot}}$	300 AU
$\theta_0$	15°
PAH abun.	$5 \times 10^{-7}$ w.r.t. H

with a power-law size distribution with slope equal to -2 and turnover point for radii larger than  $0.3 \mu\text{m}$  covered by a mantle of ices with a water ice abundance of  $1.5 \times 10^{-4}$  relative to total H, together with 29% of carbonaceous grains with a size distribution similar to that of Weingartner & Draine (2001), characterized by a turnover point at radius of  $4.5 \mu\text{m}$ , a slope of -2 and a water ice abundance of  $7.5 \times 10^{-5}$  relative to total H. A second dust population is added without the ice layer, for regions where the temperature is higher than 90 K, when ices will have evaporated. These are included by running the Monte Carlo code once with ices in the whole grid to calculate the temperature structure, and then using this information to replace the dust opacities where the temperature is higher than 90 K. The ice features include  $\text{H}_2\text{O}$ ,  $\text{CO}_2$  and  $\text{CO}$ , but not more complex species which could be responsible for (part of) the observed 6.0 and  $6.8 \mu\text{m}$  ice features.

PAHs are added as a dust species to the disk and the envelope. The PAH emission is calculated for an equal mix of neutral and singly ionized  $\text{C}_{100}\text{H}_{24}$  molecules, adopting the Draine & Li (2001) PAH emission model, using the “thermal continuous” approximation. Multi-photon events are included for the PAH excitation, following the method outlined by Siebenmorgen et al. (1992). Enhancement factors for the integrated cross sections of the 6.2, 7.7 and  $8.6 \mu\text{m}$  bands ( $E_{6.2} = 3$ ,  $E_{7.7} = 2$ ,  $E_{8.6} = 2$ ) as suggested by Li & Draine (2001) are taken into account, as also implemented in H04. We include the opacities from Mattioda et al. (2005) for near-infrared wavelengths. Model calculations by Visser et al. (2007) show that for PAHs with  $N_c = 100$  their lifetime is larger than the lifetime of the disk, and we can therefore safely discard the possibility of PAH destruction and keep the PAHs at constant abundance throughout the entire the disk.

In our template model, the total PAH abundance is the same as used in Geers et al. (2006), as a mass fraction of the dust of 0.061, which corresponds to a carbon abundance of  $5 \times 10^{-5}$  with respect to hydrogen and a  $N_c = 100$  PAH abundance of  $5 \times 10^{-7}$  with respect to hydrogen. This PAH abundance is divided into 50% ionized and 50% neutral PAHs.

A spectrum of the template model, with and without PAHs, is shown in Figure 5.4.

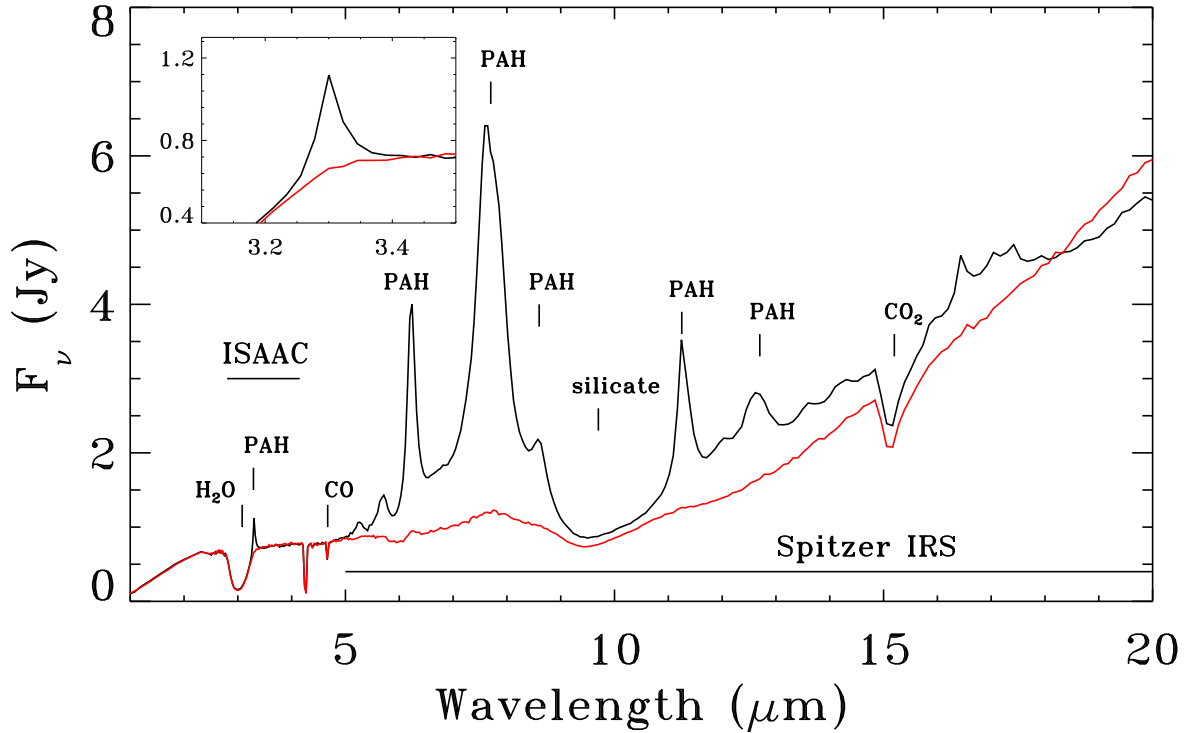


**Figure 5.4:** Model spectra at  $i = 45^\circ$  for template parameters listed in Table 5.2, with PAHs (black) and without PAHs (red). Major PAH and absorption features are indicated, as well as the wavelength coverage of the presented ISAAC and Spitzer IRS observations. The inset shows a blow-up of the  $3.3 \mu\text{m}$  feature on the red wing of the water absorption band.

The main features in the spectrum are the PAH features at  $3.3$ ,  $6.2$ ,  $7.7$ ,  $8.6$ ,  $11.2$  and  $12.7 \mu\text{m}$ , as well as water, CO, silicate and  $\text{CO}_2$  absorption features at  $3.08$ ,  $4.67$ ,  $9.7$  and  $15.2 \mu\text{m}$  respectively. The wavelength coverage of the ISAAC L-band and Spitzer IRS spectroscopy is indicated.

### 5.4.3 Modeling results

The apparent absence of PAH features toward the majority of low-mass embedded class I sources could have a number of explanations.

First, PAH molecules are primarily excited by UV photons. The precise shape and strength of the radiation field inside an embedded object is not well-known but in the class I sources the central source has already formed and is the main energy source inside the envelope. The presence or absence of excess UV will influence the PAH emission features. In particular, the high opacity of the envelope at UV and optical wavelengths, which provide the main excitation of PAHs, will constrain the region where PAHs can be excited to a small radius.

Second, even if the infrared PAH features are produced in the disk or inner en-

velope close to the star, the dust in the surrounding envelope may provide too high extinction in the optical and mid-infrared for the (PAH) emission to escape, especially if the envelope mass is (still) relatively high compared to the disk. If an outflow cavity is present, the inclination at which the object is observed will affect the extinction by the envelope.

Third, the abundance of small PAH molecules in the gas phase may be significantly lower due to freeze-out due to the low temperatures and high densities in the interior of the molecular core.

In practice, a combination of the above three causes will apply simultaneously. To estimate their effects, models are run, varying several parameters including radiation field, PAH abundance and the mass of the envelope.

### Luminosity of the central source and presence of UV excess

Models with total stellar luminosity  $L_*$  varying between 1, 3 and 6  $L_\odot$  are shown in Fig. 5.5. In addition, a model without the template Draine field for UV excess is shown for  $L_* = 6 L_\odot$ . Increasing the luminosity by a factor 6 increases the line flux of the PAH features while the PAH feature / continuum ratio is reduced by at most 20%. Excluding the excess UV field, while preserving the total stellar luminosity, decreases the PAH feature/continuum ratios by  $\sim 3$ . Interestingly, the 3.3  $\mu\text{m}$  feature is affected most because it requires higher energies to be excited than the other features. For typical luminosities observed toward low-mass embedded protostars, PAH features should be detectable, even if no UV excess is present.

### Mass of the envelope

Models with the mass of the envelope  $M_{\text{env}}$  varying from 0.1, 0.5, 1.0 to 1.5  $M_\odot$  are shown in Fig. 5.6, at  $i = 45^\circ$ . In all models the PAH features are clearly present. Increasing the envelope mass by a factor 15 results in a decrease of the emission of the central source while the sub-mm emission and the strength of the absorption features increase. The PAH features decrease in peak flux by a factor 3-4, but are in no case extinguished by the continuous extinction or silicate absorption features. This is consistent with the conclusions of Manske & Henning (1999) for higher mass YSO's.

In the template models, PAHs are located in both the envelope and the disk. To test the influence of the envelope further, model setups including PAHs only in the disk or only in the envelope were performed. A comparison is shown in Fig. 5.7, for  $M_{\text{env}} = 1.0$  and 0.1  $M_\odot$ . Including PAHs only in the disk results in a decrease of peak flux of the PAH features by a factor  $\sim 2$ . In the SED, the absence of PAHs in the envelope leads to less absorption of UV emission, which appears stronger. The mass of the envelope has no significant effect on the strength of the PAH features, although the underlying continuum changes. Including PAHs only in the envelope also results in a typical decrease of the PAH feature peak flux, by about a factor 1.5. Even if the PAHs are located only in the envelope, PAHs should be detectable if they are present at ISM abundance.

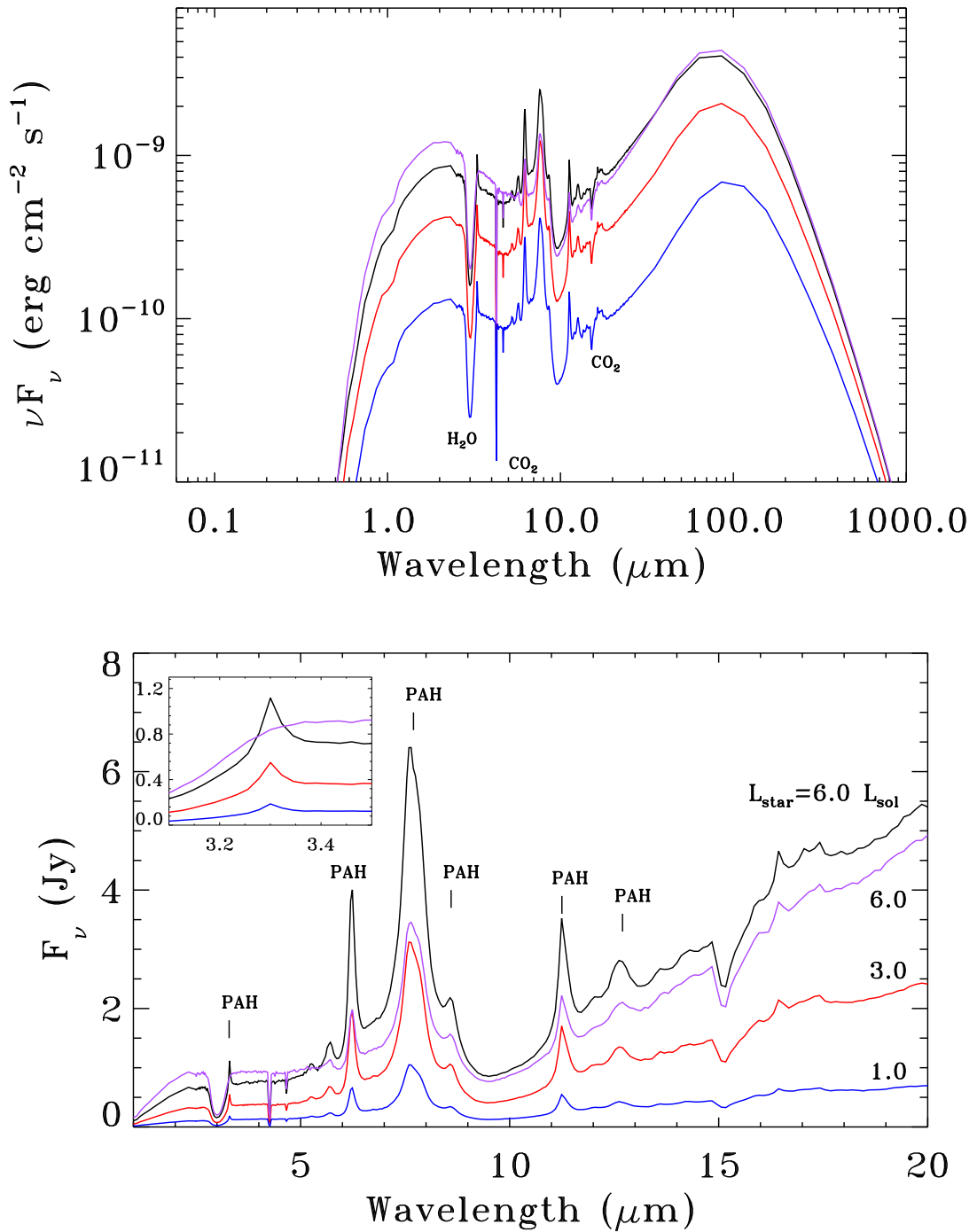


**Figure 5.5:** Model SED (top) and blow-up of spectrum (bottom) at  $i = 45^\circ$  for template model parameters and  $L_*$  varying between 6, 3, and 1  $L_\odot$  (black, red, blue respectively), all including UV excess. A model with  $L_* = 6 L_\odot$  without UV excess is shown in purple. Major PAH and absorption features are indicated. The inset shows a blow-up of the 3.3  $\mu\text{m}$  feature on the red wing of the water absorption band.

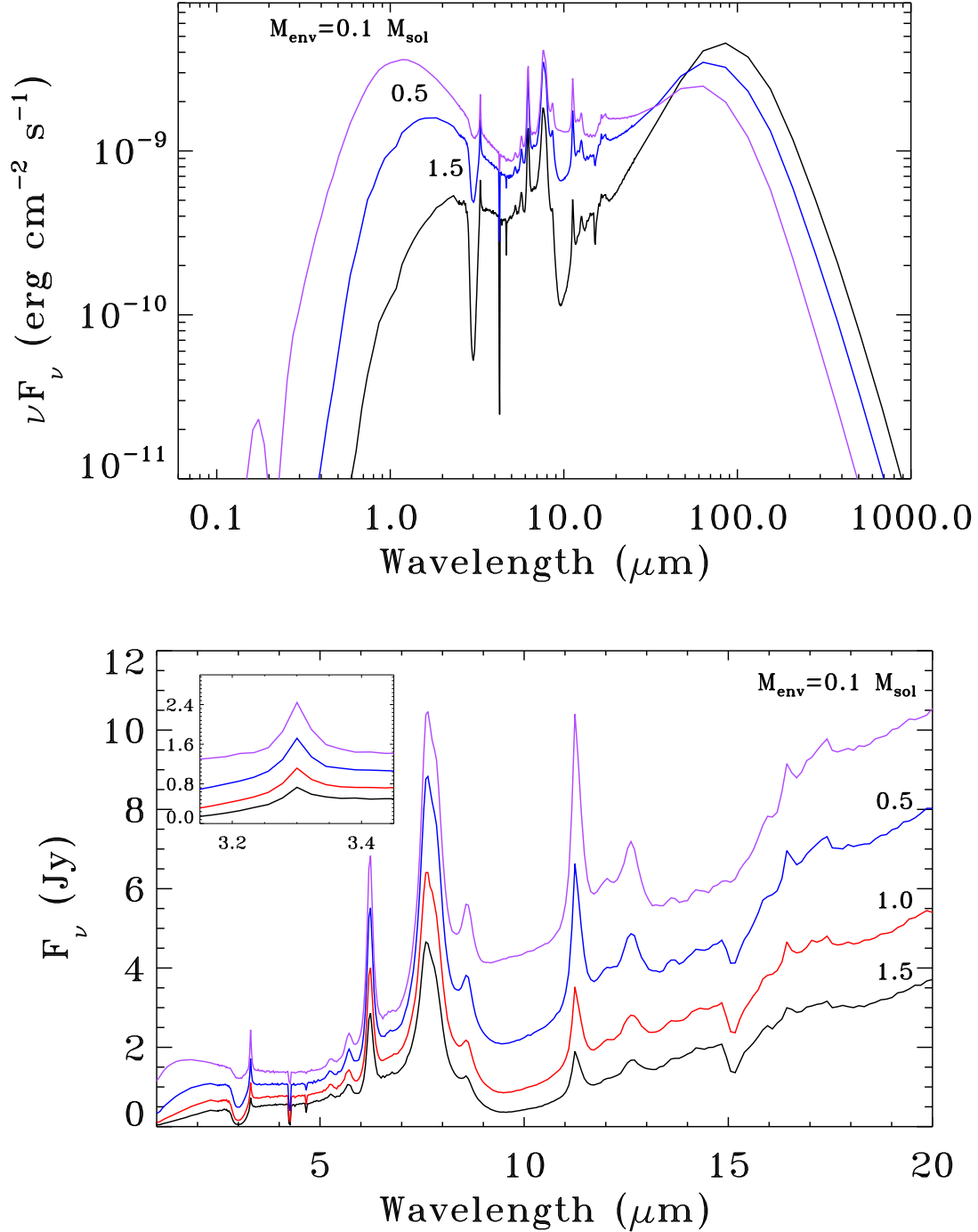


**Figure 5.6:** Model SED (top) and blow-up of spectrum (bottom) with  $M_{\text{env}} = 1.5$  (black), 1.0 (red), 0.5 (blue) and 0.1 (purple)  $M_{\odot}$  at  $i = 45^{\circ}$ . The curve for 1.0  $M_{\odot}$  was omitted from the SED plot for clarity. The inset shows a blow-up of the 3.3  $\mu$ m PAH feature.

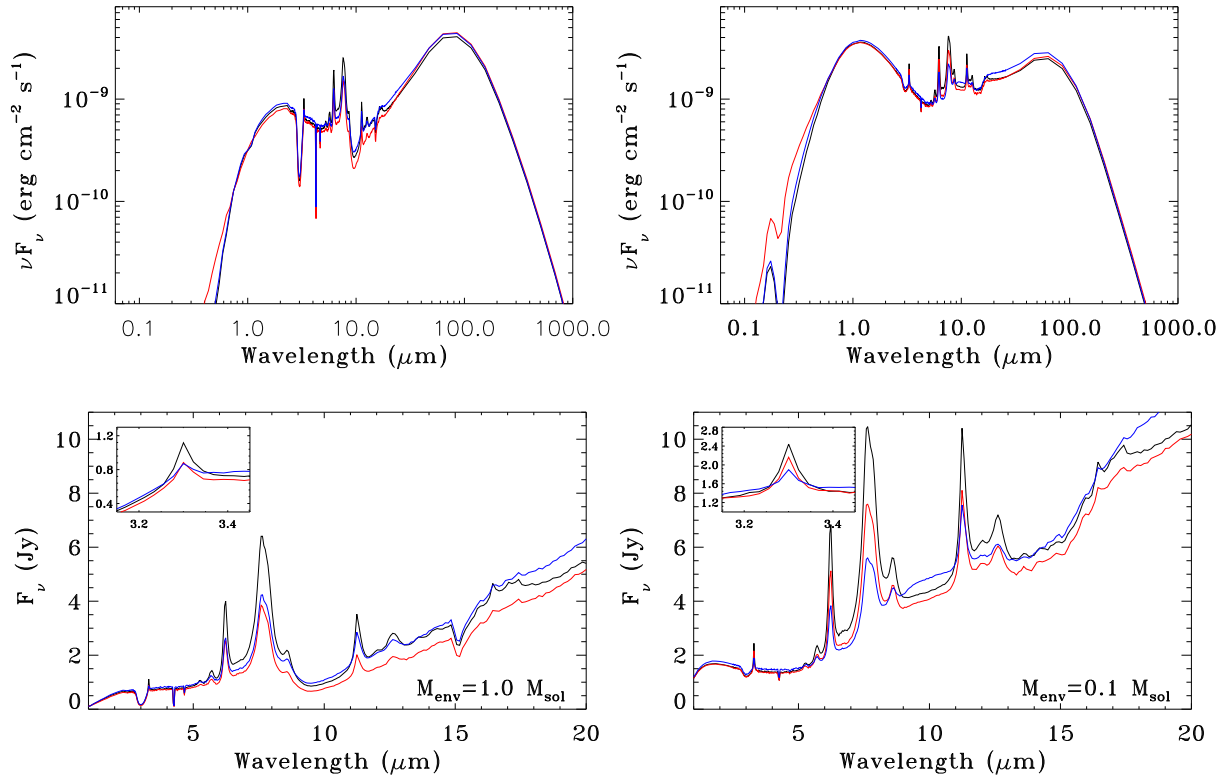


**Figure 5.7:** Model SED (top) and blow-up of spectrum (bottom) with PAHs in both envelope and disk (black), only in the disk (red) and only in the envelope (blue), at  $i = 45^\circ$ . The inset shows a blow-up of the  $3.3 \mu\text{m}$  PAH feature.

### Outflow cavity and inclination

Embedded class I objects are known to have outflows (e.g. Hogerheijde et al. 1998) so that an outflow cavity is included in our model envelope. Because of the presence of the outflow cavity, the inclination at which the object is observed is important, because at near-pole-on orientation one observes directly the central source and the disk. At larger inclinations, the envelope will be obscuring the disk.

A template model with the template PAH abundance and an envelope mass of  $1.0 M_\odot$ , seen at varying inclination angles between  $5$  and  $85^\circ$  is shown in Fig. 5.8. At an inclination of  $i = 5^\circ$  the stellar radiation field (blackbody + scaled Draine field) is directly visible and no absorption features are present. Between inclination of  $5^\circ$  and  $25^\circ$ , i.e., down the cavity and through the envelope, the appearance of the SED and the PAH features changes rapidly. The emission of the central star becomes obscured and the strength of the PAH features decreases by about a factor of 2. At increasing inclination the PAH features become weaker, but still dominate the spectrum. Ice absorption features can be seen at  $3, 4.2, 6$  and  $15 \mu\text{m}$ . At  $85^\circ$ , the disk is observed almost edge-on and the PAH emitting regions are largely masked by the disk itself. The remaining features in the spectrum extracted for an infinitely large aperture are due to scattered emission, originating from higher up in the disk atmosphere. Observed PAH feature

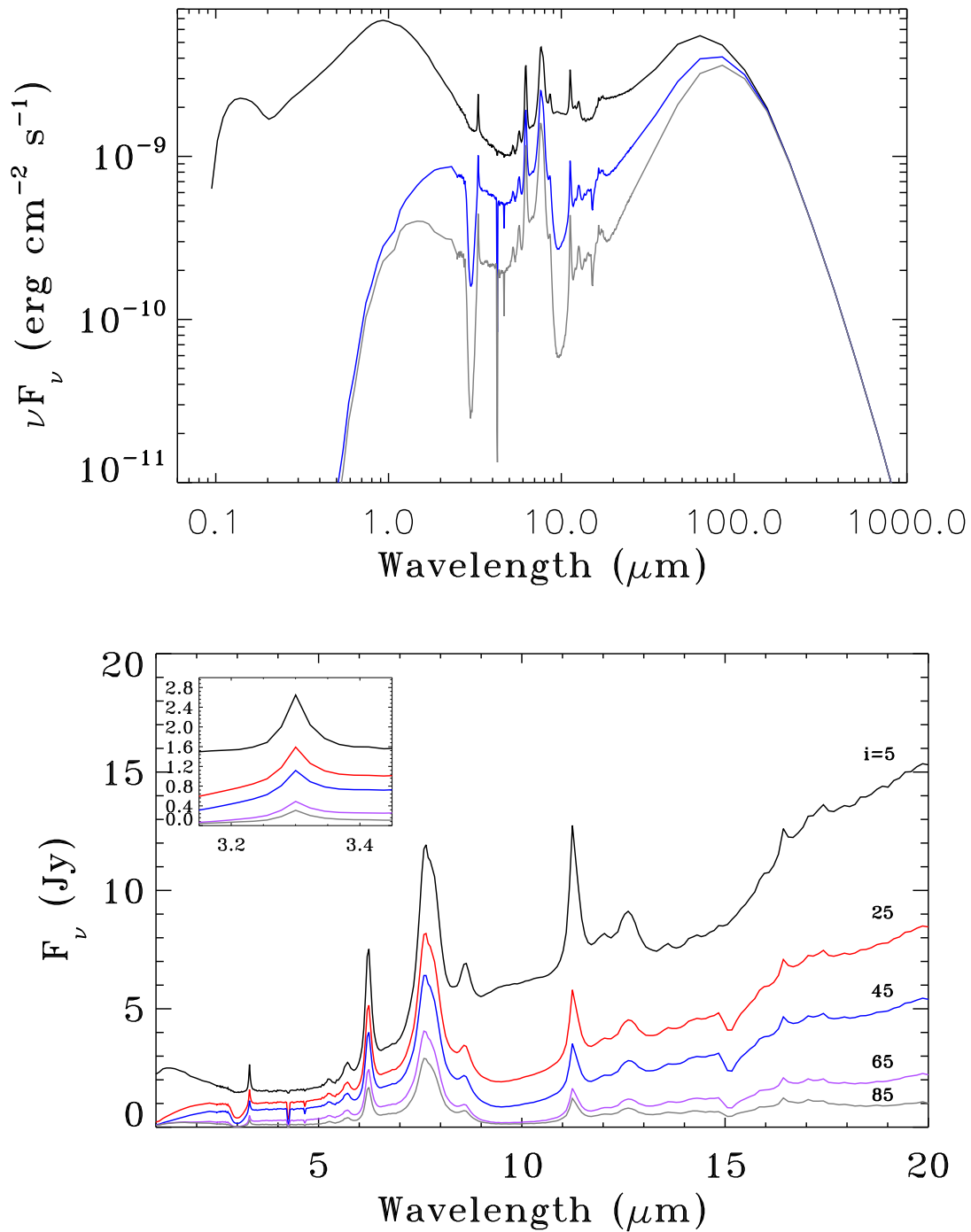


**Figure 5.8:** Model SED (top) and blow-up of spectrum (bottom) for  $i = 5, 25, 45, 65$  and  $85^\circ$  (black, red, blue, purple, gray, respectively). Curves for  $i = 25$  and  $65^\circ$  were omitted from the SED plot for clarity. The inset shows a blow-up of the 3.3  $\mu$ m PAH feature.



strengths will depend on the pointing and orientation of the limited aperture slit on the embedded source.

### PAH abundance

Models with the total PAH abundance (both ionized and neutral species) varying between the template abundance, and factors 10, 20 and 100 lower, are shown in Fig. 5.9. The envelope mass in these models is  $1.0 M_{\odot}$ . Reducing the PAH abundance by a factor 10 has the straightforward result of reducing the PAH peak flux by a factor 3. The  $3.3 \mu\text{m}$  feature is notably weak in all models, and already at a factor of 10 lower abundance not anymore detectable. Decreasing the PAH abundance also leads to an increase in the UV emission and continuum emission at far-IR wavelengths. The strongest feature,  $7.7 \mu\text{m}$ , is visible down to an abundance of  $1 \times 10^{-8}$  relative to H, i.e., a value 50x lower than the ISM.

#### 5.4.4 Summary and caveats

We find in all models that the  $7.7 \mu\text{m}$  feature is noticeably the strongest PAH feature, with the highest feature/continuum ratio. This is in sharp contrast with observational and modeling results for non-embedded class II stars with disks, where the silicate emission feature largely obscures the contribution of the  $7.7$  and  $8.6 \mu\text{m}$  features. The fact that we do not see any readily visible  $7.7 \mu\text{m}$  PAH feature in our observations then leads to the conclusion that the PAH abundance is lower than inferred for disks.

Increasing the envelope mass and decreasing PAH abundance, luminosity or UV excess all lead to weaker PAH features. The inclination has the largest influence on the PAH feature strength in the range of inclinations where the line-of-sight passes from through the envelope to through the outflow cavity. Strong PAH features are predicted to occur when observing down the outflow cavity. This situation can be recognized by a strong UV and optical part of the SED, as well as a lack of absorption features. For typical values for the luminosity, UV excess, inclination and envelope mass, derived from observational studies of embedded protostars, and assuming an ISM abundance, the PAH features should be detectable. The low detection rate of PAHs toward these sources thus suggests that the abundance of PAHs is at least 20–50x lower than in the ISM. Decreasing luminosity, UV excess or envelope mass compared with the template model changes this conclusion to a typical factor of 10–20.

One caveat remains with respect to the effect of scattering. The radiative transfer code used here assumes all scattering to be isotropic. This does not allow us to treat the effect of preferentially forward scattering of UV radiation through the outflow cavity. In the current implementation, our models could overestimate the amount of radiation received by the disk as well as overestimate the strength of the PAH features. Thus, our inferred abundance limits are on the high side. As a second caveat, an external interstellar radiation field is not included in these models. Interstellar UV radiation from outside the embedded object may become a significant source of excitation for PAHs in the envelope at large radii and would increase the predicted PAH feature

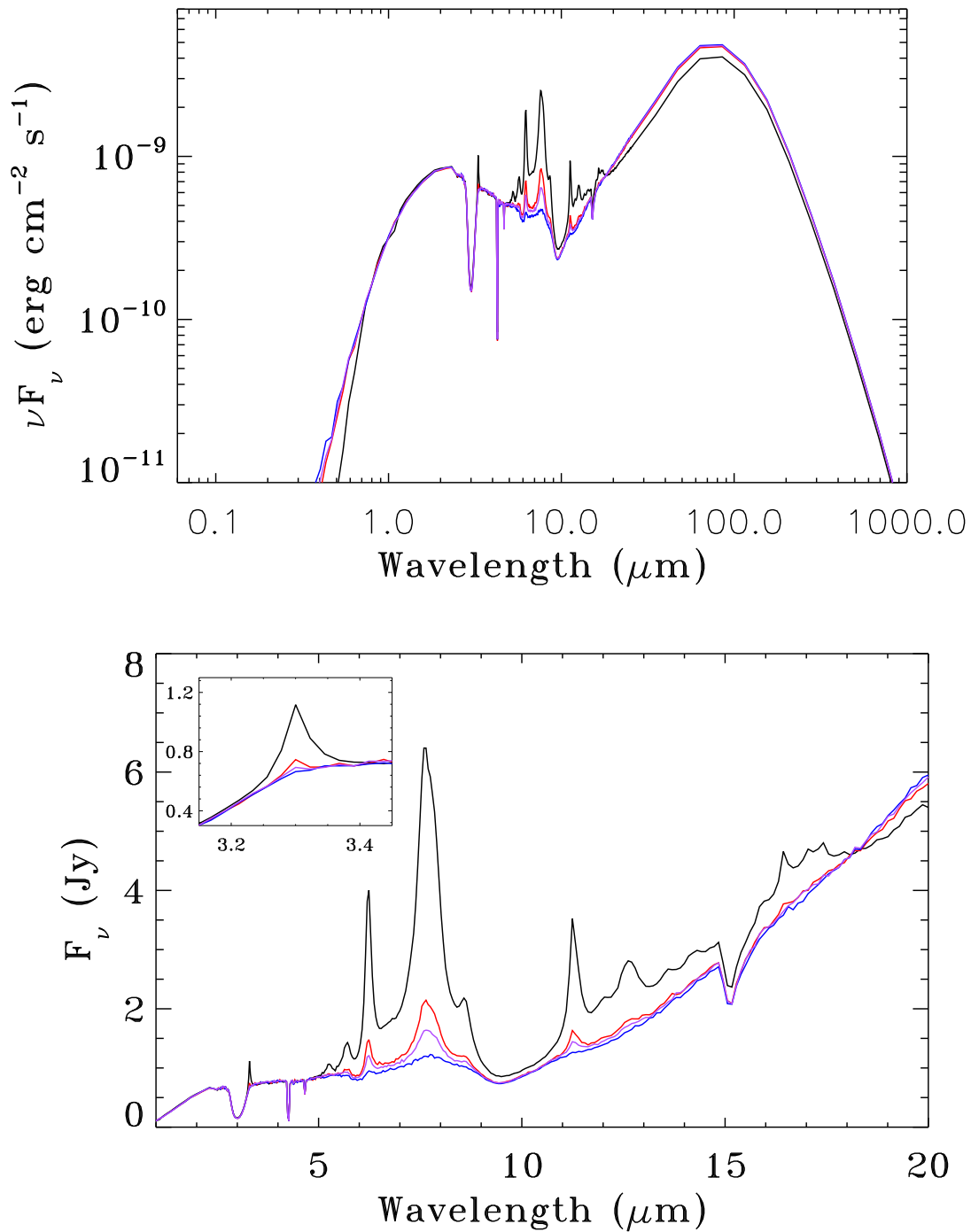


**Figure 5.9:** Model SED (top) and blow-up of spectrum (bottom) with template PAH abundance (black), and factors of 10 (red), 20 (purple) and 100 lower (blue) at  $i = 45^\circ$ . The inset shows a blow-up of the 3.3  $\mu$ m PAH feature.

strength and thus constrain the PAH abundance upper limits to smaller values.

#### 5.4.5 PAH evolution from clouds to disks

Summarizing the presence of PAHs in low-mass star formation, it is found that PAHs are observed abundantly toward the ISM and HII regions of star-forming clouds, as well as toward a small but significant fraction of class II YSO's with disks. However, in the intermediate phase of embedded low-mass class 0-I protostars PAHs appear to be absent.

Comparison with model predictions suggest that for typical conditions in class I protostars, the absence of exciting radiation and attenuation by foreground material can be excluded as reasons for the absence of the PAH features. In addition, the predicted feature / continuum ratio is well within the achieved sensitivity of the observations. This thus implies an absence of carrier as the reason for the absence of features, and the PAH abundance in the embedded protostar phase is estimated here to be at least a factor of 10–20 times lower than for typical ( $N_c = 100$ ) PAHs in the ISM. This lower abundance would be in the same range as those that inferred toward T Tauri stars in Geers et al. (2006).

What would cause this lower abundance in the embedded phase, and is this mechanism the same in the class II phase? In a cold dense environment, two possibilities for lowering the abundance of a species are recognized: coagulation or dust growth and freeze-out onto larger grains. The freeze-out of PAHs onto grains could explain the lower PAH abundance in these objects. PAH features in absorption, presumably from PAHs condensed into H<sub>2</sub>O rich ices, have been tentatively observed toward objects embedded in dense clouds (Bernstein et al. 2007, and references therein). During this phase, if exposed to UV radiation, PAHs in water ice can become significantly ionized, thus promoting ion-mediated reactions in these ices with implications for astrochemistry (Ehrenfreund et al. 2006; Gudipati & Allamandola 2006). In the class II phase, the direct irradiation of the disk by the central star can increase the temperature in the surface layers of the disk, evaporating the ice and depositing the enclosed PAHs back into the gas, thereby increasing the abundance of the PAHs again. Recent observations of edge-on disks show evidence for the continued presence of a reservoir of ice in the interior of disks (Pontoppidan et al. 2005) which can be brought to the surface by vertical mixing. However, the process of freeze-out and re-evaporation would not explain the low abundance inferred for the majority of T Tauri disk surface layers.

PAHs growing and/or agglomerating to typically 100x larger particles could be an alternative explanation of lowering the PAH abundance. This process could take place in the high density regions of the disk and envelope, in both the class I and II phase, and does not exclude freeze-out as an option. Observationally, the emission of broad emission plateaus between 6–9, 11–13 and 15–20  $\mu\text{m}$  has been attributed to large 200–2000 carbon atom PAHs and PAH clusters (Allamandola et al. 1989; Van Kerckhoven et al. 2000), which will lose their characteristic PAH emission features, thus additionally lowering the feature / continuum of these features. The detection of individual features toward T Tauri disks shows that this process is not necessarily dominant, and

that either small PAHs are still released from the ice in this phase and/or that small PAHs are still being created from, e.g., the destruction of larger grains or agglomerates through collisions.

## 5.5 CONCLUSIONS

No 3.3  $\mu\text{m}$  PAH features are detected directly associated with the embedded class I sources in the ISAAC sample of 39 objects, with the exception of IRS 48, for which other evidence suggests it is no longer an embedded object. Compact 11.2  $\mu\text{m}$  PAH emission is observed toward 2 out of 53 embedded objects in the Spitzer spectra. For all 12 sources with ISAAC and Spitzer spectra, no PAH features are detected in either. In total, PAH features are detected toward at most 2 out of 80 embedded protostars (2.5%), much lower than observed for class II T Tauri stars with disks (11–14%).

The low PAH detection rate is compared with radiative transfer model calculations. It is shown that the effects of envelope mass on the absorption of PAH features is not enough to obscure PAH features. The 7.7  $\mu\text{m}$  feature is predicted by models as the best tracer of PAH emission, while the 3.3  $\mu\text{m}$  feature is relatively weak.

Assuming typical class I stellar and envelope parameters, the absence of PAH emission is most likely explained by the absence of emitting carriers through a much lower PAH abundance in the gas, e.g., due to freeze-out of PAHs on icy layers on dust grains or agglomeration. Thus PAHs are expected to be removed from the gas already at earlier stages of star- and planet formation. Further searches for absorption PAH features are needed to constrain the presence of PAHs in icy grains.

## ACKNOWLEDGEMENTS

Support for this work, part of the Spitzer Legacy Science Program, was provided by NASA through contracts 1224608, 1230779 and 1256316 issued by the Jet Propulsion Laboratory, California Institute of Technology, under NASA contract 1407. A.C. was supported by a fellowship from the European Research Training Network “The Origin of Planetary Systems” (PLANETS, contract number HPRN-CT-2002-00308) at Leiden Observatory and by a Marie Curie Intra-European Fellowship from the European Community (contract number FP6-024227) at Observatorio Astronómico Nacional. Astrochemistry in Leiden is supported by a NWO Spinoza grant and a NOVA grant.

## REFERENCES

- Acke, B. & van den Ancker, M. E. 2004, *A&A*, 426, 151  
Allamandola, L. J., Tielens, G. G. M., & Barker, J. R. 1989, *ApJS*, 71, 733  
Basri, G. & Bertout, C. 1989, *ApJ*, 341, 340  
Bernstein, M. P., Sandford, S. A., Allamandola, L. J., et al. 1999, *Science*, 283, 1135

- Bernstein, M. P., Sandford, S. A., Mattioda, A. L., & Allamandola, L. J. 2007, *ApJ*, 664, 1264
- Chiang, E. I. & Goldreich, P. 1997, *ApJ*, 490, 368
- Cohen, M., Tielens, A. G. G. M., & Allamandola, L. J. 1985, *ApJ*, 299, L93
- Draine, B. T. & Li, A. 2001, *ApJ*, 551, 807
- Dullemond, C. P. & Dominik, C. 2004, *A&A*, 417, 159
- Dullemond, C. P. & Turolla, R. 2000, *A&A*, 360, 1187
- Ehrenfreund, P., Rasmussen, S., Cleaves, J., & Chen, L. 2006, *Astrobiology*, 6, 490
- Evans, II, N. J., Allen, L. E., Blake, G. A., et al. 2003, *PASP*, 115, 965
- Geers, V. C., Augereau, J.-C., Pontoppidan, K. M., et al. 2006, *A&A*, 459, 545
- Geers, V. C., Pontoppidan, K. M., van Dishoeck, E. F., et al. 2007, *A&A*, 469, L35
- Gudipati, M. S. & Allamandola, L. J. 2006, *ApJ*, 638, 286
- Habart, E., Natta, A., & Krügel, E. 2004, *A&A*, 427, 179
- Habart, E., Natta, A., Testi, L., & Carbillet, M. 2006, *A&A*, 449, 1067
- Hartmann, L. W. & Kenyon, S. J. 1990, *ApJ*, 349, 190
- Hogerheijde, M. R., van Dishoeck, E. F., Blake, G. A., & van Langevelde, H. J. 1998, *ApJ*, 502, 315
- Jonkheid, B., Kamp, I., Augereau, J.-C., & van Dishoeck, E. F. 2006, *A&A*, 453, 163
- Lahuis, F., Kessler-Silacci, J. E., Evans, II, N. J., et al. 2006, "c2d Spectroscopy Explanatory Supplement" (Pasadena: *Spitzer* Science Center)
- Lahuis, F., van Dishoeck, E. F., Blake, G. A., et al. 2007, *ApJ*, 665, 492
- Li, A. & Draine, B. T. 2001, *ApJ*, 554, 778
- Manske, V. & Henning, T. 1999, *A&A*, 349, 907
- Mattioda, A. L., Hudgins, D. M., & Allamandola, L. J. 2005, *ApJ*, 629, 1188
- Peeters, E., Hony, S., Van Kerckhoven, C., et al. 2002, *A&A*, 390, 1089
- Pontoppidan, K. M., Dullemond, C. P., van Dishoeck, E. F., et al. 2005, *ApJ*, 622, 463
- Pontoppidan, K. M., Fraser, H. J., Dartois, E., et al. 2003, *A&A*, 408, 981
- Ressler, M. E. & Barsony, M. 2003, *ApJ*, 584, 832
- Siebenmorgen, R., Kruegel, E., & Mathis, J. S. 1992, *A&A*, 266, 501
- Thi, W.-F., van Dishoeck, E. F., Dartois, E., et al. 2006, *A&A*, 449, 251
- Ulrich, R. K. 1976, *ApJ*, 210, 377
- van Dishoeck, E. F. & Black, J. H. 1982, *ApJ*, 258, 533
- van Dishoeck, E. F., Dartois, E., Pontoppidan, K. M., et al. 2003, *The Messenger*, 113, 49
- van Dishoeck, E. F. & van der Tak, F. F. S. 2000, in *IAU Symposium* (San Francisco: ASP), Vol. 197, *From Molecular Clouds to Planetary Systems*, ed. Y. C. Minh & E. F. van Dishoeck, 97
- Van Kerckhoven, C., Hony, S., Peeters, E., et al. 2000, *A&A*, 357, 1013
- Verstraete, L., Puget, J. L., Falgarone, E., et al. 1996, *A&A*, 315, L337
- Weingartner, J. C. & Draine, B. T. 2001, *ApJ*, 548, 296



---

# Bibliography

## REFEREED PAPERS

- *Spatially extended PAHs in circumstellar disks around T Tauri and Herbig Ae stars (Chapter 4)*  
**Geers, V.C.**, van Dishoeck, E.F., Visser, R., Pontoppidan, K.M., Augereau, J.-C., Habart, E., 2007, accepted for publication in *Astronomy & Astrophysics*
- *Cold disks: Spitzer spectroscopy of disks around young stars with large gaps*  
Brown, J.M., Blake, G.A., Dullemond, C.P., Merín, B., Augereau, J.-C., Boogert, A.C.A., Evans, N.J., II, **Geers, V.C.**, et al., 2007, *Astrophysical Journal*, 664, L107
- *Spatial separation of small and large grains in the transitional disk around the young star IRS 48 (Chapter 3)*  
**Geers, V.C.**, Pontoppidan, K.M., van Dishoeck, E.F., Dullemond, C.P., Augereau, J.-C., Merín, B., Oliveira, I., Pel, J. W., 2007, *Astronomy & Astrophysics*, 469, L35
- *Abundant crystalline silicates in the disk of a very low mass star*  
Mern, B., Augereau, J.-C., van Dishoeck, E.F., Lahuis, F., Comerón, F., Frasca, A., Brown, J.M., Kessler-Silacci, J., **Geers, V.C.**, et al., 2006, *Astrophysical Journal*, 661, 361
- *Probing protoplanetary disks with silicate emission: where is the silicate emission zone?*  
Kessler-Silacci, J.E., Dullemond, C.P., Augereau, J.-C., **Geers, V.C.**, van Dishoeck, E.F., Evans, N.J., II, Blake, G.A., Brown, J., 2006, *Astrophysical Journal Letters*, 659, 680
- *PAH chemistry and IR emission from circumstellar disks*  
Visser, R., **Geers, V.C.**, Dullemond, C.P., Augereau, J.-C., Pontoppidan, K.M., van Dishoeck, E.F., 2007, *Astronomy & Astrophysics*, 466, 229
- *Modeling Spitzer observations of VV Ser. II. An extended quantum heated nebula and a disk shadow*  
Pontoppidan, K.M., Dullemond, C.P., Blake, G.A., Evans, N.J., II, **Geers, V.C.**, Harvey, P.M., Spiesman, W., 2006, *Astrophysical Journal*, 656, 991
- *C2D Spitzer-IRS spectra of disks around T Tauri stars II. PAH emission features (Chapter 2)*  
**Geers, V.C.**, Augereau, J.-C., Pontoppidan, K.M., Dullemond, C.P., Visser, R.,

- Kessler-Silacci, J.E., Evans, N.J., II, van Dishoeck, E.F., Blake, G.A., Boogert, A.C.A., Brown, J.M., Lahuis, F., Merín, B., 2006, *Astronomy & Astrophysics*, 459, 545
- *c2d Spitzer IRS Spectra of Disks around T Tauri Stars. I. Silicate Emission and Grain Growth*  
Kessler-Silacci, J.E., Augereau, J.-C., Dullemond, C.P., **Geers, V.C.**, Lahuis, F., Evans, N.J., II, van Dishoeck, E.F., Blake, G.A., Boogert, A.C.A., Brown, J., Jørgensen, J.K., Knez, C., Pontoppidan, K.M., 2006, *Astrophysical Journal*, 639, 275
  - *Spitzer Space Telescope Spectroscopy of Ices toward Low-Mass Embedded Protostars*  
Boogert, A.C.A., Pontoppidan, K.M., Lahuis, F., Jørgensen, J.K., Augereau, J.-C., Blake, G.A., Brooke, T.Y., Brown, J., Dullemond, C.P., Evans, N.J., II, **Geers, V.C.**, et al., 2004, *Astrophysical Journal Supplement Series*, 154, 359
  - *Rotation, pulsations and magnetic field in V 2052 Ophiuchi: A new He-strong star*  
Neiner, C., Henrichs, H.F., Floquet, M., Frémat, Y., Preuss, O., Hubert, A.-M., **Geers, V.C.**, Tijani, A.H., Nichols, J.S., Jankov, S., 2003, *Astronomy & Astrophysics*, 411, 565
  - *Discovery of a magnetic field in the Slowly Pulsating B star zeta Cassiopeiae*  
Neiner, C., **Geers, V.C.**, Henrichs, H.F., Floquet, M., Frémat, Y., Hubert, A.-M., Preuss, O., Wiersema, K., 2003, *Astronomy & Astrophysics*, 406, 1019

#### CONFERENCE PROCEEDINGS

- *PAHs in circumstellar disks around T Tauri stars*  
**Geers, V.C.**, Augereau, J.-C., Pontoppidan, K.M., Dullemond, C.P., Visser, R., Boogert, A.C.A., Kessler-Silacci, J., Lahuis, F., van Dishoeck, E.F., c2d IRS Team 2005, in proceedings of "Protostars and Planets V", eds. Reipurth, B., Jewitt, D., Keil, K. (University of Arizona Press)
- *PAHs in circumstellar disks around T Tauri stars*  
**Geers, V.C.**, Augereau, J.-C., Pontoppidan, K.M., Dullemond, C.P., Visser, R., van Dishoeck, E.F., the c2d IRS Team, 2005, in proceedings of the IAU Symposium 231 on "Astrochemistry: Recent Successes and Current Challenges", eds. Lis, D.C., Blake, G.A., Herbst, E. (University Press, Cambridge)
- *TIMMI2 and VLT-ISAAC Spectroscopy of Circumstellar Dust Disks A Spatially Resolved 3.3 micron PAH Feature Around HD100546*  
**Geers, V.C.**, Augereau, J.-C., Pontoppidan, K.M., Käufel, H.-U., Lagrange, A.-M., Chauvin, G., van Dishoeck, E.F., 2005, in proceedings of ESO Workshop on "High Resolution Infrared Spectroscopy in Astronomy" (Springer Berlin, Germany, astro-ph/0403708), p. 239
- *Discovery of a magnetic field in the B2IV star ζ Cassiopeia*  
**Geers, V.C.**, Henrichs, H.F., Neiner, C., 2003, appeared in the proceedings of the conference on "Magnetism and Activity of the Sun and Stars", 2002, Toulouse, France (EAS Publication Series, Vol. 9, 2003)



---

# Polycyclische Aromatische Koolwaterstoffen in Schijven rond Jonge Zon-type Sterren

## STUDIE VAN STER- EN PLANEETVORMING

Het onderzoek in dit proefschrift betreft de vorming van sterren en planeten. Binnen dit onderzoek zijn er nog veel vragen onbeantwoord. Hoeveel zon-type sterren hebben een circumstellaire schijf? Wat is de typische grootte van deze schijven en hoeveel massa bevindt zich hier in? Blijven deze schijven lang genoeg bestaan voor de vorming van planeten? Hoe groeien de kleine stofdeeltjes naar grote rotsblokken? Waaruit bestaan de stofdeeltjes in deze schijven, die de bouwstenen van toekomstige planeten zijn, en hoe evolueert de samenstelling van dit stof?

In de afgelopen 20 jaar is het onderzoek naar het ontstaan van lage massa sterren zoals onze eigen Zon één van de snelst ontwikkelende gebieden in de moderne sterrenkunde geworden. Met de komst van telescopen die zeer gevoelig zijn voor mid-infrarode straling, op de Aarde en in de ruimte, kunnen wij nu voor het eerst deze lichtzwakke jonge sterren waarnemen in nabij gelegen stervormingsgebieden.

In dit proefschrift bestuderen wij het stof rondom deze jonge zon-type sterren, en in het bijzonder een specifiek soort stof, namelijk de Polycyclische Aromatische Koolwaterstoffen (afgekort PAKs), in het Engels aangeduid als Polycyclic Aromatic Hydrocarbons (PAHs). PAKs zijn een familie van grote moleculen, ook wel beschouwd als kleine stofdeeltjes, die alom waargenomen worden in nabij gelegen stervormingsgebieden.

In deze samenvatting wordt eerst een beschrijving gegeven van ons huidige beeld van de vorming van lage massa zon-type sterren en de planetenstelsels er omheen, gevolgd door een samenvatting van de PAKs, hun molecuul structuur en hun typische eigenschappen. Vervolgens wordt in het kort aangegeven welke waarnemingen en modelleer methoden zijn gebruikt. Als laatste wordt een overzicht van de belangrijkste vragen en resultaten in dit proefschrift gegeven.

## ONS HUIDIGE BEELD VAN LAGE MASSA STER- EN PLA-NEETVORMING

Sterren worden gevormd in grote wolken van waterstofgas en stof, met een massa tussen 100 en 1000 zonsmassa's. In het binnenste van deze wolken is het koud ( $\sim 10$  Kelvin ofwel  $-263^\circ$  Celsius) en is de dichtheid relatief hoog (10.000 – 100.000 deeltjes per kubieke centimeter) vergeleken met de omliggende ruimte tussen de sterren. Deze wolken worden in stand gehouden door magneetvelden en turbulentie van het gas. Wanneer dit magneetveld zwakker wordt en/of de turbulentie afneemt kunnen er zich gebieden met een hogere dichtheid vormen. Deze gebieden met hogere dichtheid kunnen zich via de zwaartekracht samentrekken in kernen en verdere materie aantrekken in een proces wat accretie genoemd wordt. Gedurende deze accretie fase kan de kern groeien tot een massa van één tot enkele zonsmassa's, en wordt de gravitatie energie van de materie uitgezonden als straling. In de oorspronkelijke gaswolk is er vrijwel altijd geordende rotatie van de materie aanwezig. Deze rotatie veroorzaakt een middelpuntvliedende kracht op de invallende materie waardoor deze materie deels afgeremd wordt en in het vlak van rotatie een schijf vormt rondom de ster. In deze fase is de centrale protoster en diens circumstellaire schijf nog volledig omhuld door het gas en stof in de omliggende wolk (zie linkerpaneel van Figuur 7.1), en daardoor onzichtbaar bij alle golflengten (UV, visueel, infrarood) met uitzondering van het millimeter en radiogebied. Deze fase wordt de Klasse 0 fase genoemd en duurt relatief kort (binnen tienduizend jaar na het begin van de samentrekking van de kern).

Terwijl de materie van omliggende gaswolk, ofwel omhulsel, nog steeds invalt op de schijf en via de schijf verder naar de ster beweegt, kan er een sterke uitwaartse straalstroom van materie, genaamd 'jets', ontstaan in de polaire richtingen van de ster, loodrecht op het rotatievlak. Deze jets kunnen het deel van het omhulsel rond de rotatieas wegblazen en de aanwezigheid van jets is waargenomen als gaten in gaswolken en scherp gedefinieerde uitstromingen van gas bij hoge snelheden (zie middelste paneel Figuur 7.1). De accretie van materie binnenin de sterschijf richting de ster gaat gepaard met veel botsingen en gravitationele interactie welke het materiaal in de schijf opwarmen. Hierdoor gaat de schijf met toenemende lichtkracht zelf warmtestraling in het ver-infrarood uitzenden. Deze fase wordt de Klasse 0-I fase genoemd, en duurt ongeveer honderdduizend jaar. Gedurende deze fase wordt de straling van de centrale ster en het warme stof in de schijf meestal nog steeds versluierd door het omliggende stof en gas.

Het is onvermijdelijk dat op een gegeven moment materie in het omhulsel op begint te raken en hierdoor komt er een einde aan de inval van materie. Vervolgens zal de accretie van materie binnenin de schijf richting de ster ook sterk afnemen, waardoor de lichtkracht van de sterschijf weer afneemt. De sterwind kan nu materie wegblazen in alle richtingen. De circumstellaire schijf met diens veel hogere dichtheid ondervindt in het begin weinig invloed van de sterwind. Door het uitwaaien van het omliggende gas en stof wordt geleidelijk de centrale ster en schijf zichtbaar bij alle golflengten (zie rechterpaneel Figuur 7.1).

Dit markeert de start van de Klasse II fase welke ongeveer één tot tien miljoen jaar

duurt. Gedurende deze fase is de centrale ster grotendeels gevormd en trekt de ster verder samen onder zwaartekracht totdat de druk en temperatuur in de kern hoog genoeg worden voor de start van kernfusie van eerst deuterium en daarna waterstof. Dit kernfusie proces produceert zoveel warmte en lichtstraling dat het tegendruk geeft aan de zwaartekracht zodat de samentrekking tot halt komt. Op het moment dat de ster in deze stabiele situatie is beland zegt men wel dat de ster is geboren, met leeftijd 0. Afhankelijk van de hoeveelheid beschikbare waterstof, leeft de ster in deze fase tussen de tien miljoen en tien biljoen jaar.

Gedurende de Klasse II fase is de toevoer van materie aan de schijf gestopt en begint de materie in de schijf door verschillende processen verwijderd te worden. Straling van de centrale protoster verwarmt het gas en stof in de bovenlagen van de schijf, waardoor stof verdampt en er een wind van materie van de schijf beweegt. Tegelijkertijd kunnen de stofdeeltjes in de schijf door botsingen groeien tot centimeter grote steentjes. Wanneer stofgroei tot kilometer grote stofdeeltjes leidt spreken we van planetesimalen en deze kunnen door zwaartekracht meer massa beginnen aan te trekken en de lokale structuur van de schijf beïnvloeden. De grootste van deze planetesimalen kunnen uiteindelijk planeten vormen, en leiden tot gaten in hun baan in de circumstellaire schijf rondom de jonge ster. Deze gaten worden in sommige schijven waargenomen als de afwezigheid van de infrarood straling van warm stof en deze worden "koude schijven" genoemd. Het grootste deel van het stof is in deze fase inmiddels niet meer het oorspronkelijke stof wat op de schijf is ingevallen, maar eerder stofdeeltjes die geproduceerd zijn in de botsingen tussen grotere planetesimalen.

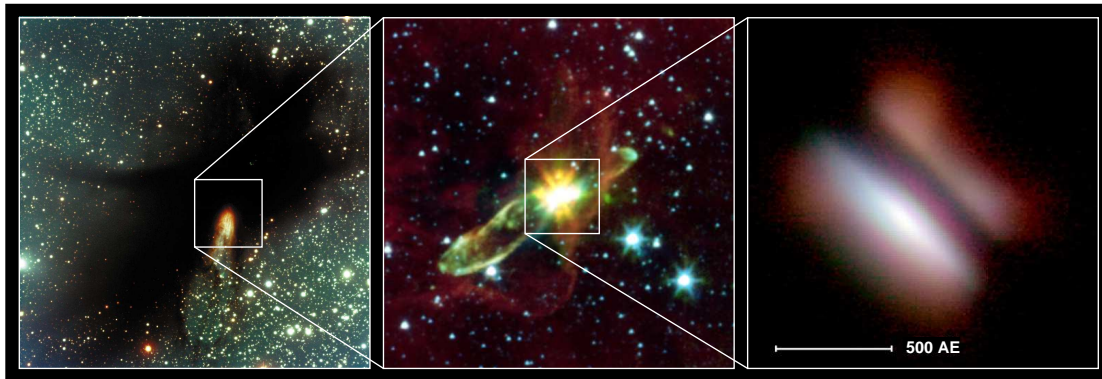
De combinatie van sterwind en stralingsdruk van de ster op de schijf veroorzaakt een erosie van de kleinste stofdeeltjes die nog niet gevangen zijn. Deze erosie verwijdert het resterende gas en stof totdat er uiteindelijk alleen een ster met een planetenstelsel overblijft. In dit proefschrift focussen wij voornamelijk op jonge sterren in de Klasse I en II fasen, tot aan de overgang naar de planetesimalen schijf.

## POLYCYCLISCHE AROMATISCHE KOOLWATERSTOFFEN

### Structuur en straling van PAKs

PAKs zijn grote moleculen opgebouwd uit meerdere ringen van ieder zes koolstofatomen, met waterstof atomen aan de uiteinden. De molecuul structuur van een aantal PAKs is weergegeven in Figuur 1.1 op pagina 3. Omdat de koolstofatomen een aantal elektronenbindingen met elkaar delen worden deze ringen aromatische structuren genoemd. Op aarde komen PAKs voornamelijk voor als product bij verbranding van materiaal, oftewel roet.

PAKs worden voornamelijk geëxciteerd door ultra-violet (UV) straling. Absorptie van een UV foton resulteert in elektronische excitatie welke intern wordt omgezet in vibrationele energie. Vervolgens zenden de PAKs de energie in meerdere infrarood fotonen weer uit. Deze infrarood straling uit zich in zeer karakteristieke emissie banden bij bepaalde golflengten. De gelijktijdige aanwezigheid van deze specifieke banden in een infrarood spectrum kan gezien worden als een soort vingerafdruk en is een



**Figuur 7.1:** Links: Donkere koude wolk van gas en stof waar binnenin een ster aan het vormen is. Midden: infra-rood close-up van een jonge ster met jets, binnenin een gaswolk. Rechts: close-up van een schijf rondom een jonge ster, gezien vanaf de zijkant. AE is Astronomische Eenheid, de gemiddelde afstand tussen de Aarde en de Zon. Merk op dat deze plaatjes richting verschillende gebieden genomen zijn.

Credits: links: VLT image van Bok globule BHR 71 (J. Alves et al., ESO); midden: Spitzer IRAC image van lage massa protoster met jet, HH46 (NASA/JPL-Caltech/A. Noriega-Crespo (SSC/Caltech), Digital Sky Survey); rechts: Keck nabij-infrarood image van schijf rondom de jonge ster PDS 144N, (Perrin et al. 2006, ApJ, 645, 1272).

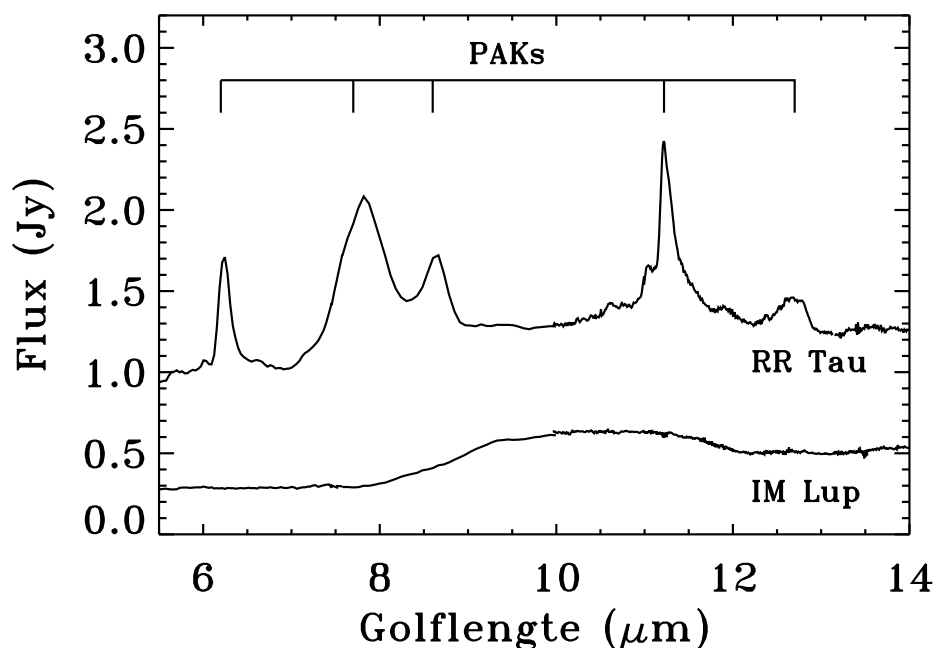
duidelijke maat voor de aanwezigheid van PAKs (zie Figuur 7.2). De grootte en de elektrische lading van PAKs kunnen de vorm en onderlinge verhouding van de sterkte van de PAK banden beïnvloeden. Grote PAKs verliezen de scherp gedefinieerde emissie banden, en zenden hun straling eerder in een brede ondiepe emissie band uit. Hierdoor kan de aanwezigheid van PAK emissie banden geïnterpreteerd worden als de aanwezigheid van relatief kleine stofdeeltjes. Daarnaast kan de onderlinge verhouding van de emissie lijnen gebruikt worden als een maat voor de lading van stof in bepaalde gebieden.

## Evolutie en rol van PAKs in de ruimte

De karakteristieke emissie banden van PAKs zijn waargenomen in veel verschillende soorten gebieden in het heelal, waaronder de sterwinden rondom uitgestorven sterren, in andere sterrenstelsels, en in stervormingsgebieden.

Men denkt dat PAKs voornamelijk gevormd worden in de sterwinden van koolstofrijke sterren welke aan het einde van hun leven zijn gekomen. In deze wind geven de relatief hoge dichtheid, hoge temperatuur en hoge fractie van het aanwezige koolstof de juiste condities voor het vormen van de eerste koolstofringen die de bouwstenen vormen voor grotere PAK moleculen. De materie in de sterwind komt uiteindelijk terecht in de ruimte tussen de sterren genaamd het interstellair medium. PAKs zijn dan ook waargenomen in het interstellair medium, met name in de buurt van heldere sterren die voor voldoende UV zorgen om de PAKs aan te stralen.

Aangezien PAKs sterk lokaal verhit worden door de UV straling gedragen PAKs



**Figuur 7.2:** Spitzer mid-infrarood spectra van twee jonge sterren met schijven. De karakteristieke emissie banden van PAKs zijn alleen zichtbaar in richting de ster RR Tau.

zich anders dan de typische stofdeeltjes. Op grote afstanden van sterren, waar de intensiteit van het interstellair stralingsveld laag is, is het meeste stof te koud om infraroodstraling uit te zenden. In deze gebieden kunnen PAKs, door UV absorptie, wel nog veel straling uitzenden in het infrarood.

PAKs spelen een belangrijke rol in de gebieden waar zij worden waargenomen. In het interstellair medium dragen ze bij aan de temperatuur balans van de materie. Ze zijn een goede markering van de aanwezigheid van UV straling en daardoor indirect een goede indicator voor stervorming in gebieden waar de dichtheid erg hoog is. In de schijf rondom jonge sterren vormen ze een maat voor de sterkte van het stralingsveld in het oppervlakte van de schijf, en kunnen ze gebruikt om de structuur van de schijf te bepalen. Daarnaast kunnen PAKs ook de schijf beïnvloeden, bijvoorbeeld door na absorptie van UV-straling elektronen uit te zenden welke de gemiddelde elektrische lading van het lokale stof veranderen en het gas door botsingen kunnen verhitten.

Ook voor de chemie zijn PAKs belangrijk. In de ruimte is de dichtheid zo laag dat chemische reacties waarbij meer dan twee deeltjes nodig zijn eigenlijk niet voorkomen omdat botsingen tussen slechts twee deeltjes al heel uitzonderlijk zijn. Als een klein stofdeeltje met een groot oppervlak vormen PAKs een lokatie voor atomen om op vast te haken, waar atomen elkaar met grotere kans kunnen vinden voor chemische reactie.

## DIT PROEFSCHRIFT

In dit proefschrift behandelen we de rol van PAKs in de omhulsels en schijven rondom jonge zon-type sterren. We behandelen daarbij de volgende vragen. Wat gebeurt er met PAKs in de vroege fase van stervorming, wanneer de protoster nog omhuld wordt door een wolk van gas en stof? Zijn PAKs aanwezig in de jonge, zich nog vormende lage massa zonnestelsels? Komt de straling van PAKs in deze bronnen van de omliggende gaswolk of van het materiaal in de circumstellaire schijf? Hoe groot zijn de moleculen zoals wij ze waarnemen in deze gebieden? Wat kunnen wij uit hun aanwezigheid leren over de schijfstructuur, de evolutie en over stofgroei?

We gebruiken in deze studie enkele van de meest moderne nieuwe infrarood spectrometers en camera's, welke in de afgelopen 3–10 jaar beschikbaar zijn gekomen, waaronder de ISAAC en VISIR instrumenten op de Very Large Telescope in Chili, en ook het IRS instrument aan boord van de NASA Spitzer Space Telescope.

In Hoofdstuk 2 presenteren wij de eerste studie met de Spitzer infrarode ruimtetelescoop naar de aanwezigheid van PAKs rondom jonge lage en middelzware jonge sterren. PAKs worden in slechts 4 van de 37 zon-type sterren gevonden ( $\pm 11\%$ ), wat een lagere fractie is dan waargenomen richting middelzware sterren (54%). Uit berekeningen met stralingstransport modellen concluderen wij dat de abundantie van PAKs in deze bronnen minstens 10–100x lager moet zijn dan in het interstellair medium en dat bij deze abundantie onze waarnemingen niet gevoelig genoeg waren voor het waarnemen van PAKs rondom nog koudere ( $T \leq 4200$ ) jonge sterren. De  $11.2 \mu\text{m}$  PAK emissie lijn wordt het best waargenomen, terwijl de emissielijnen bij  $7.7$  en  $8.6 \mu\text{m}$  in de meeste gevallen worden versluierd door de aanwezigheid van emissie van silicaten.

In Hoofdstuk 3 presenteren wij één van de eerste ruimtelijk opgeloste plaatjes van stof en PAKs in een schijf rondom een hele lage massa ster, van type M0, IRS 48. Deze ster is de laagste massa ster waarvoor PAKs zijn waargenomen. De PAKs zijn direct aanwezig in de sterschijf zelf, en diens aanwezigheid duidt op extra UV emissie van de centrale ster. Uit de plaatjes concluderen we verder dat er een gat in het binnenste deel van de schijf is gevormd waar de grootste stofdeeltjes verwijderd zijn, vermoedelijk door de aanwezigheid van een vormende planeet. Dit ogenschijnlijke gat in de stofpopulatie in het binnendeel van de schijf wordt opgevuld met PAK emissie, oftewel emissie van kleine stofdeeltjes. Deze ruimtelijke scheiding van kleine en grote stofdeeltjes duidt erop dat de twee stofpopulaties verschillend evolueren.

In Hoofdstuk 4 presenteren wij een studie naar de ruimtelijke verdeling van PAK emissie rondom protoplanetaire schijven. Hiervoor maken we gebruik van de hoge ruimtelijke resolutie van de ESO Very Large Telescope en de ISAAC, VISIR en NACO instrumenten. Uit de waarnemingen blijkt dat de PAK emissie wordt uitgezonden op kleine schaal van enkele tientallen tot  $\pm 100$  Astronomische Eenheden. Dit bevestigt dat de PAKs direct geassocieerd zijn met de schaal van de stofschijf en niet alleen toe te kennen zijn aan diffuse voorgrond emissie van de oorspronkelijke gaswolk waaruit de ster is ontstaan. Deze kleine schaal van ruimtelijke uitbreidbaarheid van de PAK emissie bij  $8.6$  en  $11.2 \mu\text{m}$  is consistent met grotere PAKs van  $\geq 100$  koolstof atomen.

In Hoofdstuk 5 presenteren wij de eerste spectroscopische studie met VLT-ISAAC en de Spitzer ruimtetelescoop naar de aanwezigheid van PAK emissie in de vroege fa-

se van lage massa jonge sterren, wanneer deze nog omgeven worden door een wolk van gas en stof (Klasse I). We vinden dat er in het overgrote deel van deze Klasse I bronnen (~97%) geen PAK emissie direct geassocieerd is met de centrale ster. Uit modelberekeningen concluderen wij dat de PAK abundantie in deze bronnen minstens een factor 10–20 lager moet zijn dan in het interstellair medium. Dit zou kunnen gebeuren doordat meerdere PAKs samengeklonterd zijn tot grotere PAKs en/of doordat PAKs in deze fase zijn uitgevroren op de ijslaagjes van stofdeeltjes.





---

# Curriculum Vitae

I was born on March 18, 1980 in the town of Naarden. I have spent the first 2 decades of my life in the city of Almere, which is only a few years older than myself. During my third year at high school, I was among a few students invited to attend a master-class at the University of Amsterdam on “Neutron Stars and Black Holes” at which point physics and astronomy really captured my interest. In 1998, I started my studies astrophysics at the University of Amsterdam and obtained my Master of Science degree (“doctoraal”) in January of 2003. During my third year I had an early opportunity to go and assist on a 12 nights observing run at the Observatoire de Pic du Midi, in the Pyrenees. As a result, I returned the next year as principal observer and wrote my Master’s Thesis on our “Discovery of a Magnetic Field in the Early B-type star  $\zeta$  Cassiopeia”, under the supervision of Prof. Dr. Huib Henrichs. I began my PhD studies at Leiden University in February 2003 under the supervision of Prof. Dr. Ewine van Dishoeck. The purpose of the thesis work was to study the dust around young low-mass stars using data from the NASA Space Infrared Telescope Facility, which is now known as the Spitzer Space Telescope.

During my time in Leiden, I have been on three observing trips to the ESO Very Large Telescope in Chile and one to the 3.6 meter Telescope at La Silla Observatory in Chile. I have had the privilege of joining the team behind one of the six large Spitzer Legacy programs, “From Molecular Cores to Planet-forming Disks”, working with highly sensitive mid-infrared spectroscopy and imaging from the Spitzer Space Telescope. I have been involved in the Guaranteed Time Observation program of the Dutch-French team working on the mid-infrared spectrometer and imager VISIR on the ESO Very Large Telescope. I have been on working visits to the Max Planck Institut in Heidelberg and the University of Texas in Austin.

In November of 2007, I will move to Canada, to work as a Postdoctoral Fellow at the University of Toronto, in the group of Prof. Dr. Ray Jayawardhana.



---

# Acknowledgements

In closing, I would like to express my gratitude to all the people without whose support this thesis would not have been possible.

First of all, I am grateful for the opportunity to do my PhD research at Leiden Observatory. The Observatory has a stimulating and professional atmosphere, with a steady stream of visitors, new students, PhDs, postdocs (and even staff) to learn from and share ideas with. A special thank you to the staff who keep the Observatory running so smoothly, especially throughout our recent period of growth. My thanks to Kirsten and Jeanne for all the times you helped me with rooms, beamers, faxes, etc., as well as the ever helpful people from the computer group, who maintain the most stable and visitor-friendly computing environment I have encountered so far.

My thesis research has been primarily funded by NWO, through the Spinoza grant of Professor Ewine van Dishoeck. In addition, I am grateful for the financial support from the Leidsche Kerkhoven Bosscha Fonds, Leids Sterrewacht Fonds, the c2d program and the European PLANET network, for conferences, work visits and observing trips.

The wealth of observations which form the basis of this thesis are all thanks to the many national and international collaborations which Leiden Observatory and particularly our Astrochemistry group are involved in. Within the Dutch astronomical community, I have enjoyed participating in the ISM/CSM meetings and the Dutch VISIR GTO team. An essential part of this thesis are the observations I have carried out at the ESO telescopes in Chile, and I'm grateful to their staff for making those visits both scientifically fruitful and enjoyable. I consider myself fortunate to have been involved in the Spitzer Legacy program "From Molecular Cores to Planet Forming Disks", which brought me, straight from the start of my thesis research, into contact with a large international group of talented researchers and which has offered many opportunities to travel the world for team meetings, conferences and work visits as well as collaborations for the future. The program has led to a wealth of interesting observations, of which only a small fraction is covered in this thesis.

On both a scientific and social level, I have really enjoyed my time with all the people from the Astrochemistry group and recently also the Disk Evolution group. I'm glad chance brought me into the North End club on the third day I started here. We never quite managed to do one of their whiskey tasting nights but I believe our New Year's party made up for it. A big thank you to all the people who have contributed to and shared in our little coffee club. At last count we have pinned up forty-two different coffee labels!

To my office mates: Jean-Charles, our discussions were always educating and enjoyable and helped me out a lot when I just started. Saskia, I have great admiration for the light-hearted manner in which you managed to complete your thesis, despite the difficult circumstances. Dave, I owe it to you for upholding our fine coffee tradition, especially after Fredrik, Jes, Jean-Charles and Klaus left.

Tot slot een woord aan mijn ouders en familie. Jullie onmisbare steun, advies en interesse hebben mij altijd geholpen om mijzelf verder te ontwikkelen.

Kerstin, jouw onvoorwaardelijke liefde, geduld en zorg hebben dit alles mogelijk gemaakt. Ik heb geluk dat ik mijn jaren in Leiden met jou mocht delen en ik kijk uit naar ons nieuwe avontuur.